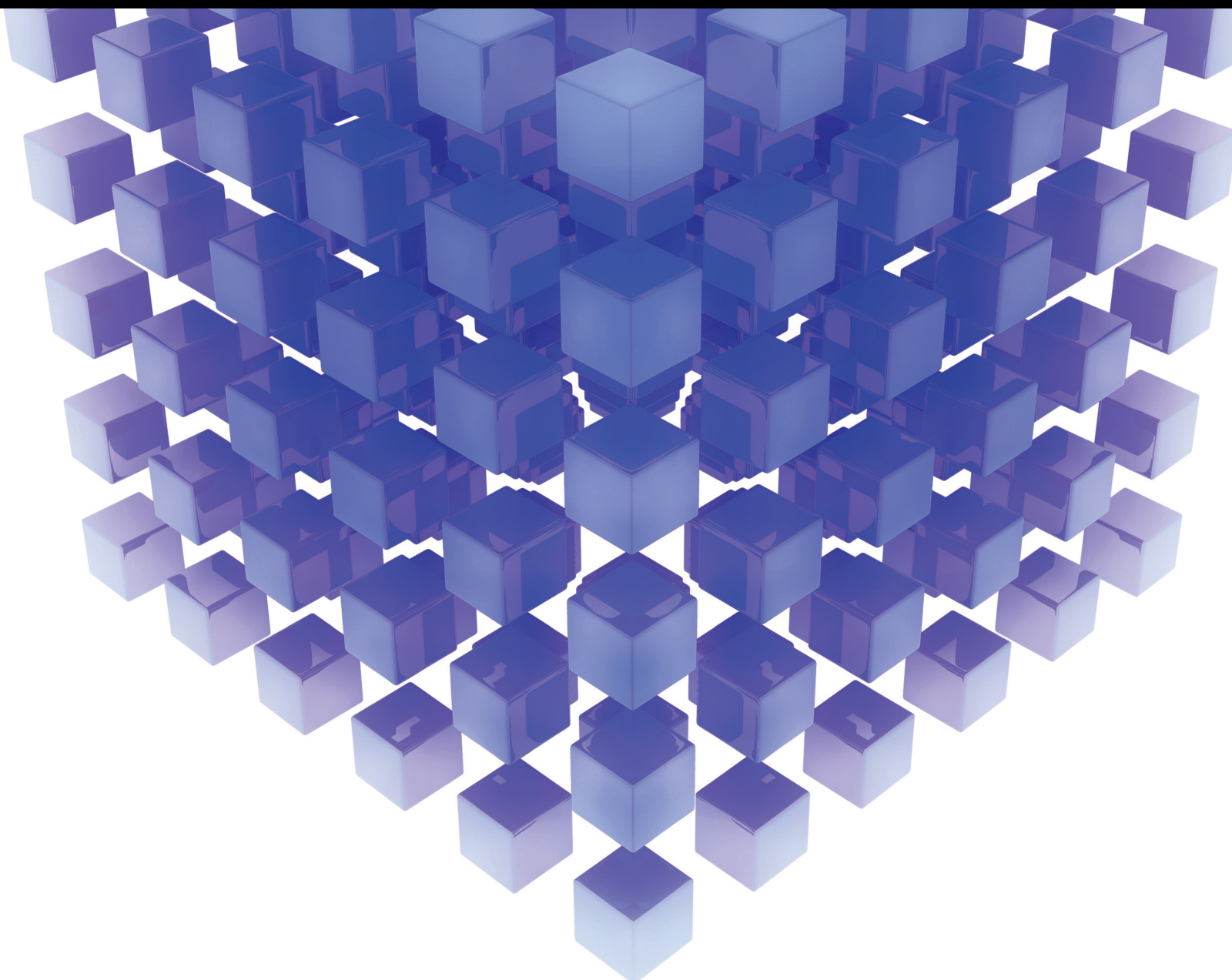


Green Transformation and Upgrading of the Manufacturing Industry

Lead Guest Editor: Conghu Liu

Guest Editors: Wei Cai and Jorge Cunha





Green Transformation and Upgrading of the Manufacturing Industry

Mathematical Problems in Engineering

**Green Transformation and Upgrading
of the Manufacturing Industry**

Lead Guest Editor: Conghu Liu


Guest Editors: Wei Cai and Jorge Cunha



Copyright © 2023 Hindawi Limited. All rights reserved.

This is a special issue published in “Mathematical Problems in Engineering.” All articles are open access articles distributed under the Creative Commons Attribution License, which permits unrestricted use, distribution, and reproduction in any medium, provided the original work is properly cited.

Chief Editor

Guangming Xie , China

Academic Editors

Kumaravel A , India
Waqas Abbasi, Pakistan
Mohamed Abd El Aziz , Egypt
Mahmoud Abdel-Aty , Egypt
Mohammed S. Abdo, Yemen
Mohammad Yaghoub Abdollahzadeh
Jamalabadi , Republic of Korea
Rahib Abiyev , Turkey
Leonardo Acho , Spain
Daniela Addessi , Italy
Arooj Adeel , Pakistan
Waleed Adel , Egypt
Ramesh Agarwal , USA
Francesco Aggogeri , Italy
Ricardo Aguilar-Lopez , Mexico
Afaq Ahmad , Pakistan
Naveed Ahmed , Pakistan
Elias Aifantis , USA
Akif Akgul , Turkey
Tareq Al-shami , Yemen
Guido Ala, Italy
Andrea Alaimo , Italy
Reza Alam, USA
Osamah Albahri , Malaysia
Nicholas Alexander , United Kingdom
Salvatore Alfonzetti, Italy
Ghous Ali , Pakistan
Nouman Ali , Pakistan
Mohammad D. Aliyu , Canada
Juan A. Almendral , Spain
A.K. Alomari, Jordan
José Domingo Álvarez , Spain
Cláudio Alves , Portugal
Juan P. Amezcua-Sanchez, Mexico
Mukherjee Amitava, India
Lionel Amodeo, France
Sebastian Anita, Romania
Costanza Arico , Italy
Sabri Arik, Turkey
Fausto Arpino , Italy
Rashad Asharabi , Saudi Arabia
Farhad Aslani , Australia
Mohsen Asle Zaem , USA

Andrea Avanzini , Italy
Richard I. Avery , USA
Viktor Avrutin , Germany
Mohammed A. Awadallah , Malaysia
Francesco Aymerich , Italy
Sajad Azizi , Belgium
Michele Bacciocchi , Italy
Seungik Baek , USA
Khaled Bahlali, France
M.V.A Raju Bahubalendruni, India
Pedro Balaguer , Spain
P. Balasubramaniam, India
Stefan Balint , Romania
Ines Tejado Balsera , Spain
Alfonso Banos , Spain
Jerzy Baranowski , Poland
Tudor Barbu , Romania
Andrzej Bartoszewicz , Poland
Sergio Baselga , Spain
S. Caglar Baslamisli , Turkey
David Bassir , France
Chiara Bedon , Italy
Azeddine Beghdadi, France
Andriette Bekker , South Africa
Francisco Beltran-Carbajal , Mexico
Abdellatif Ben Makhlof , Saudi Arabia
Denis Benasciutti , Italy
Ivano Benedetti , Italy
Rosa M. Benito , Spain
Elena Benvenuti , Italy
Giovanni Berselli, Italy
Michele Betti , Italy
Pietro Bia , Italy
Carlo Bianca , France
Simone Bianco , Italy
Vincenzo Bianco, Italy
Vittorio Bianco, Italy
David Bigaud , France
Sardar Muhammad Bilal , Pakistan
Antonio Bilotta , Italy
Sylvio R. Bistafa, Brazil
Chiara Boccaletti , Italy
Rodolfo Bontempo , Italy
Alberto Borboni , Italy
Marco Bortolini, Italy

Paolo Boscariol, Italy
Daniela Boso , Italy
Guillermo Botella-Juan, Spain
Abdesselem Boulkroune , Algeria
Boulaïd Boulkroune, Belgium
Fabio Bovenga , Italy
Francesco Braghin , Italy
Ricardo Branco, Portugal
Julien Bruchon , France
Matteo Bruggi , Italy
Michele Brun , Italy
Maria Elena Bruni, Italy
Maria Angela Butturi , Italy
Bartłomiej Błachowski , Poland
Dhanamjayulu C , India
Raquel Caballero-Águila , Spain
Filippo Cacace , Italy
Salvatore Caddemi , Italy
Zuowei Cai , China
Roberto Caldelli , Italy
Francesco Cannizzaro , Italy
Maosen Cao , China
Ana Carpio, Spain
Rodrigo Carvajal , Chile
Caterina Casavola, Italy
Sara Casciati, Italy
Federica Caselli , Italy
Carmen Castillo , Spain
Inmaculada T. Castro , Spain
Miguel Castro , Portugal
Giuseppe Catalanotti , United Kingdom
Alberto Cavallo , Italy
Gabriele Cazzulani , Italy
Fatih Vehbi Celebi, Turkey
Miguel Cerrolaza , Venezuela
Gregory Chagnon , France
Ching-Ter Chang , Taiwan
Kuei-Lun Chang , Taiwan
Qing Chang , USA
Xiaoheng Chang , China
Prasenjit Chatterjee , Lithuania
Kacem Chehdi, France
Peter N. Cheimets, USA
Chih-Chiang Chen , Taiwan
He Chen , China



































Kebing Chen , China
Mengxin Chen , China
Shyi-Ming Chen , Taiwan
Xizhong Chen , Ireland
Xue-Bo Chen , China
Zhiwen Chen , China
Qiang Cheng, USA
Zeyang Cheng, China
Luca Chiapponi , Italy
Francisco Chicano , Spain
Tirivanhu Chinyoka , South Africa
Adrian Chmielewski , Poland
Seongim Choi , USA
Gautam Choubey , India
Hung-Yuan Chung , Taiwan
Yusheng Ci, China
Simone Cinquemani , Italy
Roberto G. Citarella , Italy
Joaquim Ciurana , Spain
John D. Clayton , USA
Piero Colajanni , Italy
Giuseppina Colicchio, Italy
Vassilios Constantoudis , Greece
Enrico Conte, Italy
Alessandro Contento , USA
Mario Cools , Belgium
Gino Cortellessa, Italy
Carlo Cosentino , Italy
Paolo Crippa , Italy
Erik Cuevas , Mexico
Guozeng Cui , China
Mehmet Cunkas , Turkey
Giuseppe D'Aniello , Italy
Peter Dabnichki, Australia
Weizhong Dai , USA
Zhifeng Dai , China
Purushothaman Damodaran , USA
Sergey Dashkovskiy, Germany
Adiel T. De Almeida-Filho , Brazil
Fabio De Angelis , Italy
Samuele De Bartolo , Italy
Stefano De Miranda , Italy
Filippo De Monte , Italy

José António Fonseca De Oliveira
Correia , Portugal
Jose Renato De Sousa , Brazil
Michael Defoort, France
Alessandro Della Corte, Italy
Laurent Dewasme , Belgium
Sanku Dey , India
Gianpaolo Di Bona , Italy
Roberta Di Pace , Italy
Francesca Di Puccio , Italy
Ramón I. Diego , Spain
Yannis Dimakopoulos , Greece
Hasan Dinçer , Turkey
José M. Domínguez , Spain
Georgios Dounias, Greece
Bo Du , China
Emil Dumic, Croatia
Madalina Dumitriu , United Kingdom
Premraj Durairaj , India
Saeed Eftekhari Azam, USA
Said El Kafhali , Morocco
Antonio Elipse , Spain
R. Emre Erkmen, Canada
John Escobar , Colombia
Leandro F. F. Miguel , Brazil
FRANCESCO FOTI , Italy
Andrea L. Facci , Italy
Shahla Faisal , Pakistan
Giovanni Falsone , Italy
Hua Fan, China
Jianguang Fang, Australia
Nicholas Fantuzzi , Italy
Muhammad Shahid Farid , Pakistan
Hamed Faruqi, Iran
Yann Favennec, France
Fiorenzo A. Fazzolari , United Kingdom
Giuseppe Fedele , Italy
Roberto Fedele , Italy
Baowei Feng , China
Mohammad Ferdows , Bangladesh
Arturo J. Fernández , Spain
Jesus M. Fernandez Oro, Spain
Francesco Ferrise, Italy
Eric Feulvarch , France
Thierry Floquet, France

Eric Florentin , France
Gerardo Flores, Mexico
Antonio Forcina , Italy
Alessandro Formisano, Italy
Francesco Franco , Italy
Elisa Francomano , Italy
Juan Frausto-Solis, Mexico
Shujun Fu , China
Juan C. G. Prada , Spain
HECTOR GOMEZ , Chile
Matteo Gaeta , Italy
Mauro Gaggero , Italy
Zoran Gajic , USA
Jaime Gallardo-Alvarado , Mexico
Mosè Gallo , Italy
Akemi Gálvez , Spain
Maria L. Gandarias , Spain
Hao Gao , Hong Kong
Xingbao Gao , China
Yan Gao , China
Zhiwei Gao , United Kingdom
Giovanni Garcea , Italy
José García , Chile
Harish Garg , India
Alessandro Gasparetto , Italy
Stylianios Georgantzinou, Greece
Fotios Georgiades , India
Parviz Ghadimi , Iran
Ştefan Cristian Gherghina , Romania
Georgios I. Giannopoulos , Greece
Agathoklis Giaralis , United Kingdom
Anna M. Gil-Lafuente , Spain
Ivan Giorgio , Italy
Gaetano Giunta , Luxembourg
Jefferson L.M.A. Gomes , United Kingdom
Emilio Gómez-Déniz , Spain
Antonio M. Gonçalves de Lima , Brazil
Qunxi Gong , China
Chris Goodrich, USA
Rama S. R. Gorla, USA
Veena Goswami , India
Xunjie Gou , Spain
Jakub Grabski , Poland

Antoine Grall , France
George A. Gravvanis , Greece
Fabrizio Greco , Italy
David Greiner , Spain
Jason Gu , Canada
Federico Guarracino , Italy
Michele Guida , Italy
Muhammet Gul , Turkey
Dong-Sheng Guo , China
Hu Guo , China
Zhaoxia Guo, China
Yusuf Gurefe, Turkey
Salim HEDDAM , Algeria
ABID HUSSANAN, China
Quang Phuc Ha, Australia
Li Haitao , China
Petr Hájek , Czech Republic
Mohamed Hamdy , Egypt
Muhammad Hamid , United Kingdom
Renke Han , United Kingdom
Weimin Han , USA
Xingsi Han, China
Zhen-Lai Han , China
Thomas Hanne , Switzerland
Xinan Hao , China
Mohammad A. Hariri-Ardebili , USA
Khalid Hattaf , Morocco
Defeng He , China
Xiao-Qiao He, China
Yanchao He, China
Yu-Ling He , China
Ramdane Hedjar , Saudi Arabia
Jude Hemanth , India
Reza Hemmati, Iran
Nicolae Herisanu , Romania
Alfredo G. Hernández-Díaz , Spain
M.I. Herreros , Spain
Eckhard Hitzer , Japan
Paul Honeine , France
Jaromir Horacek , Czech Republic
Lei Hou , China
Yingkun Hou , China
Yu-Chen Hu , Taiwan
Yunfeng Hu, China
Can Huang , China
Gordon Huang , Canada
Linsheng Huo , China
Sajid Hussain, Canada
Asier Ibeas , Spain
Orest V. Iftime , The Netherlands
Przemyslaw Ignaciuk , Poland
Giacomo Innocenti , Italy
Emilio Insfran Pelozo , Spain
Azeem Irshad, Pakistan
Alessio Ishizaka, France
Benjamin Ivorra , Spain
Breno Jacob , Brazil
Reema Jain , India
Tushar Jain , India
Amin Jajarmi , Iran
Chiranjibe Jana , India
Łukasz Jankowski , Poland
Samuel N. Jator , USA
Juan Carlos Jáuregui-Correa , Mexico
Kandasamy Jayakrishna, India
Reza Jazar, Australia
Khalide Jbilou, France
Isabel S. Jesus , Portugal
Chao Ji , China
Qing-Chao Jiang , China
Peng-fei Jiao , China
Ricardo Fabricio Escobar Jiménez , Mexico
Emilio Jiménez Macías , Spain
Maolin Jin, Republic of Korea
Zhuo Jin, Australia
Ramash Kumar K , India
BHABEN KALITA , USA
MOHAMMAD REZA KHEDMATI , Iran
Viacheslav Kalashnikov , Mexico
Mathiyalagan Kalidass , India
Tamas Kalmar-Nagy , Hungary
Rajesh Kaluri , India
Jyottheswara Reddy Kalvakurthi, India
Zhao Kang , China
Ramani Kannan , Malaysia
Tomasz Kapitaniak , Poland
Julius Kaplunov, United Kingdom
Konstantinos Karamanos, Belgium
Michal Kawulok, Poland

Irfan Kaymaz , Turkey
Vahid Kayvanfar , Qatar
Krzysztof Kecik , Poland
Mohamed Khader , Egypt
Chaudry M. Khalique , South Africa
Mukhtaj Khan , Pakistan
Shahid Khan , Pakistan
Nam-Il Kim, Republic of Korea
Philipp V. Kiryukhantsev-Korneev ,
Russia
P.V.V Kishore , India
Jan Koci , Czech Republic
Ioannis Kostavelis , Greece
Sotiris B. Kotsiantis , Greece
Frederic Kratz , France
Vamsi Krishna , India
Edyta Kucharska, Poland
Krzysztof S. Kulpa , Poland
Kamal Kumar, India
Prof. Ashwani Kumar , India
Michal Kunicki , Poland
Cedrick A. K. Kwuimy , USA
Kyandoghere Kyamakya, Austria
Ivan Kyrchei , Ukraine
Márcio J. Lacerda , Brazil
Eduardo Lalla , The Netherlands
Giovanni Lancioni , Italy
Jaroslaw Latalski , Poland
Hervé Laurent , France
Agostino Lauria , Italy
Aimé Lay-Ekuakille , Italy
Nicolas J. Leconte , France
Kun-Chou Lee , Taiwan
Dimitri Lefebvre , France
Eric Lefevre , France
Marek Lefik, Poland
Yaguo Lei , China
Kauko Leiviskä , Finland
Ervin Lenzi , Brazil
ChenFeng Li , China
Jian Li , USA
Jun Li , China
Yueyang Li , China
Zhao Li , China






























Zhen Li , China
En-Qiang Lin, USA
Jian Lin , China
Qibin Lin, China
Yao-Jin Lin, China
Zhiyun Lin , China
Bin Liu , China
Bo Liu , China
Heng Liu , China
Jianxu Liu , Thailand
Lei Liu , China
Sixin Liu , China
Wanquan Liu , China
Yu Liu , China
Yuanchang Liu , United Kingdom
Bonifacio Llamazares , Spain
Alessandro Lo Schiavo , Italy
Jean Jacques Loiseau , France
Francesco Lolli , Italy
Paolo Lonetti , Italy
António M. Lopes , Portugal
Sebastian López, Spain
Luis M. López-Ochoa , Spain
Vassilios C. Loukopoulos, Greece
Gabriele Maria Lozito , Italy
Zhiguo Luo , China
Gabriel Luque , Spain
Valentin Lychagin, Norway
YUE MEI, China
Junwei Ma , China
Xuanlong Ma , China
Antonio Madeo , Italy
Alessandro Magnani , Belgium
Toqeer Mahmood , Pakistan
Fazal M. Mahomed , South Africa
Arunava Majumder , India
Sarfranz Nawaz Malik, Pakistan
Paolo Manfredi , Italy
Adnan Maqsood , Pakistan
Muazzam Maqsood, Pakistan
Giuseppe Carlo Marano , Italy
Damijan Markovic, France
Filipe J. Marques , Portugal
Luca Martinelli , Italy
Denizar Cruz Martins, Brazil

Francisco J. Martos , Spain
Elio Masciari , Italy
Paolo Massioni , France
Alessandro Mauro , Italy
Jonathan Mayo-Maldonado , Mexico
Pier Luigi Mazzeo , Italy
Laura Mazzola, Italy
Driss Mehdi , France
Zahid Mehmood , Pakistan
Roderick Melnik , Canada
Xiangyu Meng , USA
Jose Merodio , Spain
Alessio Merola , Italy
Mahmoud Mesbah , Iran
Luciano Mescia , Italy
Laurent Mevel , France
Constantine Michailides , Cyprus
Mariusz Michta , Poland
Prankul Middha, Norway
Aki Mikkola , Finland
Giovanni Minafò , Italy
Edmondo Minisci , United Kingdom
Hiroyuki Mino , Japan
Dimitrios Mitsotakis , New Zealand
Ardashir Mohammadzadeh , Iran
Francisco J. Montáns , Spain
Francesco Montefusco , Italy
Gisele Mophou , France
Rafael Morales , Spain
Marco Morandini , Italy
Javier Moreno-Valenzuela , Mexico
Simone Morganti , Italy
Caroline Mota , Brazil
Aziz Moukrim , France
Shen Mouquan , China
Dimitris Mourtzis , Greece
Emiliano Mucchi , Italy
Taseer Muhammad, Saudi Arabia
Ghulam Muhiuddin, Saudi Arabia
Amitava Mukherjee , India
Josefa Mula , Spain
Jose J. Muñoz , Spain
Giuseppe Muscolino, Italy
Marco Mussetta , Italy

Hariharan Muthusamy, India
Alessandro Naddeo , Italy
Raj Nandkeolyar, India
Keivan Navaie , United Kingdom
Soumya Nayak, India
Adrian Neagu , USA
Erivelton Geraldo Nepomuceno , Brazil
AMA Neves, Portugal
Ha Quang Thinh Ngo , Vietnam
Nhon Nguyen-Thanh, Singapore
Papakostas Nikolaos , Ireland
Jelena Nikolic , Serbia
Tatsushi Nishi, Japan
Shanzhou Niu , China
Ben T. Nohara , Japan
Mohammed Nouari , France
Mustapha Nourelfath, Canada
Kazem Nouri , Iran
Ciro Núñez-Gutiérrez , Mexico
Włodzimierz Ogryczak, Poland
Roger Ohayon, France
Krzysztof Okarma , Poland
Mitsuhiro Okayasu, Japan
Murat Olgun , Turkey
Diego Oliva, Mexico
Alberto Olivares , Spain
Enrique Onieva , Spain
Calogero Orlando , Italy
Susana Ortega-Cisneros , Mexico
Sergio Ortobelli, Italy
Naohisa Otsuka , Japan
Sid Ahmed Ould Ahmed Mahmoud , Saudi Arabia
Taoreed Owolabi , Nigeria
EUGENIA PETROPOULOU , Greece
Arturo Pagano, Italy
Madhumangal Pal, India
Pasquale Palumbo , Italy
Dragan Pamučar, Serbia
Weifeng Pan , China
Chandan Pandey, India
Rui Pang, United Kingdom
Jürgen Pannek , Germany
Elena Panteley, France
Achille Paolone, Italy

George A. Papakostas , Greece
Xosé M. Pardo , Spain
You-Jin Park, Taiwan
Manuel Pastor, Spain
Pubudu N. Pathirana , Australia
Surajit Kumar Paul , India
Luis Payá , Spain
Igor Pažanin , Croatia
Libor Pekař , Czech Republic
Francesco Pellicano , Italy
Marcello Pellicciari , Italy
Jian Peng , China
Mingshu Peng, China
Xiang Peng , China
Xindong Peng, China
Yuxing Peng, China
Marzio Pennisi , Italy
Maria Patrizia Pera , Italy
Matjaz Perc , Slovenia
A. M. Bastos Pereira , Portugal
Wesley Peres, Brazil
F. Javier Pérez-Pinal , Mexico
Michele Perrella, Italy
Francesco Pesavento , Italy
Francesco Petrini , Italy
Hoang Vu Phan, Republic of Korea
Lukasz Pieczonka , Poland
Dario Piga , Switzerland
Marco Pizzarelli , Italy
Javier Plaza , Spain
Goutam Pohit , India
Dragan Poljak , Croatia
Jorge Pomares , Spain
Hiram Ponce , Mexico
Sébastien Poncet , Canada
Volodymyr Ponomaryov , Mexico
Jean-Christophe Ponsart , France
Mauro Pontani , Italy
Sivakumar Poruran, India
Francesc Pozo , Spain
Aditya Rio Prabowo , Indonesia
Anchasa Pramuanjaroenkij , Thailand
Leonardo Primavera , Italy
B Rajanarayan Prusty, India

Krzysztof Puszynski , Poland
Chuan Qin , China
Dongdong Qin, China
Jianlong Qiu , China
Giuseppe Quaranta , Italy
DR. RITU RAJ , India
Vitomir Racic , Italy
Carlo Rainieri , Italy
Kumbakonam Ramamani Rajagopal, USA
Ali Ramazani , USA
Angel Manuel Ramos , Spain
Higinio Ramos , Spain
Muhammad Afzal Rana , Pakistan
Muhammad Rashid, Saudi Arabia
Manoj Rastogi, India
Alessandro Rasulo , Italy
S.S. Ravindran , USA
Abdolrahman Razani , Iran
Alessandro Reali , Italy
Jose A. Reinoso , Spain
Oscar Reinoso , Spain
Haijun Ren , China
Carlo Renno , Italy
Fabrizio Renno , Italy
Shahram Rezapour , Iran
Ricardo Rianza , Spain
Francesco Riganti-Fulginei , Italy
Gerasimos Rigatos , Greece
Francesco Ripamonti , Italy
Jorge Rivera , Mexico
Eugenio Roanes-Lozano , Spain
Ana Maria A. C. Rocha , Portugal
Luigi Rodino , Italy
Francisco Rodríguez , Spain
Rosana Rodríguez López, Spain
Francisco Rossomando , Argentina
Jose de Jesus Rubio , Mexico
Weiguo Rui , China
Rubén Ruiz , Spain
Ivan D. Rukhlenko , Australia
Dr. Eswaramoorthi S. , India
Weichao SHI , United Kingdom
Chaman Lal Sabharwal , USA
Andrés Sáez , Spain

Bekir Sahin, Turkey
Laxminarayan Sahoo , India
John S. Sakellariou , Greece
Michael Sakellariou , Greece
Salvatore Salamone, USA
Jose Vicente Salcedo , Spain
Alejandro Salcido , Mexico
Alejandro Salcido, Mexico
Nunzio Salerno , Italy
Rohit Salgotra , India
Miguel A. Salido , Spain
Sinan Salih , Iraq
Alessandro Salvini , Italy
Abdus Samad , India
Sovan Samanta, India
Nikolaos Samaras , Greece
Ramon Sancibrian , Spain
Giuseppe Sanfilippo , Italy
Omar-Jacobo Santos, Mexico
J Santos-Reyes , Mexico
José A. Sanz-Herrera , Spain
Musavarah Sarwar, Pakistan
Shahzad Sarwar, Saudi Arabia
Marcelo A. Savi , Brazil
Andrey V. Savkin, Australia
Tadeusz Sawik , Poland
Roberta Sburlati, Italy
Gustavo Scaglia , Argentina
Thomas Schuster , Germany
Hamid M. Sedighi , Iran
Mijanur Rahaman Seikh, India
Tapan Senapati , China
Lotfi Senhadji , France
Junwon Seo, USA
Michele Serpilli, Italy
Silvestar Šesnić , Croatia
Gerardo Severino, Italy
Ruben Sevilla , United Kingdom
Stefano Sfarra , Italy
Dr. Ismail Shah , Pakistan
Leonid Shaikhet , Israel
Vimal Shanmuganathan , India
Prayas Sharma, India
Bo Shen , Germany
Hang Shen, China

Xin Pu Shen, China
Dimitri O. Shepelsky, Ukraine
Jian Shi , China
Amin Shokrollahi, Australia
Suzanne M. Shontz , USA
Babak Shotorban , USA
Zhan Shu , Canada
Angelo Sifaleras , Greece
Nuno Simões , Portugal
Mehakpreet Singh , Ireland
Piyush Pratap Singh , India
Rajiv Singh, India
Seralathan Sivamani , India
S. Sivasankaran , Malaysia
Christos H. Skiadas, Greece
Konstantina Skouri , Greece
Neale R. Smith , Mexico
Bogdan Smolka, Poland
Delfim Soares Jr. , Brazil
Alba Sofi , Italy
Francesco Soldovieri , Italy
Raffaele Solimene , Italy
Yang Song , Norway
Jussi Sopanen , Finland
Marco Spadini , Italy
Paolo Spagnolo , Italy
Ruben Specogna , Italy
Vasilios Spitas , Greece
Ivanka Stamova , USA
Rafał Stanisławski , Poland
Miladin Stefanović , Serbia
Salvatore Strano , Italy
Yakov Strelniker, Israel
Kangkang Sun , China
Qiuqin Sun , China
Shuaishuai Sun, Australia
Yanchao Sun , China
Zong-Yao Sun , China
Kumarasamy Suresh , India
Sergey A. Suslov , Australia
D.L. Suthar, Ethiopia
D.L. Suthar , Ethiopia
Andrzej Swierniak, Poland
Andras Szekrenyes , Hungary
Kumar K. Tamma, USA

Yong (Aaron) Tan, United Kingdom
Marco Antonio Taneco-Hernández , Mexico
Lu Tang , China
Tianyou Tao, China
Hafez Tari , USA
Alessandro Tasora , Italy
Sergio Teggi , Italy
Adriana del Carmen Téllez-Anguiano , Mexico
Ana C. Teodoro , Portugal
Efstathios E. Theotokoglou , Greece
Jing-Feng Tian, China
Alexander Timokha , Norway
Stefania Tomasiello , Italy
Gisella Tomasini , Italy
Isabella Torcicollo , Italy
Francesco Tornabene , Italy
Mariano Torrisi , Italy
Thang nguyen Trung, Vietnam
George Tsiatas , Greece
Le Anh Tuan , Vietnam
Nerio Tullini , Italy
Emilio Turco , Italy
Ilhan Tuzcu , USA
Efstratios Tzirtzilakis , Greece
FRANCISCO UREÑA , Spain
Filippo Ubertini , Italy
Mohammad Uddin , Australia
Mohammad Safi Ullah , Bangladesh
Serdar Ulubeyli , Turkey
Mati Ur Rahman , Pakistan
Panayiotis Vafeas , Greece
Giuseppe Vairo , Italy
Jesus Valdez-Resendiz , Mexico
Eusebio Valero, Spain
Stefano Valvano , Italy
Carlos-Renato Vázquez , Mexico
Martin Velasco Villa , Mexico
Franck J. Vernerey, USA
Georgios Veronis , USA
Vincenzo Vespri , Italy
Renato Vidoni , Italy
Venkatesh Vijayaraghavan, Australia

Anna Vila, Spain
Francisco R. Villatoro , Spain
Francesca Vipiana , Italy
Stanislav Vitek , Czech Republic
Jan Vorel , Czech Republic
Michael Vynnycky , Sweden
Mohammad W. Alomari, Jordan
Roman Wan-Wendner , Austria
Bingchang Wang, China
C. H. Wang , Taiwan
Dagang Wang, China
Guoqiang Wang , China
Huaiyu Wang, China
Hui Wang , China
J.G. Wang, China
Ji Wang , China
Kang-Jia Wang , China
Lei Wang , China
Qiang Wang, China
Qingling Wang , China
Weiwei Wang , China
Xinyu Wang , China
Yong Wang , China
Yung-Chung Wang , Taiwan
Zhenbo Wang , USA
Zhibo Wang, China
Waldemar T. Wójcik, Poland
Chi Wu , Australia
Qihong Wu, China
Yuqiang Wu, China
Zhibin Wu , China
Zhizheng Wu , China
Michalis Xenos , Greece
Hao Xiao , China
Xiao Ping Xie , China
Qingzheng Xu , China
Binghan Xue , China
Yi Xue , China
Joseph J. Yame , France
Chuanliang Yan , China
Xinggang Yan , United Kingdom
Hongtai Yang , China
Jixiang Yang , China
Mijia Yang, USA
Ray-Yeng Yang, Taiwan

Zaoli Yang , China
Jun Ye , China
Min Ye , China
Luis J. Yebra , Spain
Peng-Yeng Yin , Taiwan
Muhammad Haroon Yousaf , Pakistan
Yuan Yuan, United Kingdom
Qin Yuming, China
Elena Zaitseva , Slovakia
Arkadiusz Zak , Poland
Mohammad Zakwan , India
Ernesto Zambrano-Serrano , Mexico
Francesco Zammori , Italy
Jessica Zangari , Italy
Rafal Zdunek , Poland
Ibrahim Zeid, USA
Nianyin Zeng , China
Junyong Zhai , China
Hao Zhang , China
Haopeng Zhang , USA
Jian Zhang , China
Kai Zhang, China
Lingfan Zhang , China
Mingjie Zhang , Norway
Qian Zhang , China
Tianwei Zhang , China
Tongqian Zhang , China
Wenyu Zhang , China
Xianming Zhang , Australia
Xuping Zhang , Denmark
Yinyan Zhang, China
Yifan Zhao , United Kingdom
Debao Zhou, USA
Heng Zhou , China
Jian G. Zhou , United Kingdom
Junyong Zhou , China
Xueqian Zhou , United Kingdom
Zhe Zhou , China
Wu-Le Zhu, China
Gaetano Zizzo , Italy
Mingcheng Zuo, China

Contents


Development and Application of Visualization System of Gas Geological Dynamic Characteristics under Big Data Framework

Xiao Liu , Sen Xu, Haixiao Lin , Xiaoming Ni, and Dequan Xuan
Research Article (13 pages), Article ID 2393411, Volume 2023 (2023)



Data-Driven-Based Study on Sustainable Improvement of the Regional Logistics Industry

Yujia Liu  and Heping Ding 
Research Article (13 pages), Article ID 5048297, Volume 2023 (2023)

Selecting Online Channel Mode for Green Products in a Capital-Constrained Platform Supply Chain

Guobao Zhang, Xinhui Cheng, Zhichao Zhang , and Yanyan Zheng
Research Article (16 pages), Article ID 5918897, Volume 2023 (2023)



Synergistic Agglomeration of Manufacturing and Logistics Industries and Urban Green Economy Efficiency: Influence and Upgrading

Qian Zhang  and Ye Tao 
Research Article (19 pages), Article ID 8118981, Volume 2023 (2023)

How Does the Electronic Products Retailer Transform Operational Modes Considering Consumer Preferences for Leasing?

Gaidi Tian , Chunfa Li , and Dongdong Li 
Research Article (17 pages), Article ID 6071288, Volume 2022 (2022)




Data-Driven Green Development Efficiency of Regional Sci-Tech Finance: A Case Study of the Yangtze River Delta

Yuan Wang, Hongjun Liu , Shuling Zhou, Fan Liu, Yaliu Yang , Juan Zhu, and Yi Xu
Research Article (13 pages), Article ID 3408342, Volume 2022 (2022)


Sensor Optimization for Variation Diagnosis in Multistation Assembly Processes

Kang He , Xiaobiao Li , Fei Sun , Quan Yang, Bo Wu , and Chao Meng 
Research Article (8 pages), Article ID 7904677, Volume 2022 (2022)


DEM Investigation of Discrete Heat Transfer Behavior of the Grinding Media in Ball Mills

Zixin Yin , Nan Wang , and Tongqing Li 
Research Article (9 pages), Article ID 4249726, Volume 2022 (2022)



Mullite Reinforced SiC/Al₂O₃ Composites Prepared by Microwave Sintering Based on Green Manufacturing

Xudan Dang , Shaojie Shi, Linjun Li, Fei Luo, and Zheng Ding
Research Article (13 pages), Article ID 7782595, Volume 2022 (2022)

Pushing Pose Sensing of Underground Mobile Supporting Robot

Nan Wang, Hao Liu, Xiaobiao Li, Meizi Tian, and Lin Zhang 
Research Article (12 pages), Article ID 6978943, Volume 2022 (2022)

Vision-Based Mobile Manipulator for Handling and Transportation of Supermarket Products

Muhammad Zia Ur Rahman , Muhammad Usman, Adhban Farea , Nasir Ahmad, Imran Mahmood, and Muhammad Imran

Research Article (10 pages), Article ID 3883845, Volume 2022 (2022)

Gas Seepage Model and Experiment Based on Bedding Effect of Fractured Coal Body

Kunyun Tian  and Erjian Wei 

Research Article (11 pages), Article ID 3863267, Volume 2022 (2022)

Research Article

Development and Application of Visualization System of Gas Geological Dynamic Characteristics under Big Data Framework

Xiao Liu ^{1,2} Sen Xu,¹ Haixiao Lin ¹ Xiaoming Ni,¹ and Dequan Xuan³

¹Henan Polytechnic University, Jiaozuo 454003, China

²Collaborative Innovation Center of Coal Work Safety and Clean High Efficiency Utilization, Jiaozuo 454003, China

³School of Safety Science and Emergency Management, Wuhan University of Technology, Wuhan 430070, China

Correspondence should be addressed to Xiao Liu; liuxiao@hpu.edu.cn

Received 31 July 2022; Accepted 13 September 2022; Published 20 April 2023

Academic Editor: Conghu Liu

Copyright © 2023 Xiao Liu et al. This is an open access article distributed under the Creative Commons Attribution License, which permits unrestricted use, distribution, and reproduction in any medium, provided the original work is properly cited.

In this study, coal and gas outbursts are the “biggest killer” of mine safety production. With the deepening of mining, the mine gas disaster is becoming more and more serious. From the perspective of big data, the establishment of a dynamic visualization system of gas geology integrating gas geology, gas drainage, dynamic outburst prevention, and other information can effectively improving the defects of gas disaster prevention and control in the coal industry, such as insufficient advance, lack of systematic identification methods and backward information collection methods, which is of great significance to improve the ability of gas hazard identification. Based on the precise detection of geology, structure, and gas, this paper proposes to use information technology, the Internet of things, big data analysis, and other technologies to comprehensively analyze the changes in gas occurrence and coal seam occurrence on the basis of the causes of mine gas geological outburst, fully consider the logical relationship between different factors and outburst and adopt the disciplinary advantages of grey theory, fault tree theory, BP neural network, and so on. The tree of coal and gas outburst accidents with general significance is constructed by 24 relatively independent factors. The input vector is determined as the matrix composed of eight main factors affecting and controlling outburst, including gas pressure, coal mechanical strength, comprehensive characteristic coefficient of coal fragmentation, the permeability coefficient of coal, comprehensive characteristic coefficient of coal seam bifurcation and combination, comprehensive characteristic coefficient of coal thickness and coal thickness change, fault complexity coefficients and interlayer sliding comprehensive characteristic coefficient. The geological data affecting coal and gas outbursts are analyzed and calculated scientifically so that the gas geological data can be updated in time, and the change of gas geological laws is presented dynamically, so as to guide the mine to predict the gas disaster more scientifically and reliably.

1. Introduction

Coal and gas outburst (hereinafter referred to as “outburst”) is one of the most serious disasters in the coal mine, which is extremely destructive. The shock wave formed when the outburst occurs can destroy the roadway and ventilation facilities; the coal and rock thrown out will bury the mining equipment and operators; and the large amount of gas emitted will cause personnel suffocation or gas explosion accidents. Therefore, the outburst disaster is the key prevention and control object for coal mine safety in

our country. Long-term outburst prevention practice shows that outburst is controlled by gas geological conditions. [1–6] In the 21st century, a new round of technological and energy reform is being gestated. The development momentum of industrial informatization, automation, and intelligence is strong, and the technology is becoming more and more mature, which provides new development opportunities and challenges for the transformation of typical and major disaster management in coal mines from traditional qualitative and empirical prevention to modern quantitative and precise prevention

and control; and it is also an effective way to curb major accidents in coal mines [7–12].

The outburst risk of mine working face is generally dynamic, which requires that the safety technology and measures should be adjusted in real time [13–15]. The existing outburst disaster prevention and control technology and management methods are mostly static and manual analysis and management in the analysis of coal and rock outburst risks and the construction management of prevention and control technology measures. The automatic monitoring and information detection level of hazard information is not high, and it cannot adapt to the dynamic change of outburst risk of working face. The precision, comprehensiveness, and reliability of mine gas geological analysis, gas extraction analysis, gas emission analysis, and daily outburst prevention and control are not enough, which cannot realize the comprehensive and precise control of gas disaster diversification and automation, and restrict the effectiveness and scientific nature of coal and gas outburst disaster prevention and control technology [16–18]. From the perspective of big data, the establishment of a gas geological dynamic feature system integrating gas geology, gas drainage, dynamic outburst prevention and other information is of great significance to improve the identification ability of hidden dangers of gas disasters and can effectively improve the shortcomings of insufficient advance of gas disaster prevention and control in the coal industry, the lack of systematic identification methods, and backward information collection methods. Many mines have used digitalization and informatization to guide gas prevention and control work, Yangquan mining area has established a two-level coal and gas outburst dynamic prediction method, and the combination of gas geological analysis method and GIS spatial analysis technology to establish a gas geological dynamic analysis system has also been developed. Xinjing Company has made a great breakthrough in gas intelligent technology by using GIS digitalization technology. Thus, a relatively perfect gas geological intelligent dynamic outburst prevention management system is constructed and formed [19–22].

2. Design Ideas of Gas Geological Dynamic Characteristics Visualization System Based on Big Data Framework

The visualization of gas geological dynamic characteristics based on big data framework is based on solving the precise prevention and control of gas disasters, mainly based on the precise detection of geology, structure and gas, using information technology, Internet of things, big data analysis, and other technologies, based on the causes of mine gas geological outburst disasters, giving full play to the role of rich gas geological data in mines, and adopting the disciplinary advantages of grey theory, fault tree theory, BP neural network, and so on, to carry out scientific analysis and calculation on the geological data affecting coal and gas outburst, so that the gas geological data can be updated in time, and dynamically show the changes of gas geological

laws, so as to guide the mine to predict gas disasters more scientifically and reliably [23–26].

2.1. Design Purpose

- (1) The organic combination of gas geological theory and information technology can be realized in the form of visualization, which provides an advanced research direction for the prediction and prevention of coal mine gas disasters.
- (2) Compared with the traditional paper gas geological map, it is convenient to compile, short in cycle, high in accuracy and belongs to the dynamic map, which can update, output and reflect the gas geological information in the dynamic mining process in real time, and is not easy to damage or easy to save.
- (3) Try to form a new technology of digital compilation of mine gas geological map, and enrich and improve the research methods of gas geology.
- (4) The establishment of visual management of mine gas geology with database support not only makes the entry, query, and update of gas geological information convenient and fast, but also provides data sources for the compilation and update of gas geological maps, making the drawing of gas geological map more standardized and scientific.
- (5) Establish a visualization system of gas geological dynamic characteristics based on big data framework so that gas geological data can be better expressed in the form of visualization, so that field managers can clearly and vividly understand the current mining dynamics and the development and changes of gas parameters, and provide a basis for guiding safe production in time.

2.2. Data Development Structure. The gas geological information applied to the prediction and prevention of coal mine gas outburst mainly has two parts: The first is the data obtained directly through on-site collection, sorting, and testing, such as the layout and characteristics of mining engineering in the mine field or stope (coal seam), the characteristics of coal structure, the distribution of folds and fractures, gas emission and basic parameters, the description of outburst accidents that have occurred, and the data obtained from on-site and indoor tests; the second is the processing information obtained from the comprehensive analysis, processing, and calculation based on the obtained data, for example, through the comprehensive analysis of the coal seam gas occurrence and emission characteristics in the mined area and through the numerical analysis to predict the gas emission status in the nonmined area [27–29].

To realize the gas geological information management of outburst prevention, including the basic links of data acquisition, processing, transmission, storage, and information extraction. Due to the huge number, it is necessary to use computers for auxiliary analysis to improve the speed

and quality of information acquisition. In general, it mainly includes the following aspects.

- (1) Acquisition and management of original information: a large number of different types of gas geological data, data and maps are constantly exposed in the exploration stage and production process of the coal mine. In order to effectively apply it to safety management, it is necessary to collect and master these information in detail; at the same time, the classified management of information needs to be implemented after the examination and verification of the data and the elimination of the false and the preservation of the true. The purpose of this work is to lay a foundation for later information query, modification, editing and output.
- (2) Analysis and refinement of information: the ultimate purpose of acquiring and managing information is to achieve safety management in the production process. Therefore, it is necessary to analyze and calculate based on the mastered original information to obtain deeper secondary information (knowledge). For the safety management of coal and gas outburst, that is to effectively realize the prediction and prediction of accident hidden dangers, and based on this, formulate safe and reliable prevention and control measures in time.
- (3) Establishment of database and database management system: because the types of information affecting and controlling gas outburst are complex and diverse, and each type of information contains many factors, in order to facilitate the storage, editing, display and output of information, the above information is usually classified (this paper adopts the layer management method), and the corresponding database (model base) and database (model base) management system are established.

The development structure of this “visualization of dynamic characteristics of gas geology under the condition of big data framework” is shown in Figures 1 and 2. The development is mainly divided into two parts according to the data flow. One is to use MapObjects control to display the electronic map data and query the map data; the second is to use ADO components to access the metadata of electronic map data, which describes the classification information of the map data in detail. Through the query of metadata, the query types can be further subdivided.

3. Analysis and Establishment of Gas Geological Database

3.1. Attributes of Gas Geological Database. In a vector data structure, spatial entities and objects are expressed by basic collection elements such as point, line (line segment, arc segment, line), and surface (polygons). The position of each

entity is defined in terms of its relative or absolute coordinates in a spatial coordinate system. As the data expressed by vector data is continuous, it can accurately mark the position, length, and area of spatial entities.

In two-dimensional geographic space, object entities are formed by (X, Y) coordinate pairs in appropriate coordinate systems. In vector data structure, the most basic set elements include point, line, and surface, as shown in Figure 3.

Gas geological phenomena mainly include three aspects: geological phenomena, gas, and geological prospecting engineering related to gas prediction and prevention. The following is to analyze the geological phenomenon of Vass from these three aspects, so as to make clear the composition and main sources of gas geological data, as shown in Figure 4.

Geological phenomena: geological phenomena are extremely complex. The main geological phenomena involved in GIS are strata, faults, ore bodies, and deposits. The stratum is usually an irregular surface, which cannot be expressed by mathematical expressions. In 3D GIS, a method similar to a digital elevation model (DTM) can also be used to represent the stratum interface. The fault is close to the stratum but usually has a certain width. On the other hand, it is often perpendicular or oblique to the topographic surface. In GIS, if the DTM method is adopted, its projection plane and projection angle need to be considered. In the coal seam, the fracture is mainly represented by normal and reverse faults. An ore body is a three-dimensional entity, but it is often extremely irregular, so it is impossible to determine how many faces it is composed of. An approximate expression method is to imitate the DTM method, express its top digital surface model and bottom digital surface model, and then consider its projection plane and projection boundary. In the coal seam, the soft coal stratification and gangue inclusion are similar to the ore body in geometric shape, which can be treated by similar methods. The deposit may include several ore bodies, faults, exploration engineering and other geological phenomena, so the deposit is a composite phenomenon of various geological phenomena, which can be expressed in the form of complex ground features. Here, mineral deposits refer to coal seams.

Gas: for gas, the distribution of gas and its change under the influence of mining are mainly considered. Because the gas is in a continuous distribution state in the coal seam, and the gas distribution changes very little in the vertical direction in the same coal seam, the gas distribution can be displayed by the surface map, and the surface map can be processed by DTM.

Geological exploration engineering: it mainly includes the exploration boreholes in the exploration stage and the borehole data of gas emission and gas content at the working face.

3.2. Structural Design of Gas Geological Attribute Database. The basic parameters of coal mine gas can be divided into drilling data, gas content and related data, gas emission data

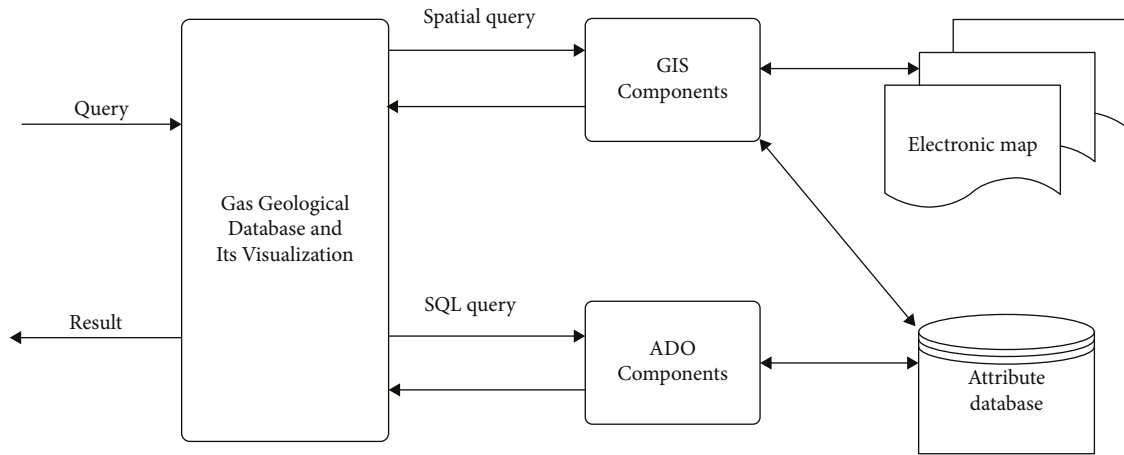


FIGURE 1: Gas geology database and visualization developing structure.

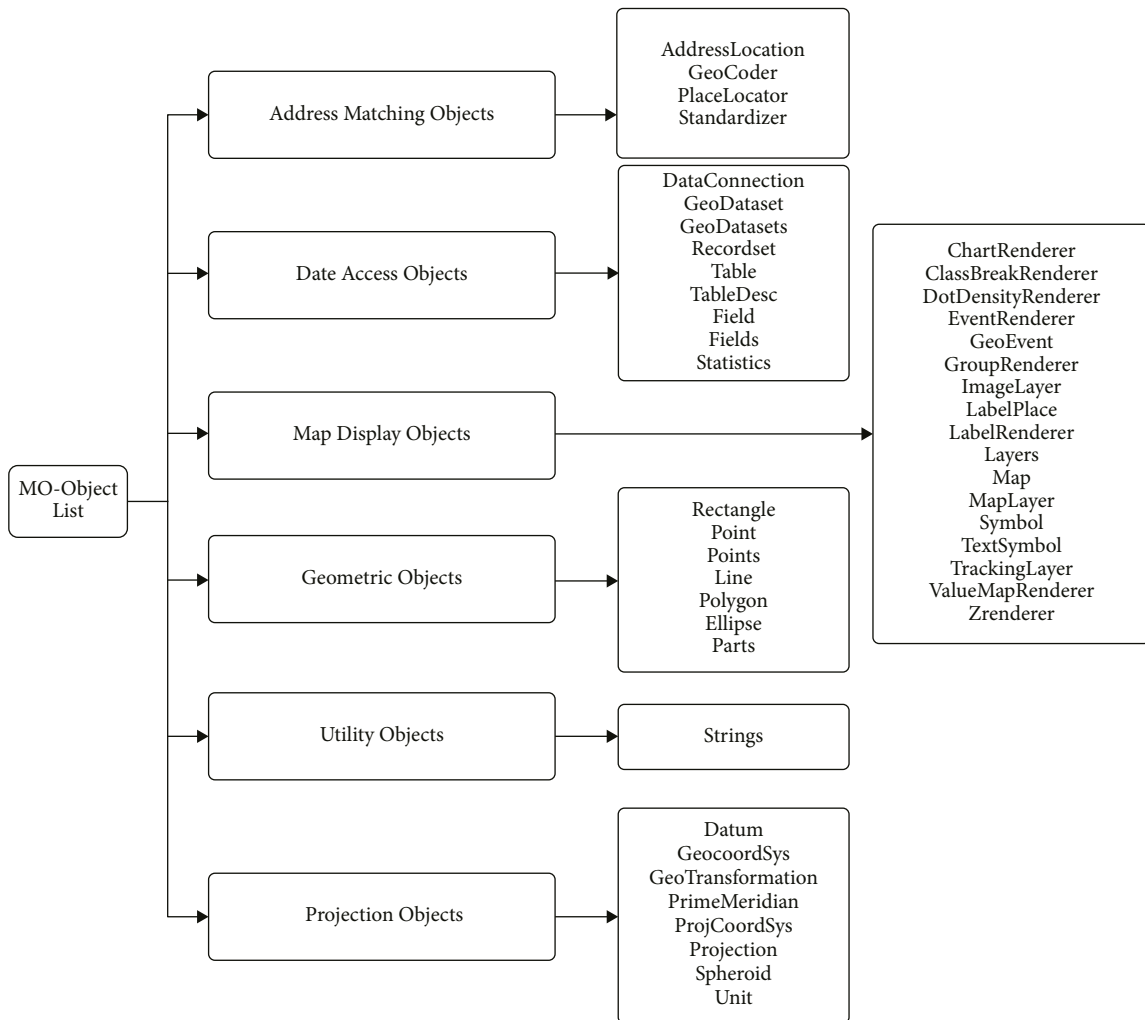


FIGURE 2: MapObjects structure chart.

of mining face, gas emission data of heading face, and outburst data. 37 table structure designs of gas parameters related databases have been established and some of them are shown in Tables 1 to 5.

3.3. *Gas Geological Database Establishment Process.* Basic databases are the core of information systems, and poor data organization, data structure, and data quality directly affects the quality of visualization of gas geological

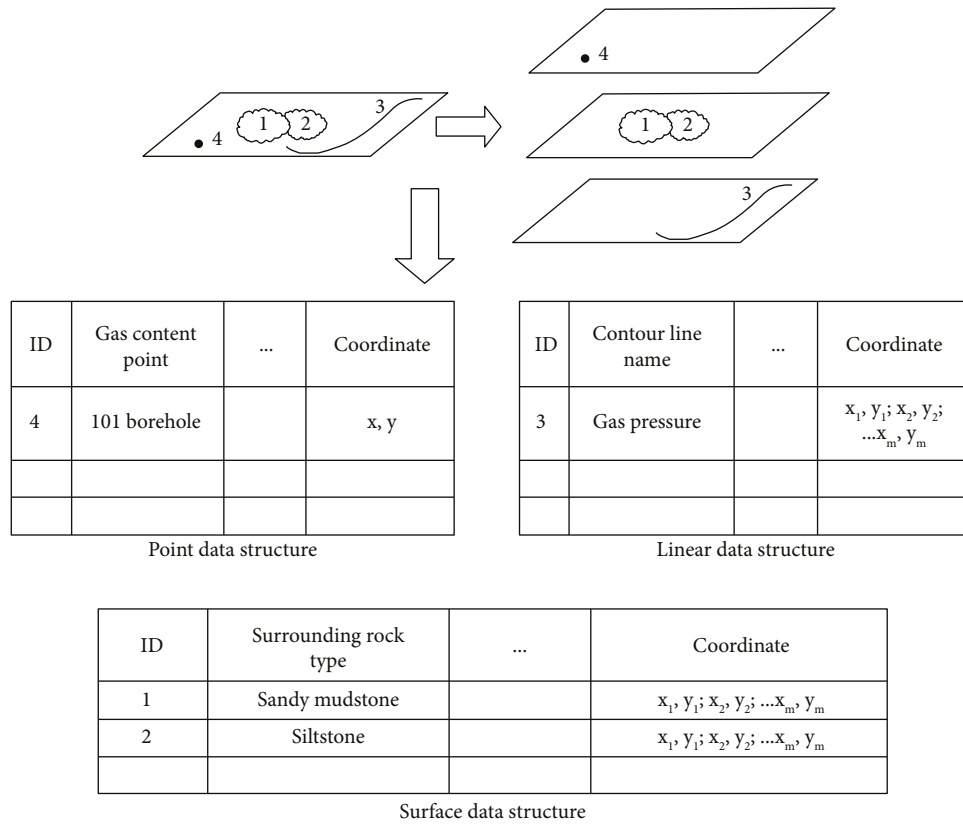


FIGURE 3: Vector data storage scheme.

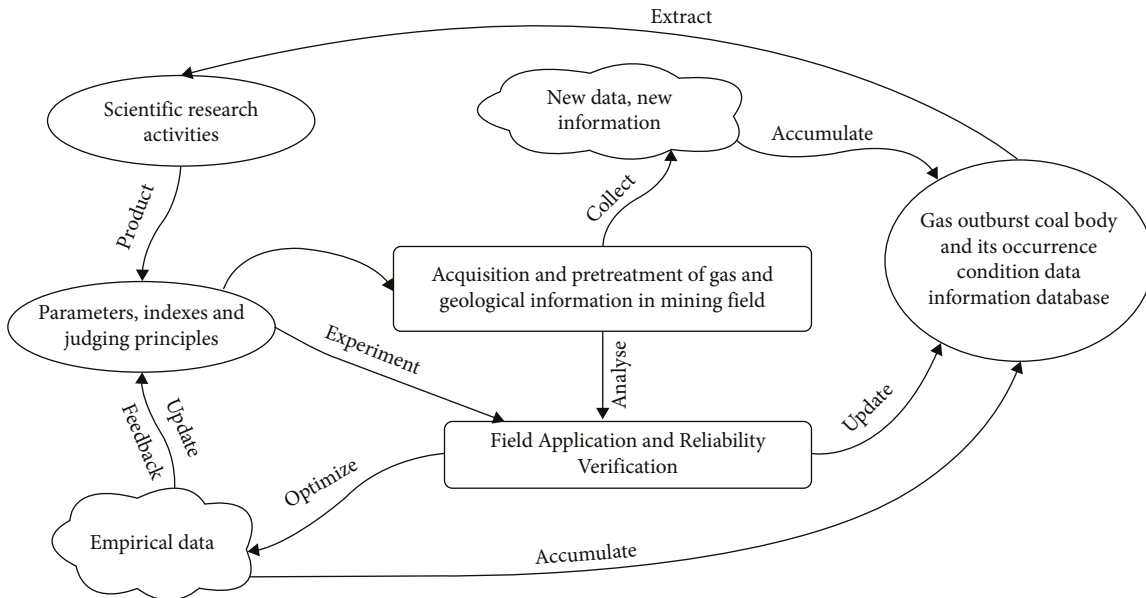


FIGURE 4: Data composition and sources.

dynamic characteristics. Therefore, we must strictly grasp every technical link in the process of database construction. Specifically, the database building operation is to adopt various inspection methods and necessary

means to ensure that all data can enter the database system correctly. The workflows of the established gas geological dynamic data framework are shown in Figures 5 and 6.

TABLE 1: Surface drilling datasheet structure.

Field number	Field name	Field type	Field length	Decimal places	Field name meaning
1	ID	Long	4	0	Serial number
2	CQ	Char	16	—	Mining area
3	ZK_num	Long	8	0	Drilling number
4	ZK_X	Long	12	2	Hole X coordinates
5	ZK_Y	Long	12	2	Hole Y coordinate
6	ZK_depth	Single	8	2	Hole termination depth
7	ZK_level	Single	8	2	Elevation of bore hole
8	ZK_coal	Logical	2	—	Whether see coal
9	MC_ply	Single	4	2	Coal seam thickness
10	ZK_obliquity	Single	2	2	Drilling angle

TABLE 2: The volume of gas discharge on coal face datasheet structure.

Field number	Field name	Field type	Field length	Decimal places	Field name meaning
1	ID	Long	4	0	Serial number
2	CQ	Char	16	—	Mining area
3	GZM_name	Char	16	—	Working face name
4	KC_depth	Single	8	2	Mining depth
5	JL_date	Data	8	—	Record time
6	MC_thick	Single	6	2	Average coal seam thickness
7	KC_thick	Single	6	2	Height mining
8	HC_ways	Char	16	—	Extraction method
9	TF_volume	Single	8	2	Air volume
10	WS_con	Single	8	2	Gas concentration
11	RCL	Single	8	2	Average daily production
12	WS_X	Single	8	2	Gas emission point X coordinate
13	WS_Y	Single	8	2	Gas emission point Y coordinate

TABLE 3: Gas pressure datasheet structure.

Field number	Field name	Field type	Field length	Decimal places	Field name meaning
1	ID	Long	4	0	Serial number
2	CQ	Char	16	—	Mining area
3	CS_site	Char	16	—	Test site
4	CS_data	Date	8	—	Test time
5	JM_level	Single	8	2	See coal elevation
6	WS_press	Single	8	2	Gas pressure
7	CS_X	Single	8	2	Test point X coordinate
8	CS_Y	Single	8	2	Test point Y coordinate
9	BZ	Char	64	—	Remark

TABLE 4: Gas content datasheet structure.

Field number	Field name	Field type	Field length	Decimal places	Field name meaning
1	ID	Long	4	0	Serial number
2	CS_site	Char	16	—	Test site
3	CQ	Char	16	—	Mining area
4	CS_depth	Single	8	2	Test depth
5	M_density	Single	8	2	The density of coal sample
6	MC_temper	Single	8	2	Temperature of coal seam
7	WS_content	Single	8	2	Gas content
8	Porosity	Single	8	4	Porosity
9	XF_a	Single	8	4	Adsorption constant a
10	XF_b	Single	8	4	Adsorption constant b
11	M_wet	Single	8	2	Moisture
12	M_Mash	Single	8	2	Ash
13	Volatilization	Single	8	2	Volatile
14	M_vol weight	Single	8	2	Bulk density of coal
15	CS_X	Single	8	2	Test point X coordinate
16	CS_Y	Single	8	2	Test point Y coordinate

TABLE 5: The dot of gas outburst datasheet structure.

Field number	Field name	Field type	Field length	Decimal places	Field name meaning
1	ID	Long	4	0	Serial number
2	CQ	Char	16	—	Mining area
3	TC_site	Char	16	—	Coal and gas outburst location
4	TC_depth	Single	8	2	Coal and gas outburst depth
5	TC_data	Date	8	0	Coal and gas outburst time
6	TC_coal vol	Single	8	2	Coal and gas outburst coal quantity
7	TC_gas vol	Single	8	2	Coal and gas outburst gas amount
8	TC_type	Char	8	—	Types of coal and gas outburst
9	TC_X	Single	8	2	Outburst point X coordinates
10	TC_Y	Single	8	2	Outburst point Y coordinates

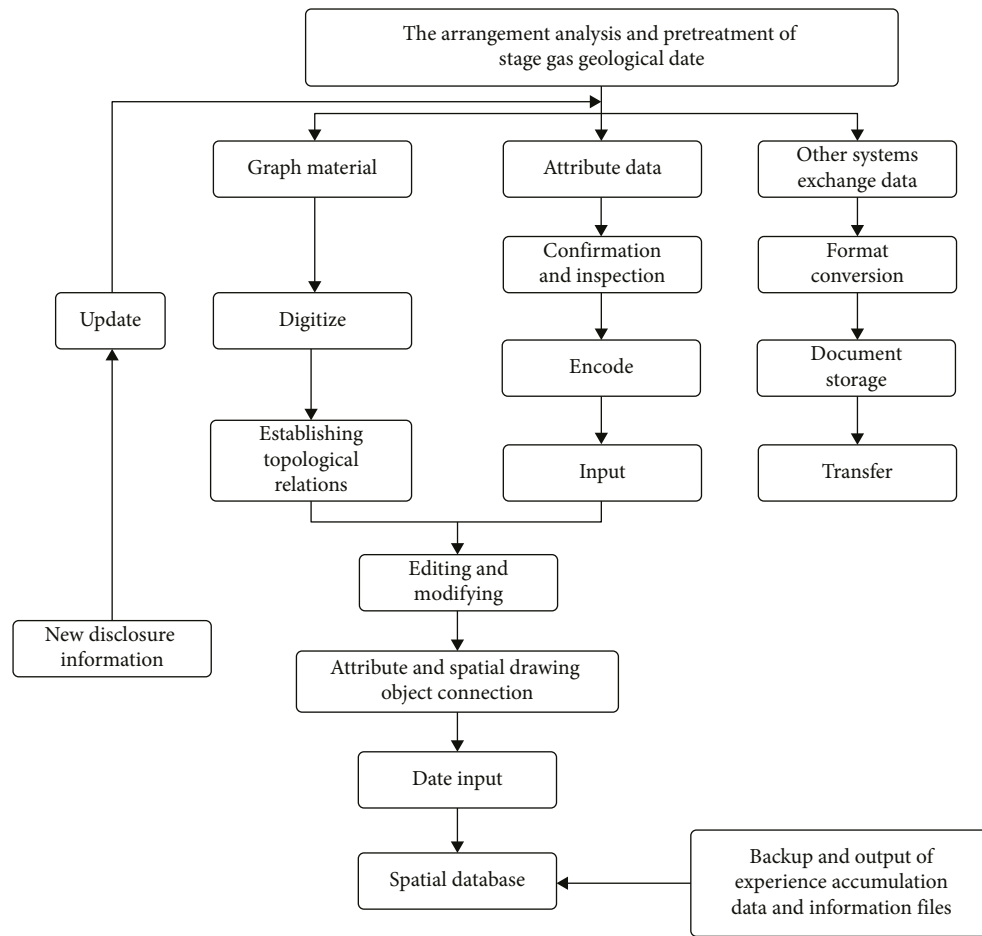


FIGURE 5: Working flow of building gas geology database.

4. Gas Geological Database Modeling

The diversified and accurate prevention and control technology of gas disasters is mainly based on the accurate detection of geology, structure, and gas; based on the current information technology, Internet of things, big data analysis, and other technologies, guided by the scientific concept of accurate coal mining, based on the causes and occurrence rules of mine gas outburst disasters, and supported by multisource information acquisition and sensing equipment, computers, and multinet network fusion transmission equipment, Taking the diversified and accurate prevention

and control models and software of gas disasters as tools, the accurate analysis and zoning of gas geology are carried out from the perspective of accurate control of mine gas geology; the intelligent evaluation of gas drainage reaching the standard and the optimal design of drainage boreholes are carried out from the perspective of accurate and reliable gas drainage, and the continuous monitoring and early warning of outburst anomalies are carried out from the perspective of intelligent early warning of gas emission. From the perspective of daily outburst prevention management norms, they carry out the standardized management and integrated analysis of the “four in one” comprehensive outburst

Features	Gas outbu	Vertical del	Elevation	Roadway	Location	Thickness	Geological
1 Pulverized	150	583	-580	Coal road	II 816CM	8	
2 Pulverized	200	583	-580	Coal road	II 816CM	8	Small fold
3	0	615	615	Rock lane	II 816CM	8~12	Thicken
4 Pulverized	1230000	613	-590	Stone gate	II 818CM	8~13	Thicken
5	2200	613	-590	Rock lane	II 818	8~13	Thicken
6 f=0.2-0.4	0	552	-529	Stone gate	II 814CM	8~13	Thicken
7 f=0.4	5000	552	-529	Semi coal	II 814CM	2.0	Coal seam
8 f=0.3	0	552	-529	Stone gate	II 814CM	8~15	Thicken
9	521	378	-355	Stone gate	3#MY	7.2	Not mined
10 Gas pressu	1600	321	-298	Stone gate	4#MY	10.0	8.9 thicke
11 Gas pressu	513	321	-298	Stone gate	4#MY	9.1	Small flod
12 Gas pressu	300	425	-400	Drift	Pit bottom	9	
13	1890	460	-437	Stone gate	II 821CM	8	
14	6528	396	-373	Stone gate	1#MY	10.5	8.9 thicke
15 f=0.2	2000	483	-460	Coal road	II 823CM	10~13	Coal seam
16 f=0.3	13000	454	-431	Coal road	II 822CM	10	Coal seam
17 f=0.3	100	435	-412	Coal road	II 822CM	12	Top plate
18 f=0.3	2000	454	-431	Coal road	II 822CM	11	Flod
19	0	379	-358	Stone gate	4#MY	12.7	Fault
20	1930	413	-390	Stone gate	2#MY	8	Fault
21	234	365	-342	Stone gate	4-84MY	12.2	Flod
22	600	347	-324	Drift	8#ZC	8.5	
23 Gas pressu	938	347	-324	Stone gate	6#MY	8.5	
24	1584	388	-383			8.5	

FIGURE 6: Attributes list scanning.

prevention measures information, realize the dynamic acquisition and comprehensive analysis of data in various links of the mine, such as “gas geology → gas drainage → gas monitoring → daily outburst prevention”, and carry out the accurate prevention and control of diversified gas disasters.

The gas geological database is the basis of developing the gas geological law. In the face of much gas geological data, scientific and effective analysis is the key to developing gas geological law research. In order to meet the needs of gas geological data with different attributes to carry out gas geological law research, different gas geological data models need to be used. In this paper, the fault tree model, the BP neural network, and grey theory are used to study the geological characteristics of gas. First, digital fusion is carried out, and the multiple information of mine gas parameters, coal seam parameters, geological exploration, geological structure, working face, and roadway are classified, fitted, and analyzed by the fault tree method to determine the main controlling factors of gas storage. Then, the BP neural gas network is used to establish a multiple regression analysis model of gas parameters and various factors. On the basis of the above research, the grey theory is used for quantitative fitting, and the contour of gas parameters is automatically drawn, and finally the geological law integrating gas, structure, coal seam, geology, and other factors is generated. [30, 31].

4.1. Accident Tree Modeling. Coal and gas outbursts are the result of the comprehensive action of gas, coal structure, in-situ stress, and other factors. Geological structures control the distribution of outburst risk by controlling gas occurrence, coal seam occurrence, and structural stress. More than 80% of the accidents occurred near faults and other geological structures. [32] Therefore, gas geological analysis and control takes geological structure as the monitoring focus, analyzes gas occurrence and coal seam occurrence changes in parallel, [33, 34] fully considers the logical relationship

between different factors and outburst, simplifies and merges some repeated basic events, and finally, determines the general model of coal and gas outburst fault tree with general significance constructed by 24 relatively independent factors (Figure 7).

4.2. BP Neural Network Modeling. The key to the establishment of the BP network model is to determine the number of nodes in the input layer, output layer, and hidden layer of the network, that is, to determine the input vector, output vector, and intermediate vector. Considering the organic combination with the general fault tree model of coal and gas outburst, this paper takes all 24 basic events ($X_1 \sim X_{24}$) of the fault tree model as the input vector of the BP network model. In the BP network model of gas outburst area prediction, the input vector is determined to be the matrix composed of 8 main factors affecting and controlling the outburst of the mine, which are: C1-gas pressure P , C2-coal mechanical strength, C3-coal body crushing comprehensive characteristic coefficient, C4-coal permeability coefficient, C5-coal seam bifurcation and combination comprehensive characteristic coefficient, C6-coal thickness and coal thickness change comprehensive characteristic coefficient, C7-fault complexity coefficient C8-comprehensive characteristic coefficient of interlayer sliding.

The output vector is the risk characteristics of a gas outburst. According to the outburst intensity, it is divided into four types: no outburst (type I); outburst threat (with dynamic phenomenon or abnormal gas emission, type II); general outburst (coal 0~100t, accompanied by a large amount of gas, type III); and serious outburst (coal more than 100t, accompanied by a large amount of gas, type IV). The output matrix is O1 (1, 0, 0, 0), O2 (0, 1, 0, 0), O3 (0, 0, 1, 0), and O4 (0, 0, 0, 1).

In general, the general relationship between the value of the hidden layer (middle layer) and the number of input vectors (m) and the number of output vectors (n) is ($2m + n$).

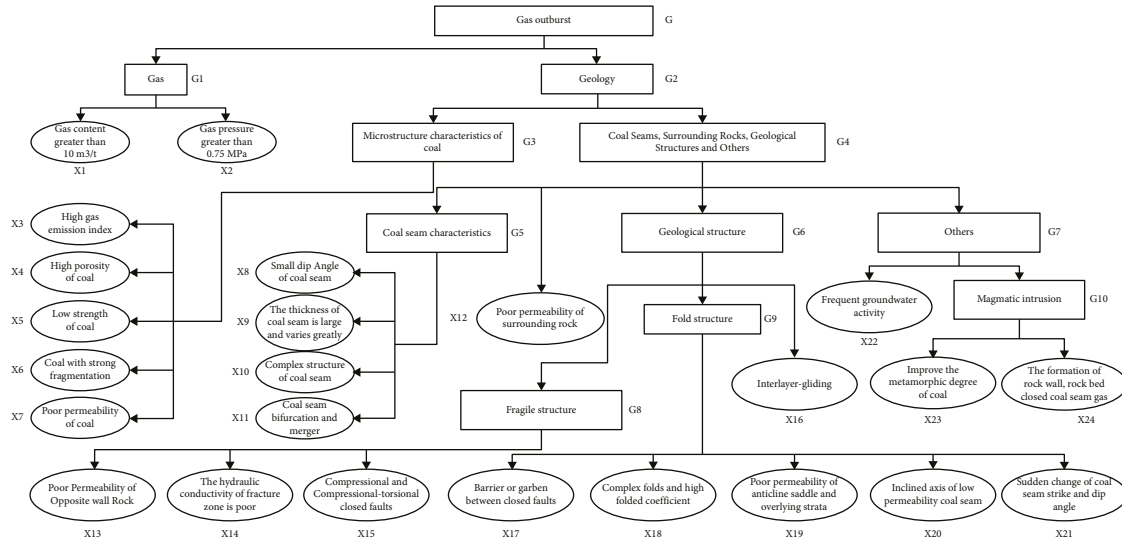


FIGURE 7: Accident tree model diagram.

According to this principle and experience, the initial value of the number of hidden layer (middle layer) vector elements here is 20.

4.3. Grey Theory Modeling. The sequence composed of gas emissions (2.72, 3.03, 4.86, and 6.98) is relatively small compared with the observed values of the whole period, but it has a great disturbance to the whole sequence. It can be said that these values are not the real behavior sequence of the grey system, and modeling and prediction with these distorted values of the whole grey system is bound to reduce the prediction accuracy. Therefore, we should weaken the sequential growth trend. The second-order weakening operator is introduced to obtain: $XD2 = (5.57, 5.96, 6.45, \text{ and } 6.98)$. Replace $XD2$ at the corresponding position of the original sequence to get a new sequence:

$X = (5.57, 5.96, 6.45, 6.98, 6.87, 7.46, 7.32, 7.69, 7.66, 7.92, 8.18, 8.11, \text{ and } 8.63)$; GM (1, 1) model is established by using the 1st~8th data in the sequence X to predict the gas emission of II914 working face. The modeling process is as follows:

$$X^{(0)} = (5.57, 5.96, 6.45, 6.98, 6.87, 7.46, 7.32),$$

$$X^{(1)} = 1 - AGOX^{(0)} \tag{1}$$

$$= (5.57, 11.53, 17.98, 24.96, 31.83, 39.29, 46.61).$$

Least square estimation of parameter columns $\hat{a} = (a, b)^T$,

$$\hat{a} = (a, b)^T$$

$$= (B^T B)^{-1} B^T Y_N \tag{2}$$

$$= \begin{bmatrix} -0.03748 \\ 5.87891 \end{bmatrix}.$$

Determine the model: $dx^{(1)}/dt - 0.03748X^{(1)} = 5.87891$

Determine the time response sequence:

$$\hat{x}(k+1) = 162.3934e^{0.03748k} - 156.8234$$

Comparison between sequence $\hat{x}^{(0)}(k)$ and sequence $\hat{x}^{(1)}(k)$ Table 6.

As can be seen from the calculated results in Table 6, the residuals of the resulting prediction models are -0.07, +0.26, -0.16, -0.07, and -0.39, and the relative error prediction values are 1.01%, 3.48%, 2.18%, 0.91%, and 5.01%, all of which meet the accuracy requirements.

5. Visualization of Gas Geological Dynamic Characteristics under Big Data Framework

The design of coal and gas outburst prediction information systems is the core content of the whole system. Its main work is to transform the system logical model proposed in the system analysis stage into a realizable physical model; that is, the problem of “what to do” proposed in the system analysis stage is further concretized and refined into the problem of “how to do”. In this paper, the design of coal and gas outburst regional prediction information system adopts modular and open design ideas, follows the principles of systematization, practicality, versatility, and scalability, and strives to make the system a practical information system with advanced technology, reliable operation, and high efficiency. The whole system function development adopts a rapid prototyping method and submodule implementation. The visualization function module of gas geological dynamics under the condition of a big data framework is shown in Figure 8.

Thematic mapping is a method with powerful analysis functions and data visualization. By using thematic graphics to represent and display data and using certain thematic rendering means, the information status and change trend that can hardly be displayed in the data list can be displayed intuitively and clearly. Usually, thematic maps use color rendering, hatch patterns, symbols, rectangles, pie charts, and other ways to express data. Different thematic maps can

TABLE 6: The verifying conclusions using predicting model.

Time	k	Measure value $x^{(0)}(k)$	Predicted value $\hat{x}^{(0)}(k)$	Residual error $\epsilon^{(0)}(k) = x^{(0)}(k) - \hat{x}^{(0)}(k)$	Relative error $\Delta k = \epsilon^{(0)}(k) /x^{(0)}(k)$ (%)
2005.4	5	6.87	6.94	-0.07	1.01
2005.5	6	7.46	7.20	+0.26	3.48
2005.6	7	7.32	7.48	-0.16	2.18
2005.7	8	7.69	7.76	-0.07	0.91
2005.8	9	7.66	8.05	-0.39	5.01

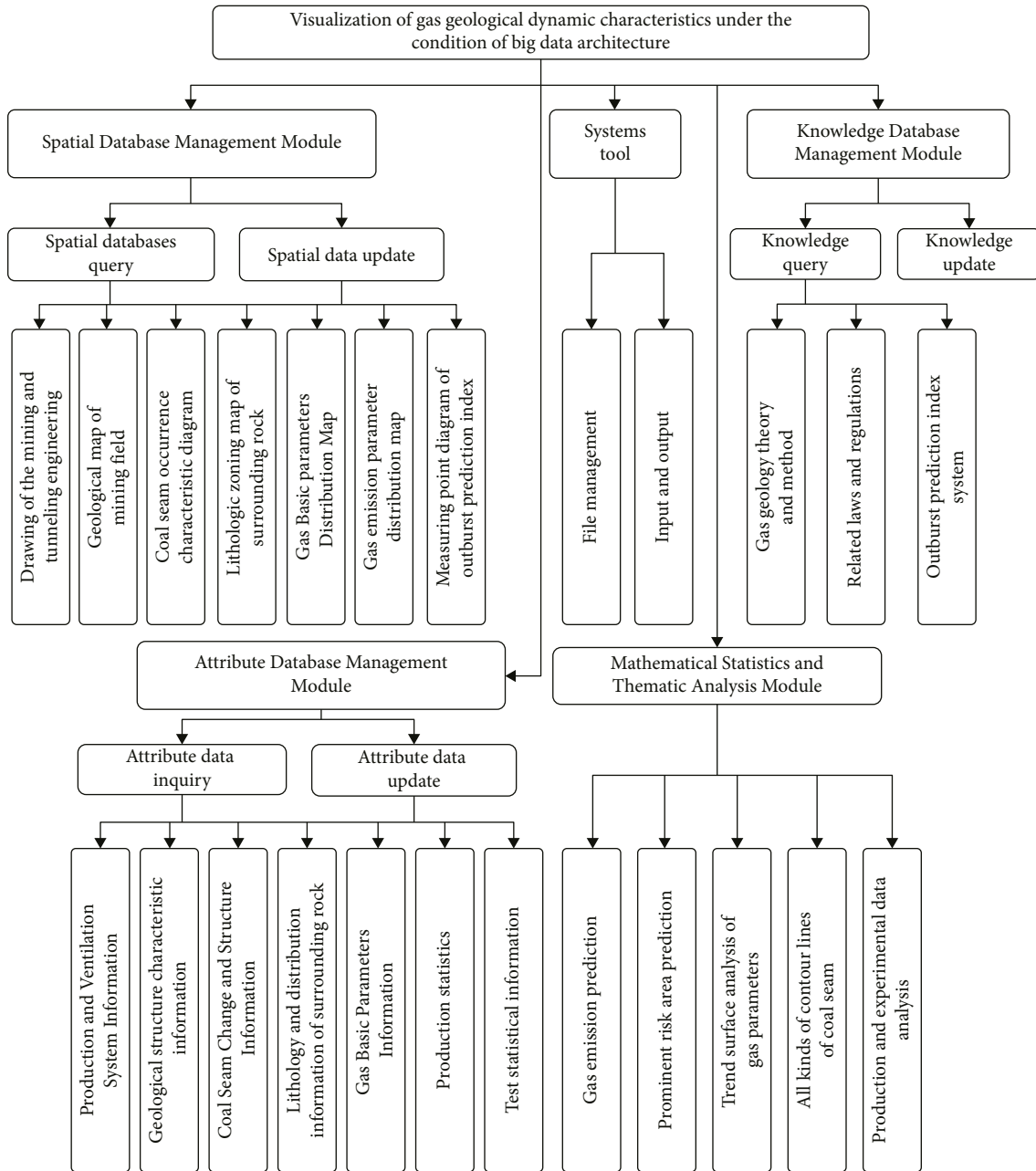


FIGURE 8: Vass geological dynamic visualization framework under big data framework.

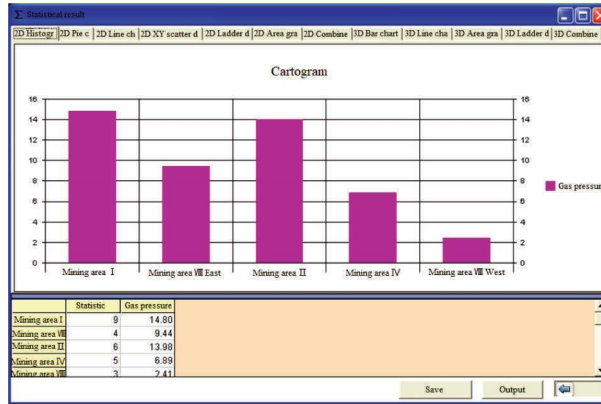


FIGURE 9: The block diagram of gas content in eighth coal of Luling mining.

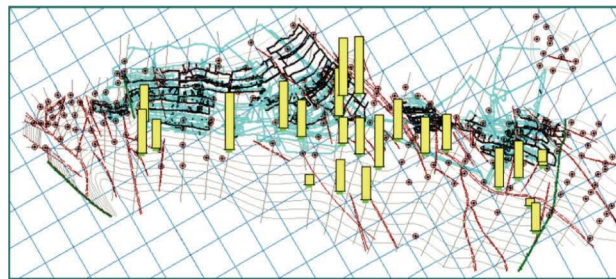


FIGURE 10: The point diagram of the gas press in the eighth coal of Luling mining.

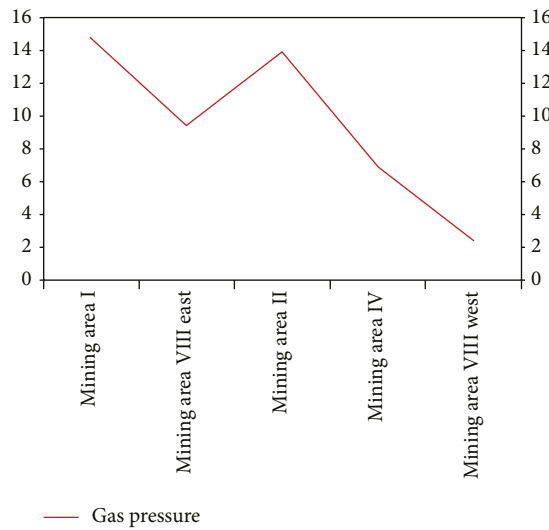


FIGURE 11: The gas press by mine section in the eighth coal of Luling mining.

be created by assigning these colors, patterns, or symbols according to specific values in the data. In the gas geological database and its visualization system, MapObjects can be used to analyze various thematic maps such as the following

level symbol maps, range maps, independent value maps, pie charts, and histograms, as shown in Figures 9–12.

Only parts of the thematic maps are listed above. The thematic maps of gas emission and coal thickness points of 8

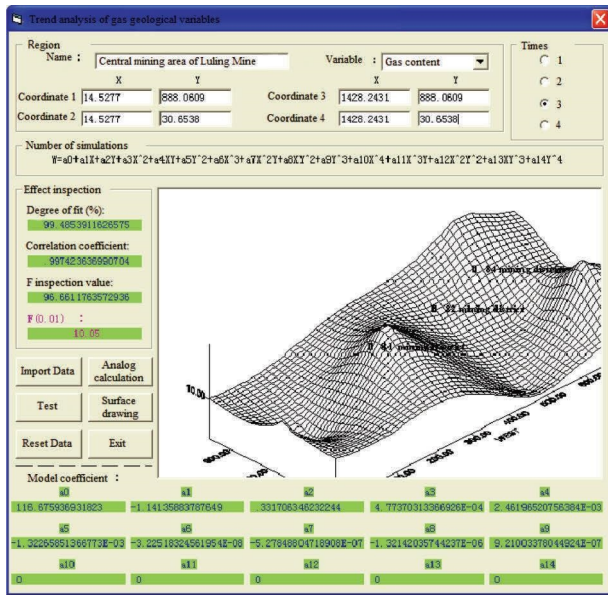


FIGURE 12: Trend analysis of gas geological variables.

coal seams in Luling Mine are similar to this, and they are not listed here one by one.

6. Conclusions

The irresistible development momentum of industrial informatization, automation, and intelligence has provided new development opportunities and challenges for the transformation of typical and major disaster management in coal mines from traditional qualitative and empirical prevention to modern quantitative and precise prevention. Based on the causes of coal mine gas outburst disasters, this paper adopts information technology, the Internet, big data analysis, and other technologies and gives full play to the role of abundant coal mine gas geological data, and combines relevant disciplines to scientifically analyze and calculate the geological data that affect coal and gas outburst, so that the gas geological data can be updated in time and the changes of gas geological laws can be dynamically displayed. The main conclusions are as follows:

- (1) A gas geological attribute database is established based on borehole data, gas content and related data, gas emission data, and outburst data of mining faces on the basis of accurate gas detection.
- (2) A coal and gas outburst fault tree constructed by 24 relatively independent factors is established through grey theory, fault tree theory, BP neural network, and other disciplines.
- (3) Taking the matrix composed of 8 main factors affecting and controlling outburst in Luling coal mine as the input vector, then the geological data of coal and gas outburst are scientifically analyzed and calculated. As a result, the possibility of visualization and real-time gas geological data is verified.

Data Availability

All data generated or analyzed during this study are included in this published article.

Conflicts of Interest

The authors declare that they have no conflicts of interest.

Acknowledgments

This study was supported by the National Natural Science Foundation of China Youth Science Foundation Project (No.51804100) and National Natural Science Foundation of China Joint Fund Project (No.U1904126).

References

- [1] Y. K. Ma, B. s Nie, X. q He, X. c Li, J. q Meng, and D. z Song, "Mechanism investigation on coal and gas outburst: an overview," *International Journal of Minerals Metallurgy and Materials*, vol. 27, no. 7, pp. 872–887, 2020.
- [2] Y. P. Cheng and P. Zhejun, "Reservoir properties of Chinese tectonic coal: a review[J]," vol. 260, *Fuel*, Article ID 116350, 2020.
- [3] T. R. Jia, Z. Feng, G. Wei, and Y. Ju, "Shear deformation of fold structures in coal measure strata and coal-gas outbursts: c," *Energy Exploration & Exploitation*, vol. 36, no. 2, pp. 185–203, 2018.
- [4] F. H. An, "The Effect of a Tectonic Stress Field on Coal and Gas Outbursts[J]," *Scientific World Journal*, vol. 2014, no. 1, Article ID 813063, 55 pages, 2014.
- [5] D. Y. Xu and D. Guo, "Dome-basin structure and its influence on coal and gas outbursts," *Polish Journal of Environmental Studies*, vol. 27, no. 4, pp. 1823–1831, 2018.
- [6] X. J. Chen, L. Li, Y. Yuan, and H. Li, "Effect and mechanism of geological structures on coal seam gas occurrence in Changping minefield," *Energy Science & Engineering*, vol. 8, no. 1, pp. 104–115, 2020.
- [7] N. N. Zhu, *Study on the Microseismic Precursor Characteristics and Early-Warning Model of Coal and Gas Outburst*, China Coal Research Institute, vol. 54, Bei Jing Shi, China, , 2018.
- [8] L. Yuan, "Research progress of mining response and disaster prevention and control in deep coal mines," *Journal of China Coal Society*, vol. 46, no. 3, pp. 716–725, 2021.
- [9] G. Y. Wei, F. C. Kang, B. B. Qin, T. R. Jia, J. W. Yan, and Z. D. Feng, "A novel method for evaluating proneness of gas outburst based on gas-geological complexity," *Natural Hazards*, vol. 104, no. 2, pp. 1841–1858, 2020.
- [10] C. Guo, F. Jinyang, J. Deyi, and L. Jiajun, "Method and practice of gas geological grading evaluation on coal mining face of high gas mine," *Journal of China Coal Society*, vol. 44, no. 8, pp. 2409–2418, 2019.
- [11] A. Finsne and O. Esen, "Coal and gas outburst hazard in Zonguldak Coal Basin of Turkey, and association with geological parameters," *Natural Hazards*, vol. 74, no. 3, pp. 1363–1390, 2014.
- [12] Y. Wan, *Research on Prediction Method of Coal and Gas Outburst Risk*, Lanzhou Jiaotong University, vol. 1, no. 2009, , pp. 173–179, China, Gan Su Sheng, 2021.
- [13] Q. H. Zhang, R. Gao, and J. Yang, "Research on dynamic prediction technology of coal and gas outburst in high-yield

- and high-efficiency mine,” *Coal Science and Technology*, vol. 46, no. 10, pp. 65–72, 2018.
- [14] J. Han, “Nappe structure’s kinetic features and mechanisms of action to coal and gas outburst,” *Journal of China Coal Society*, vol. 37, no. 2, pp. 247–252, 2012.
- [15] C. J. Fan, S. Li, M. Luo, W. Du, and Z. Yang, “Coal and gas outburst dynamic system,” *International Journal of Mining Science and Technology*, vol. 27, no. 1, pp. 49–55, 2017.
- [16] Y. S. Pan, “Integrated study on compound dynamic disaster of coal-gas outburst and rockburst,” *Journal of China Coal Society*, vol. 41, no. 1, pp. 105–112, 2016.
- [17] G. W. Dong, “The evolution of ejective folds and their influence on coal and gas outburst,” *Journal of China University of Mining & Technology*, vol. 41, no. 6, pp. 912–916, 2012.
- [18] F. H. An and Y. P. Cheng, “An explanation of large-scale coal and gas outbursts in underground coal mines: the effect of low-permeability zones on abnormally abundant gas,” *Natural Hazards and Earth System Sciences*, vol. 14, no. 8, pp. 2125–2132, 2014.
- [19] T. H. Yang, “Coupling model of stress-damage-flow and its application to the investigation of instantaneous seepage mechanism for gas during unloading in coal seam with depth,” *Chinese Journal of Rock Mechanics and Engineering*, no. 16, pp. 2900–2905, 2005.
- [20] J. H. Mou, H. Liu, Y. Zou, and Q. Li, “A new method to determine the sensitivity of coal and gas outburst prediction index,” *Arabian Journal of Geosciences*, vol. 13, no. 12, p. 465, 2020.
- [21] Y. P. Cheng, “Research progress of sensitive index and critical values for coal and gas outburst prediction,” *Coal Science and Technology*, vol. 49, no. 1, pp. 146–154, 2021.
- [22] H. Fu, “Study on double coupling algorithm based model for coal and gas outburst prediction,” *China Safety Science Journal*, vol. 28, no. 3, pp. 84–89, 2018.
- [23] K. B. Huang, “Based on grey theory and BP neural network gas emission prediction research,” *Journal of North China Institute of Science and Technology*, vol. 17, no. 2, pp. 16–22, 2020.
- [24] J. T. Lu, “Assessment of coal mine gas explosion risk based on grey-matter element model,” *China Safety Science Journal*, vol. 31, no. 2, pp. 99–105, 2021.
- [25] Z. Y. Sun, “Dynamic prediction of gas concentration in mining face based on long short-term memory neural network,” *Safety In Coal Mines*, vol. 50, no. 12, pp. 152–157, 2019.
- [26] Y. Q. Liang, D. Guo, Z. Huang, and X. Jiang, “Prediction model for coal-gas outburst using the genetic projection pursuit method,” *International Journal of Oil, Gas and Coal Technology*, vol. 16, no. 3, pp. 271–282, 2017.
- [27] Y. B. Li, “Prediction method of methane geological law based on the multifractal singularity theory: an example from the Panyi Coalmine, Huainan coalfield, China,” *Journal of China Coal Society*, vol. 43, no. 12, pp. 3436–3446, 2018.
- [28] D. Y. Guo, “Early warning of coal and gas outburst by GIS and neural network,” *Journal of University of Science and Technology Beijing*, vol. 31, no. 1, pp. 15–18, 2009.
- [29] T. R. Jia, J. Yan, X. Liu, Z. Feng, G. Wei, and L. Cao, “Analysis method of the occurrence law of coalbed gas based on gas-geology units: a case study of the guhanshan mine field, jiaozuo coalfield, China,” *ACS Omega*, vol. 7, no. 14, pp. 12296–12306, 2022.
- [30] W. Wang, H. Wang, B. Zhang, S. Wang, and W. Xing, “Coal and gas outburst prediction model based on extension theory and its application,” *Process Safety and Environmental Protection*, vol. 154, pp. 329–337, 2021.
- [31] L. Kong, W. Hanpeng, Z. Bing, W. Su, and X. Wenbin, “Coal and gas outburst prediction model based on Improved BP neural network,” *Science & Technology Vision*, vol. 21, pp. 111–112, 2015.
- [32] L. Chen, E. Wang, J. Ou, and J. Fu, *Geosciences Journal*, vol. 22, no. 1, pp. 171–182, 2018.
- [33] Y. P. Cheng, “Causality between tectonic coal and coal and gas outbursts,” *Journal of China Coal Society*, vol. 46, no. 1, pp. 180–198, 2021.
- [34] Y. X. Cao, C. G. David, and H. Dingdong, “Characteristics of coal and gas outburst and controlling mechanism of stress field in the hanging wall of normal faults,” *Coal Geology & Exploration*, vol. 52, no. 4, pp. 61–69, 2022.

Research Article

Data-Driven-Based Study on Sustainable Improvement of the Regional Logistics Industry

Yujia Liu  and Heping Ding 

Business School, Suzhou University, 026 County Road, Education Park, Yongqiao District, Suzhou 234000, Anhui, China

Correspondence should be addressed to Heping Ding; dingheping@ahszu.edu.cn

Received 8 August 2022; Revised 29 September 2022; Accepted 24 November 2022; Published 20 February 2023

Academic Editor: Adiel T. de Almeida-Filho

Copyright © 2023 Yujia Liu and Heping Ding. This is an open access article distributed under the Creative Commons Attribution License, which permits unrestricted use, distribution, and reproduction in any medium, provided the original work is properly cited.

The rapid growth and development of the logistics industry has brought productivity to commerce and trade and greatly contributed to national economy, but at the expense of vast energy consumption, which significantly affects sustainability. To improve sustainability of the development of the logistics industry (LISD) and identify its potential influencing factors more directly and efficiently, this study proposes a data-driven-based evaluation and optimisation method. First, a comprehensive evaluation index system is constructed for LISD from the aspects of economy, society, and environment (including the logistics industry, degree of specialisation, environmental effects, and innovation capability). Second, considering the diversity of dimensions and units, a min-max standardisation is utilised for data normalisation, providing dimensionless indicators for further weight determination via an entropy value method. Third, two coupling degree models are adopted to evaluate the degree of correlation among subsystems. Subsequently, a degree of obstacle model is applied to analyse the interaction between factors, providing theoretical support for improving regional LISD. Finally, an evaluation of LISD in Anhui Province is used as a case study to validate the practicability and feasibility of the proposed method, establish theoretical basis, and propose policy recommendations for future sustainable development.

1. Introduction

1.1. Research Background. The logistics industry (LI) is a composite service industry that integrates transportation, warehousing, freight, and information industries [1]. The sustainable development of the logistics industry (LISD) has great significance for the promotion of industrial structure and improvement of the competitiveness of national economies [2]. However, the LI is also a major industry related to energy consumption and carbon emissions [3]. To fulfill the requirements of sustainable economic development, the traditional LI needs to be updated to the modern LI, following the guidance of advanced operation and management concepts, thus, the energy consumption and traffic pressure can be effectively reduced [4].

Despite extensive research on LISD, previously developed models have emphasised the economic performance unilaterally, which is no longer suitable for the development of the

regional LI [5]. Therefore, the enhancement of LISD in coordination has received increasing emphasis in the academic field [6–10]; the existing research can be divided into the following aspects:

- (1) Research on the index evaluation system of regional logistics sustainability

Due to the serious environmental pollution, resource depletion, and climate deterioration, the LISD has received extensive attention [11–13], and related studies proposed that companies should integrate the concept of sustainability into business operations to improve their long-term competitiveness [14]. Therefore, various indicator systems for LISD have been constructed from the perspective of economy, society, environment, technological innovation, and industry policy [15]. Particularly, detailed indicators include the logistics carrying capacity [16], industrial performance, innovation capacity, emissions and industry output [17],

logistics packaging sustainability [18], and ecological efficiency [19].

Based on the constructed indicator system, scholars in different fields explored methods to quantify the level of sustainability industries. For example, Liu [20] processed data from the perspective of energy. Kayikci [21] developed a stream processing data-driven decision-making model, resilience of the logistics infrastructure. As for the specific operation method, Cao [22] focused on using the DEA-Bayes method to study the sustainable development efficiency of the urban LI, while Long [23] employed the super-SBM-DEA model to evaluate regional differences in logistics efficiency. Huang [1] selected the entropy weight method to assign values to various indicators.

(2) Research on the improvement of the LISD

Besides the studies on the index evaluation system and calculation methods, the benefits and losses of logistics practitioners were investigated under the analysis of different policy environments, such as urban route planning, public space management [24], carbon tax policy [25], producer responsibility [26], policy subsidies, and construction logistics, which can provide suggestions for practitioners' optimal decision-making and reference for government policy equation. From the perspective of policy advice research methods, Liu [27, 28] used the Nash equilibrium strategy to study how to coordinate a three-party sustainable supply chain and improve the internal coordination of the sustainable supply chain for economic and environmental benefits. Previous studies have assessed regional logistics sustainability and incentive policies, but the evaluative indicators for regional logistics are relatively incomplete. Specifically, most of the index evaluation systems in the existing literature are focused on the national level [29] or are aimed at developed regions, and their index weight setting methods may not be appropriate when researching other regions; most existing literature focus on specific perspectives, such as logistics service providers [30], considering the government and the public less when setting the indicator system. Therefore, these evaluation methods require further studies.

1.2. Research Limitations. The existing research constructed a good foundation for determining the sustainable development level of the LI and its development path. However, the breadth and depth of this research must be further improved. For instance, the perspective of the existing research mostly from the government or LI practitioners unilaterally. Moreover, while analysing the calculation process, the impact of the COVID-19 has not been sufficiently taken into consideration. Despite the wide application of evaluation methods, such as the DEA and TOPSIS models, the process of selecting quantitative indicators is affected by subjective factors and can easily be disturbed by extreme values during data processing. Therefore, this study proposes a data-driven-

based evaluation and optimisation method for LISD and further provides targeted optimisation countermeasures correspondingly. In the proposed approach, a comprehensive evaluation index system was first constructed from the aspects of economy, society, and environment (including the logistics industry, degree of specialisation, environmental effects, and innovation capability) for LISD. Then, due to the diversity of dimensions and units, a min-max standardisation was utilised for data normalisation, which provides dimensionless indicators for further indicator weight determination via the entropy value method. Following this, two coupling degree models were adopted to evaluate the degree of correlation and coordination among the subsystems, avoiding low system or the false coordination. This model can help different subsystems cooperate properly and achieve the overall improvement of the system. Subsequently, a degree of the obstacle model was applied to analyse the interaction between various factors, which provides theoretical support for improving the sustainability of the regional LI. Finally, the sustainability evaluation for the LI in Anhui Province was adopted as a case study to validate the practicability and feasibility of the proposed method and policy recommendation. In brief, this paper proposes a data-driven approach to evaluate the LISD, and the main novelty of the paper are: (1) Researching the LISD from a data-driven perspective and applying a quantitative evaluation model to explore the degree of the LISD. (2) A targeted government incentive mechanism is designed and through considering the cooperative relationship among logistics, the government and the market, provide policy recommendations to improve the LISD. These are the contributions and novelty of this paper. A theoretical basis for in-depth research on the development of the regional economy was provided for sustainable development. This paper contributes to studying the LISD in areas with economic potential. By comprehensively and systematically quantifying the sustainable development capability of the industry, it finds the factors that hinder the development and promotes the coordinated development of the regional economy. Anhui Province, located in the Yangtze River Delta region with abundant economic resources, has an above-average economy in China. Despite possessing an obvious location advantage, the GDP of Anhui Province still drops behind of that of surrounding provinces by a substantial amount. Therefore, with superior objective development conditions, the development potential of Anhui Province can be improved through critical suggestions.

1.3. Structure. This paper is organised as follows: Section 1 describes the development status of the LI in Anhui Province through the operation of the local logistics industry and energy consumption. Section 2 presents the model development and data processing method. Section 3 evaluates the LISD in Anhui Province and proposes corresponding development suggestions according to the calculation results. Section 4 presents the background and data analysis. In Section 5, the management implications and future work are discussed. Finally, the conclusion is given in Section 6.

2. Materials and Methods

In the following sections, the proposed methods, including model selection, data processing, result analysis, and further suggestions are systematically described.

2.1. Method Flow. This paper evaluated LISD and put forward development suggestions based on data from four aspects: logistics industry basis, degree of specialisation, environmental effects, and innovation ability. Specifically, this research first adopted the min-max standardisation method to perform dimensionless and standardised processing of the original data. Then, the entropy method was utilised to determine the index weight and calculate the sustainability of the logistics industry according to the indicator weights. Subsequently, two coupling degree models are adopted to evaluate the degree of correlation and coordination among subsystems, respectively. Finally, the targeted optimisation countermeasures and suggestions were put forward. The flowchart of the proposed method is illustrated in Figure 1.

2.2. Data Collection. The data was mainly obtained from the China Logistics Yearbook, Anhui Provincial Statistical Yearbook, China Energy Statistical Yearbook, and similar sources. Some missing data were obtained by a weighted average method. By collecting various data of the regional LI in a fixed period, a comprehensive assessment of the LI was carried out to determine the key influencing factors. The detailed evaluation indicators are shown listed in Table 1. “LI basic” refers to the inherent factors of sustainable development of the LI, including many measurement factors such

as employees, equipment, infrastructure construction, and gross production value. “Degree of specialisation” demonstrates the service efficiency and benefits of the corresponding logistics services. “Environmental effects” refer to environmental pollution and resource utilisation [26, 27]. Lastly, the “ability of innovation” refers to the drive of sustainable development and evaluates the deepest benches in high-tech, scientific payoffs, and financial support. The logistics industry basic and degree of specialisation represent the existing development foundation. Moreover, degree of specialisation and ability of innovation indicate the ability that the region’s natural and social resources can support the LISD in the future.

2.3. Data Processing

2.3.1. Min-Max Standardisation. Due to the different characteristics of the original data, with some being positive and some being negative indicators, mechanical aggregation was not advisable. Moreover, as the units of the collected data were different, data standardisation is required to remove the unit limitation of the original data and perform co-chemotropic/dimensionless processing before data analysis. After data standardisation, a min-max normalisation approach was adopted to transform the dimensionless evaluation indicators linearly. To avoid results deviation induced by the occurrence of 0 and 1, $\min\{X_{ij}\}$ was set as 0.99 times the actual minimum value of $\{X_{ij}\}$, while $\max\{X_{ij}\}$ was set as 1.01 times the actual maximum value of $\{X_{ij}\}$. The specific calculation steps and corresponding equations were as follows [28]:

Positive indicators:

$$X_{ij}^* = \frac{X_{ij} - \min\{X_{ij}\}}{\max\{X_{ij}\} - \min\{X_{ij}\}} + 0.1, i = 1, 2, 3 \dots, m; j = 1, 2, 3 \dots, n. \quad (1)$$

Negative indicators:

$$X_{ij}^* = \frac{\max\{X_{ij}\} - X_{ij}}{\max\{X_{ij}\} - \min\{X_{ij}\}} + 0.1, i = 1, 2, 3 \dots, n; j = 1, 2, 3 \dots, m, \quad (2)$$

where n is the number of the first level indicators, m is the number of the second level indicators, X_{ij} is the j^{th} second level indicator of the first level indicator I , $\max\{X_{ij}\}$ and $\min\{X_{ij}\}$ are the maximum and minimum of X_{ij} , respectively. The calculation result of these two equations, i.e., X_{ij}^* , was the data after non-negative processing.

2.3.2. Entropy Value Method for Determining Index Weight. The entropy method is an objective weighting method which can determine the index weights according to the degree of variation in the values of each index, avoiding the interference of human factors. The weight of indicators X_{ij} and μ_{ij} was determined as follows [28–30]:

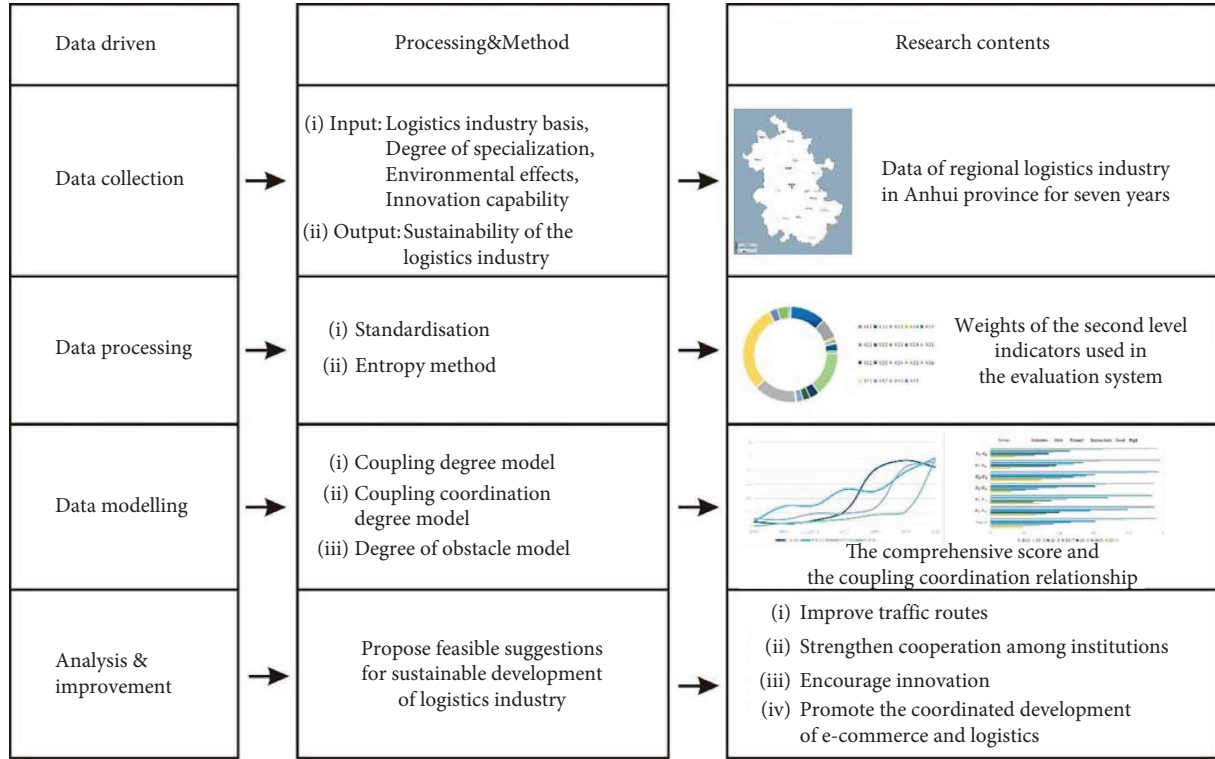


FIGURE 1: Flowchart of the proposed method.

TABLE 1: Evaluation index system of the sustainable development of the logistics industry (LISD).

Primary indicators	Secondary indicators	Direction of indicators
Logistics industry basic X_1	X_{11} number of employed persons in urban nonprivate units in the logistics industry (persons)	+
	X_{12} GDP of the logistics industry (100 million RMB)	+
	X_{13} fiscal expenditure general public services (100 million RMB)	+
	X_{14} fixed asset investment in the logistics industry (10,000 RMB)	+
	X_{15} number of trucks in urban highway operation (vehicles)	+
Degree of specialisation X_2	X_{21} ratio of total logistics costs to GDP	-
	X_{22} number of business outlets (offices)	+
	X_{23} transport line length (km)/service area (km ²)	+
	X_{24} permanent population/business outlets	-
Environmental effects X_3	X_{31} added value of the logistics industry (billion)	+
	X_{32} total energy consumption of the logistics industry (10,000 tons of standard coal)	-
	X_{33} wastewater discharge in the logistics industry (10,000 tons)	-
	X_{34} exhaust gas emissions from the logistics industry (10,000 tons)	-
	X_{35} solid waste discharge in the logistics industry (10,000 tons)	-
	X_{36} energy consumption per unit of logistics output (= total energy consumption of the logistics industry/added value of the logistics industry)	-
Ability of innovation X_4	X_{41} number of authorised patent applications for logistics technology innovation (items)	+
	X_{42} income from the education funds of higher education schools (10,000 RMB)	+
	X_{43} research and experimental development (R&D) expenditure (10,000 RMB)	+
	X_{44} number of graduate students in colleges and universities	+

$$X_{ij}, \mu_{ij} = \frac{X_{ij}}{\sum X_{ij}}. \quad (3)$$

$$e_j = -k \sum \mu_{ij} \times \ln \mu_{ij}, k = \left(\frac{1}{\ln m} \right). \quad (4)$$

The information entropy of index j (e_j) was calculated as follows:

The value of the information entropy redundancy of index g_j , behaves as follows: the higher the value, the higher the index redundancy, and it was calculated as:

$$g_i = 1 - e_j. \quad (5)$$

The weight of the indicator w_j was calculated as follows:

$$w_j = \frac{g_i}{\sum g_i}. \quad (6)$$

2.4. Data Modelling

- (1) Determining the comprehensive score of the indicators

The sustainability level of the LI was calculated according to the standardised logistics industry-related data weights, which were determined by the entropy value method [31, 32]:

$$\gamma_i = \sum_j (w_j \times X_{ij}^*), \quad (7)$$

where γ_i is the comprehensive score of the sustainability level of the LI and is used to calculate the comprehensive level of various first level indicators similarly (including logistics industry basic, degree of specialisation, environmental effects, and innovation ability).

- (2) Coupling degree model

Based on the obtained comprehensive score of the sustainability level of each first level indicator, the coupling degree (A) between the four first level indicators was calculated using the following equation [33–35]:

$$A = \frac{5 \times \sqrt[5]{X_1 X_2 X_3 X_4 X_5}}{X_1 + X_2 + X_3 + X_4 + X_5}, \quad (8)$$

where A is in the interval of $(0, 1)$, $X_1, X_2, X_3,$ and X_4 are the comprehensive levels of industry basics, specialisation, environmental effects, and innovation ability, respectively. In this method, a higher coupling degree value indicates the greater degree of coupling relationship between the internal indicators of the LISD.

- (3) Coupling coordination degree model

The coupling model described above was employed to evaluate the degree of correlation between the subsystems; however, this model cannot reflect the coordination within the system. Therefore, the coupling coordination model was used to evaluate the degree of benign coupling between the subsystems, i.e., low-quality mutual hindrance or high-quality mutual promotion [36–38].

$$B = \sqrt{A \times Z}, Z = aX_1 + bX_2 + cX_3 + dX_4, \quad (9)$$

where B is the coupling degree, Z is the comprehensive evaluation index used to reflect the overall level of subsystem (including logistics industry basic, degree of specialisation, environmental effects, and innovation capability), and $a, b, c,$ and d are the

undetermined weight coefficients. This model assumes that each subsystem is equally important in the LISD, so $a = b = c = d = 1/4$. Based on the determined coupling degree, the coordination level is divided into seven grades: high-quality coordination, good coordination, intermediate coordination, primary coordination, mild dysregulation, moderate maladjustment, and serious maladjustment, which has been proven to be the most practical. Table 2 shows the standard values of these seven divisions.

- (4) Degree of obstacle model

The degree of obstacle was calculated as follows [39, 40]:

$$\mu_{ij} = \frac{(1 - X_{ij}^*) \times w_{ij \times 100\%}}{\sum (1 - X_{ij}^*) \times w_{ij}}, \quad (10)$$

$$\mu_i = \sum \mu_{ij},$$

where μ_{ij} is the obstacle degree of the j^{th} second level index in the first level index i , μ_i represents the obstacle degree of the first level index, X_{ij}^* represents the standardised value of the j^{th} second level index, $1 - X_{ij}^*$ indicates the degree of deviation of the index, and w_{ij} is the weight of the j^{th} indicator.

3. Method Application

As shown in Figure 2, the proposed LISD approach consists of three stages. To systemically weigh the indicators at all levels after standardising the original data and calculate the sustainability scores of different subsystems in the logistics industry, an entropy method is utilised for experimental design in the first stage. During the second stage, the coupling degree and coupling coordination degree models were adopted to evaluate the degree of benign coupling between the subsystems. For the third stage, an obstacle degree model was utilised to calculate the obstacle degree of each index and identify the obstacle factors and the key breakthroughs in the sustainable development of the regional LI. Finally, based on the combined data processing results and official government documents, feasible development suggestions were proposed for optimising LISD. In this research, the data which were collected from various fields, including GDP of regional logistics industry, infrastructure construction, wastewater, waste gas, solid waste discharge, and scientific research results in a fixed period, will be used to construct a comprehensive evaluation index system for the regional LISD. Also, scientific methods were applied to the industry operation process, providing positive feedback to optimise and improve the logistics industry.

4. Results

4.1. Background. Anhui Province covers an area of 140,100 km². In 2020, its total population was 61.027 million and the corresponding GDP was 3,868.063 billion RMB, ranking 11th in China. It is located in the Yangtze River

TABLE 2: Seven levels of classification for the evaluation of the coupling harmonious degree.

Harmonious degrees	Harmonious levels
0–0.3	Serious maladjustment
0.3–0.4	Moderate maladjustment
0.4–0.5	Mild maladjustment
0.5–0.6	Primary coordination
0.6–0.7	Intermediate coordination
0.7–0.8	Good coordination
0.8–1	High-quality coordination

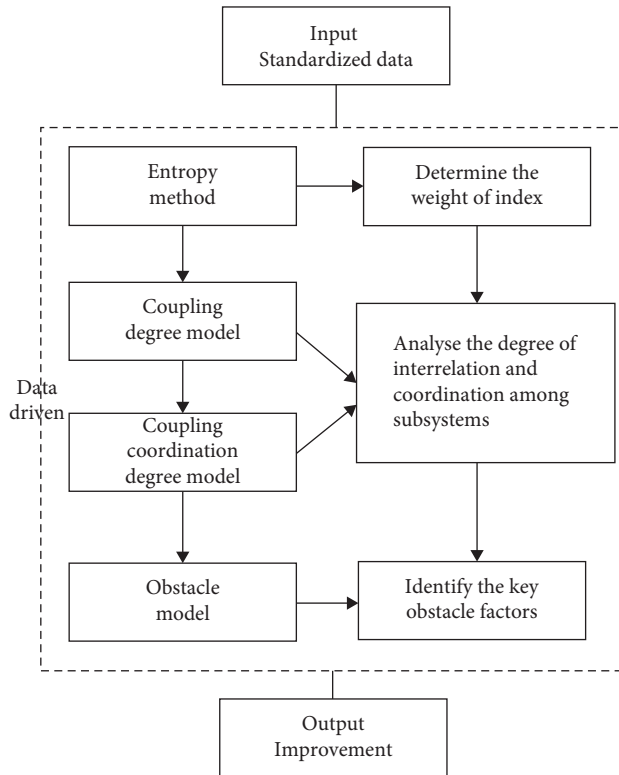


FIGURE 2: Data analysis process of the LISD.

Delta region, which has many metropolitan circles along the river, such as the Nanjing Metropolitan Circle, Central Plains Economic Circle, and Hangzhou Metropolitan Circle, providing abundant outside resources for economic development. Anhui Province gains the economic benefits of the coastal areas. In 2020, the total social logistics of the LI in Anhui Province was 7,021.3 billion RMB with a year-to-year increase of 3.5%. Moreover, the ratio between total social logistics costs and GDP in the same year was 14.7%, which was a 0.2% decrease from the previous year, and the overall trend was steadily rising (Anhui Provincial Statistical Yearbook, 2020). In terms of policies, the published “14th Five-Year Plan for the Development of the Logistics Industry in Anhui Province” pointed out the direction for the sustainable legal exhibition of the LI in Anhui Province. Specifically, while strengthening the construction of logistics infrastructure and improving logistics efficiency, Anhui Province has improved city- and county-level township

nodes and introduced multimodal transportation to reduce logistics costs by building a high-quality comprehensive three-dimensional transportation network. To sum up, Anhui Province has a relatively superior geographical location, population, and infrastructure, but the development of the LI lags behind the surrounding provinces. The inconsistency between the actual development of Anhui Province of LI and the anticipation remains to be investigated. Therefore, this study adopted Anhui Province as a case study, providing relevant development suggestions for the local LI and validating the effectiveness of the employed method.

4.2. *Data Analysis.* Dimensionless standard processing was performed, and the processed original data are shown in Table 3.

Following that, based on equation (7), a comprehensive score of the 2014–2020 Anhui logistics industry sustainability evaluation was obtained, which is shown in Table 4.

As shown in Figure 4, the comprehensive scores of various indicators of the LI in Anhui Province demonstrated an overall upward trend from 2014 to 2020, but the increase in specific time periods varied individually. Specifically, the composite score of industry basic indicator increased slowly from 2014 to 2017 and rapidly from 2017 to 2019, reaching its peak in 2019 followed by a downward trend. This trend was mainly attributed to the development plan of the Anhui Provincial Government for the logistics industry in 2017 and 2018.

To improve the logistics network, the Anhui Provincial Government has reconstructed and expanded some roads, built new bridges to connect them, improving the hub collection and distribution system. These policies mean that the government has increased the financial support for the logistics industry and improved the industry foundation. While improving the transportation network, the Provincial Department of Transportation urges noncompliant transport vehicles to be updated and eliminated in an orderly fashion as soon as possible. In general, the comprehensive score of the industry’s basic indicators has improved significantly from 2017 to 2019 and declined slightly after 2019. This phenomenon was related to the reduction in employees and transport vehicles caused by the optimisation and upgrade of the logistics industry.

The degree of specialisation refers to indicators such as the ratio of total logistics costs to GDP and density of transportation routes. Over the past five years, it has mainly shown a fluctuating upward trend. This phenomenon is closely linked to the government’s policies to promote e-commerce and express logistics, as well as to the cold chain infrastructure network. Environmental effects mainly include the burden caused by the LISD on the environment. The increase rate was relatively low from 2014 to 2018, and increased exponentially from 2018 to 2019, after which the level improved gradually. Similar to the reason for the changes in the degree of specialisation, this phenomenon mainly occurs because the Anhui Provincial government

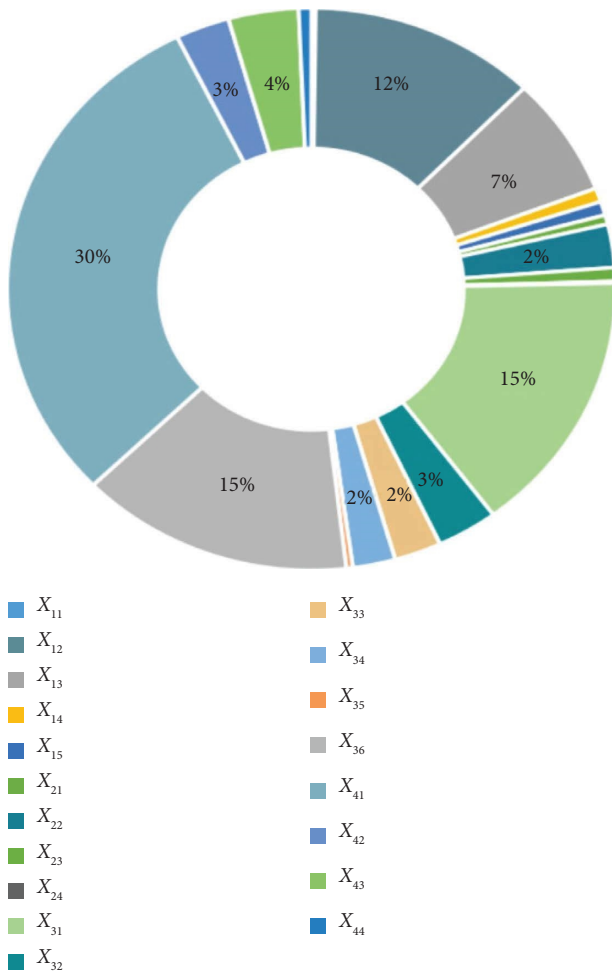


FIGURE 3: Weights of second level indicators in the adopted evaluation system.

vigorously built grassroots express outlets and planned the coordinated development of e-commerce and express logistics.

The innovation capability indicator is mainly used to measure the input and output of science and education in Anhui Province. From 2014 to 2019, its comprehensive score increased steadily and slightly, after which it started to increase sharply. This was mainly because the number of authorised patent applications for logistics technology innovation increased rapidly during this period. Based on the coupling coordination degree model and equation (9), the four first level indicators were calculated, and the results are shown in Figure 5. Specifically, the internal comprehensive coupling coordination level of the LISD in Anhui Province increased at a relatively stable rate from 2014 to 2020. The degree of coupling coordination among the four first level indicators (the average values in 2014 and 2020 were 0.2046 and 0.9596, respectively) has changed from serious imbalance to quality coordination. This showed that the logistics industry development policy of Anhui Province took both economic and environmental benefits into consideration by improving the transportation network, increasing investments in science and education, and promoting the mutual beneficial effects of various subsystems.

On the other hand, the coupling coordination level between the industry foundation-specialisation degree and the degree of specialisation-environmental effects is relatively high. This is because of the geographical location of Anhui Province and the relatively complete basic transportation network. Compared with the abovementioned coordination relationship, the level of coupling coordination between industry basic-innovation ability, degree of specialisation-innovation ability, and environmental effect-innovation ability was relatively poor.

According to equation (10), the obstacle degree model was utilised to analyse and compare the obstacle degree of each index and diagnose the obstacle factor of the LISD in Anhui Province. As shown in Figure 6, the main obstacles to the LISD in Anhui Province are innovation ability and environmental effects. From 2014 to 2017, the values of the barrier factors of each indicator were relatively stable, and the main barrier obstacles including innovation ability and environmental effects. This was mainly because the early development model of the logistics industry in Anhui Province was relatively extensive (by high cost and low efficiency), relying on the blind abuse of road networks and human and economic resources (obtained from the number of employees and the emission data in the statistical year-book and combined with the logistics policies of Anhui Province in that period). From 2018 to 2020, the barrier to innovation capability increased initially and then decreased to 19.93%. Conversely, the industry-based barrier increased to 40% in this period. This drastic change in the degree of barriers was closely related to the outbreak of COVID-19 in 2019. After the outbreak of the new crown pneumonia, Anhui Province implemented traffic control, and closed type management was adopted in residential areas. Therefore, the demand in the private logistics market decreased sharply, resulting in a substantial increase in the basic obstacles for the logistics industry. Meanwhile, different types of anti-epidemic materials from around the world had to be sorted, repackaged, and transported within a specific time. The demand for the distribution of medical and disaster relief material distribution as well as e-commerce terminal surged, consequently increased the energy consumption and emission of the regional LI.

5. Discussion

5.1. Policy Suggestions. Based on the abovementioned calculations and analyses, this research provides the following suggestions for the LISD in Anhui Province:

- (1) The grassroots traffic network should be improved, and transportation vehicles require an upgrade to lay a solid foundation for the LISD. To optimise the layout of the express logistics network, the density of the road network, traffic capacity, and rural distribution network should be improved in coordination. The implementation plan of the Anhui Provincial Department of Transportation and the Provincial Department of Finance shows that the proportion of highways (above the third level) in the

TABLE 3: Standardised values (X_1 - X_2) of original data of the LISD in Anhui Province from 2014 to 2020.

Years	X_1 logistics industry basic					X_2 degree of specialisation					X_3 environmental effects					X_4 ability of innovation				
	X_{11}	X_{12}	X_{13}	X_{14}	X_{15}	X_{21}	X_{22}	X_{23}	X_{24}	X_{31}	X_{32}	X_{33}	X_{34}	X_{35}	X_{36}	X_{41}	X_{42}	X_{43}	X_{44}	
2014	0.51384	0.00646	0.06861	0.00993	0.86109	0.45691	0.00306	0.02373	0.01291	0.00645	0.94140	0.08006	0.01214	0.96405	0.03394	0.00069	0.01437	0.01058	0.02881	
2015	0.08180	0.01246	0.02269	0.34546	0.24758	0.22017	0.24857	0.41137	0.58094	0.01244	0.83052	0.02225	0.16348	0.64676	0.01746	0.01596	0.16938	0.11315	0.35098	
2016	0.32665	0.04134	0.04537	0.68150	0.44245	0.07813	0.27136	0.49820	0.60378	0.04128	0.67231	0.70158	0.63799	0.76840	0.04729	0.02036	0.27557	0.22979	0.47257	
2017	0.79683	0.08138	0.32433	0.85785	0.51339	0.55161	0.50949	0.52023	0.80439	0.08122	0.27605	0.90761	0.73893	0.96345	0.03777	0.01117	0.46814	0.47123	0.59375	
2018	0.90992	0.89696	0.62370	0.90002	0.91357	0.45691	0.49630	0.50581	0.79058	0.17193	0.11722	0.92094	0.80922	0.64137	0.19375	0.04208	0.64140	0.69719	0.82821	
2019	0.61040	0.96791	0.96786	0.92846	0.33021	0.83570	0.69639	0.95616	0.89066	0.98378	0.06734	0.74392	0.40192	0.04514	0.97381	0.04010	0.82493	0.97972	0.90304	
2020	0.29130	0.98376	0.67473	0.98036	0.07808	0.93040	0.98710	0.96684	0.99693	0.98123	0.23519	0.98740	0.99772	0.31088	0.99229	0.98942	0.97602	0.67156	0.96186	

The abovementioned standardised data were adopted by equations (3)-(6), and the weight of each indicator was obtained using the entropy method. Figure 3 shows the weight of each second-level indicator. The results show that the following indicators have a greater weight than those of the other indicators: the GDP of the LI, number of patent applications for logistics technology innovation, energy consumption per unit of logistics output, and financial expenditures of public services. Thus, the economic background, technology level, and financial support were important conditions for LISD.

TABLE 4: Comprehensive scores of the 2014–2020 Anhui logistics industry sustainability evaluation.

	2014	2015	2016	2017	2018	2019	2020
Logistics industry basic	0.06500	0.03822	0.08537	0.21530	0.80750	0.93837	0.83972
Degree of specialisation	0.06980	0.28605	0.29919	0.52488	0.50024	0.77306	0.97546
Environmental effects	0.11041	0.09939	0.18279	0.18259	0.26699	0.84307	0.91726
Ability of innovation	0.00325	0.04358	0.06918	0.10296	0.16804	0.21018	0.95609

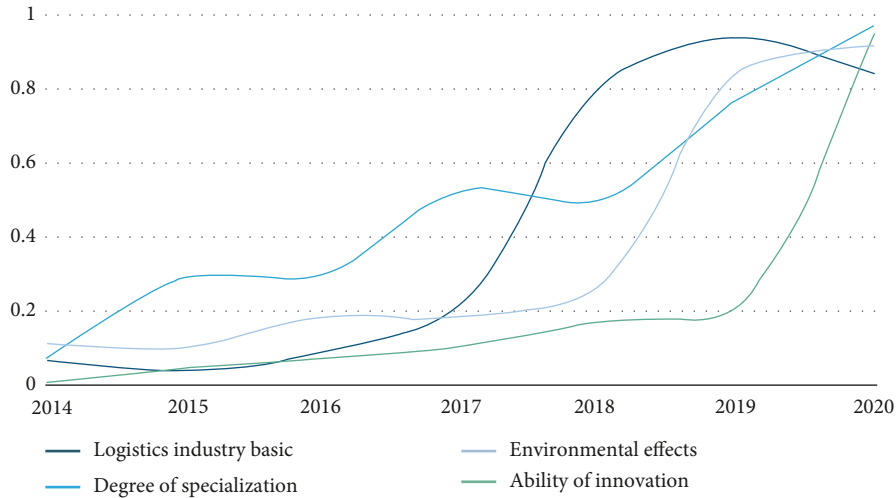


FIGURE 4: Visualised comprehensive scores of the first level indicators corresponding to Table 4.

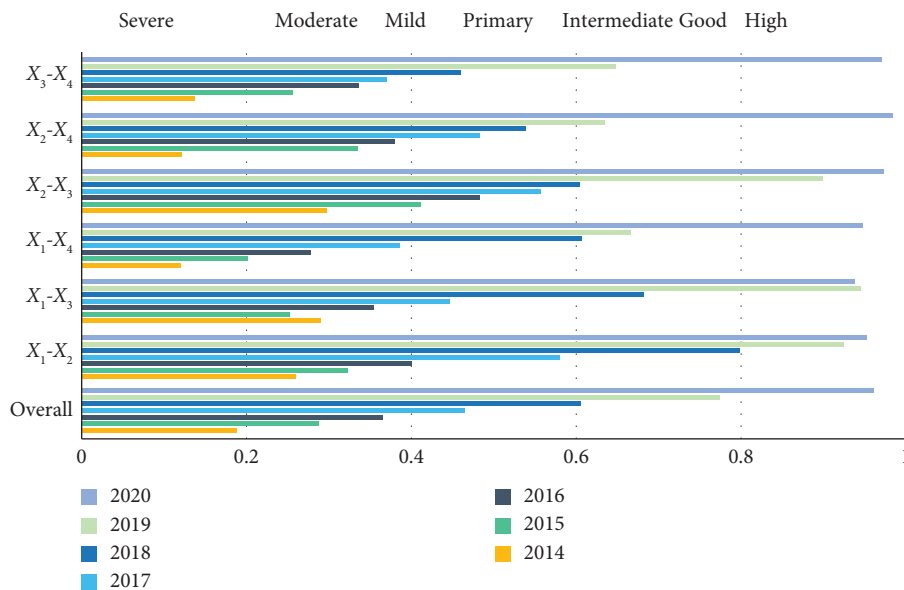


FIGURE 5: The coupling coordination relationship among the first level indicators.

demonstration counties and county roads was $\geq 85\%$ in 2017. At the same time, according to the Anhui Provincial Statistical Yearbook, the number of people engaged in economic activities in Anhui Province has also risen steadily over the same period. These measures are also conducive to increasing local employment rates and promoting consumption growth. In addition, the operating vehicles engaged

in the logistics industry should be strictly regulated, substandard vehicles required to be scrapped in time, and new energy vehicles need to be promoted vigorously, which is conducive to energy saving and emission reduction. Overall, improving the grassroots road network and upgrading transportation vehicles can promote energy consumption in the short term, but in the long run, it is conducive to

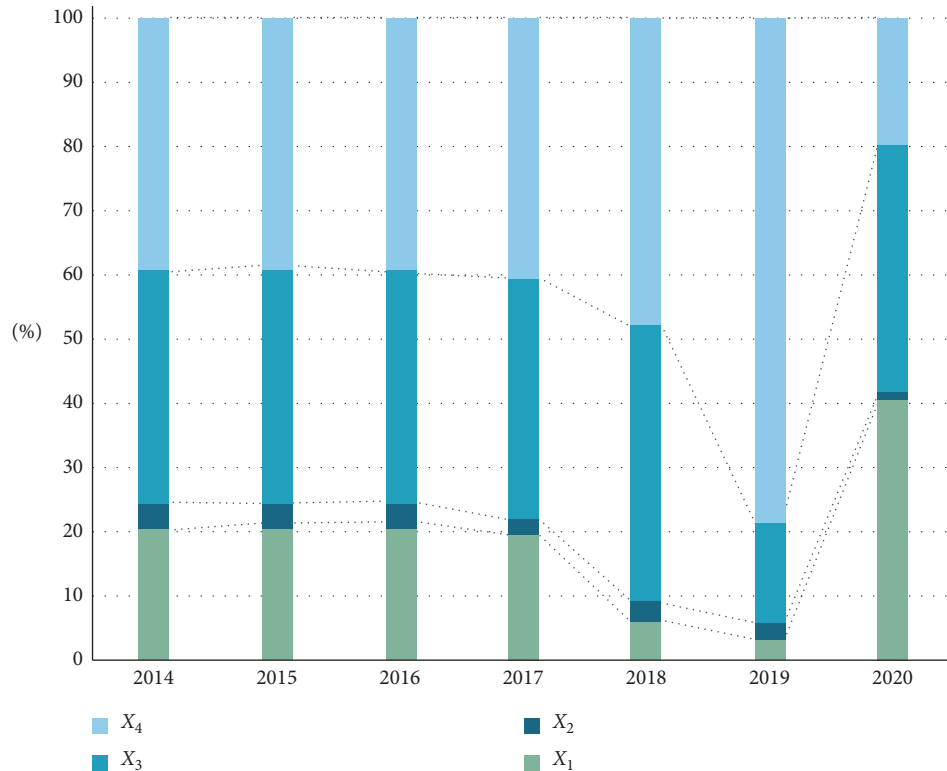


FIGURE 6: Obstacles of the first level indicators in Anhui province from 2014 to 2020.

energy saving and emission reduction as well as to improving the local LISD.

- (2) The cooperation among scientific research institutions, colleges and universities, and enterprises should be strengthened to encourage the innovation and application of logistics technology. Specifically, scientific research institutions should attract high-precision professionals, increase capital investment, and promote the research and transformation of the logistics technology to achieve innovation-driven industrial development. Colleges and universities in the province should offer courses to provide students with the skills required by contemporary logistics practitioners. Enterprises should undertake their own social responsibilities actively, assist in building a logistics laboratory platform in colleges and universities, and help students exercise their business practice ability.
- (3) The coordinated development of e-commerce and express logistics should be promoted, along with precise positioning, and the construction of logistics parks should be expedited. In particular, the local government and practitioners should consider the economic background and local market demand comprehensively and combine on-site market research to locate logistics parks [27]. On the one hand, it is necessary to clarify the location advantages, make full use of the transportation advantages in combination with the location characteristics, give priority to road transportation, and consider

multimodal transportation. On the other hand, avoiding the blind and disorderly construction of logistics parks can decrease the waste of resources. For instance, the scale and number of logistics parks should be set mainly according to the local market demand, and the needs of potential customers should be determined through on-the-spot investigation to ensure the continuous operation of local logistics parks.

5.2. Management Implications. Compared with existing research, this research provides some improvements from different aspects. First, the entropy method is adopted to analyse the status of the LISD in 16 cities in Anhui Province, providing a more comprehensive and objective measurement standard for quantitative research on the LISD, and offering a theoretical basis for in-depth research on high-quality development of the regional economy. Second, the two-coupling model is utilised to reveal the coordinated development level among the subsystems and the key obstacle factors hindering the LISD. The adopted model can analyse the problems and causes of obstacles, determine the sustainable development direction of the LI in Anhui Province, and propose countermeasures accordingly. Therefore, the analysis process and results can help the government to analyse, evaluate, and predict the sustainability of the development of the regional logistics industry, and can contribute tools for the analysis and evaluation of the LISD based on data-driven methods, providing a reference for the sustainable development of regional logistics.

Based on the abovementioned research, the following management implications are suggested:

Primarily, as there are many factors involved in the sustainability of the LI, the proposed research identifies, analyses, and optimises the influencing factors according to the actual situation, to build a set of evaluation indicators (a system) for LISD to evaluate the actual level of sustainable development of the industry. The weight of different indicators is calculated by the entropy method, which reflects the importance of each indicator in theory. The government can start from the most influential factor, logistics industry basic, and try to determine the impact of a single indicator on the LISD. Only then can the government understand and grasp the status quo of LISD and provide a reasonable direction for further improvement of the sustainable development of the logistics industry.

Moreover, as the sustainable development system of the logistics industry is a complex ecosystem and the interaction between the internal subsystems affects the level of LISD, the LI should be studied as an organic whole, and the system theory should be emphasised. Moreover, LISD is a basic industry for a country's economic development. Hence, related research needs to achieve the sustainability of economy, society, and environment, and to provide corresponding optimisation policy recommendations from different perspectives.

6. Conclusions

The rapid development of the LI not only contributes to economic development but also reveals problems such as environmental pollution and misuse of resources. Carrying out technological innovations and improving the efficiency of resource utilisation are inevitable requirements for improving the regional LISD. Therefore, a comprehensive sustainability evaluation model for the LI was established in Anhui Province based on the data-driven model, providing suggestions for the development direction of the LI based on the results of the model analysis.

Compared with the existing research, this article provides improvements from different aspects as follows: (1) we evaluated several historical indicators of the LI comprehensively, considering the industry development background, environmental pollution, and development potential, and estimated the LISD in Anhui Province in the past seven years accurately and quantitatively; (2) we revealed the degree of mutual influence and coordinated development between different development indicators within the logistics industry development system using the coupling coordination degree model; (3) we identified the main obstacle factors affecting the development of the logistics industry through the obstacle degree model, and proposed corresponding suggestions to the government, enterprises, logistics industry practitioners, and colleges and universities, mainly including infrastructure, personnel training, technology research, and development and applications.

The logistics industry is the mainstay of regional economic development, while research on LISD involves many

aspects. With the deepening of related research and improvement of various regional cases, the regional LI sustainability evaluation model will achieve higher accuracy and applicability. However, the model does not consider regional development differences caused by the radiation of surrounding economic regions; when we analysed indicators data, indicators are divided into positive and negative indicators, but in practice, the impact of different factors may be inverted in different a period. Therefore, future research should design more comprehensive models that combine universality and particularity. More aspects can be considered when establishing the evaluation index system and designing model, such as regional synergies, the degree of packaging recycling in the logistics, and the interaction among data that used in the model.

Data Availability

All data included in this study are available from the corresponding author upon request.

Conflicts of Interest

The authors declare that there are no conflicts of interest regarding the publication of this paper.

Authors' Contributions

Heping Ding conceptualized the study. Yujia Liu performed investigation. Heping Ding provided resources. Yujia Liu and Heping Ding performed methodology and data curation, wrote the original draft, and reviewed the manuscript.

Acknowledgments

This research work was supported by the Suzhou University, based on the research on evaluation and improvement of the sustainability of manufacturing logistics based on data-driven approach (Grant number: 2022ykf08).

References

- [1] Y. Huang, Q. Li, and X. Wang, "Lean path for high-quality development of Chinese logistics enterprises based on entropy and gray models," *Entropy*, vol. 21, no. 7, p. 641, 2019.
- [2] A. Rakhmangulov, A. Sladkowski, and N. Osintsev, "Green logistics: element of the sustainable development concept," *Naše More*, vol. 64, no. 3, pp. 120–126, 2017.
- [3] S. A. R. Khan, A. Sharif, H. Golpira, and A. Kumar, "A green ideology in Asian emerging economies: from environmental policy and sustainable development," *Sustainable Development*, vol. 27, no. 6, pp. 1063–1075, 2019.
- [4] O. Seroka-Stolka, "The development of green logistics for implementation sustainable development strategy in companies," *Procedia - Social and Behavioral Sciences*, vol. 151, pp. 302–309, 2014.
- [5] S. Winkelhaus and E. H. Grosse, "Logistics 4.0: a systematic review towards a new logistics system," *International Journal of Production Research*, vol. 58, no. 1, pp. 18–43, 2020.
- [6] T. A. Banihashemi, J. Fei, and P. S. L. Chen, "Exploring the relationship between reverse logistics and sustainability

- performance: a literature review,” *Modern Supply Chain Research and Applications*, vol. 1, 2019.
- [7] A. S. Karaman, M. Kilic, and A. Uyar, “Green logistics performance and sustainability reporting practices of the logistics sector: the moderating effect of corporate governance,” *Journal of Cleaner Production*, vol. 258, Article ID 120718, 2020.
- [8] M. Klumpp and H. Zijm, “Logistics innovation and social sustainability: how to prevent an artificial divide in human–computer interaction,” *Journal of Business Logistics*, vol. 40, no. 3, pp. 265–278, 2019.
- [9] A. Szmelter-Jarosz and J. Rzeźny-Cieplińska, “Priorities of urban transport system stakeholders according to crowd logistics solutions in city areas. A sustainability perspective,” *Sustainability*, vol. 12, no. 1, p. 317, 2019.
- [10] P. Pourhejazy, O. K. Kwon, and H. Lim, “Integrating sustainability into the optimization of fuel logistics networks,” *KSCE Journal of Civil Engineering*, vol. 23, no. 3, pp. 1369–1383, 2019.
- [11] R. Ren, W. Hu, J. Dong, B. Sun, Y. Chen, and Z. Chen, “A systematic literature review of green and sustainable logistics: bibliometric analysis, research trend and knowledge taxonomy,” *International Journal of Environmental Research and Public Health*, vol. 17, no. 1, p. 261, 2019.
- [12] F. H. Qaiser, K. Ahmed, M. Sykora, A. Choudhary, and M. Simpson, “Decision support systems for sustainable logistics: a review and bibliometric analysis,” *Industrial Management & Data Systems*, vol. 117, no. 7, pp. 1376–1388, 2017.
- [13] K. Grzybowska, A. Awasthi, and R. Sawhney, *Sustainable Logistics and Production in Industry 4.0. New Opportunities and Challenges*, Springer, Cham, Switzerland, 2020.
- [14] R. Rauter, J. Jonker, and R. J. Baumgartner, “Going one’s own way: drivers in developing business models for sustainability,” *Journal of Cleaner Production*, vol. 140, pp. 144–154, 2017.
- [15] A. K. Reda, G. Gebresenbet, L. Tavasszy, and D. Ljungberg, “Identification of the regional and economic contexts of sustainable urban logistics policies,” *Sustainability*, vol. 12, no. 20, p. 8322, 2020.
- [16] M. He, J. Shen, X. Wu, and J. Luo, “Logistics space: a literature review from the sustainability perspective,” *Sustainability*, vol. 10, no. 8, p. 2815, 2018.
- [17] E. B. Mariano, J. A. Gobbo, F. D. C. Camioto, and D. Rebelatto, “CO₂ emissions and logistics performance: a composite index proposal,” *Journal of Cleaner Production*, vol. 163, pp. 166–178, 2017.
- [18] J. García-Arca, A. Garrido, and J. C. Prado-Prado, “Sustainable packaging logistics. The link between sustainability and competitiveness in supply chains,” *Sustainability*, vol. 9, no. 7, p. 1098, 2017.
- [19] C. Wang, C. Zhang, F. Hu, Y. Wang, L. Yu, and C. Liu, “Energy-based ecological efficiency evaluation and optimization method for logistics park,” *Environmental Science and Pollution Research*, vol. 28, no. 41, pp. 58342–58354, 2021.
- [20] C. Liu, J. Chen, and W. Cai, “Data-driven remanufacture ability evaluation method of waste parts,” *IEEE Transactions on Industrial Informatics*, vol. 18, no. 7, pp. 4587–4595, 2022.
- [21] Y. Kayikci, “Stream processing data decision model for higher environmental performance and resilience in sustainable logistics infrastructure,” *Journal of Enterprise Information Management*, vol. 34, no. 1, pp. 140–167, 2020.
- [22] C. Cao, “Measuring sustainable development efficiency of urban logistics industry,” *Mathematical Problems in Engineering*, vol. 2018, Article ID 9187541, 9 pages, 2018.
- [23] R. Long, H. Ouyang, and H. Guo, “Super-slack-based measuring data envelopment analysis on the spatial–temporal patterns of logistics ecological efficiency using global Malmquist Index model,” *Environmental Technology & Innovation*, vol. 18, Article ID 100770, 2020.
- [24] M. Abbasi and F. Nilsson, “Developing environmentally sustainable logistics: exploring themes and challenges from a logistics service providers’ perspective,” *Transportation Research Part D: Transport and Environment*, vol. 46, pp. 273–283, 2016.
- [25] S. Wang, F. Tao, and Y. Shi, “Optimization of location–routing problem for cold chain logistics considering carbon footprint,” *International Journal of Environmental Research and Public Health*, vol. 15, no. 1, p. 86, 2018.
- [26] Z. Liu, M. D. Wan, X. X. Zheng, and S. L. Koh, “Fairness concerns and extended producer responsibility transmission in a circular supply chain,” *Industrial Marketing Management*, vol. 102, pp. 216–228, 2022.
- [27] Z. Liu, X. X. Zheng, D. F. Li, C. N. Liao, and J. B. Sheu, “A novel cooperative game-based method to coordinate a sustainable supply chain under psychological uncertainty in fairness concerns,” *Transportation Research Part E: Logistics and Transportation Review*, vol. 147, Article ID 102237, 2021.
- [28] Z. Liu, K. W. Li, J. Tang, B. Gong, and J. Huang, “Optimal operations of a closed-loop supply chain under a dual regulation,” *International Journal of Production Economics*, vol. 233, Article ID 107991, 2021.
- [29] K. Rashidi and K. Cullinane, “Evaluating the sustainability of national logistics performance using Data Envelopment Analysis,” *Transport Policy*, vol. 74, pp. 35–46, 2019.
- [30] P. Evangelista, L. Santoro, and A. Thomas, “Environmental sustainability in third-party logistics service providers: a systematic literature review from 2000–2016,” *Sustainability*, vol. 10, no. 5, p. 1627, 2018.
- [31] T. R. Morgan, M. Tokman, R. G. Richey, and C. Defee, “Resource commitment and sustainability: a reverse logistics performance process model,” *International Journal of Physical Distribution & Logistics Management*, vol. 48, no. 2, pp. 164–182, 2018.
- [32] M. Salama, *Principles of Sustainable Project Management*, Goodfellow Publishers Ltd, Oxford, UK, 2018.
- [33] C. Baah, K. T. Amponsah, K. Issau, and D. Opoku, “Examining the interconnections between sustainable logistics practices, environmental reputation and financial performance: a mediation approach,” *Vision*, vol. 25, no. 1, pp. 47–64, 2021.
- [34] M. Björklund and H. Forslund, “Exploring the sustainable logistics innovation process,” *Industrial Management & Data Systems*, vol. 118, no. 1, pp. 204–217, 2018.
- [35] E. Eftestøl-Wilhelmsson, S. Sankari, and A. Bask, *Sustainable and Efficient Transport: Incentives for Promoting a Green Transport Market*, Edward Elgar Publishing, Cheltenham, UK, 2019.
- [36] D. I. Godil, Z. Yu, A. Sharif, R. Usman, and S. A. R. Khan, “Investigate the role of technology innovation and renewable energy in reducing transport sector CO₂ emission in China: a path toward sustainable development,” *Sustainable Development*, vol. 29, no. 4, pp. 694–707, 2021.
- [37] J. Huang, Y. Shuai, Q. Liu, H. Zhou, and Z. He, “Synergy degree evaluation based on synergetics for sustainable logistics enterprises,” *Sustainability*, vol. 10, no. 7, p. 2187, 2018.

- [38] D. Klimecka-Tatar, M. Ingaldi, and M. Obrecht, "Sustainable development in logistic – a strategy for management in terms of green transport," *Management Systems in Production Engineering*, vol. 29, no. 2, pp. 91–96, 2021.
- [39] S. Lan, M. L. Tseng, C. Yang, and D. Huisingh, "Trends in sustainable logistics in major cities in China," *Science of the Total Environment*, vol. 712, Article ID 136381, 2020.
- [40] H. Lu, L. Li, X. Zhao, and D. Cook, "A model of integrated regional logistics hub in supply chain," *Enterprise Information Systems*, vol. 12, no. 10, pp. 1308–1335, 2018.

Research Article

Selecting Online Channel Mode for Green Products in a Capital-Constrained Platform Supply Chain

Guobao Zhang,¹ Xinhui Cheng,¹ Zhichao Zhang ,¹ and Yanyan Zheng²

¹College of Management, Anhui Science and Technology University, Bengbu 233100, China

²School of Management, Xi'an Polytechnic University, Xi'an 710048, China

Correspondence should be addressed to Zhichao Zhang; zhangzc@nuaa.edu.cn

Received 1 August 2022; Revised 18 September 2022; Accepted 27 September 2022; Published 6 February 2023

Academic Editor: Conghu Liu

Copyright © 2023 Guobao Zhang et al. This is an open access article distributed under the Creative Commons Attribution License, which permits unrestricted use, distribution, and reproduction in any medium, provided the original work is properly cited.

This paper investigates operational decisions and online channel mode selection for green products with an e-commerce supply chain in which the manufacturer is subject to capital constraint. Starting from a Stackelberg game framework where the platform acts as a leader, two different online channel modes applied with an e-commerce supply chain are explored for equilibria, respectively. This paper then extends to a different supply chain with a reversed channel leadership, so as to reveal how the supply chain leaderships affect the equilibriums and supply chain performance. With the analytical studies, several important and interesting insights are derived. For example, but not limited to, the following is found: (a) the equilibrium decisions of the capital-constrained supply chain highly rely on the associated interest rate but are independent of the initial capital level of the financially-constrained manufacturer; (b) the platform and the capital-constrained manufacturer act largely differently when choosing the optimal online channel mode for themselves; (c) a win-win situation benefiting two parties holds when and only when the two members choose the agency mode under certain conditions; (d) the impacts of the supply chain leaderships and online channel modes on the consumer surplus and social welfare are clearly revealed. These results derived in our paper shed lights on industrial practitioner on how to effectively make such decision-making in platform economy. The members in an e-commerce supply chain can appropriately determine their decisions such as commission and slotting fee to reach a win-win situation for two parties.

1. Introduction

With the rapid increase in the environmental awareness of the general public, many firms are well devoted to producing green products partly for developing a green economy and improving eco-environment in different industries around the world. These green products include the electric cars produced by American car-maker Tesla, the fluorine-free air conditioner made by Japanese home appliance manufacturer Panasonic, and others [1–4]. In addition to these manufacturing producers, some leading retailers are also engaged in the investment and promotion of green products. For example, one of the giant home appliance retailers in the world, Best Buy, sells ENERGY STAR-certified products to help businesses and consumers save money and protect our climate through superior energy efficiency.

Transforming from producing a regular product to a green one requires a large amount of capital, including product design, product publicity, and technological innovation. Hence, the capital constraint may constitute a major obstacle restricting this transformation of the firms, especially for the small and medium-sized ones, which always suffers from the financial difficulties even during regular operations. To ease the capital shortage, the firms can borrow loans to invest in green innovation, and the most common way is to finance from Bank. For example, by the end of 2021, 15 major banks in China have issued a total of 220.3 billion carbon emission reduction loans, supporting 2,246 projects to assist enterprises in producing low-carbon products [5]. Inevitably, the capital-constrained firms will pay additional costs to raise the capital, such as paying the interest to the lender, which in

turn affects its operation and the associated performance. Hence, an interesting issue has arisen here to reveal how the financing affects the firm's selling and greening operation.

Nowadays, especially during the COVID-19 epidemic, online retailing has gradually become a mainstream alternative for the firms to distribute their various products [6, 7]. It is noticed from the industrial practice that the two complementary online channel modes are available for the firms to sell the products with an online marketplace, i.e., one is online agency channel and the other is online reselling channel. In terms of the online agency mode, the firm directly sells the products to the end consumers, paying commission sales to the e-commerce platform as the revenue share. In this case, the firm takes the ownership over the products, and the platform just serves as an online marketplace. By contrast, with the online reselling mode, the seller first wholesales products to the platform, and after that, the platform retails the products to end consumers. Under this circumstance, the platform takes the ownership over products and thus acts as an online reseller. The conventional wisdom suggests that the online agency mode will mitigate the double-marginalization effect and may require a low capital level to cover production. Therefore, the online channel mode will induce a significant impact on the financing decisions. Given different features of the two online channel modes, the two online channel modes will pose a key role in the operation decisions of the members, thereby decreasing or increasing the individual profits with an e-commerce platform supply chain. Herein, an interesting issue has arisen to explore the optimal online channel mode for the individuals with this e-commerce platform supply chain.

As a matter of fact, different individuals may act contradictorily when selecting the online channel modes. Essentially, it is the bargaining power among different individuals that finally determines the online channel mode selection between the individuals. Thus, it is worth investigating how the channel leaderships between the individuals affect the optimal online channel mode selection as well as the individual surplus, such as consumer and social community.

Motivated by the previous industrial practice, this paper develops an e-commerce supply chain consisting one platform and one capital-constrained manufacturer with two different online channel modes, in which the capital-constrained manufacturer chooses bank loan to ease capital shortage. To be specific, the main research questions of this paper are addressed as follows:

- (i) How does the financing affect the operation and the individual profits with an e-commerce platform supply chain?
- (ii) When should the individual select the online agency mode and when should it select the online reselling mode instead?
- (iii) What are the impacts of the channel leadership on the consumer surplus and the social welfare?

The remainder of this paper is organized as follows: Section 2 reviews the most related literature. The problem descriptions are explicitly exhibited in Section 3, followed by which we develop an e-commerce supply chain system with the online agency mode in Section 4 and with the online reselling mode in Section 5, respectively. By comparing the equilibrium profits across two different online channel modes, Section 6 further investigates the optimal online channel mode selections for the manufacturer and the platform, respectively. This paper extends to a supply chain with a different leaderships and discusses the impacts of the consumer surplus and the social welfare on the two different supply chains in Section 7. Section 8 concludes the key findings with the managerial insights and future researches. For clarity, all proofs of the results are collected together in the Appendix.

2. Literature

The literature closely related to this paper is threefold, namely, green supply chain, supply chain finance, and online channel mode selection.

2.1. Green Supply Chain. As the increasing pressure of the environmental protection, the governmental regulation, and the continuous development in green product, green supply chain design and management has gradually become an environmentally sustainable strategy for the supply chain decision-makers and has thus been paid notable attention in academia.

A large number of studies in the green supply chain mainly focus on the green innovation and operational decisions. Chen and Sheu [8] apply a differential game model to demonstrate that a proper design of environment-regulation pricing strategy can boost the extended product responsibility for green supply chain, especially in a highly competitive market. Bhaskaran and Krishnan [9] propose various mechanisms of collaboration between two firms in the development of green products yielding technology uncertainty. Ghosh and Shah [10] examine the green investment in an apparel serial supply chain in which the players cooperate or act individually. Li et al. [11] explore a dual-channel supply chain where the manufacturer produces green products for the environmental conscious and investigate the joint pricing and greening strategies for the chain members in both centralized and decentralized cases. Meng et al. [12] use game theory to analytically explore the pricing policy in a green supply chain of a dual-channel structure, in which consumers' green preference and channel preference are considered. Huang et al. [1] investigate the optimal green and pricing strategies in a capital-constrained supply chain with different governmental green subsidies. Das Roy and Sana [13] examine a multiechelon green supply chain system in which a traditional production process is integrated with a remanufacturing in a single-setup-multidelivery system under setup cost reduction. Liu et al. [14] study how the retailer's fairness concern levels affect the cooperation in a three-stage sustainable supply

chain. Sana [15] look into a newsvendor inventory problem where comparisons between green and nongreen marketing are explicitly analyzed including subsidy and tax implementation by the governmental regulation.

2.2. Supply Chain Finance. Capital shortage has always been a most important issue that the firms suffer from during the production and operation process, especially for those small and medium ones. Financing is an effective way for those capital-constrained firms to deal with the capital shortage and thus has drawn much attention in academic studies by scholars.

Chen and Cai [16] look into an extended supply chain model with a supplier, a budget-constrained retailer, a bank, and a 3PL firm, where the retailer has insufficient initial budget and can borrow loans from either a bank or a 3PL firm. Cai et al. [17] investigate the roles of bank and trade credits in a supply chain with a capital-constrained retailer yielding demand uncertainty. Zhang et al. [18] propose a portfolio financing strategy of bank loan financing and retailer credit financing for a closed-loop supply chain consisting of a financially constraint manufacturer and a retailer. Jin et al. [19] develop a proper financing scheme and discuss its efficiency of supplier intermediation in retailer financing in the case of unreliable products. Yan et al. [20] examine a dual-channel supply chain where the retailer and e-commerce platform can freely use the other's sales efforts and the e-commerce platform can provide online finance services to the capital-constrained supplier. Zheng et al. [21] consider a remanufacturing supply chain in which the retailer is capital-constrained and examine the optimal financing decision in terms of the market uncertainty. Sana et al. [22] discuss the operational and financial decisions among the supply chain individuals including one manufacturer and one distributor. Yan et al. [23] introduce supplier finance and supplier investment to a capital-constrained supply chain in which the retailer is subject to a capital constraint and investigate the impacts of retailer's loss aversion on the supply chain financing decisions.

2.3. Online Channel Mode Selection. In recent years, the online selling has been paid notable attention in supply chain management. Extended studied focusing on this research stream mainly includes the following aspects, such as competition and cooperation [6, 24], information disclosure [25–27], return policy [28–30], online reviews [31–33], interactions of online and offline channels [34, 35], and online value-add services [36, 37].

Specifically, this paper contributing to this research stream lies in the optimal online channel modes in an e-commerce platform supply chain. It is well noticed that the two online channel modes, i.e., the agency mode and the reselling mode, are typically adopted by the e-commerce platform to their upstream suppliers. Hence, the most related researching line of this stream in regards to the online channel mode is to identify the optimal online channel mode for the different individuals and reveal the key drivers behind deriving this strategic online channel mode selections.

For example, Tian et al. [6] indicate how to select a better online channel mode for an e-commerce platform based on which the two competing suppliers sell the complementary products through the platform. Qin et al. [36] look into the interplay of the logistics service provision and online channel mode and focus on how the logistics service strategy affect the optimal online channel mode selection in a platform supply chain. Zhang and Zhang [38] study the e-tailer information sharing strategy with supplier offline entry in which the e-tailer can choose either online agency channel or online reselling channel. Chen et al. [39] investigate the optimal online channel mode for an e-seller and explore who is better off to offer the return-freight insurance in a platform supply chain. Yu et al. [40] explore a manufacturer's production decisions and a government's choice between cap-and-trade and carbon tax regulation in which the manufacturer sells the product through offline and online channels where the online channel can be the reselling mode or the agency mode. Zhang et al. [41] investigate how to select an optimal online channel mode for a manufacturer in an e-commerce platform supply chain in the presence of a secondary marketplace. Wang et al. [42] consider a multiple echelon supply chain where an upstream supplier can retail its products through an online e-commerce platform and a live streaming sales channel, and the online platform company can choose the reselling channel mode or the agency channel mode.

This paper contributes to the literature from the following aspects: Firstly, this paper focuses on the joint financing and green decisions in a capital-constrained platform supply chain. The aim of this paper is to investigate the mutual impacts of financing and operational decision in this platform supply chain. Secondly, in contrast to the existing studies on the optimal online channel mode selection in an e-commerce supply chain with sufficient capital, the fundamental difference of this paper lies in the fact that this paper explicitly selects the optimal online channel mode for the two parties when the manufacturer is subject to the capital constraint.

For better exhibiting the key differences between this paper and the most related literature, Table 1 thus formulates.

3. Model Formulation

We consider an e-commerce platform supply chain consisting of an e-platform and a capital-constrained manufacturer. It is well noticed from the industrial practice that the platform typically provides two options with their manufacturer to sell products [6, 7, 39], that is, the capital-constrained manufacturer has two choices to sell the green product via the platform's online marketplace; one is the online reselling mode and the other is the online agency mode. In terms of the reselling mode, the manufacturer wholesales the products to the platform at wholesale price (w), and after that, the platform sells them to the end consumers at retail price (p). Under this circumstance, the platform takes the ownership over products and acts as an online reseller. In contrast, with the agency mode, the

TABLE 1: Positioning of this paper in the literature.

Paper	Green product	Financing	Channel mode	Channel leadership	Consumer surplus	Social welfare
Ghosh and Shah [10]	√			√		
Li et al. [11]	√					
Huang et al. [1]	√				√	√
Zheng et al. [21]		√				
Zhang et al. [18]		√				
Zhang et al. [41]			√			
[43]			√	√		
Zhang et al. [7]			√	√		
Our work	√	√	√	√	√	√

manufacturer directly charges a retail price (p) and sells products to the consumers after paying a sales commission (θ) and a slotting fee (F) to the platform as the revenue share. In this case, the manufacturer takes the ownership over products, and the platform purely serves as an online marketplace.

To encourage green product development, the capital-constrained manufacturer invests in green R&D technology, and the green effort is denoted as e . Product with a higher greenness can improve the environmental benefit (or reduce environmental pollution) but also incurs a higher R&D cost. By following Huang et al. [1], a quadratic R&D cost of green investment is given by

$$C(e) = \frac{ke^2}{2}. \quad (1)$$

On the market side, it is well noticed that consumers are willing to purchase the green products because of their high greenness and lower environmental damages. The greener the product, the more the consumers will pay for it. This paper applies a linear demand function to capture such a phenomenon by following the related literature [1, 44, 45], such as

$$D(p, e) = a - p + \lambda e, \quad (2)$$

where a ($a > 0$) denotes the market potential, p is the retail price, and λ ($0 < \lambda \leq 1$) measures how much the consumers concern about the environmental awareness.

The capital-constrained manufacturer faces financing obstacles when producing the green products. The marginal cost of a unit product for the manufacturer is cD . To focus on a capital-constrained manufacturer, the initial capital level (K) is not sufficient to maintain the production, incurring that $K < cD + (ke^2/2)$. The capital-constrained manufacturer can choose to borrow the loans from bank with paying a fraction of interest (r). Hence, the financing costs for the manufacturer are $(cD + (ke^2/2) - K)r$.

For eases of exposition and clarity, the notation used in this paper can be found in Table 2.

4. Reselling Mode-Scenario R

With the reselling mode, the manufacturer produces the product with green degree e and wholesales the product to the e-platform at price w , and after that, the platform sells the product to the end consumers at price p .

Mathematically, the profits of the manufacturer and the e-platform are, respectively, formulated as follows:

$$\pi_M^R(w, e) = (w - c)D - \frac{ke^2}{2} - r\left(cD + \frac{ke^2}{2} - K\right), \quad (3)$$

$$\pi_E^R(p) = (p - w)D.$$

Applying the backward induction, the equilibrium decisions are achieved in Proposition 1.

Proposition 1. *With the reselling mode, the equilibrium decisions are given by*

$$w^{R*} = \frac{(1+r)[ak - 2c\lambda^2 + 3ck(1+r)]}{4k(1+r) - 2\lambda^2},$$

$$e^{R*} = \frac{\lambda[a - c(1+r)]}{4k(1+r) - 2\lambda^2}, \quad (4)$$

$$p^{R*} = \frac{(3ak + 2ck - c\lambda^2)(1+r) + ckr^2 - ck - a\lambda^2}{4k(1+r) - 2\lambda^2},$$

and the associated equilibrium profit for the manufacturer and the e-platform are

$$\pi_M^{R*} = \frac{k(1+r)[a - c(1+r)]^2}{8[2k(1+r) - \lambda^2]} + Kr,$$

$$\pi_E^{R*} = \frac{k(1+r)[a - c(1+r)]^2}{4[2k(1+r) - \lambda^2]}. \quad (5)$$

According to Proposition 1, the resulting demand for the product is $D^{R*} = (k(1+r)[a - c(1+r)] / (4k(1+r) - 2\lambda^2)$, and the following corollary is obtained:

Corollary 1. *With the reselling mode, the impacts of the interest rate on the equilibriums and individual profits are as follows:*

- (i) $(\partial e^{R*} / \partial r) < 0$ and $(\partial D^{R*} / \partial r) < 0$;
- (ii) if $0 \leq r < r_1$, then $(\partial w^{R*} / \partial r) < 0$ and if $r_1 \leq r \leq 1$, then $(\partial w^{R*} / \partial r) > 0$;
- (iii) if $0 \leq r < r_2$, then $(\partial p^{R*} / \partial r) < 0$ and if $r_2 \leq r \leq 1$, then $(\partial p^{R*} / \partial r) > 0$;

TABLE 2: List of notations.

Parameters	
a	The market potential
λ	The consumer's sensitivity to the environmental awareness
D	The resulting demand of the product
k	The cost factor when the manufacturer invests in green technology
c	The marginal cost of a unit product
K	The initial capital of the capital-constrained manufacturer
r	The interest rate set by bank
θ	The commission. With the online agency mode, the capital-constrained manufacturer pays a sales commission (θ) to the E-platform and keeps the remaining fraction $(1 - \theta)$ of sales
F	The capital-constrained manufacturer pays the slotting fee (F) to the E-platform with the online agency mode
CS	Consumer surplus
SW	Social welfare
Decision variables	
w	The wholesale price of the product when the capital-constrained manufacturer selects the online reselling mode
p	The retail price of the product with the both reselling and agency modes
e	The green effort of the manufacturer

(iv) $(\partial\pi_M^{R*}/\partial r) < 0$ and $(\partial\pi_E^{R*}/\partial r) < 0$.

In the previous corollary, $r_1 = (-3c(2k - \lambda^2) + \sqrt{3}\lambda\sqrt{c(2ak - c\lambda^2)})/(6ck)$ and $r_2 = (-c(2k - \lambda^2) + \lambda\sqrt{c(2ak - c\lambda^2)})/(2ck)$.

It is seen from Corollary 1 that the product's greenness, the resulting market demand, and the individual profits of the manufacturer and the platform decrease with an increase in the interest rate. This phenomenon is naturally understandable that with an increase in the financing rate, the associated financing cost also increases. Therefore, the manufacturer has to reduce investments in the product's greenness by balancing the production amount and the financing cost, which results in a decrease of the resulting demand. Also, it is obvious that an increase in the interest rate signifies that bank extracts more profits from the entire supply chain. Consequently, the two individuals will obtain less profits with a higher interest rate set by bank.

Corollary 1 also indicates how the interest rate affects the wholesale and retail prices, which is largely relied on the specific interest rate. To be specific, an increase in the interest rate first decreases the wholesale and retail prices and then increases the wholesale and retail prices. On the one hand, when the interest rate is relatively small as $0 \leq r < r_1$ (or $0 \leq r < r_2$), the wholesale price (or the retail price) decreases with the interest rate. On the other hand, the wholesale price (or the retail price) increases with a higher interest rate when it is relatively high as $r_1 \leq r \leq 1$ (or $r_2 \leq r \leq 1$).

It is obvious to verify that $r_1 < r_2$. It is interesting to find that the manufacturer will increase the wholesale price, yet the platform will decrease the retail price with a higher interest rate when $r_1 < r < r_2$. This indicates that the manufacturer and the platform act differently on the pricing decisions in response to a higher interest rate. This occurs because the platform has to balance the margin profit and the resulting demand of the green product.

5. Agency Mode-Scenario A

With the agency mode, by paying a slotting fee and commission sales to the platform, the manufacturer takes the ownership over products and directly retails them to the end consumers via the platform's online marketplace. Similarly, the profit functions of the platform and the manufacturer are respectively achieved as follows:

$$\pi_M^A(p, e) = [(1 - \theta)p - c]D - F - \frac{ke^2}{2} - r\left(cD + \frac{ke^2}{2} - K\right),$$

$$\pi_E^A = \theta pD + F. \tag{6}$$

It is noticed from the industrial practice that the e-platform publicly and advancingly declares the commissions in response to the product categories for all the potential suppliers every year. For example, JD.com offers and updates the commissions in response to every product category for any potential suppliers [46]. Thus, this paper considers an exogenous commission. Such an assumption can also be seen in the related literature, such as [47, 48] and [6]. Hence, the equilibrium decisions and the individual profits can be obtained in Proposition 2.

Proposition 2. *With the agency mode, the equilibrium decisions are given by*

$$p^{A*} = \frac{(1 + r)\{ak(1 - \theta) + c[k(1 + r) - (1 - \theta)\lambda^2]\}}{(1 - \theta)[2k(1 + r) - (1 - \theta)\lambda^2]},$$

$$e^{A*} = \frac{\lambda[a(1 - \theta) - c(1 + r)]}{2k(1 + r) - (1 - \theta)\lambda^2}, \tag{7}$$

and the individual profits for the manufacturer and the platform are as follows:

$$\pi_M^{A*} = k(1+r) \frac{c^2(1+r)^2 - 2ac(1+r)(1-\theta) + a^2(1-\theta)^2}{2(1-\theta)[2k(1+r) - (1-\theta)\lambda^2]} + Kr - F, \tag{8}$$

$$\pi_E^{A*} = \frac{k(1+r)^2 [a(1-\theta) - c(1+r)] \theta \{ ak(1-\theta) + c[k(1+r) - (1-\theta)\lambda^2] \}}{(1-\theta)^2 [2k(1+r) - (1-\theta)\lambda^2]^2} + F.$$

Based on Proposition 2, the resulting demand with the agency mode is achieved as $D^{A*} = (k(1+r)[a(1-\theta) - c(1+r)] / ((1-\theta)[2k(1+r) - (1-\theta)\lambda^2])$, and the following results hold in Corollary 2.

Corollary 2. *With the agency mode, the impacts of the commission on the equilibriums are obtained as follows:*

- (i) $(\partial e^{A*} / \partial \theta) < 0$;
- (ii) $(\partial p^{A*} / \partial \theta) > 0$;
- (iii) $(\partial D^{A*} / \partial \theta) < 0$.

Corollary 2 clearly indicates the impacts of the commission on the greenness, retail price, and the resulting demand. It is seen that with a higher commission, the manufacturer will pay more sales to the platform. Naturally, the manufacturer reduces investments in green technology and charges a higher retail price to balance its profit and the revenue share to the platform. Also, the greenness and the retail price of the product play a comprehensive effect on the resulting demand, and it signifies that the negative impact of the greenness on the demand and it signifies that the negative effect caused by the greenness on the demand is much more to balance the positive one caused by the retail price on the demand.

6. Online Channel Mode Selection

In this section, we investigate the optimal online channel mode for the manufacturer and the platform, which is shown in Propositions 3 and 4, respectively.

Proposition 3. *The manufacturer will choose the agency mode under the following circumstance and will choose the reselling mode otherwise, such that*

$$\frac{F}{k(1+r)} + \frac{(1+r)(a - c(1+r/1 - \theta))\theta [ak + c(k(1+r/1 - \theta) - \lambda^2)]}{(2k(1+r) - (1-\theta)\lambda^2)^2} > \frac{[a - c(1+r)]^2}{4[2k(1+r) - \lambda^2]}. \tag{10}$$

Similarly, Proposition 3 reveals the optimal online channel mode selection for the platform. It is easy to verify that a higher slotting fee will push the platform to choose the agency mode. However, the impact of the commission rate on the platform's selection is more comprehensive, and we apply the numerical experiments to show how the

$$\frac{(a - c(1+r/1 - \theta))^2}{2k(1+r/1 - \theta) - \lambda^2} - \frac{2F}{k(1+r)} > \frac{[a - c(1+r)]^2}{4[2k(1+r) - \lambda^2]}. \tag{9}$$

It is noticed from Proposition 3 that the commission rate and the slotting fee jointly play a key role in the manufacturer's optimal online channel mode selection. Herein, we can verify that an increase in either the commission rate or the slotting fee will shift the manufacturer to choose the reselling mode. This is understandable that the manufacturer will pay more sales to the platform with the agency mode when the platform sets a higher commission or a higher slotting fee. Consequently, the manufacturer will turn to the reselling mode instead when suffering a relatively high commission rate or/and a higher slotting fee. The impacts of other key factors on this selection are more complexed, and we apply the numerical experiments to graphically show such effects derived by the interest rate and product cost in the following part.

In the practice, the manufacturer typically decides which online channel is to be selected for its products' sale through the platform's online marketplace. However, to a certain extent, the platform poses more powers over the manufacturer on such type of decision-making, such as pricing and channel distribution and among others. Hence, it is necessary to compare the platform's profit across these two different online channel modes, so as to reach an advantage outcome that satisfies both the manufacturer and the platform.

Next, we investigate the optimal online channel mode for the platform, which is shown in Proposition 4.

Proposition 4. *The platform will choose the agency mode under the following circumstance and will choose the reselling mode otherwise, such that*

commission affects the platform's optimal online channel selection. By following the literature [3, 49–51] and setting the parameters $a = 2$, $c = 0.5$, $r = 0.08$, $\lambda = 0.8$, and $K = 0$, Figure 1 shows that an increase in the commission will shift the platform to choose the agency mode. Furthermore, it is intuitively shown that the slotting fee and the commission

jointly play crucial roles in selecting the optimal online channel mode for both the manufacturer and the platform. For example, in terms of the manufacturer (see Figure 1(a)), when the commission rate is very low ($\theta < 0.2$), the manufacturer will choose the agency mode, and it will choose the reselling mode when the commission rate is relatively high ($\theta > 0.42$), regardless of the slotting fee. At a low level of the slotting fee, the manufacturer will choose the agency mode, whereas the manufacturer will choose the reselling mode with a relatively high slotting fee. A similar observation can be found for the platform in Figure 1(b).

Obviously, based on Proposition 3 and 4, we can infer that both the manufacturer and the platform will likely choose the same online channel mode to sell the product under certain market conditions. To graphically show this advantage situation satisfying the two parties, Figure 1(c) indicates that when the platform sets a moderate commission, both the manufacturer and the platform will reach an agreement and choose the agency mode. The win-win situation herein holds for the two parties. Also, it signifies that the win-win situation will purely exist when both the manufacturer and the platform choose the agency mode. Furthermore, a higher commission along with a low slotting fee is constructive for the two parties to reach the win-win situation and vice versa.

The following applies the numerical experiments to further reveal the other key factors behind to derive this selection. Figures 2 and 3 investigate the impacts of the interest rate and the product cost on the optimal online channel mode selection, respectively.

Letting Figure 1 be a benchmark, when facing a relatively low interest rate, it is seen that both the manufacturer and the platform will likely choose the agency mode, given a commission rate and a slotting fee. Hence, the region of the win-win situation becomes large in this case as shown in Figure 2(c). This clearly indicates that a sufficiently low interest rate will push both the manufacturer and the platform, which will reach an agreement and choose the agency mode. Similarly, it is seen from Figure 3 that an increase in the product cost will shift the manufacturer to choose the reselling mode and platform to select the agency mode. Obviously, this kind of transforming on the online channel mode selection for the two parties will narrow the region of the win-win situation as shown in Figure 3(c).

7. Extension and Discussion

This section firstly extends to a supply chain with a reverse channel leadership in which the manufacturer acts as the leader and the platform is the follower and then explores and compares the consumer surplus and the social welfare across different business scenarios.

7.1. Extension to a Supply Chain with Different Leadership. It is noticed that the platform generally poses more bargaining powers over the most manufacturers in controlling the retailing channel and consumers' preferences. However,

some leading manufacturers with big brand names may have more powers when bargaining with the platform to a certain extent. In this subsection, we consider a situation in which the manufacturer acts as a Stackelberg leader and the platform is the follower. Parallel to Sections 4 and 5, the two different scenarios are, respectively, referred as Scenario R' and Scenario A' . The associated equilibrium decisions can thus be achieved in a similar manner, which is shown in the following proposition.

Proposition 5. *With the reselling mode, the equilibrium decisions are given by*

$$\begin{aligned} w^{R'*} &= \frac{(1+r)\{2k[a+c(1+r)]-c\lambda^2\}}{4k(1+r)-\lambda^2}, \\ e^{R'*} &= \frac{[a-c(1+r)]\lambda}{4k(1+r)-\lambda^2}, \\ p^{R'*} &= \frac{(1+r)\{3ak+c[k(1+r)-\lambda^2]\}}{4k(1+r)-\lambda^2}, \end{aligned} \quad (11)$$

and the associated equilibrium profits for the manufacturer and the e-platform are

$$\begin{aligned} \pi_M^{R'*} &= \frac{k(1+r)[a-c(1+r)]^2}{8k(1+r)-2\lambda^2} + Kr, \\ \pi_E^{R'*} &= \frac{k^2(1+r)^2[a-c(1+r)]^2}{[4k(1+r)-\lambda^2]^2}. \end{aligned} \quad (12)$$

Clearly, when the manufacturer acts as the Stackelberg leader with the online agency mode, the equilibrium decisions and the profits are the same as those given in Section 4. To focus on the online channel mode selection for two parties, the following continues to investigate the optimal online channel mode for the manufacturer and the platform, which is shown in Proposition 6 and Proposition 7, respectively.

Proposition 6. *With a different supply chain leadership, the manufacturer will choose the agency mode under the following circumstance and will choose the reselling mode otherwise, such that*

$$\frac{(a-c(1+r/1-\theta))^2}{2k(1+r/1-\theta)-\lambda^2} - \frac{2F}{k(1+r)} > \frac{[a-c(1+r)]^2}{4k(1+r)-\lambda^2}. \quad (13)$$

Parallel to the associated channel mode selections, when the platform acts a leader, Propositions 6 and 7 reveal how to select the optimal online channel mode when the manufacturer serves as a leader. That is, the slotting fee and the commission induce a similar pattern on the effects of the optimal online channel mode for the two parties, which is not elaborated here. Similarly, the following applies the numerical experiments to focus on the other key factors behind to derive this selection.

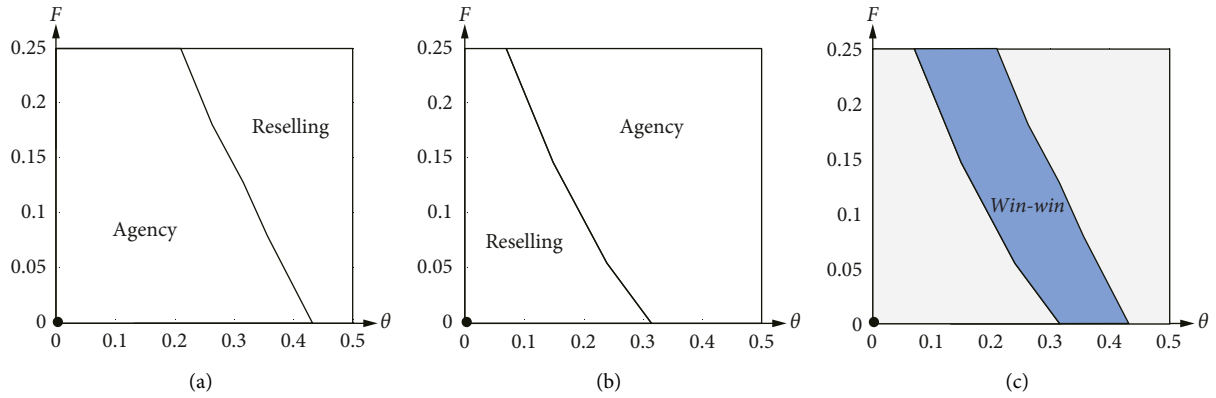


FIGURE 1: Optimal online channel mode selection ($c = 0.5$ and $r = 0.08$). (a) Manufacturer's selection. (b) Platform's selection. (c) Integrated selection.

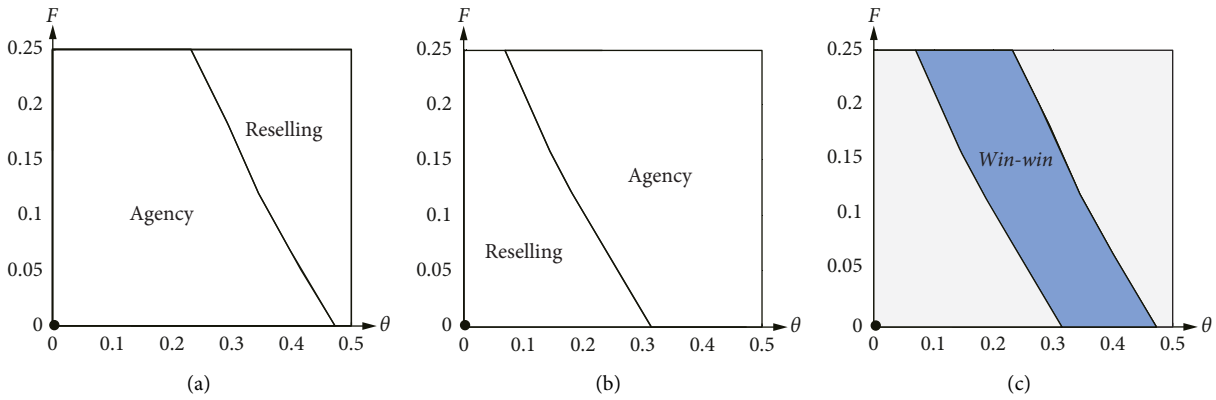


FIGURE 2: Optimal online channel mode selection ($c = 0.5$ and $r = 0.04$). (a) Manufacturer's selection. (b) Platform's selection. (c) Integrated selection.

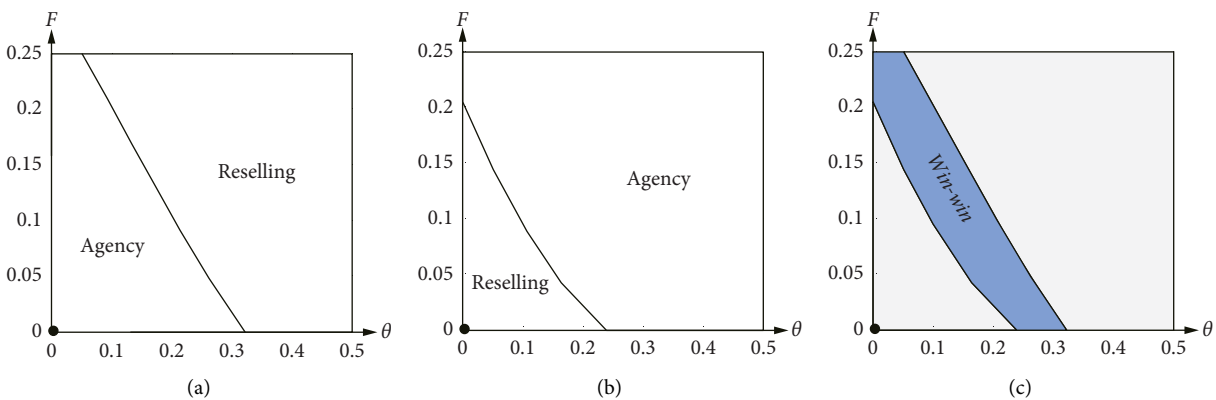


FIGURE 3: Optimal online channel mode selection ($c = 0.8$ and $r = 0.08$). (a) Manufacturer's selection. (b) Platform's selection. (c) Integrated selection.

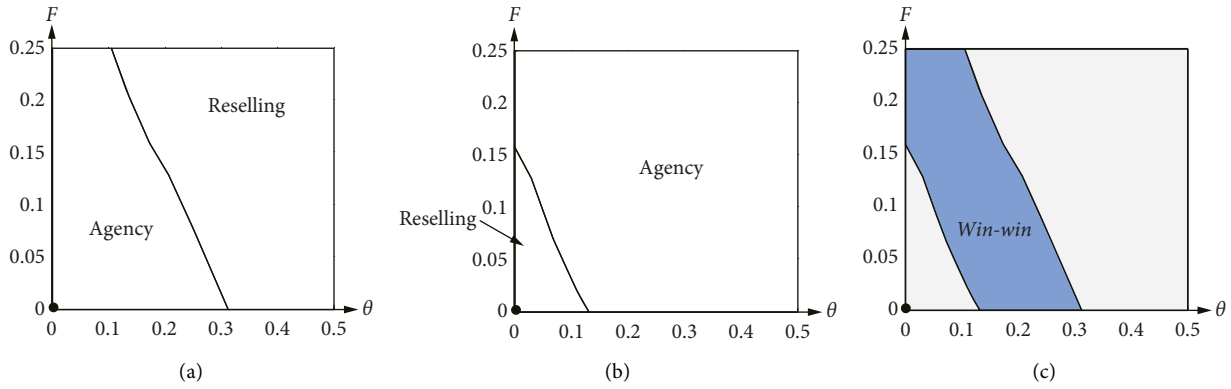


FIGURE 4: Optimal online channel mode selection ($c = 0.5$ and $r = 0.08$). (a) Manufacturer's selection. (b) Platform's selection. (c) Integrated selection.

Proposition 7. *With a different supply chain leadership, the platform will choose the agency mode under the following*

circumstance and will choose the reselling mode otherwise, such that

$$\frac{(a - c(1 + r/1 - \theta))\theta[k(a + c(1 + r/1 - \theta)) - c\lambda^2]}{[2k(1 + r) - (1 - \theta)\lambda^2]^2} + \frac{F}{k(1 + r)^2} > \frac{k[a - c(1 + r)]^2}{[4k(1 + r) - \lambda^2]^2}. \quad (14)$$

It is seen from Figure 4 that both the slotting fee and the commission induce a similar effect on the optimal online channel mode for the two parties when the manufacturer acts as a leader. To be specific, an increase in the slotting fee and/or the commission will shift the manufacturer to choose the reselling mode yet shift the platform to choose the agency mode. Additionally, a mild commission with an appropriate slotting fee will pose an advantage selection for two parties, where both the manufacturer and the platform select the agency mode.

Furthermore, from Figures 5 and 6, we know that a low interest rate set by bank is likely to derive a win-win situation for the two parties, and a higher product cost will exacerbate the differences between manufacturer and platform on the online channel mode selection.

Combining with Section 6, we know that both the slotting fee and the commission will move the manufacturer and the platform toward different directions on the online channel selection, regardless of the different supply chain leaderships. No matter who leads the supply chain, the platform and the manufacturer will reach a win-win situation when the commission becomes moderate along with an appropriate slotting fee. In the case of the win-win situation, the platform and the manufacturer are willing to choose the agency mode.

7.2. Discussion to the Consumer Surplus and the Social Welfare. Consumer surplus reflects the amount of utility or gain that customers receive when they buy products and services. By designing and developing a green product, consumer surplus is very important for the firms to consider,

because consumers that derive a large benefit from buying products are more likely to purchase the green products again in the future. In practice, when the firms make such type of operational decisions, they not only care about their own profits but also take their shareholders' profit into account. As a main stakeholder in the supply chain, consumers have become a key focus of firms in making decisions. This subsection shall next consider how the consumer surplus and the social welfare affect the individual's optimal online channel mode selection in this platform supply chain. By following the literature [52, 53], we measure the consumer surplus as given by

$$\begin{aligned} CS &= \int_p^{p_{\max}} D(p, e) dp \\ &= \int_p^{a+\lambda e} (a - p + \lambda e) dp \\ &= \frac{(a - p + \lambda e)^2}{2}. \end{aligned} \quad (15)$$

Herein, the social welfare for the supply chain is obtained as follows:

$$SW = \pi_E + \pi_M + CS. \quad (16)$$

Based on the associated equilibrium decisions and individual profit, it is easy to compute the consumer surplus and the social welfare, respectively. Furthermore, we compare the consumer surplus and the social welfare across two different supply chain leaderships.

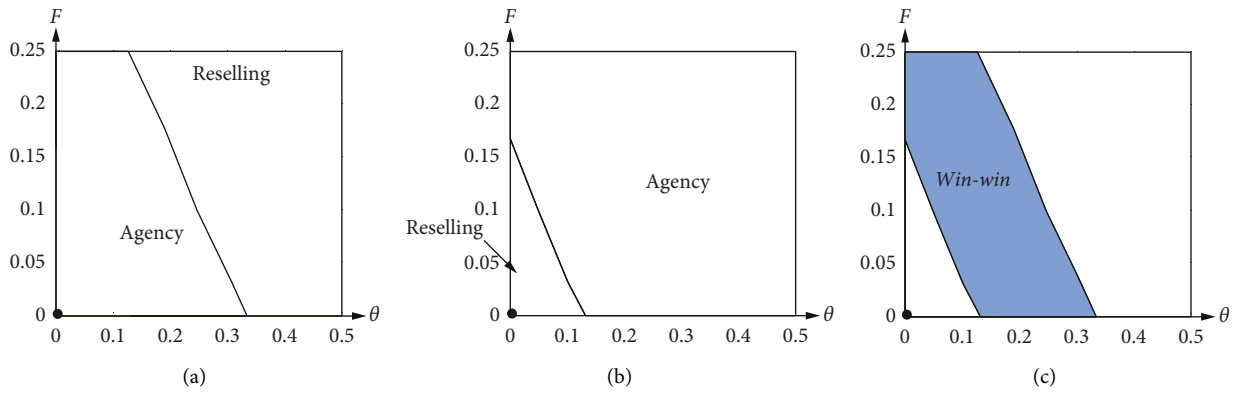


FIGURE 5: Optimal online channel mode selection ($c = 0.5$ and $r = 0.04$). (a) Manufacturer's selection. (b) Platform's selection. (c) Integrated selection.

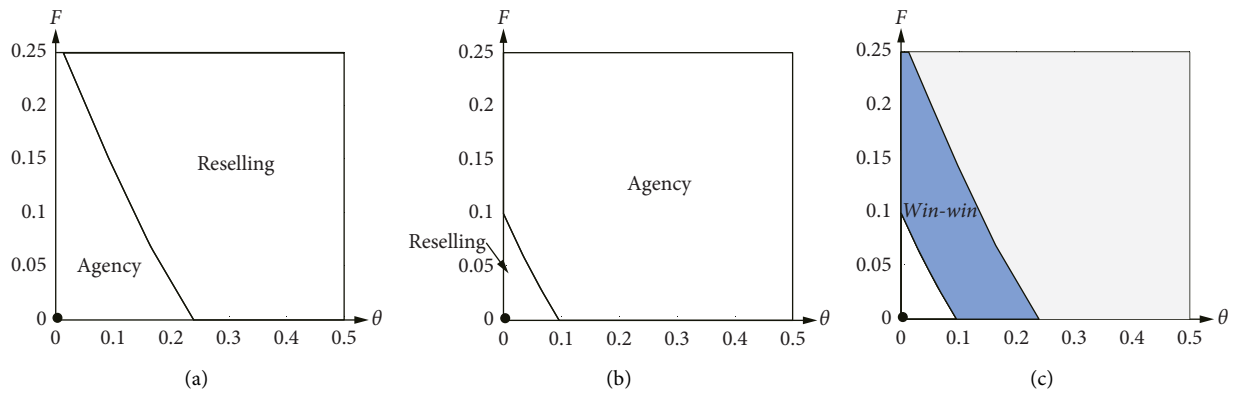


FIGURE 6: Optimal online channel mode selection ($c = 0.8$ and $r = 0.08$). (a) Manufacturer's selection. (b) Platform's selection. (c) Integrated selection.

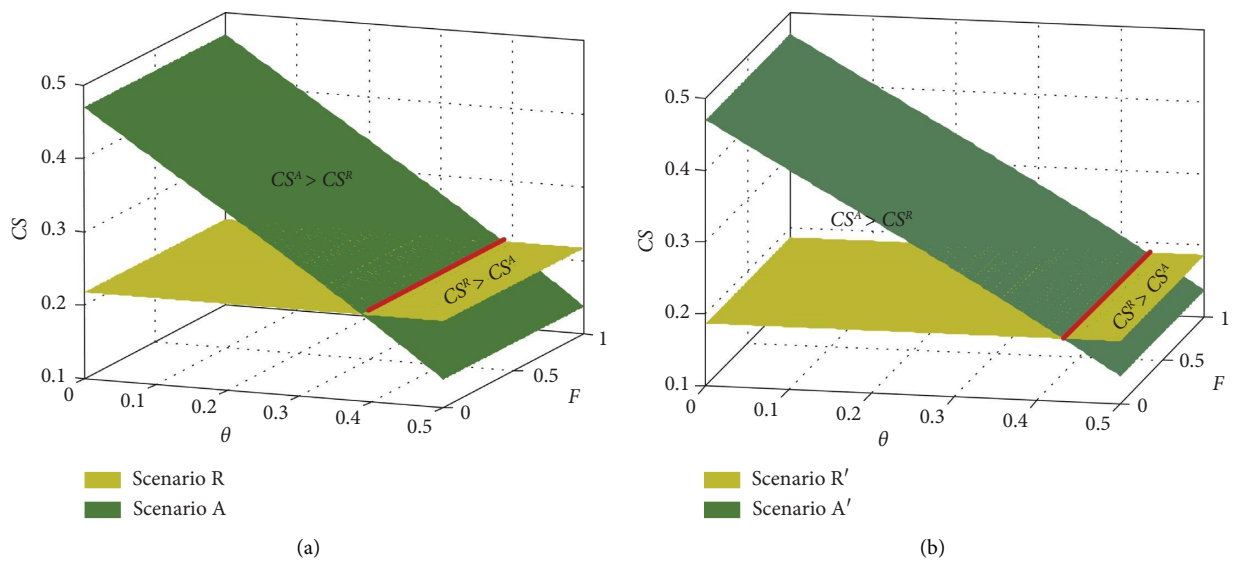


FIGURE 7: Consumer surplus. (a) Platform leads the supply chain. (b) Manufacturer leads the supply chain.

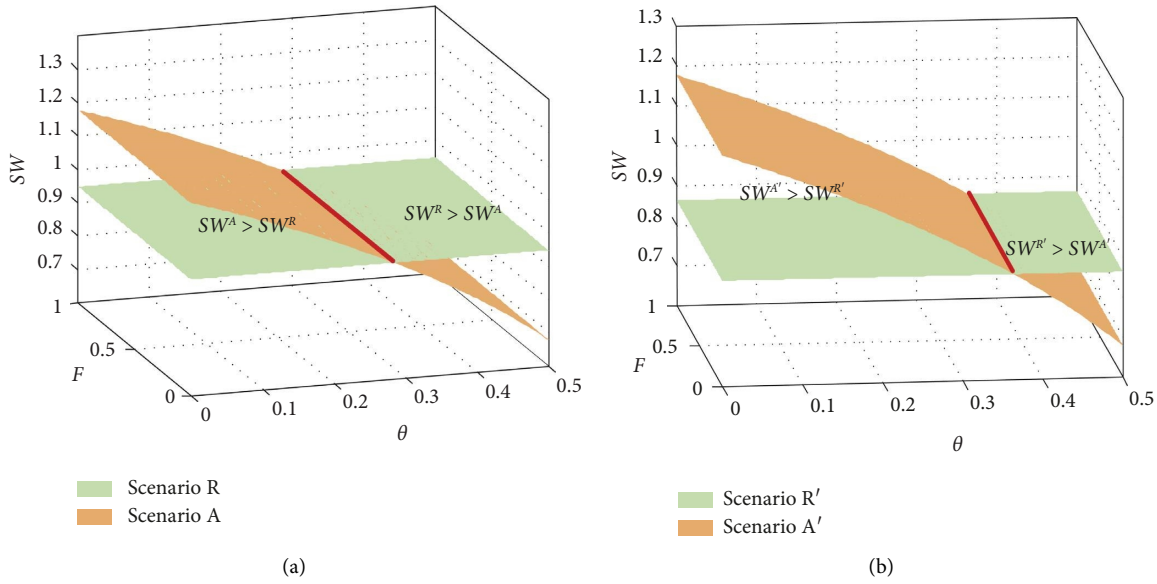


FIGURE 8: Social welfare. (a) Platform leads the supply chain. (b) Manufacturer leads the supply chain.

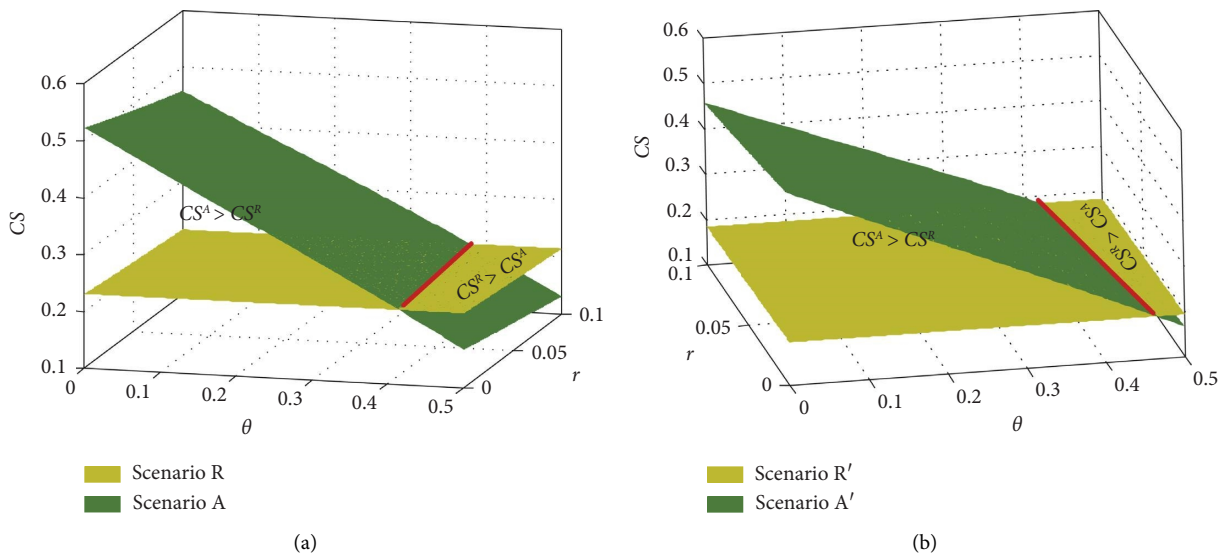


FIGURE 9: Consumer surplus. (a) Platform leads the supply chain. (b) Manufacturer leads the supply chain.

It is seen from Figure 7 that the relative consumer surplus across the two online channel modes relies largely on the commission. To be specific, when the commission is relatively low, the agency mode will benefit the consumers and thus the consumers will obtain more surpluses. Otherwise, the reselling mode is meaningful to boost the consumer surplus when the commission is sufficiently high. This is understandable that when the commission is very low, the manufacturer will naturally pay less revenue to the platform and thus determine a relatively low retail price, thereby stimulating the consumer surplus. In addition, we find that the slotting fee exerts no effect on the relative consumer surplus with the two different supply chains with different channel leaderships. The reason behind is that the slotting fee is a fixed revenue that distributes between the platform and the manufacturer, which does not affect the retail prices.

Figure 8 clearly reveals the relative social welfare across the two online channel modes with the two supply chains with different channel leaderships. Similarly, we find that the slotting fee has no effects on the relative social welfare, and the relative social welfare is highly relied on the commission. In particular, the agency mode with a lower commission will benefit the social welfare, mostly compared with the reselling mode. This indicates that when the supply chain concerns more about the social welfare, the platform will pay a relatively low commission to the manufacturers.

Next, we investigate how the interest rate affects the relative consumer surplus and social welfare across different online channel modes and supply chain leaderships. It is seen from Figures 9 and 10 that an increase in the interest rate signifies that the supply chain will enjoy a higher social welfare with more consumer surpluses with the reselling

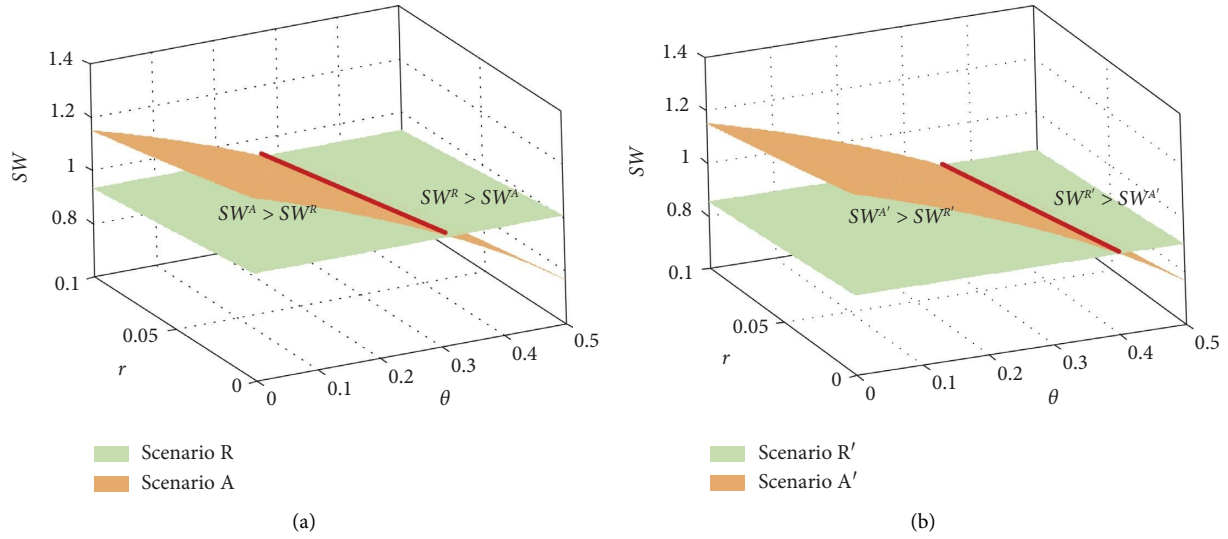


FIGURE 10: Social welfare. (a) Platform leads the supply chain. (b) Manufacturer leads the supply chain.

mode. This indicates that when the capital-constrained manufacturer suffers a relatively high interest rate set by bank, it is optimal for the platform supply chain to choose the reselling mode to achieve a better performance in both consumer surplus and the social welfare.

8. Conclusions

This paper develops an e-commerce platform supply chain that consists of one platform company and one capital-constrained manufacturer. By borrowing the loans from bank, the capital-constrained manufacturer can raise sufficient capital to produce and sell the products through the platform's online marketplace with either the online agency channel mode or the online reselling channel mode. The focal point of this paper is to, respectively, investigate the optimal online channel mode for the manufacturer and the platform. The current work also extends to a different supply chain with a different leadership, based on which we explore the impacts of supply chain leaderships on the consumer surplus as well as the social welfare.

8.1. Key Findings. With the analytical study, the key findings of this paper are collected as follows:

Firstly, we find that the initial capital level has no effect on the equilibrium decisions of the two supply chain members but largely affect the manufacturer's profit with two different online channel modes. It is the interest rate that plays a critical role in determining the respective equilibrium decisions.

Secondly, the optimal online channel mode selections for the manufacturer and the platform are, respectively, investigated and the factors behind deriving these strategic selections are also revealed. It clearly exhibits that an increase in either commission or the slotting fee will make the manufacturer and platform act differently in selecting the

optimal online channel mode, that is, the manufacturer will choose the online reselling mode, while the platform will select the online agency mode. Interestingly, we find that the manufacturer and the platform will reach a consensus and choose the online agency mode to achieve a win-win situation under certain market conditions.

Finally, this paper compares the supply chain performances from different perspectives. The impacts of different online channel modes on the consumer surplus and social welfare are explored with different supply chain leaderships. It is found that the commission plays a key role in the relative consumer surplus and social welfare whereas the slotting fee has no such effects on them. The supply chain performs better in both the consumer surplus and social welfare with the reselling mode when bank sets a relatively high interest rate.

8.2. Managerial Implications. Based on the key findings derived in this paper, herein, the contributions to the industrial practice are collected in the following:

Firstly, considering a situation that the green product manufacturer may suffer the capital shortage, this paper incorporates two different online channel modes to an e-commerce platform supply chain with the capital-constrained manufacturer selecting bank loan financing. We explicitly reveal the impacts of the financing on the equilibrium decisions and individual profits. Managerial implications for firms on selecting the optimal online channel mode are obtained, based on which we find a win-win situation benefiting the two parties when choosing the online agency mode under certain market conditions. This results compliment the existing studies on the online channel mode selection [6, 7, 54].

Secondly, this paper then reveals how the different supply chain leaderships affect the individual profits and consumer surplus as well as social welfare. It is well noticed that the commission set by the platform plays a crucial role

in determining the relative consumer surplus and social welfare, whereas the slotting fee has no such effects on them across the two different online channel modes. The supply chain will perform better in both consumer surplus and social welfare when applying the online reselling mode along with facing a relatively high interest rate set by bank. This provides managerial insights for industrial practicer on how to effectively make such decision-making in platform economy.

8.3. Limitations and Further Research. The following summarizes the limitations and the researching opportunities of the current paper: Firstly, this paper purely considers the bank loan financing for the capital-constrained manufacturer. In practice, the capital-constrained manufacturer may have several different financing resources, such as financing from an e-commerce platform or trade credit financing. Herein, it would be interesting to investigate other financing strategies in such a platform supply chain and compare the impacts of different financing resources on the supply chain performances. Secondly, this paper develops an e-commerce platform supply chain in which the manufacturer can choose either the agency mode or the reselling mode in an online marketplace. Recently, it poses an uptrend that the manufacturer can distribute its products simultaneously through both the online agency mode and the online reselling mode. A promising extension of this paper is to incorporate these two online channel modes simultaneously for a capital-constrained manufacturer in this platform supply chain. Thirdly, in practice, the government often provides some subsidies of the green investments to the manufacturer. Hence, it is valuable to investigate the optimal subsidy policy for the government. Lastly, this paper considers the demand of the green product to be deterministic. Another promising and challenging extension of this paper is to explore the case with a stochastic demand of the green product in such an e-commerce platform supply chain.

Appendix

A. Proof of Proposition 1

With the reselling mode, the platform moves first and sets the markup t for the product, then the manufacturer determines the wholesale price w and the green effort e , where $t = p - w$. According to equation (3), we can compute the Hessian matrix of π_M as

$$H_{\pi_M} = \begin{vmatrix} \frac{\partial^2 \pi_M}{\partial w^2} & \frac{\partial^2 \pi_M}{\partial w \partial e} \\ \frac{\partial^2 \pi_M}{\partial e \partial w} & \frac{\partial^2 \pi_M}{\partial e^2} \end{vmatrix} \quad (\text{A.1})$$

$$= \begin{vmatrix} -2 & \lambda \\ \lambda & -k(1+r) \end{vmatrix}.$$

Clearly, H_{π_M} is negatively defined when $2k(1+r) > \lambda^2$. Hence, we can obtain the optimal wholesale price and the green effort for the manufacturer as $w = ((1+r)[ak - kt + c(k + kr - \lambda^2)] / (2k(1+r) - \lambda^2))$ and $e = ([a - c(1+r) - t]\lambda) / (2k(1+r) - \lambda^2)$ by simultaneously solving $(\partial \pi_M / \partial w) = 0$ and $(\partial \pi_M / \partial e) = 0$. By substituting w and e , we have $(\partial^2 \pi_E / \partial t^2) = -(2k(1+r)) / (2k(1+r) - \lambda^2) < 0$. Thus, π_E is strictly concave on t , and the optimal markup for the platform is $t = (a - c(1+r)/2)$ by solving $(\partial \pi_E / \partial t) = 0$. The equilibrium decisions and the individual profits can thus be easily obtained in Proposition 1.

B. Proof of Corollary 1

- (i) Based on Proposition 1, it always has $(\partial e^{R^*} / \partial r) = -(\lambda(2ak - c\lambda^2)) / (2[2k(1+r) - \lambda^2]^2) < 0$ and $(\partial e^{R^*} / \partial r) = -(k[a\lambda^2 + 2c(1+r)(k + kr - \lambda^2)]) / (2[2k(1+r) - \lambda^2]^2) < 0$.
- (ii) $(\partial w^{R^*} / \partial r) = (-ak\lambda^2 + 2c[3k^2(1+r)^2 - 3k(1+r)\lambda^2 + \lambda^4]) / (2[2k(1+r) - \lambda^2]^2)$. Let $(\partial w^{R^*} / \partial r) = 0$, then we have $r_1 = (-3c(2k - \lambda^2) + \sqrt{3}\lambda\sqrt{c(2ak - c\lambda^2)}) / (6ck)$, so as to if $0 < r < r_1$ then $(\partial w^{R^*} / \partial r) < 0$; if $r > r_1$, then $(\partial w^{R^*} / \partial r) > 0$ holds.
- (iii) $(\partial p^{R^*} / \partial r) = (-ak\lambda^2 + c[2k^2(1+r)^2 - 2k(1+r)\lambda^2 + \lambda^4]) / (2[2k(1+r) - \lambda^2]^2)$. Let $(\partial p^{R^*} / \partial r) = 0$, then we have $r_2 = (-c(2k - \lambda^2) + \lambda\sqrt{c(2ak - c\lambda^2)}) / (2ck)$, so as to if $0 < r < r_2$ then $(\partial p^{R^*} / \partial r) < 0$; if $r > r_2$, then $(\partial p^{R^*} / \partial r) > 0$ holds.
- (iv) $(\partial \pi_E^{R^*} / \partial r) = (a - c(1+r)/2)(\partial D^{R^*} / \partial r) - (c/2)D^{R^*} < 0$ and $(\partial \pi_M^{R^*} / \partial r) = K - (k(a - c(1+r)(a\lambda^2 + c(1+r)(4k(1+r) - 3\lambda^2))) / (8(2k(1+r) - \lambda^2)^2)$ and $K < cD^{R^*} + (ke^{R^*2}/2)$, it holds $(\partial \pi_S^{R^*} / \partial r) < 0$.

Corollary 1 is thus completed.

C. Proof of Proposition 2

With the the agency mode, the manufacturer sets the retail price and the green effort simultaneously. Similarly, the Hessian matrix of π_M can be computed as

$$H_{\pi_M^A} = \begin{vmatrix} \frac{\partial^2 \pi_M^A}{\partial p^2} & \frac{\partial^2 \pi_M^A}{\partial p \partial e} \\ \frac{\partial^2 \pi_M^A}{\partial e \partial p} & \frac{\partial^2 \pi_M^A}{\partial e^2} \end{vmatrix} \quad (C.1)$$

$$= \begin{vmatrix} -2(1-\theta) & \lambda(1-\theta) \\ \lambda(1-\theta) & -k(1+r) \end{vmatrix}.$$

$$\frac{\partial e^{A*}}{\partial \theta} = -\frac{(1+r)\lambda(2ak - c\lambda^2)}{[2k(1+r) - (1-\theta)\lambda^2]^2} < 0,$$

$$\frac{\partial p^{A*}}{\partial \theta} = \frac{(1+r)(2ck^2(1+r)^2 - k(1-\theta)(a + 2c(1+r) - a\theta)\lambda^2 + c(1-\theta)^2\lambda^4)}{(1-\theta)^2[2k(1+r) - (1-\theta)\lambda^2]^2} > 0, \quad (D.1)$$

$$\frac{\partial D^{A*}}{\partial \theta} = -\frac{k(1+r)\{a(1-\theta)^2\lambda^2 + 2c(1+r)[k(1+r) - (1-\theta)\lambda^2]\}}{(1-\theta)^2[2k(1+r) - (1-\theta)\lambda^2]^2} < 0.$$

Proposition 2 is thus completed.

E. Proofs of Propositions 3 and 4

Based on Propositions 1 and 2, we have $\pi_M^{R*} = (k(1+r)[a - c(1+r)]^2)/(8[2k(1+r) - \lambda^2] + Kr)$, and $\pi_M^{A*} = k(1+r)(c^2(1+r)^2 - 2ac(1+r)(1-\theta) + a^2(1-\theta)^2)/(2(1-\theta)[2k(1+r) - (1-\theta)\lambda^2] + Kr - F)$. Thus, it can be computed that $\pi_M^{A*} - \pi_M^{R*} = \frac{k(1+r)(([a - c(1+r)]/(1-\theta))^2/(2k(1+r)) - (1-\theta) - \lambda^2) - (2F)/(k(1+r)) - ([a - c(1+r)]^2/4[2k(1+r) - \lambda^2])}{(1-\theta)^2[2k(1+r) - (1-\theta)\lambda^2]^2} + F)$. Similarly, for the platform, we have $\pi_E^{R*} = (k(1+r)[a - c(1+r)]^2)/(4[2k(1+r) - \lambda^2])$, and $\pi_E^{A*} = (k(1+r)^2[a(1-\theta) - c(1+r)]\theta\{ak(1-\theta) + c[k(1+r) - (1-\theta)\lambda^2]\})/((1-\theta)^2[2k(1+r) - (1-\theta)\lambda^2]^2) + F)$. Thus, it is easy to compute that $\pi_E^{A*} - \pi_E^{R*} = k(1+r)((1+r)[a - c(1+r)]/(1-\theta)\theta\{ak + c[k(1+r)/(1-\theta) - \lambda^2]\}/[2k(1+r) - (1-\theta)\lambda^2]^2 + (F/k(1+r)) - ([a - c(1+r)]^2/4[2k(1+r) - \lambda^2])$.

Propositions 3 and 4 can thus be easily obtained.

Data Availability

The data used to support the findings of this study are available from the corresponding author upon request.

Clearly, the H_{π_M} is negatively defined when $2k(1+r) > \lambda^2(1-\theta)$. Hence, we can compute the optimal decisions for the manufacturer as $p = ((1+r)\{ak(1-\theta) + c[k(1+r) - (1-\theta)\lambda^2]\})/((1-\theta)[2k(1+r) - (1-\theta)\lambda^2])$ and $e = (\lambda[a(1-\theta) - c(1+r)])/(2k(1+r) - (1-\theta)\lambda^2)$.

Proposition 2 is thus completed.

D. Proof of Corollary 2

Based on Proposition 2, it always has

Conflicts of Interest

The authors declare that they have no conflicts of interest.

Acknowledgments

The authors would like to acknowledge the financial support from the National Social Science Fund of China (Grant number: 19BGL095), the Education Department of Shaanxi Provincial Government (Grant number: 19JK0355), and the Shaanxi Science and Technology Department (Grant number: 2020KRM001).

References

- [1] S. Huang, Z. P. Fan, and N. Wang, "Green subsidy modes and pricing strategy in a capital-constrained supply chain," *Transportation Research Part E: Logistics and Transportation Review*, vol. 136, Article ID 101885, 2020.
- [2] C. Liu, J. Chen, and W. Cai, "Data-driven remanufacturability evaluation method of waste parts," *IEEE Transactions on Industrial Informatics*, vol. 18, no. 7, pp. 4587–4595, 2022.
- [3] C. Y. Liu, H. Wang, J. Tang, C. T. Chang, and Z. Liu, "Optimal recovery model in a used batteries closed-loop supply chain considering uncertain residual capacity," *Transportation*

- Research Part E: Logistics and Transportation Review*, vol. 156, Article ID 102516, 2021b.
- [4] R. S. Widrick, S. G. Nurre, and M. J. Robbins, "Optimal policies for the management of an electric vehicle battery swap station," *Transportation Science*, vol. 52, no. 1, pp. 59–79, 2018.
 - [5] Reuters, "China's central bank rolls out lending tool for carbon emission cuts," 2022, <https://www.reuters.com/business/sustainable-business/china-central-bank-provide-low-cost-loans-carbon-emission-cuts-2021-11-08/>.
 - [6] L. Tian, A. J. Vakharia, Y. R. Tan, and Y. Xu, "Marketplace, reseller, or hybrid: strategic analysis of an emerging e-commerce model," *Production and Operations Management*, vol. 27, no. 8, pp. 1595–1610, 2018.
 - [7] Z. Zhang, H. Xu, G. Y. Ke, and K. Chen, "Selecting online distribution modes for differentiated products in a platform supply chain," *International Journal of Production Economics*, vol. 244, Article ID 108384, 2022b.
 - [8] Y. J. Chen and J. B. Sheu, "Environmental-regulation pricing strategies for green supply chain management," *Transportation Research Part E: Logistics and Transportation Review*, vol. 45, no. 5, pp. 667–677, 2009.
 - [9] S. R. Bhaskaran and V. Krishnan, "Effort, revenue, and cost sharing mechanisms for collaborative new product development," *Management Science*, vol. 55, no. 7, pp. 1152–1169, 2009.
 - [10] D. Ghosh and J. Shah, "A comparative analysis of greening policies across supply chain structures," *International Journal of Production Economics*, vol. 135, no. 2, pp. 568–583, 2012.
 - [11] B. Li, M. Zhu, Y. Jiang, and Z. Li, "Pricing policies of a competitive dual-channel green supply chain," *Journal of Cleaner Production*, vol. 112, pp. 2029–2042, 2016.
 - [12] Q. Meng, M. Li, W. Liu, Z. Li, and J. Zhang, "Pricing policies of dual-channel green supply chain: considering government subsidies and consumers' dual preferences," *Sustainable Production and Consumption*, vol. 26, pp. 1021–1030, 2021.
 - [13] M. Das Roy and S. S. Sana, "Multi-echelon green supply chain model with random defectives, remanufacturing and rework under setup cost reduction and variable transportation cost," *Sādhanā*, vol. 46, no. 4, pp. 211–218, 2021.
 - [14] Z. Liu, X. X. Zheng, D. F. Li, C. N. Liao, and J. B. Sheu, "A novel cooperative game-based method to coordinate a sustainable supply chain under psychological uncertainty in fairness concerns," *Transportation Research Part E: Logistics and Transportation Review*, vol. 147, Article ID 102237, 2021c.
 - [15] S. S. Sana, "Price competition between green and non green products under corporate social responsible firm," *Journal of Retailing and Consumer Services*, vol. 55, Article ID 102118, 2020.
 - [16] X. Chen and G. G. Cai, "Joint logistics and financial services by a 3pl firm," *European Journal of Operational Research*, vol. 214, no. 3, pp. 579–587, 2011.
 - [17] G. Cai, X. Chen, and Z. Xiao, "The roles of bank and trade credits: Theoretical analysis and empirical evidence," *Production and Operations Management*, vol. 23, no. 4, pp. 583–598, 2014.
 - [18] Z. C. Zhang, H. Y. Xu, and K. B. Chen, "Operational decisions and financing strategies in a capital-constrained closed-loop supply chain," *International Journal of Production Research*, vol. 59, no. 15, pp. 4690–4710, 2020b.
 - [19] X. Jin, H. Zhou, and J. Wang, "Joint finance and order decision for supply chain with capital constraint of retailer considering product defect," *Computers & Industrial Engineering*, vol. 157, Article ID 107293, 2021.
 - [20] N. Yan, Y. Zhang, X. Xu, and Y. Gao, "Online finance with dual channels and bidirectional free-riding effect," *International Journal of Production Economics*, vol. 231, Article ID 107834, 2021.
 - [21] Y. Zheng, Y. Zhao, N. Wang, X. Meng, and H. Yang, "Financing decision for a remanufacturing supply chain with a capital constrained retailer: a study from the perspective of market uncertainty," *International Journal of Production Economics*, vol. 245, Article ID 108397, 2022.
 - [22] S. S. Sana, J. Ferro-Correa, A. Quintero, and R. Amaya, "A system dynamics model of financial flow in supply chains: a case study," *RAIRO - Operations Research*, vol. 52, no. 1, pp. 187–204, 2018.
 - [23] N. Yan, X. He, and Y. Liu, "Financing the capital-constrained supply chain with loss aversion: supplier finance vs. supplier investment," *Omega*, vol. 88, pp. 162–178, 2019.
 - [24] J. K. Ryan, D. Sun, and X. Zhao, "Competition and coordination in online marketplaces," *Production and Operations Management*, vol. 21, no. 6, pp. 997–1014, 2012.
 - [25] T. M. Choi, L. Feng, and R. Li, "Information disclosure structure in supply chains with rental service platforms in the blockchain technology era," *International Journal of Production Economics*, vol. 221, Article ID 107473, 2020.
 - [26] B. Jiang, K. Jerath, and K. Srinivasan, "Firm strategies in the "mid tail" of platform-based retailing," *Marketing Science*, vol. 30, no. 5, pp. 757–775, 2011.
 - [27] Q. Xu and Y. He, "Optimal information disclosure strategies for a retail platform in the blockchain technology era," *International Journal of Production Research*, pp. 1–12, 2021.
 - [28] A. Hasani, S. H. Zegordi, and E. Nikbaksh, "Robust closed-loop global supply chain network design under uncertainty: the case of the medical device industry," *International Journal of Production Research*, vol. 53, no. 5, pp. 1596–1624, 2015.
 - [29] J. Wang and S. He, "Optimal decisions of modularity, prices and return policy in a dual-channel supply chain under mass customization," *Transportation Research Part E: Logistics and Transportation Review*, vol. 160, Article ID 102675, 2022.
 - [30] T. Zhang and T. M. Choi, "Optimal consumer sales tax policies for online-offline retail operations with consumer returns," *Naval Research Logistics*, vol. 68, no. 6, pp. 701–720, 2021.
 - [31] C. Dellarocas, "The Digitization of Word of Mouth: Promise and Challenges of online Feedback mechanisms," *Management Science*, vol. 49, no. 10, pp. 1407–1424, 2003.
 - [32] Y. Deng, J. Zheng, W. Khern-am nuai, and K. Kannan, "More than the quantity: the value of editorial reviews for a user-generated content platform," *Management Science*, vol. 68, 2021.
 - [33] K. Kaushik, R. Mishra, N. P. Rana, and Y. K. Dwivedi, "Exploring reviews and review sequences on e-commerce platform: a study of helpful reviews on Amazon.in," *Journal of Retailing and Consumer Services*, vol. 45, pp. 21–32, 2018.
 - [34] S. S. Sana, "Sale through dual channel retailing system—a mathematical approach," *Sustainability Analytics and Modeling*, vol. 2, Article ID 100008, 2022.
 - [35] P. Zhang, Y. He, and C. V. Shi, "Retailer's channel structure choice: online channel, offline channel, or dual channels?" *International Journal of Production Economics*, vol. 191, pp. 37–50, 2017.
 - [36] X. Qin, Z. Liu, and L. Tian, "The optimal combination between selling mode and logistics service strategy in an e-commerce market," *European Journal of Operational Research*, vol. 289, no. 2, pp. 639–651, 2021.

- [37] J. Sun, P. Yuan, and L. Hua, "Pricing and financing strategies of a dual-channel supply chain with a capital-constrained manufacturer," *Annals of Operations Research*, pp. 1–21, 2022.
- [38] S. Zhang and J. Zhang, "Agency selling or reselling: E-tailer information sharing with supplier offline entry," *European Journal of Operational Research*, vol. 280, no. 1, pp. 134–151, 2020.
- [39] Z. Chen, Z. P. Fan, and X. Zhao, "Offering return-freight insurance or not: strategic analysis of an e-seller's decisions," *Omega*, vol. 103, Article ID 102447, 2021.
- [40] Y. Yu, X. Li, and X. Xu, "Reselling or marketplace mode for an online platform: the choice between cap-and-trade and carbon tax regulation," *Annals of Operations Research*, vol. 310, no. 1, pp. 293–329, 2022.
- [41] Z. Zhang, H. Xu, K. Chen, Y. Zhao, and Z. Liu, "Channel mode selection for an e-platform supply chain in the presence of a secondary marketplace," *European Journal of Operational Research In press*, vol. 305, 2022a.
- [42] Q. Wang, N. Zhao, and X. Ji, "Reselling or agency selling? the strategic role of live streaming commerce in distribution contract selection," *Electronic Commerce Research*, pp. 1–34, 2022.
- [43] J. Wei, J. Lu, and J. Zhao, "Interactions of competing manufacturers' leader-follower relationship and sales format on online platforms," *European Journal of Operational Research*, vol. 280, no. 2, pp. 508–522, 2020.
- [44] J. Huang, M. Leng, and M. Parlar, "Demand functions in decision modeling: a comprehensive survey and research directions," *Decision Sciences*, vol. 44, no. 3, pp. 557–609, 2013.
- [45] W. Zhu and Y. He, "Green product design in supply chains under competition," *European Journal of Operational Research*, vol. 258, no. 1, pp. 165–180, 2017.
- [46] Jd, "Commissions and slotting fees announced publicly on jd.com," 2022, <https://rule.jd.com/rule/ruleDetail.action?ruleId=638209647311982592&btype=1>.
- [47] X. Geng, Y. R. Tan, and L. Wei, "How add-on pricing interacts with distribution contracts," *Production and Operations Management*, vol. 27, no. 4, pp. 605–623, 2018.
- [48] X. Guo, S. Zheng, Y. Yu, and F. Zhang, "Optimal bundling strategy for a retail platform under agency selling," *Production and Operations Management*, vol. 30, no. 7, pp. 2273–2284, 2021.
- [49] Z. Liu, K. W. Li, B. Y. Li, J. Huang, and J. Tang, "Impact of product-design strategies on the operations of a closed-loop supply chain," *Transportation Research Part E: Logistics and Transportation Review*, vol. 124, pp. 75–91, 2019.
- [50] T. M. Choi, P. S. Chow, C. H. Lee, and B. Shen, "Used intimate apparel collection programs: a game-theoretic analytical study," *Transportation Research Part E: Logistics and Transportation Review*, vol. 109, pp. 44–62, 2018.
- [51] Z. Liu, M. D. Wan, X. X. Zheng, and S. L. Koh, "Fairness concerns and extended producer responsibility transmission in a circular supply chain," *Industrial Marketing Management*, vol. 102, pp. 216–228, 2022.
- [52] P. Ma, J. Shang, and H. Wang, "Enhancing corporate social responsibility: contract design under information asymmetry," *Omega*, vol. 67, pp. 19–30, 2017.
- [53] Z. Zhang, H. Xu, Z. Liu, and Y. Fang, "Implications for pure profit, environmental impact and social welfare in a socially responsible supply chain," *Kybernetes*, vol. 50, 2020a.
- [54] Y. Kwark, J. Chen, and S. Raghunathan, "Platform or wholesale? a strategic tool for online retailers to benefit from third-party information," *MIS Quarterly*, vol. 41, no. 3, pp. 763–785, 2017.

Research Article

Synergistic Agglomeration of Manufacturing and Logistics Industries and Urban Green Economy Efficiency: Influence and Upgrading

Qian Zhang ¹ and Ye Tao ²

¹School of Humanities, Anhui Polytechnic University, Wuhu 241000, China

²School of Materials, Anhui Polytechnic University, Wuhu 241000, China

Correspondence should be addressed to Ye Tao; taoye@mail.ahpu.edu.cn

Received 11 October 2022; Revised 23 October 2022; Accepted 24 November 2022; Published 3 February 2023

Academic Editor: Conghu Liu

Copyright © 2023 Qian Zhang and Ye Tao. This is an open access article distributed under the Creative Commons Attribution License, which permits unrestricted use, distribution, and reproduction in any medium, provided the original work is properly cited.

Synergistic industrial agglomeration has an impact on green economy. In this research, the evaluation index system of urban green economic efficiency (GEE) is constructed; the superefficiency SBM model, Malmquist index method, location entropy method, and Tobit regression analysis are used to analyse the static and dynamic GEE, the industrial agglomeration level of manufacturing and logistics industries, the synergistic agglomeration level of the two, and the influencing factors of GEE of 41 cities and four provinces in the Yangtze River Delta (YRD) region from 2010 to 2019. The results show that the urban GEE in the YRD region is generally not high, and the annual change trend of efficiency is U-shaped. In the YRD region as a whole and in each province, the relationship between the synergistic agglomeration level of the two industries and the GEE presents regional heterogeneity and GEE is influenced by various factors. Synergistic alignment and integrated development of the two industries are good ways to optimize and upgrade industrial structure transformation. The government can improve urban GEE by adjusting the horizontal and vertical intergovernmental relations as well as adjusting the talent support mechanism to promote integration of technologies with industry and optimizing the upgrading and transformation of industrial structure to achieve sustainable industry development.

1. Introduction

1.1. Research Background. The concept of green economic efficiency (GEE) was first proposed by environmental economist Pearce in 1989 [1]. It mainly refers to the economic development efficiency including the input factor of energy consumption and the output factor of environmental pollution, and it clearly demonstrates the importance of ecological and environmental factors in economic development and transformation. The efficiency of green economy includes two aspects: green efficiency and economic efficiency. By taking environmental pollution factors into account in the undesirable output, the efficiency of sustainable development of economy can be more accurately measured.

In 2019, the State Council of China approved the overall plan for the Yangtze River Delta (YRD) Eco-Green Integrated Development Demonstration Zone, which emphasized the urgency of industrial green transformation in the YRD region. In 2021, the Office for the Steering Group of the YRD region Integrated Development promulgated the YRD Regional Integrated Development Programme for the implementation of the 14th National 5-Year Plan, in which prospects and plans are put forward to strengthen regional coordinated development, promote interprovincial cooperation in linkage agglomeration areas, promote ecological environment construction, and build a green YRD region. Figure 1 shows the overall map of the YRD region. As a region with relatively rapid economic development, better innovation capability, and more mature institutional system

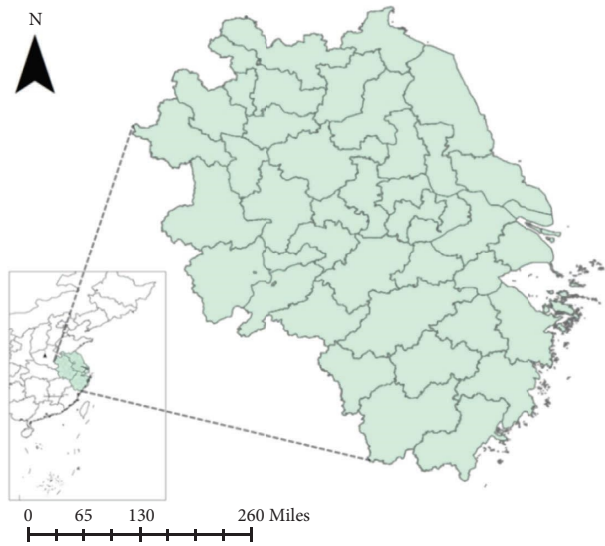


FIGURE 1: Overall map of the research region.

compared to the national average, the YRD region attracts a large number of inward investment enterprises, and industrial agglomeration becomes one of the core factors to promote regional economic progress. However, industrial aggregation promotes resource and information sharing, reduces production, innovation, and environmental protection costs, but at the same time, it may lead to environmental pollution and hinder sustainable development. With the deepening of the concept of green growth and sustainability to meet the “Double Carbon” (in 2020, the Chinese president pledged at the United Nations General Assembly that China would peak its carbon emissions by 2030 and become carbon neutral by 2060) goal set by Jinping Xi, the President of China, how to adapt such agglomeration in the YRD region to improve GEE has become a concern.

The coordinated development and collaborative production mode of the manufacturing and producer services industries can optimize resource allocation, push the transformation of the manufacturing industry from the traditional extensive development mode to that of green and knowledge-technology intensive growth, and promote the green transformation of the industry and the green economic development of regions [2]. Logistics is an important part of the producer services industry which is closely connected with the manufacturing industry [3]. Since the State Council listed the interactive development of the manufacturing and logistics industries as one of the “Nine Major Projects” in 2009, the two industries have gradually presented a pattern of integrated development, and their synergistic agglomeration has become an important stage in the evolution of future industrial integration and green transformation and upgrading and has become a potential factor that may influence the increase of regional green economic efficiency.

Researching on the status quo of the synergistic agglomeration level of the manufacturing and logistics industries and GEE in the region, exploring the influencing factors of GEE, analyzing the influencing mechanism of

the two industries’ synergistic agglomeration on GEE, and investigating regional heterogeneity can provide a clear image of the direction of optimizing and upgrading industrial structure transformation by synergistic agglomeration and contribute to the green upgrading of the two industries as well as the sustainable development of the region.

1.2. Literature Review

1.2.1. Studies on the Synergistic Agglomeration of Manufacturing and Logistics Industries. Synergistic industrial agglomeration plays a significant role in promoting industrial integration as well as regional economic development. Collaborative development of the manufacturing and logistics industries is required in order to improve the competitiveness of the manufacturing industry [4], and the synergistic agglomeration of the two industries is the main manifestation of coordinated linkage and integrated development of the two industries [5].

In terms of synergistic agglomeration status, the research findings on the synergistic agglomeration status of the two industries can be summarized from three dimensions: synergistic agglomeration mechanism dimension, time dimension, and space dimension. Specifically, we have (1) studies on the mechanism of collaborative agglomeration between the two industries. Zhan et al. [6], Zhao and Chen [7], and Lu [8] believe that manufacturing and producer services can spur each other, and the agglomeration of manufacturing affects the synergistic amalgamation of the two. Qi [9], Zhou [10], and Yan [3] all demonstrate that the logistics industry is a spin-off from the manufacturing industry, and the coordinated development of the two can save costs, add value, and improve efficiency for the latter. Some scholars also discussed that the degree of agglomeration of different industries within the two industries is different; for example, Zhu et al. studied the agglomeration patterns of the manufacturing and logistics industries and found that the agglomeration level of resource-intensive industries increased significantly [11]. In many of these studies, logistics is regarded as a subindustry of producer services or an industry separate from manufacturing, but studies taking the logistics industry as an independent industry and analysing the mechanism of synergistic agglomeration between logistics and manufacturing industries are limited. (2) The degree of collaborative agglomeration changes with time. For example, Tang et al. studied the collaborative agglomeration level of the two industries in the new land-sea corridor in western China and found that its level declined first and then rebounded, and the collaborative agglomeration level was affected by government intervention, city scale, human capital, economic development, and other factors [12]. (3) The level of collaborative agglomeration in different regions is different; for example, Jin made regional comparisons of the degree of agglomeration of two industries, i.e., manufacturing and producer services, and found that the synergistic level is higher in large and medium-sized cities and economically developed regions [13]. Zhang and

Wu, through empirical analysis, found that the collaborative agglomeration level of the logistics industry and the manufacturing industry in China's provinces showed a spatial evolution pattern of decreasing gradient from east to west [14].

Scholars generally agree that modern industrial integration is not only the amalgamation of labour and geographical location but also the integration of knowledge, resources, technology, and information. The agglomeration status of the two industries presents regional heterogeneity and changes with time, but there is no uniform conclusion on the manifestation form of regional heterogeneity in academia.

In terms of the research method, quantitative analysis is more frequently used. By constructing an input-output index system, researchers use models such as grey correlation, data envelopment, and the location entropy method [15–18] to measure and analyze the correlation between the manufacturing and producer services industries. Most scholars believe that the manufacturing industry plays a strong driving role in the collaborative integration of the two industries, and logistics, now recategorized to be a part of the producer services industry, plays an obvious role in enhancing the value chain.

1.2.2. Studies on GEE. The key point of green economy is that economic development should be coordinated with green development. Economic growth should not be at the cost of the environment, and environmental protection should not be at the cost of economic slowdown. The analysis of GEE in academia is mainly based on empirical research, and the research content can be mainly divided into two aspects:

- (1) The construction of the GEE measurement index. Methods used by researchers mainly include entropy weight, factor analysis, and principal component analysis. [19]. The input index analyzed by scholars mainly includes the input of capital, manpower, and energy, and the output index mainly includes the expected economic benefits and unexpected environmental pollution. Table 1 gives an overview of indexes selected by scholars for measuring GEE of regional levels in recent years.

Table 1 shows that scholars are very unified in using regional GDP as the indicator for expected output. For unexpected output, the common indicator is the industrial emissions of “three wastes” or the comprehensive pollution index calculated by the entropy method based on the discharge of industrial wastes. It is a popular practice to integrate multiple inputs including capital, labor, and energy in the process of economic production into the evaluation of GEE. Its advantage is that it can take into account the substitution effect between various factors.

However, most literature focuses on the measurement of GEE at the provincial or industry level in China instead of the city level [27]. Taking the

provinces as decision-making units is too macro, thus it is not conducive to capturing micro information. Moreover, as the implementation of the “double carbon” target is accelerated, it is necessary to promote the formation of a new mode of green and low-carbon development, but in existing studies, carbon dioxide emissions are not often included in the unexpected output to measure the GEE from the perspective of cities.

- (2) Efficiency measurement method and analysis. As a common method to measure efficiency, the data envelopment analysis method is widely used in the measurement of GEE [29–32]. The DEA method is extensively used to measure the efficiency of technological progress by quantifying the relevant elements of environmental pollution and incorporating them into input indicators. With the improvement of the DEA method, methods to measure the efficiency of green economy have also been developed. Researchers often use the SBM model to measure the GEE by incorporating energy input, capital, and labour input into the input index and adding quantitative indicators related to pollution into the unexpected output index to construct an input-output model [33–37]. Most of the research studies conclude that GEE still needs to be improved and there are regional differences. GEE is influenced by various factors, which mainly include government intervention, human capital, environmental regulation, and technological innovation.
- (3) Influencing factors of GEE. Research on the influencing factors of GEE is abundant. Scholars mainly explore the influencing factors from two perspectives. The first is the core influencing factor related to their research studies. For example, Jiang and Jiang [38], Zeng and Xiao [39], and Guan et al. [40] focused on the impact of digital economy on GEE; Zhang et al. [26], Zhou and Gu [22], Li et al. [25], and Roumei and Deng [41] studied the influence of factor resources such as labor force, land, and infrastructure on GEE; Zhang and Tu [24], Zhang and Guo [42], and Ren et al. [43] focused on the influence of industrial agglomeration such as manufacturing and service industries' agglomeration on GEE. The second is the environmental factors. The main content of PEST analysis is that the external environment is mainly composed of four parts: political, economic, social, and technological. Scholars generally select government intervention, economic environment, social development, talent level, and foreign investment environment as macro environmental factors influencing GEE, which is also consistent with PEST theory.

1.2.3. Studies on the Impact of Synergistic Industrial Agglomeration on GEE. Research studies on the relationship between synergistic industry agglomeration and GEE can be divided into three main aspects: first, the agglomeration

TABLE 1: Selected input and output indexes in the existing articles.

Input indexes	Expected output	Unexpected output	Author and year
Total energy consumption Capital stock Number of employed population	Regional GDP	Total industrial pollution (calculated from the discharge of three industrial wastes using the entropy method)	Wang et al. 2022 [19]
Number of employed population Capital stock Electricity consumption of the whole society	Regional GDP	Total industrial pollution (calculated from the discharge of three industrial wastes using the entropy method)	Cai and Xu, 2022 [20]
Number of employed population Capital stock Power consumption	Regional GDP	Industrial emissions of “three wastes”	Cai et al. 2022 [21]
Construction land area Electricity consumption of the whole society Number of employed population Capital stock	Regional GDP	Industrial emissions of “three wastes”	Zhou and Gu, 2022 [22]
Total energy consumption Capital stock Number of nonagricultural employed population	Regional nonagricultural GDP	Industrial emissions of “three wastes” CO ₂ emission	Lin, 2021 [23]
Number of employed population Capital stock Electricity consumption of the whole society	Regional GDP	Industrial emissions of “three wastes”	Zhang and Tu, 2021 [24]
Number of employed population Capital stock Power consumption	Regional GDP	Industrial emissions of “three wastes”	Li et al. 2021 [25]
Number of employed population Capital stock Total energy consumption	Regional GDP	Chemical oxygen deemand SO ₂ emission Production of industrial solids	Zhang et al. 2020 [26]
Capital stock Quantity of labour force Total energy consumption	Regional GDP	Industrial emissions of “three wastes”	Lin and Tan, 2019 [27]
Investment in fixed assets Number of employed population Electricity consumption of the whole society	Regional GDP	Concentration index of PM2.5 & PM10 industrial emissions of “three wastes”	Zhu et al. 2018 [28]

provides opportunity for the sharing of all kinds of resources, promotes the formation of scale economies, reduces costs, and improves efficiency of productivity, so it is conducive to economic growth and sustainable utilization of resources. For example, Wu and Yang believe that the synergistic agglomeration of manufacturing and producer services industries can promote the high-quality development of regions and cities [44]. Zhang et al. analyzed the same phenomenon in eastern coastal areas and found that it has a continuous role in driving the regional green economy development [45]. Second, the coordinated industrial agglomeration leads to intensive market transactions, which

not only brings pressure to the construction and use of infrastructure but also creates a burden for the environment. For example, Wu argued that in the eastern part of China, the synergistic agglomeration of services and strategic industries inhibited economic growth [46]. Third, there are differences in natural resources and economic development in different regions, so the impact of industrial agglomeration patterns on the environment is different. Also, the relationship between them may be nonlinear. For example, Zhao et al. believe that the aggregation of scientific and technological talents in certain regions has a threshold effect on the impact of industrial synergistic agglomeration on

high-quality economic development [47]. Fang et al. believe that such agglomeration needs technological innovation as an intermediary variable to promote sustainable economic development [48]. Ma et al. believe that the agglomeration will inhibit high-quality economic development in the initial stage and that its impact will turn from negative to positive when it reaches a certain threshold [49]. Feng et al. investigated the industrial agglomeration and green development of 285 cities in China and found that the impact of such consolidation on green development was nonlinear and the spillover effect was greater than the direct effect [50]. The academic consensus is that synergistic industrial agglomerations have an impact on green development, and it is vitally important to study the impact in order to promote sustainable development, but there is no unified conclusion on the impact mechanism.

1.2.4. Studies on the Impact of Synergistic Agglomeration of Manufacturing and Logistics Industries on Green Economy Efficiency. There are limited studies on the relationship of the synergistic industrial agglomeration of the two sectoral groups, i.e., manufacturing and logistics, on GEE. Liu studied the impact of the collaborative agglomeration of the two on high-quality economic development [51]. Relevant statements about green and sustainable development are included in his description of high-quality economic development, but he did not explore them in depth. Yan and Wang studied the impact of professional and collaborative agglomeration of the two on regional economic growth and demonstrated that the agglomeration development of the two industries is not only an important means to promote the deep integration of the two, but it is also an important measure to promote economic growth and supply-side structural reform [52]. The synergistic agglomeration of the two industries has a relatively large impact on regional economic growth and a significant positive spillover effect on other regions. However, this research did not discuss the influence of the agglomeration of the two industries on green development either.

The existing studies have laid a solid foundation for improving awareness of the impact of industrial collaborative agglomeration on GEE, building the synergistic relationship between the two industries, constructing the evaluation index system for GEE, and have also provided an important reference for exploring the influencing factors of GEE, as well as selecting the method to calculate GEE. However, there are still problems:

- (1) There are many studies on the collaborative agglomeration of manufacturing and producer services, but few studies are on the collaborative agglomeration of logistics and manufacturing. As an important separate component of the manufacturing industry, the logistics industry can return value and embed a new value chain for the former through agglomeration. Therefore, it is necessary to explore the synergistic agglomeration level between the logistics industry and the manufacturing industry and the influence mechanism of this level on sustainable

economic efficiency. Also, with the rapid development of the economy, the level of professional and collaborative agglomeration of industries changes rapidly. Putting the research period in recent years is also conducive to observing the spatial and temporal evolution of the collaborative agglomeration level of the two industries.

- (2) The decision-making units of the existing studies are mostly provinces in China, and the research results are relatively macroscopic. The spatial differences of economic development in China are remarkable, which are not only reflected in the provinces, but they are also reflected in the regions and cities. Paying attention to the GEE of economic development hotspots (such as the YRD region) is conducive to seeking sustainable development strategies and improving GEE according to local conditions.
- (3) With the acceleration of the implementation of the “double carbon” target, green and low-carbon development transition is imminent. However, in the existing studies, carbon dioxide emissions are not often included in the unexpected output to measure urban GEE.
- (4) The sharing of resources, information, knowledge, technology, and other elements formed in the collaborative agglomeration of industries may bring agglomeration advantages and promote the green and high-quality development of the economy. However, the collaborative agglomeration of industries may also lead to the waste of resources and the aggravation of pollution, which is not conducive to the improvement of the GEE. At present, there is no unified conclusion on the influence mechanism of industrial collaborative agglomeration on GEE; thus, further research is needed. Also, since the synergistic agglomeration of the logistics and manufacturing industries has a relatively large impact on regional economic growth and since green and sustainable development are important components of high-quality economic growth, it is necessary to explore the relationship between synergistic agglomeration of the manufacturing and logistics industries and green economy efficiency.

In this research, under the guidance of the “double carbon” target, carbon dioxide emissions are included in the unexpected output, and the superefficiency SBM model and Malmquist index model are used to calculate the GEE of 41 cities in the YRD region. Then, the location entropy method is used to calculate the agglomeration level of the manufacturing and logistics industries and the synergistic agglomeration level of the two in 41 cities. Moreover, with the GEE calculated by super-SBM used as the dependent variable, the professional and synergistic agglomeration level of the manufacturing and logistics industries used as the core independent variable, and other environmental factors used as control variables, the Tobit model is used to calculate the influencing factors of urban GEE of the region. Finally,

based on the empirical analysis, corresponding policy suggestions are put forward. The research framework is shown in Figure 2. The contribution of this research is mainly in three aspects:

- (1) Theoretically, taking the collaborative agglomeration of manufacturing and logistics industries as the breakthrough point, this research jumps out of the discussion paradigm of “collaborative agglomeration of producer services and manufacturing industries” as the independent variables in the existing research. The research object is more focused, which enriches the perspective and content of the research on industrial collaborative agglomeration to promote GEE. Also, responding to the call of energy saving and carbon reduction policies, CO₂ emission is included in the unexpected output index used to evaluate urban GEE, and by doing this, the evaluation index model of urban GEE can be enriched.
- (2) Methodologically, on the one hand, the static and dynamic GEE and its influencing factors of 41 cities are calculated through the consistent use of the SBM–Malmquist–Tobit model methods. It is of innovative and practical significance since the professional agglomeration of the manufacturing and logistics industries and the collaborative agglomeration of the two industries measured by the location entropy method are taken as explanatory variables so as to discuss their influences on the GEE. On the other hand, ArcGIS geographic information system software is used to draw a colored map of the industrial agglomeration level of 41 cities in the YRD region, which directly reflects the industrial agglomeration level, and lays a foundation for deducing the influence of the industrial collaborative agglomeration level on GEE.
- (3) Practically, the discussion of this research is of practical value for optimizing the green transformation of industrial structure and agglomeration and is of practical significance to local governments in the YRD region and the central government of China to formulate corresponding policies to guide the route of industry transformation, technology progress, and thus the development of green economy.

2. Materials and Methods

2.1. Model Construction

2.1.1. Superefficiency SBM Model. The radial data envelopment analysis method (DEA), first proposed by Charnes et al. [53], has been widely used in the academic field. This method is suitable for measuring the efficiency of multiple DMUs (decision-making units) with the same input and output indexes. However, this method cannot consider the possible effects of undesired output and slack variables. Tone [54] proposed the SBM model that can avoid the above-mentioned problems when calculating, but it is easy to have

multiple DMUs with effective measurement results, which is not conducive to the efficiency comparison. Therefore, he improved the model and proposed the superefficiency SBM model. In this research, the nonoriented superefficiency SBM model is selected, and its basic expression is as follows:

$$\min \rho^* = \frac{1/m \sum_{i=1}^m x' / x_{ik}}{1/r + p(\sum_{s=1}^r y^d y_{sk}^d + \sum_{q=1}^{r_2} y^u y_{qk}^u)},$$

$$s.t. \begin{cases} x' \geq \sum_{j=1, \neq k}^n x_{ij} \lambda_j; \\ y^d \leq \sum_{j=1, \neq k}^n y_{sj}^d \lambda_j; \\ y^d \geq \sum_{j=1, \neq k}^n y_{qj}^d \lambda_j; \\ x' \geq xk; \\ y^d \leq y_{d'}^k; \\ y^u \geq y_k^u; \\ \lambda_j \geq 0, i = 1, 2, \dots, m; j = 1, 2, \dots, n, j \neq 0, \\ s = 1, 2, \dots, r; q = 1, 2, \dots, p. \end{cases} \quad (1)$$

In equation (1), ρ^* represents the GEE value of 41 cities in the YRD region, n represents the number of DMUs, i.e., 41 cities, m represents the number of input indicators, r and p represent the number of expected and unexpected output indicators, x is the element of the corresponding input matrix, y^d and y^u represent the elements of the corresponding expected and unexpected output matrices, and λ is the weight vector. When $\rho^* \geq 1$, it means that the GEE of the city or region is effective and when $\rho^* < 1$, it means that the green economy input of the city or region does not bring the expected output.

2.1.2. Malmquist Index Model. In order to explore the dynamic efficiency changes of GEE of cities in the YRD region, this research uses the Malmquist index model to calculate the annual and regional changes. This index is mainly composed of technical efficiency (effch) and technological progress efficiency (techch), among which technical efficiency can be decomposed into pure technical efficiency (pech) and scale efficiency (sech). Using this index, the total factor productivity of green economy (tfpch) of cities in the YRD region can be measured. The following formulas give the mathematical expression of the Malmquist index model:

$$tfpch = \text{effch} \times \text{techch} = (\text{pech} \times \text{sech}) \times \text{techch}. \quad (2)$$

Total factor productivity values greater than 1, equal to 1, and less than 1 indicate the GEE improvement, unchanged, and decline, respectively.

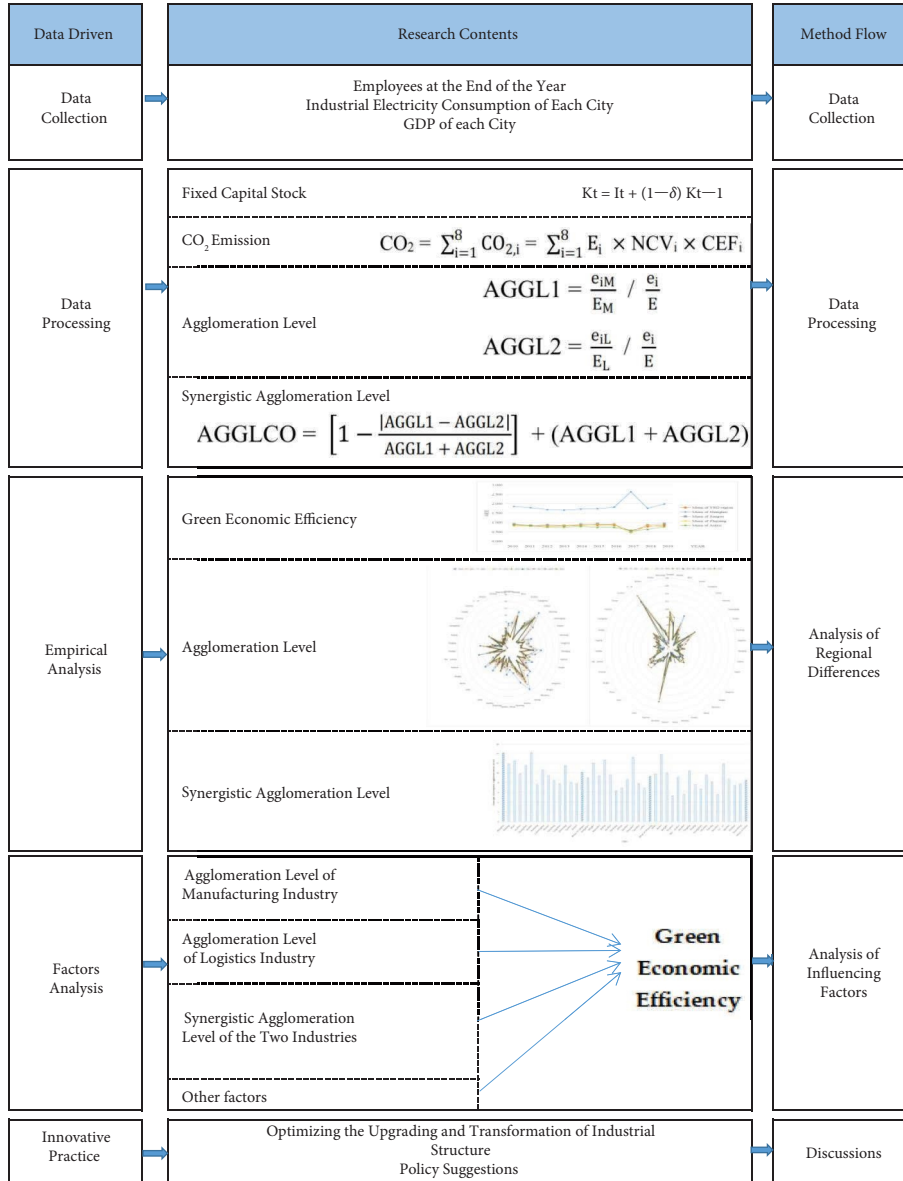


FIGURE 2: Research process.

2.1.3. *Location Entropy Method.* Methods that are frequently used to measure the level of industrial agglomeration mainly include the location entropy method, Herfindahl–Hirschman index, DO index, EG index, and space Gini coefficient. This research draws on the practice of Chen and Chen [55] and uses the location entropy method to, respectively, measure the agglomeration level of the manufacturing and logistics industries, as well as the synergistic agglomeration level of the two industries. The specific model is

$$\begin{aligned}
 AGGL1 &= \frac{e_{iM}/E_M}{e_i/E}, \\
 AGGL2 &= \frac{e_{iL}/E_L}{e_i/E}.
 \end{aligned}
 \tag{3}$$

AGGL1 and AGGL2 represent the agglomeration level of manufacturing industry and logistics industry, respectively. e_{iM} and e_{iL} represent the number of employees of the two industries of each city in each year, respectively, and E_M and E_L represent the number of corresponding employees in China in each year, respectively. e_i represents the number of employees in all industries of each city in each year. E represents the number of employees in all industries of China in each year. With reference to Meng et al. [2], a calculation model for synergistic agglomeration of the two industries is constructed as follows, in which AGGLCO represents the synergistic agglomeration level of the two industries, and AGGL1 and AGGL2 are the professional agglomeration levels calculated in equation (3).

$$\text{AGGLCO} = \left[1 - \frac{|\text{AGGL1} - \text{AGGL2}|}{\text{AGGL1} + \text{AGGL2}} \right] + (\text{AGGL1} + \text{AGGL2}). \quad (4)$$

2.1.4. Tobit Regression. The Tobit model was proposed by Tobin in 1958 [56], which is mainly applied to regression analysis where the value of explained variables is restricted or truncated. In order to avoid the possible estimation bias caused by the ordinary least squares method, this research adopts the random effects panel Tobit model to measure the influencing factors of the GEE of cities in the YRD region. The expression of the Tobit regression model is

$$Y_{it} = \alpha + \beta X_{it} + \mu_{it}, \quad (5)$$

$$Y_{it} = \begin{cases} 0, & Y_{it} \leq 0, \\ Y_{it}, & Y_{it} > 0. \end{cases}$$

In equation (5), i represents city, t represents year, Y_{it} is the GEE value of the i^{th} city in the year t calculated using the superefficiency SBM model, X_{it} represents each explanatory variable, α is the constant term, β is the regression coefficient vector, and μ is the random interference term.

2.2. Index Selection and Data Sources

2.2.1. Evaluation Index of GEE. The choice of input and output indicators should take into account not only the availability of data but also the objective needs of evaluation. According to Douglas production function, labour and capital inputs are the basic elements of input factors. Therefore, capital input is expressed by fixed capital stock of each city, and labour input is expressed by employees at the end of each year. Among them, the fixed capital stock cannot be directly obtained from the statistical data; thus, the perpetual inventory method is used to estimate the fixed capital stock over the past years. The calculation formula of capital stock is

$$K_t = I_t + (1 - \delta)K_{t-1}, \quad (6)$$

where K_t represents the capital stock in year t , K_{t-1} represents the capital stock in year $t-1$, I_t represents the investment in year t , and δ represents the depreciation rate in year t . We refer to the research of Zhang et al. [57], $\delta = 9.6\%$ and $I_t = I_0 / (\delta + g)$. I_0 represents the investment in fixed assets in 2010, and g is the aggregate average growth rate of new fixed assets in the whole society. In addition, considering the availability of data and with reference to Wu and Wu [58], the industrial electricity consumption of each city is used to represent the energy input. The GDP of each city is selected as the expected output to reflect the development level. The comprehensive pollution index and CO_2 emission of each city are selected as the undesirable output to reflect the environmental pollution status. Among them, industrial wastewater discharge, industrial sulfur dioxide emission, and general industrial solid waste production are selected as the basic indicators, and the entropy value method is used to

calculate the comprehensive pollution index of three main industrial wastes in each city. The relevant data mentioned previously are collected from China Urban Statistical Yearbook. The calculation of CO_2 emission includes three aspects: combustion consumption of various energy sources, average low calorific value of various energy sources, and carbon dioxide emission factors of various energy sources. The calculation method is as follows:

$$\text{CO}_2 = \sum_{i=1}^8 \text{CO}_{2,i} = \sum_{i=1}^8 E_i \times \text{NCV}_i \times \text{CEF}_i. \quad (7)$$

In equation (6), E_i represents the consumption of each energy ("Each energy" includes coal, coke, crude oil, gasoline, kerosene, diesel oil, fuel oil, and natural gas. Their NCV values (kJ/kg) are 20908, 28435, 41816, 43070, 43070, 42652, 41816, and 38931, respectively. Their CEF values (kg/TJ) are 95977, 105966, 73333, 71500, 74067, 77367, and 56100, respectively. Data are obtained from IPCC (United Nations Intergovernmental Panel on Climate Change) (2016)), NCV_i represents the average low calorific value of each energy, and CEF_i represents the CO_2 emission factor of each energy. Relevant data are collected from China Energy Statistical Yearbook, China Industrial Statistical Yearbook, and China Environment Statistical Yearbook, the method can be used to calculate the overall CO_2 emissions of provinces in China, and then referring to the estimation method used by Ding et al. [59], the ratio of urban GDP to provincial GDP is used to estimate CO_2 emissions for each city. The evaluation index of GEE is shown in Table 2.

2.2.2. Influencing Factor Index Selection. The efficiency value of urban green economy measured by the superefficiency SBM model is used as the dependent variable, and the agglomeration levels of the manufacturing industry (AGGL1) and the logistics industry (AGGL2), as well as the synergistic agglomeration levels of the two industries calculated by the location entropy method, are taken as the core independent variables (AGGLCO). Combined with political, economic, and social factors, the control variables of external influencing factors are selected as follows:

(1) *Government Intervention (GOV)*. Government intervention is an important means for the government to carry out macrocontrol, aiming to promote the effective operation of the economy and the positive development of the industry. The typical method of regulation and control is fiscal expenditure, which is represented by the general public budget expenditure of each city; (2) *social development level (SOCIAL)*: the urbanization rate is one of the important indicators of Chinese urban social development, which is represented by the ratio of the permanent urban resident population to the total urban resident population including nonpermanent city dwellers such as people living in rural places and migrant workers at the end of the year; (3) *industrial structure (INSTRU)*: represented by the ratio of the output value of the secondary industry to the local GDP to reflect the industrial structure relationship of the city; (4)

TABLE 2: Evaluation index of GEE.

Types	Measure dimension	Measure index	Symbol
Input	Financial capital	Fixed capital stock	X1
	Labour capital	Employees at the end of the year	X2
	Energy	Industrial electricity consumption of each city	X3
Output	Expected output	GDP of each city	Y1
	Unexpected output	Comprehensive pollution index of three main industrial wastes	Z1
		CO ₂ emission	Z2

human resource level (EDU): the professional and comprehensive ability of human resources may have a crucial impact on industrial upgrading and transformation and urban green development, and this is represented by the number of university students per 10,000 people; (5) opening to the outside world (FOREIGN): the opening to the outside world can reflect the overall development level of a city, and this is represented by the actual amount of foreign investment in each year (Table 3). The missing data have been interpolated by using the equivalent mean imputation method. The construction model is as follows:

$$\begin{aligned}
 GEE_{it} = & C + \alpha_1 AGGL1_{it} + \alpha_2 AGGL2_{it} + \alpha_3 AGGLCO_{it} \\
 & + \alpha_4 InGOV_{it} + \alpha_5 SOCIAL_{it} + \alpha_6 INSTRU_{it} \\
 & + \alpha_7 InEDU_{it} + \alpha_8 InFOREIGN_{it} + \varepsilon_{it}.
 \end{aligned} \tag{8}$$

Of which, GEE_{it} represents the urban green economy efficiency value of the i^{th} city in the t year measured by the superefficiency SBM model, C is the intercept term, $\alpha_1-\alpha_8$ are regression coefficients of explanatory variables, and ε_{it} is the random error term. The units of general public budget expenditure of each city have been converted to US dollars at the latest exchange rate. To avoid heteroscedasticity, logarithms of the general public budget expenditure of each city, the actual amount of foreign investment, and the number of university students per 10,000 people were taken.

3. Results

3.1. *Static Analysis.* Data are imported into MATLAB software, and the superefficiency SBM model containing undesired output is used to calculate the GEE of 41 cities in the YRD region. The research period is from 2010 to 2019. The results are as follows.

3.1.1. *Current Status of GEE.* In order to compare the GEE of 41 cities (with Shanghai municipality taken as a city) and four provinces (with Shanghai municipality taken as a province) in the YRD region, the efficiency values of 41 cities and four provinces are calculated, respectively (Table 4).

From the perspective of 41 cities, from 2010 to 2019, the average GEEs of Shanghai, Suzhou, and Wuxi in Jiangsu Province and Huangshan, Chizhou, and Bozhou in Anhui Province are greater than 1, indicating that the GEE of these six cities has been effective and the ecological environment and economy have developed in harmony. Among them, during 2016–2019, Suzhou’s carbon emissions per ten thousand yuan GDP decreased by 23.3%; since Wuxi City

took the lead in establishing an international ecological urban agglomeration in 2013, it has been adhering to the green economic development path of ecological priority and also to the green development concept and therefore has become one of the first demonstration cities of ecological civilization construction in China; Huangshan City is located at the foot of Huangshan Mountain, a world cultural and natural heritage, and Chizhou City has the national 5A Jiuhua Mountain scenic spot, thus thanks to the advantaged natural resources and tourism city development strategy, these two cities have better green economic development ability; Bozhou City has greatly increased forestation since 2013, and the forest coverage rate has repeatedly set new highs.

However, the average GEEs of other cities are lower than 1, among which 22 cities have an efficiency value lower than 0.8, and 5 cities are between 0.3 and 0.6, indicating that the overall GEE of the YRD region is less than satisfactory. From the perspective of the four provinces, the average GEE of Jiangsu, Zhejiang, and Anhui is lower than 1, and the ranking in this respect is Shanghai > Jiangsu > Zhejiang > Anhui. Shanghai’s economic development level is higher, the technological innovation ability is good, and the traditional extensive production pattern is gradually transforming to an intensive pattern. Owing to its high-end talent pool and more advanced industrial base, Shanghai has increased digital empowerment in industry transformation and has gradually built a modern industrial system and infrastructure, providing a more favourable condition for promoting green development. The average efficiency of Anhui Province however is lagging behind. The first reason may be that the dependence on traditional manufacturing leads to a long transformation cycle; the second reason perhaps is that resource-based cities such as Huainan are facing the dilemma of resource exhaustion, and the past economic growth is at the cost of the environment resulting in resource depletion, which is difficult to make up in a short term.

3.1.2. *Time Evolution of GEE.* Figure 3 shows the time evolution of the GEE of the four provinces from 2010 to 2019. Overall, the GEE shows a U-shaped change, and the efficiency values between Shanghai and the other three provinces show obvious differences. From 2010 to 2016, the overall GEE did not fluctuate much. In 2016–2017, the efficiency of Shanghai achieved a significant increase, but all the other provinces saw a decline, and the overall GEE of the four provinces and the YRD region was on a downward

TABLE 3: Influencing factors of the index system.

Types	Measure dimensions	Measure indexes	Symbols
Core explanatory variable	Industrial agglomeration level	Agglomeration level of the manufacturing industry	AGGL1
		Agglomeration level of the logistics industry	AGGL2
		Synergistic agglomeration level of manufacturing and logistics industries	AGGLCO
Other explanatory variable	Government intervention	General public budget expenditure of each city	<i>In</i> GOV
	Social development level	Urbanization rate	SOCIAL
	Industrial structure	Ratio of the output value of the secondary industry to local GDP	INSTRU
	Opening to the outside world	Actual amount of foreign investment	<i>In</i> FOREIGN
	Human resource level	Number of university students per 10,000 people	<i>In</i> EDU

TABLE 4: Annual mean value and ranking of GEE of 41 cities in the YRD region in 2010–2019.

City (year)	2010	2019	Annual mean	Rank
Shanghai	1.8600	1.9836	1.8633	1
Nanjing	0.6423	1.0762	0.8009	19
Wuxi	1.0046	1.2195	1.0611	5
Xuzhou	0.7387	1.0655	0.7287	24
Changzhou	1.0610	1.0460	0.9689	10
Suzhou	1.4385	0.8170	1.0849	4
Nantong	0.9320	0.7776	0.8591	15
Lianyungang	0.6701	0.7333	0.6254	34
Huaian	0.5499	1.0361	0.6808	31
Yancheng	1.0688	1.0000	0.9722	9
Yangzhou	1.0000	0.9564	0.8704	14
Zhenjiang	0.8384	1.0325	0.8893	13
Taizhou	1.0533	0.6806	0.8523	16
Suqian	0.9413	0.7145	0.6892	29
Hangzhou	0.6424	0.7473	0.7282	25
Ningbo	0.7928	1.0998	0.8325	18
Wenzhou	1.0000	0.7716	0.9066	11
Jiaxing	0.5750	0.6416	0.6049	36
Huzhou	0.5662	0.6202	0.5790	37
Shaoxing	1.0258	0.6134	0.7289	23
Jinhua	1.0260	0.7092	0.9051	12
Quzhou	0.6504	0.6011	0.5513	38
Zhoushan	0.6449	1.0081	0.9981	7
Taizhou	1.0000	0.7251	0.8428	17
Lishui	1.0000	1.0258	0.9833	8
Hefei	0.7944	1.0267	0.7668	21
Wuhu	0.6643	0.6659	0.6126	35
Bengbu	0.5902	1.0481	0.7037	28
Huainan	0.4041	0.5514	0.4490	41
Ma'anshan	0.6896	0.4983	0.5094	40
Huaibei	0.5364	0.6178	0.5327	39
Tongling	1.0909	0.4725	0.7159	27
Anqing	1.0000	0.7329	0.7163	26
Huangshan	1.1771	1.2830	1.2179	2
Chuzhou	0.9381	0.8067	0.7513	22
Fuyang	0.6434	0.7232	0.7955	20
Suzhou	0.5913	0.7537	0.6552	32
Lu'an	1.0003	0.4815	0.6854	30
Bozhou	1.5088	1.0639	1.0460	6
Chizhou	1.0624	1.0766	1.1064	3
Xuancheng	1.1085	0.5962	0.6322	33
Mean of Shanghai	—	—	1.8633	—
Mean of Jiangsu	—	—	0.8526	—
Mean of Zhejiang	—	—	0.7874	—
Mean of Anhui	—	—	0.7435	—

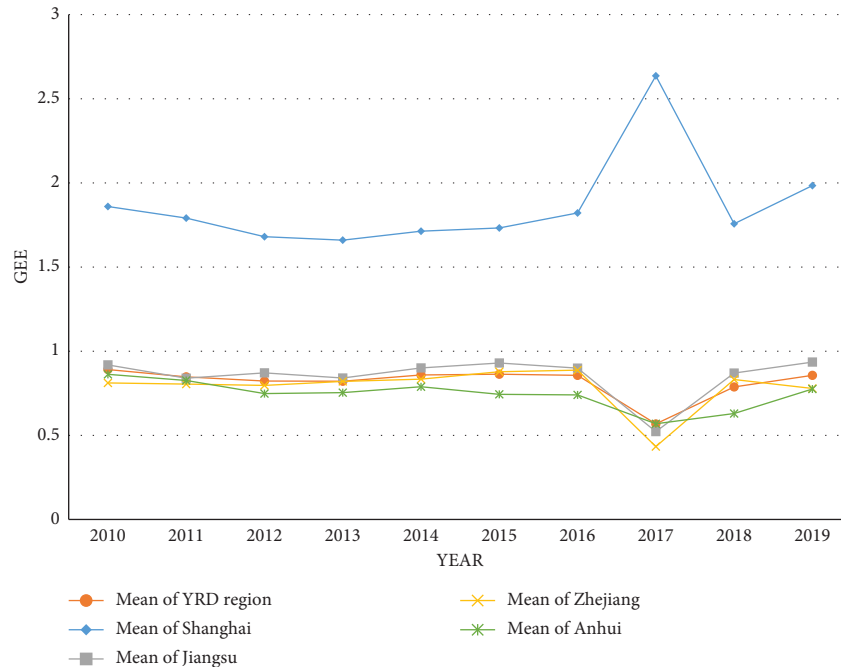


FIGURE 3: Average GEE of four provinces and the whole YRD region in 2010–2019.

trajectory. From 2017 to 2018, the green economic efficiency of Jiangsu, Zhejiang, and Anhui provinces and the YRD region as a whole saw an upward trend, but that of Shanghai showed a pullback. Then in 2018–2019, slight increase can be seen for Shanghai, Jiangsu, Anhui, and the whole YRD region.

3.1.3. Spatial Evolution of GEE. In 2010, the number of cities with effective green economy in the YRD region was 19, and the number reduced to 16 in 2019. During the research period, the GEE of cities changed significantly. From the perspective of the mean value during 2010–2019, effective cities are mainly located in Shanghai, Jiangsu, and Anhui; in 2010, the effective cities generally showed an average distribution in four provinces, while in 2019, the effective cities were mainly concentrated in Shanghai and in cities of Jiangsu Province (Figure 4). In 2010, 7 cities had an efficiency value below 0.6, while in 2019, the number decreased to 5. It can be seen that the number of cities in the medium and the low efficiency level in 2019 decreased compared with that of 2010.

3.2. Dynamic Analysis

3.2.1. On the Yearly Basis. In order to measure the change of urban GEE in the YRD region, this research uses DEAP 2.1 software to measure the Malmquist index of 41 cities and its decomposition. The results are shown in Table 5. From 2010 to 2019, except for the mean value of technological progress efficiency, all the average values of the index were less than 1,

indicating that the GEE of cities in the YRD region showed an overall downward trend, and the average annual total factor productivity declined by 1.5%, which was not a significant drop. The average value of the index of technological progress efficiency was 1.005. From 2010 to 2017, it showed an overall upward trend except for a slight decline from 2013 to 2014. Driven by the improvement of technological progress efficiency, the value of GEE from 2010 to 2017 was also mostly greater than 1. From 2017 to 2019, the efficiency of technological progress fell sharply, leading to a synchronous decline in the GEE. It can be seen that technological progress is the most important factor affecting the urban GEE in the YRD region. Both scale efficiency and pure technical efficiency underwent fluctuating changes but showed no significant impact on the overall efficiency.

3.2.2. Based on Location. From 2010 to 2019, the average Malmquist index of GEE in Shanghai, Jiangsu, Zhejiang, and Anhui was 1.083, 0.982, 0.982, and 0.992, respectively. Among the four provinces, only Shanghai achieved an efficiency improvement of 8.3%. In terms of index decomposition, the technological progress indexes of Shanghai, Jiangsu, and Zhejiang were all greater than or equal to 1. Among them, the technological progress efficiency of Shanghai increased by 15.1%, which greatly promoted the improvement of regional GEE. This further indicates that technological progress is the biggest factor influencing the improvement of urban GEE in the YRD region. The scale efficiency of four provinces was less than 1, indicating that the efficiency of resource utilization needs to be improved (Table 6).

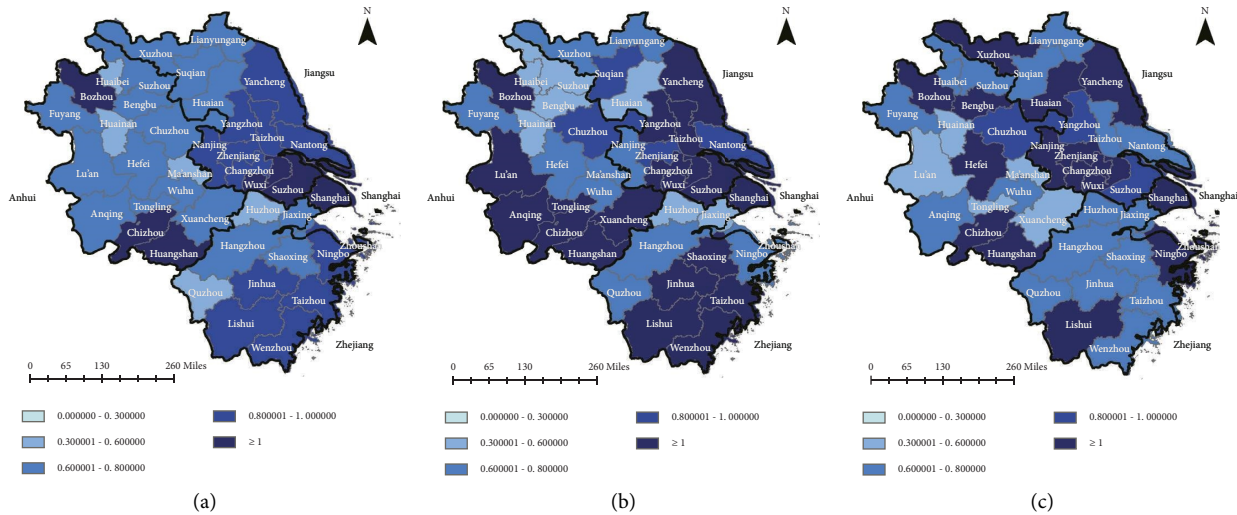


FIGURE 4: (a) The color map of the mean efficiency; (b) the color map of efficiency in 2010; (c) the color map of efficiency in 2019.

TABLE 5: Annual change of green economic efficiency in the YRD region in 2010–2019.

Years	effch	techch	pech	sech	tfpch
2010-2011	0.852	1.104	0.961	0.886	0.941
2011-2012	1.007	1.017	1.011	0.996	1.024
2012-2013	1.018	1.018	1.004	1.014	1.036
2013-2014	1.127	0.918	1.041	1.083	1.034
2014-2015	0.915	1.150	0.973	0.94	1.052
2015-2016	0.979	1.125	0.984	0.995	1.102
2016-2017	0.917	1.272	0.983	0.933	1.166
2017-2018	1.063	0.608	1.018	1.044	0.646
2018-2019	0.972	0.996	1.003	0.969	0.968
Mean	0.98	1.005	0.997	0.983	0.985

3.3. Industrial Agglomeration Level and Level of Industrial Synergy Agglomeration

3.3.1. Agglomeration Level of the Manufacturing Industry and the Logistics Industry. The location entropy method is used to calculate the industrial agglomeration level. The larger the resulting value, the higher the agglomeration level. It can be seen from Figure 5 that, on the whole, the manufacturing agglomeration level in Jiangsu Province is the highest, followed by Zhejiang, Shanghai, and Anhui. The agglomeration level of logistics industry in Shanghai is the highest, followed by Anhui and Jiangsu Provinces, and Zhejiang Province is the lowest in general. In terms of agglomeration trend, the manufacturing industry showed an initial trend of decline before rising slowly, while the improvement of the logistics industry was of a more volatile nature. At the city level, Wuxi, Suzhou, and Jiaxing have the highest level of manufacturing agglomeration, while Huainan, Huaibei, Huangshan, and Suzhou have the lowest. Shanghai, Zhoushan, and Lu'an have the highest agglomeration level of the logistics industry, while Nantong, Suqian, Shaoxing, and Taizhou have the lowest. Cities with a high level of manufacturing agglomeration are mainly located in Jiangsu and Zhejiang, while cities with a low level are mainly in

Anhui. The agglomeration level of the logistics industry in each city is not uniform (Figure 6).

3.3.2. Synergistic Agglomeration Level of the Manufacturing and Logistics Industries. In general, Shanghai has the highest level of synergistic agglomeration, followed by Jiangsu and Zhejiang, and Anhui has the lowest level (Figure 7). In terms of city scope, in addition to Shanghai, cities with a high level of synergistic agglomeration also include Suzhou, Jiaxing, Zhoushan, Wuhu, and Lu'an. These cities, especially Shanghai, Suzhou, Jiaxing, and Wuhu, have played a very positive role in driving the level of synergistic agglomeration of their surrounding cities. However, it can be seen from the analysis that the agglomeration level of a single industry is not necessarily high in cities with a high level of industrial synergistic agglomeration (ISA level).

3.4. Influencing Factors. Using EViews 8 software, the Tobit regression analysis method is used to calculate the relationship between the ISA level, other environmental factors, and GEE in the YRD region and its four provinces. The results can be seen in Table 7.

3.4.1. Influence of Industry Agglomeration and Synergistic Agglomeration. From the perspective of the whole YRD region, the coefficients of manufacturing industry agglomeration and logistics industry agglomeration and the ISA level of the two are all positive, and among them, the P value of collaborative agglomeration is significant at the 1% level ($P < 0.01$). This indicates that with the increase of the ISA level of the manufacturing and logistics industries in the YRD region, the GEE increased significantly.

From the perspective of four provinces, firstly, the situation of Anhui is consistent with that of the whole YRD region. Both the agglomeration levels of the two industries in Shanghai have a significant positive effect on GEE, whereas the synergistic agglomeration of the two industries has a

TABLE 6: Regional change of green economic efficiency in the YRD region in 2010–2019.

Cities	effch	techch	pech	sech	tfpch
Shanghai	0.941	1.151	1	0.941	1.083
Nanjing	0.971	1.014	0.997	0.974	0.985
Wuxi	0.981	0.977	0.982	0.999	0.958
Xuzhou	1.004	0.983	1.022	0.983	0.987
Changzhou	0.986	1.003	0.99	0.996	0.989
Suzhou	0.989	0.984	0.993	0.997	0.973
Nantong	0.997	0.996	1.016	0.981	0.993
Lianyungang	0.973	0.968	0.997	0.975	0.941
Huaian	0.979	0.997	0.997	0.983	0.977
Yancheng	0.959	0.977	0.997	0.962	0.937
Yangzhou	1.013	1.003	1.025	0.989	1.017
Zhenjiang	0.995	0.98	1.024	0.972	0.975
Taizhou	0.992	0.99	1.013	0.979	0.981
Suqian	0.98	0.974	1.001	0.979	0.955
Hangzhou	0.925	1.091	1	0.925	1.009
Ningbo	0.943	1.044	0.987	0.955	0.984
Wenzhou	0.953	1.087	1	0.953	1.035
Jiaxing	0.951	0.98	0.981	0.969	0.933
Huzhou	0.966	0.976	0.986	0.98	0.943
Shaoxing	0.944	1.027	0.98	0.963	0.97
Jinhua	0.938	0.967	0.967	0.97	0.907
Quzhou	0.996	0.972	1.001	0.995	0.968
Zhoushan	1.037	1.099	1.037	1	1.14
Taizhou	0.934	1.057	0.973	0.96	0.987
Lishui	0.952	0.972	0.955	0.996	0.925
Hefei	0.994	0.978	1	0.994	0.972
Wuhu	1.004	0.986	1.021	0.983	0.99
Bengbu	1.032	0.989	1.035	0.997	1.021
Huainan	0.968	1.032	0.97	0.998	0.999
Ma'anshan	1.054	0.986	1.044	1.009	1.039
Huaibei	1	1.014	0.993	1.006	1.014
Tongling	1.051	1.016	1.045	1.006	1.067
Anqing	0.969	0.99	0.981	0.988	0.96
Huangshan	0.991	1.025	1	0.991	1.016
Chuzhou	0.951	0.967	0.97	0.98	0.919
Fuyang	0.932	1.02	0.946	0.985	0.951
Suzhou	0.983	1.051	0.981	1.002	1.034
Lu'an	1.029	1.042	1.021	1.008	1.072
Bozhou	0.959	0.987	0.959	0.999	0.946
Chizhou	1	0.963	1.011	0.989	0.963
Xuancheng	0.989	0.923	0.997	0.992	0.914
Mean of Shanghai	0.941	1.151	1	0.941	1.083
Mean of Jiangsu	0.983	1.000	1.004	0.979	0.982
Mean of Zhejiang	0.958	1.025	0.988	0.970	0.982
Mean of Anhui	0.994	0.998	0.998	0.995	0.992
Mean	0.980	1.005	0.997	0.983	0.985

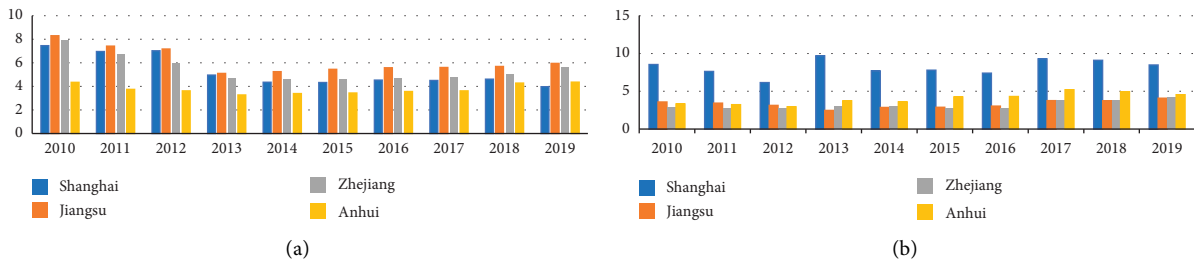


FIGURE 5: (a) The average agglomeration level of the manufacturing industry in 2010–2019 and (b) average agglomeration level of the logistics industry in 2010–2019.

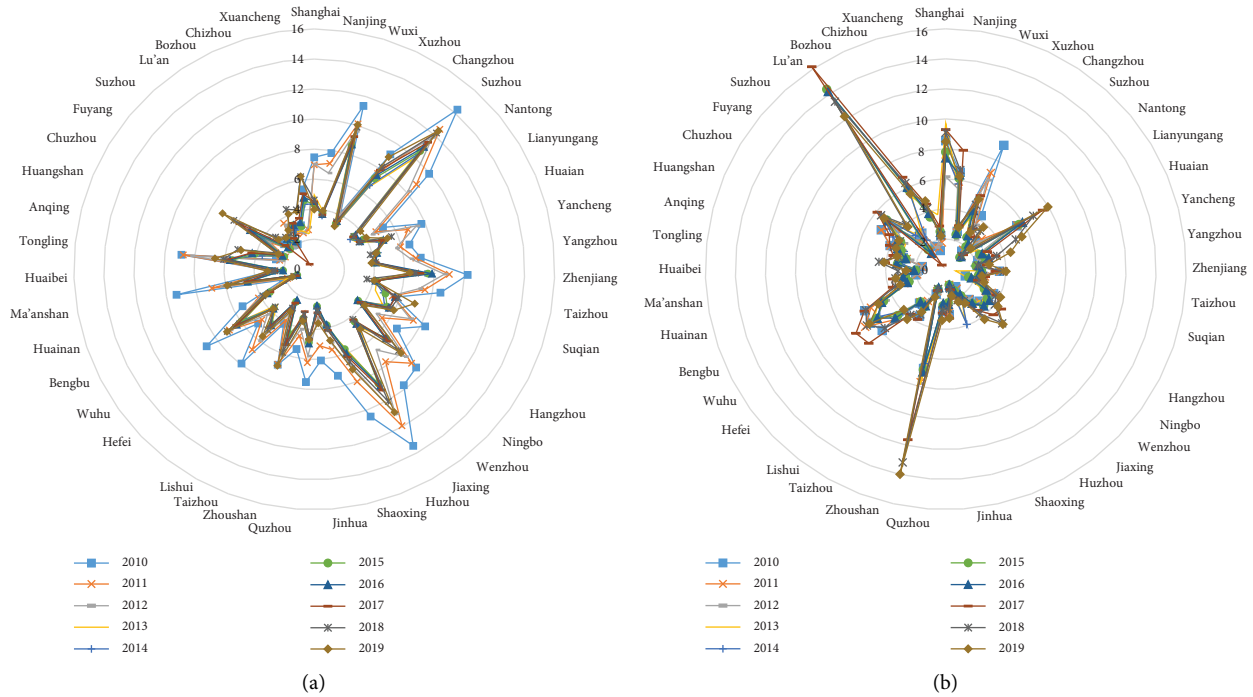


FIGURE 6: (a) The agglomeration level of the manufacturing industry and (b) agglomeration level of the logistics industry.

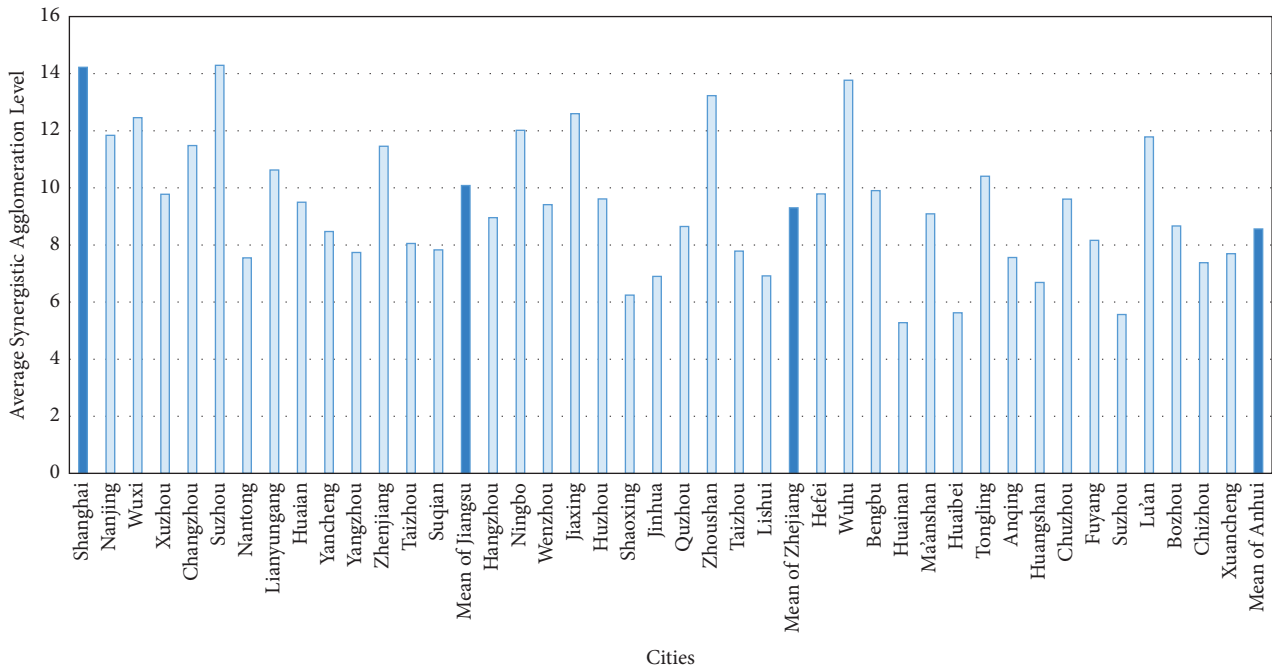


FIGURE 7: Mean of the synergistic agglomeration level of the two industries in 2010–2019.

negative but not significant effect on GEE. By comparing the calculation of the level of ISA in Figure 4, it can be found that the ISA level in Shanghai is relatively high, which is very likely to indicate that the level of synergistic agglomeration of the two industries in Shanghai has brought about “congestion effect.” For Jiangsu and Zhejiang, the agglomeration of the manufacturing industry has a negative effect

on GEE, while the agglomeration of the logistics industry and the synergistic agglomeration of the two industries have a positive effect on GEE, but these effects are not significant.

Overall, the impact of the synergistic agglomeration level of manufacturing and logistics industries on the four provinces and in the YRD region shows obvious regional heterogeneity. In a less developed province such as Anhui,

TABLE 7: Tobit regression results of the main influencing factors of GEE.

Terms	YRD region		Shanghai		Jiangsu		Zhejiang		Anhui	
	Co	Prob.	Co	Prob.	Co	Prob.	Co	Prob.	Co	Prob.
C	0.784	0.024	99.850	0.003	0.149	0.860	1.547	0.035	0.181	0.789
InGOV	0.045	0.127	-6.072	0.000	0.052	0.410	-0.046	0.417	0.107	0.067
SOCIAL	-0.001	0.507	-0.710	0.007	-0.011	0.023	0.002	0.759	-0.001	0.761
INSTRU	-0.008	0.006	-0.347	0.000	0.003	0.768	-0.004	0.642	-0.011	0.007
InEDU	0.005	0.812	1.867	0.000	0.009	0.853	-0.071	0.205	0.083	0.024
InFOREIGN	-0.032	0.087	3.743	0.000	0.034	0.576	0.013	0.718	-0.092	0.018
AGGL1	0.010	0.188	0.734	0.000	-0.005	0.674	-0.009	0.636	0.018	0.362
AGGL2	0.005	0.499	0.536	0.000	0.016	0.337	0.017	0.287	0.014	0.242
AGGLCO	0.016	0.002	-0.010	0.832	0.012	0.199	0.018	0.116	0.031	0.001

the improvement of the synergistic agglomeration level can still lead to green economy, whereas in a more developed region such as Shanghai, “congestion effect” is showing.

3.4.2. Influence of Other Influencing Factors. In the YRD region as a whole, the government’s intervention in Shanghai and Zhejiang has not played the role of promoting the efficiency of green economy. Too much fiscal investment may lead to low efficiency of capital utilization, resulting in diminishing marginal returns and consequently restricting the development of green economy. In the YRD region in general and Jiangsu Province in particular, the fiscal support provided by the government has promoted the GEE, but the promotion effect is not obvious. In Anhui, government intervention is significantly related to GEE positively. Therefore, it can be inferred that the more developed the region, the less dependent it is on financial support and the higher the requirement for the rationality of financial input; on the contrary, for less developed regions, financial support is still one of the powerful means to promote green development.

The higher the level of urbanization, the higher the requirements for infrastructure construction, which may provide more facilitation to regional development. In general, the level of urbanization promotes the GEE in Zhejiang, but the promoting effect is not significant. However, in the whole YRD region and the other three provinces, the larger the urban population, the more pollution and waste discharge from production and household activities, which restrict the improvement of the GEE. In Shanghai and Jiangsu, this situation is more serious.

In Jiangsu, the increase in the proportion of the secondary industry promotes the improvement of regional GEE; however, in the whole YRD region and other three provinces, the higher the proportion of the output value of the secondary industry in the total output value, the greater the environmental pressure it will bring in the production process, and this situation is particularly serious in the whole YRD region, Shanghai, and Anhui but less serious in Zhejiang. This is most likely because the majority components of the secondary industry have not entered the stage of high-quality and high-tech development, and the increase of output value is accompanied by environmental pollution

inhibiting GEE improvement; thus, adjustment of the industrial structure is imperative.

The education level of human resources has a facilitating effect on GEE in the YRD region and most of its provinces. The higher the level of education, the greater the potential of technological innovation and the possibility of promoting high-quality and green development of the industry. The boost is particularly evident in Shanghai, where high-end talents are gathered, and a stronger sense of green development is rooted in people’s minds. This is also consistent with the reason why Shanghai has the highest GEE as stated in the previous analysis of the GEE result.

The influence of the level of opening to the outside world on the GEE shows regional heterogeneity. Among them, the level of opening to the outside world of Shanghai greatly promotes the improvement of the efficiency of green economy. As a city with the highest level of opening-up in China, Shanghai’s dependence on foreign investment not only promotes its development but also promotes its green development. But in inland areas such as Anhui, the deepening of the degree of opening to the outside world increases the demand of domestic enterprises for export, which to a certain extent intensifies the consumption of resources and environmental pollution.

4. Conclusion and Discussion

4.1. Conclusion. Based on the panel data of 41 cities of the YRD region, the efficiency of urban green economy is measured using the superefficiency SBM model, the agglomeration level of the manufacturing and the logistics industries, as well as the synergistic agglomeration level of the two industries, is calculated using the location entropy method, and the Tobit regression model is used to analyse the influencing factors and influence mechanism of factors on the GEE. The conclusions of the research study can be given as follows.

First is static efficiency. The overall GEE of the YRD region is not ideal, and the ranking of the efficiency value is Shanghai > Jiangsu > Zhejiang > Anhui; the level of economic development and the ability of technological innovation promote the improvement of green efficiency; cities with beautiful natural environmental resources and adhering to the concept of green development have higher

GEE; resource-based cities are faced with the dilemma of resource depletion and the challenge on improving the GEE.

Second is dynamic efficiency. The GEE of the YRD region shows a U-shaped change, and technological progress is the most important factor affecting the regional GEE. Both scale efficiency and pure technological efficiency show fluctuating changes, which have no significant impact on the overall efficiency.

Third is the level of agglomeration and synergistic agglomeration. Cities with a high level of manufacturing agglomeration are mainly located in Jiangsu and Zhejiang, while those with a low level are mainly in Anhui. The agglomeration level of the logistics industry among cities is not uniform. In general, Shanghai has the highest ISA level of the two industries, followed by Jiangsu and Zhejiang, and Anhui has the lowest level. Many cities with a high level of synergistic agglomeration can play a good role in driving the synergistic agglomeration of their satellite towns and cities around them.

Finally, with the improvement of the synergistic agglomeration level of the manufacturing and logistics industries in the YRD region, the GEE tends to improve significantly. The effect of the ISA level of the two industries within the four provinces shows regional heterogeneity. The more developed the region, the less significant the effect of government financial support on GEE; the population gathering in cities may bring pollution, which is not conducive to the improvement of GEE; simply increasing the proportion of the secondary industry may not promote green development, and industrial structure transformation is imminent; high-quality talents can promote the improvement of GEE on the whole; developed coastal provinces with convenient transportation can strengthen the level of opening to the outside world, while less developed inland provinces may not pay too much attention to opening to the outside world to avoid waste of resources and too much development burden that may lead to low GEE.

By taking the collaborative agglomeration of the manufacturing and logistics industries as the starting point, this research enriches the perspective and content of the theoretical research on industrial collaborative agglomeration to promote the GEE. Also, this research takes the data of 41 cities in the YRD region as the sample to carry out the analysis and investigates the impact of the collaborative agglomeration of “two industries” on improving GEE from the level of Chinese prefecture-level cities, which is an effective supplement to the current relevant studies which mainly take provincial-level data as the empirical sample. By researching on the status quo of the synergistic agglomeration level of the manufacturing and logistics industries and GEE in the YRD region, exploring the influencing factors of GEE, analyzing the influencing mechanism of the two industries’ synergistic agglomeration on GEE, and investigating regional heterogeneity, this research provides a clear image of the synergistic agglomeration status of the two industries in the region, as well as the static and dynamic GEE and its influencing factors, which is of practical significance in finding the problems in the process of industry transformation and regional green development.

4.2. Discussion. Based on the conclusions mentioned previously, there are two parts worth thinking about. First is the way of optimizing the green transformation of industrial structure. Second is the improvement and direction setting of the government policy.

4.2.1. The Way of Optimizing the Green Transformation of Industrial Structure. Optimizing the green transformation of industrial structure is necessary. A reasonable industrial structure can promote the green development of the YRD region. However, in the whole YRD region and three of its provinces, the higher the proportion of the secondary industry, the more restricted the green development, and for the other provinces, the facilitation effect is not obvious. In view of the situation, modern upgrading is not only relevant to the traditional strengthening of the secondary and tertiary industries but also imperative to the cultivation of the emerging industries. On the one hand, it is undeniable that the rapid development of the YRD region in the past was inseparable from the dependence on the secondary industry. Although manufacturing has brought about environmental troubles, it has also accumulated resources and laid a foundation for the development of the region; on the other hand, it can be found from the empirical analysis that it is not advisable to increase the proportion of the secondary industry at the expense of the environment. In the face of the gradual depletion of resources, priority should be given to the development of advanced and technology-intensive industries, and industrial transition and transformation should follow the criteria of environmental friendliness, ecological green, and high quality. Resource and factor advantages created by the industrial synergistic agglomeration should be fully utilized to leverage the role of synergistic industrial agglomeration in urban green development. From the perspective of the synergistic agglomeration of manufacturing and logistics industries, the synergistic alignment and integrated development of the two are good ways to optimize and upgrade industrial structure transformation. Logistics, as a separate component of the traditional manufacturing industry, can fully create the value spillover effect through provincial cooperation and regional cooperation of the industry in setting up a scientific, systematic, advanced logistics network and value chain.

4.2.2. Policy Suggestions. Local governments should not only strengthen the indoctrination of the green development concept in society and among enterprises and use natural resources sustainably, but they should also realize horizontal and vertical coordination of intergovernmental cooperation in policy and build a guarantee mechanism for the interaction of industry, technology, and talent. Specific policy recommendations are as follows:

- (1) We strengthen horizontal intergovernmental cooperation, adjust the degree of industrial collaboration, avoid congestion effect, and optimize resource allocation. In Shanghai, empirical results show that the synergistic agglomeration of the two industries may

have evidenced the trend of “congestion effect,” thus, it is important to grasp the degree and orientation of industry synergistic agglomeration. In the whole YRD region and three other provinces, synergistic agglomeration of the two industries gradually play a great role in promoting the green development of cities. Therefore, the geographical advantages of the YRD region can be used to strengthen cooperation among provinces and cities. To be more specific, on the one hand, provinces with “congestion effect” can appropriately transfer the manufacturing and logistics enterprises to the industrial parks in neighbouring cities. On the other hand, the awareness of cooperation among provinces and cities should also be raised. High-quality development also requires high-quality synergistic agglomeration, which is not only the traditional agglomeration of labour and geographical location but also includes the agglomeration of technology, innovation, resources, advanced equipment, and high-end talents. Provinces and cities that develop faster can share high-end talents, technology, and information resources with those that develop slower and should leverage their leading role, focusing on the present situation of the surrounding cities, to make full use of potential cooperation space and resources so that more proper allocation of resources in the whole YRD region can be achieved, and in this way, bottlenecks can be alleviated in areas impacted by the “congestion effect,” and at the same time, the utilization efficiency of resources can be improved, resource waste can be reduced, cost saving can be realized, and green development can be promoted.

- (2) We adjust the vertical intergovernmental relationship at all levels, realign government support, and realize the balance between competition and cooperation among local governments. It can be found from the empirical research that the synergistic agglomeration levels of manufacturing and logistics industries are different, and the influence mechanism of each influencing factor also has regional heterogeneity. In deciding how to optimize the allocation of local resources, how to reform the economic system, and how to upgrade the industrial structure, local governments play the “key actors” role [60]. With the deepening of the reform process of China, resources such as land, labour, energy, and natural resources are increasingly scarce, the government tends to use more fiscal resources that are more controllable to serve the local people and the market. Fiscal support is one of the good instruments for promoting development, but in the absence of competitive pressure and a clearer orientation of funding, pure fiscal support can lead to a weak sense of efficiency and is therefore detrimental to green and high-quality development. Specifically, the vertical allocation of fiscal revenue may lead to the lack of efficiency and competition awareness of local

governments, resulting in low efficiency in the use of funds. Therefore, optimizing the fiscal relationship between vertical governments and maximizing the role of fiscal funding can stimulate local governments to increase investment in transformation. Adjusting vertical intergovernmental relations, urging local governments to improve their financial self-sufficiency rate, and enhancing their awareness of efficiency are conducive to governments when seeking a balance between competition and cooperation and when exploring more favorable models for high-quality and green development.

- (3) We build a comprehensive mechanism for personnel training to promote technological progress and green development. The accumulation of talent resources usually includes introduction, cultivation, and safeguarding a talent pool. The establishment of a comprehensive talent management mechanism is conducive to providing an all-round good development environment for talent training, service, incentivization, and secure provision.

4.2.3. Further Discussion. In this research, GEE and its influencing factors, especially the influence of the manufacturing and logistics industries synergistic agglomeration in it on the city scale, are studied, which has great reference significance for adjusting industrial structure and government regulation. But attention should also be paid to the following deficiencies and new discussions can be raised: first, as time goes by, data sources will become richer, and the efficiency measurement indicators and influencing factor indicators selected in this research can be updated accordingly. Secondly, this research explores the influencing factors of urban GEE, but the influence may be nonlinear or there may be mediating variables, which can be further discussed in future research.

Data Availability

The data are collected from China Urban Statistical Yearbook, China Energy Statistical Yearbook, China Industrial Statistical Yearbook, and China Environment Statistical Yearbook. All data used to support the findings in this manuscript can be made available upon request to the corresponding author.

Conflicts of Interest

The authors declare that they have no conflicts of interest.

Acknowledgments

This research was financially supported by the Key Humanities and Social Science Research Project of Universities in Anhui Province (SK2021A0288) and Science and Technology Activities Project for Returnees from Overseas Study in Anhui Province (S012014016).

References

- [1] D. W. Pearce, *Blueprint for a Green Economy: A Report*, Earthscan Publications Ltd, London, UK, 1989.
- [2] W. J. Meng, X. L. Zhang, and Q. S. Xing, "Research on the influence of industrial Co-agglomeration on urban green economy development: based on the Yangtze River Delta urban agglomeration," *Ecological Economy*, vol. 38, no. 2, pp. 67–74, 2022.
- [3] F. Yan, "Spatial correlation and influencing factors of logistics industry and manufacturing industry Co-agglomeration," *Statistics & Decisions*, vol. 37, no. 7, pp. 113–117, 2021.
- [4] Q. Wei, "Empirical study of linkage evolvement between manufacturing and logistics industry," *Journal of Zhongnan University of Economics and Law*, vol. 1, pp. 115–119, 2011.
- [5] H. S. Ma, F. Zhao, and Y. S. Yan, "Research on the formation and evolution conditions of manufacturing and logistics synergistic agglomeration," *Journal of Highway Communication Technology*, vol. 39, no. 6, pp. 169–176, 2022.
- [6] Y. D. Zhan, G. H. Han, and M. Dong, "Study on cooperative mechanism between production services and manufacturing," *Journal of Harbin University of Commerce (Natural Science Edition)*, vol. 28, no. 1, pp. 118–122, 2012.
- [7] F. Zhao and D. Chen, "Industry relevancy between producer services and manufacturing in east asia," *World Economy Study*, vol. 7, pp. 73–80, 2012.
- [8] J. B. Lu, "Coordination effect of producer service based on manufacturing agglomeration," *Chinese Journal of Management*, vol. 11, no. 3, pp. 396–401, 2014.
- [9] W. C. Qi, "Research on the mechanism and mode of the linkage development of manufacturing and logistics industry," *Technology Innovation and Application*, vol. 14, p. 259, 2015.
- [10] L. Zhou, "Mechanism and mode of manufacture and logistics integration," *Logistics Technology*, vol. 5, pp. 102–105, 2015.
- [11] H. Zhu, G. G. Zhou, and G. Y. Ren, "Research on spatial Co-agglomeration between manufacturing industry and logistics industry: a case study of six provinces in Central China," *Economic Geography*, vol. 11, pp. 117–124, 2015.
- [12] H. X. Tang, W. Y. Xia, and Y. Huang, "Identification of influencing factors and breakthrough path of collaborative agglomeration of manufacturing industry and logistics industry in new land-sea corridor in western China," *China Soft Science*, vol. 8, pp. 131–139, 2022.
- [13] X. Y. Jin, "City size, industrial linkage and Co-agglomeration - based on the industrial linkage and spatial interaction between manufactures and producer services," *Industrial Economic Review*, vol. 6, pp. 35–46, 2015.
- [14] H. Zhang and S. L. Wu, "Influence of Co-agglomeration of logistics industry and manufacturing industry on resident consumption expansion: an empirical analysis based on the dubin model of dynamic space," *Consumer Economics*, vol. 38, no. 2, pp. 41–56, 2022.
- [15] L. Deng, "The empirical analysis on the linkage development of the manufacturing and logistics industry in China," *China Business and Market*, vol. 7, pp. 29–36, 2013.
- [16] Z. Z. Wang, "Self-organization evolutionary dynamic model of manufacturing industry and logistics industry," *Statistics & Decisions*, vol. 17, pp. 36–39, 2014.
- [17] X. Q. Jin, "Interactive development between manufacturing industry and logistics industry in the Yangtze River economy belt," *Journal of Nantong University (Social Sciences Edition)*, vol. 1, pp. 16–22, 2017.
- [18] Z. J. Jiang and Q. L. Dong, "The study on competing relationship of interactive development between manufacturing and logistics industry - based on integrated field," *Technoeconomics & Management Research*, vol. 8, pp. 13–16, 2015.
- [19] B. Wang, Z. Yang, Y. Y. Chen, J. J. Li, and J. Chen, "Green economy efficiency influence mechanism," *Shanghai Economic Research*, vol. 6, pp. 62–77, 2022.
- [20] X. C. Cai and H. X. Xu, "Economic policy uncertainty and green economic efficiency," *Journal of Nanjing University of Finance and Economics*, vol. 1, pp. 54–63, 2022.
- [21] D. F. Cai, Q. J. Dong, Y. Zhu, and Y. S. Lian, "Industrial agglomeration, population structure and green economy efficiency," *Statistics & Decisions*, vol. 38, no. 7, pp. 112–116, 2022.
- [22] Y. Q. Zhou and F. Gu, "Research on the impact of land resource mismatch on the efficiency of urban green economy," *Academic Exploration*, vol. 2, pp. 104–115, 2022.
- [23] X. X. Lin, "The influence of economic agglomeration on green economy efficiency," *Finance and Economics*, vol. 5, pp. 89–102, 2021.
- [24] P. D. Zhang and X. W. Tu, "The bilateral impact of manufacturing agglomeration on green economy efficiency," *Economic Theory and Business Management*, vol. 41, no. 11, pp. 35–53, 2021.
- [25] J. P. Li, L. Q. Xu, F. C. Tang, and D. Yao, "The impact of public transport facility scale on green economy efficiency," *Journal of Systems Management*, vol. 30, no. 6, pp. 1053–1066, 2021.
- [26] Z. Zhang, X. S. Li, and C. Wang, "Labor price distortion and the loss of green economic efficiency," *Journal of Yunnan University of Finance and Economics*, vol. 36, no. 4, pp. 51–63, 2020.
- [27] B. Q. Lin and R. P. Tan, "Economic agglomeration and green economy efficiency in China," *Economic Research Journal*, vol. 54, no. 2, pp. 119–132, 2019.
- [28] L. Y. Zhu, T. Li, L. Y. Ma, and G. Z. Sun, "Cities' green economy efficiency evaluation under haze constraint: an empirical study of metropolitan area of jing-jin-ji, Yangtze River Delta and pearl River Delta," *Science and Technology Management Research*, vol. 38, no. 22, pp. 58–63, 2018.
- [29] L. Yang and X. Z. Hu, "Analysis on regional difference and convergence of the efficiency of China's green economy based on DEA," *Economist*, vol. 2, pp. 46–54, 2010.
- [30] H. L. Wang, X. Y. Lian, and D. M. Lin, "Effects of green technological innovation efficiency on regional green growth performance: an empirical analysis," *Science and Management of S. & T.* vol. 37, no. 6, pp. 80–87, 2016.
- [31] Z. J. Feng, C. J. Yang, and X. Kang, "Green innovation and green growth of industrial enterprises: an empirical study based on guangdong," *S & T Management Research*, vol. 37, no. 20, pp. 230–235, 2017.
- [32] Z. Li and S. Yang, "Fiscal Decentralization, Government innovation preferences and regional innovation efficiency," *Management World*, vol. 34, no. 12, pp. 29–42, 2018.
- [33] L. D. Zhao, L. Zhang, R. J. Li, and M. Y. Yang, "Energy Endowments, Human capital and China's economic performance under the dual regulation of the resources and the environment," *Modern Economic Science*, vol. 35, no. 4, pp. 74–84, 2013.
- [34] Y. M. Li and M. Hua, "Green efficiency of Chinese cities: measurement and influencing factors," *Urban and Environmental Studies*, vol. 2, pp. 36–52, 2014.
- [35] Y. B. Liu, H. X. Yuan, and W. Zhe, "Dynamic panel data modeling of the effects of cultural industry clusters on green

- economic efficiency,” *Resources Science*, vol. 39, no. 4, pp. 747–755, 2017.
- [36] J. L. Sun and P. Y. Zhu, “Evaluation of ‘belt and road’ provinces’ green economic efficiency and analysis of influencing factors based on SBM-malmquist-tobit,” *S & T Management Research*, vol. 39, no. 4, pp. 230–237, 2019.
- [37] H. N. Zhang, Z. R. Geng, R. S. Yin, and W. Zhang, “Regional differences and convergence tendency of green development competitiveness in China,” *Journal of Cleaner Production*, vol. 254, Article ID 119922, 2020.
- [38] H. L. Jiang and P. C. Jiang, “Research on the impact of digital finance on the efficiency of urban green economy,” *Soft Science*, vol. 36, no. 4, pp. 37–43, 2022.
- [39] F. H. Zeng and S. Y. Xiao, “The impact of digital finance on the efficiency of urban green economy,” *Statistics & Decisions*, vol. 38, no. 15, pp. 144–148, 2022.
- [40] N. Guan, X. Y. He, and B. Y. Li, “Research on the impact of digital service economy on green economy efficiency in beijing-tianjin-hebei region,” *Macroeconomic Study*, vol. 7, pp. 105–119, 2022.
- [41] S. Roumei and F. Deng, “The nonlinear effect of human capital agglomeration on green economy efficiency,” *Social Scientist*, vol. 8, pp. 96–102, 2020.
- [42] N. Zhang and A. J. Guo, “Study on the impact of service agglomeration on green economic efficiency of cities in the yellow river basin,” *City Problems*, vol. 86, no. 4, pp. 35–44, 2022.
- [43] Y. J. Ren, Y. X. Qi, and D. Liang, “The effect of producer services agglomeration on the efficiency of urban green economy,” *Statistics & Decisions*, vol. 19, pp. 120–123, 2022.
- [44] X. F. Wu and Y. D. Yang, “Have Co-agglomeration of producer services and manufacturing promote urbanization level,” *Finance and Economics*, vol. 11, pp. 79–90, 2016.
- [45] J. T. Zhang, Y. Zhu, and B. You, “Research on the influence of industrial collaborative agglomeration on the green development of urban economy,” *Urban Problems*, vol. 2, pp. 66–74, 2021.
- [46] Z. H. Wu, “The service industry, collaborative agglomeration of strategic emerging industries and high-quality economic growth - empirical analysis based on provincial panel data from 2005 to 2018,” *Journal of Henan Normal University (Philosophy and Social Sciences Edition, Bimonthly)*, vol. 4, pp. 44–50, 2020.
- [47] Q. X. Zhao, C. X. Xia, and J. J. Shi, “Sci-tech talents agglomeration, industry agglomeration and regional innovation capability: empirical analysis based on jing-jin-ji region, Yangtze River Delta and pearl River Delta,” *S & T Management Research*, vol. 24, pp. 54–62, 2019.
- [48] M. Fang, S. G. Yang, J. J. Zhou, and Y. L. Lei, “The innovative development path of industry agglomeration in Yangtze River economic belt under the background of high-quality development,” *China Soft Science*, vol. 5, pp. 137–150, 2019.
- [49] Y. Ma, Y. H. Qiu, and X. Y. Wang, “Research on the effect of high-tech industry agglomeration and innovation on high-quality economic development - regression model based on panel smoothing transformation,” *Journal of Industrial Technological Economics*, vol. 2, pp. 13–20, 2020.
- [50] X. M. Feng, R. J. Zhang, and P. Y. Yang, “Has synergistic industrial agglomeration promoted green development? Spatial econometric analysis based on 285 cities,” *Journal of Finance and Economics*, vol. 3, pp. 71–81, 2022.
- [51] M. Liu, “The influence of collaborative agglomeration of logistics industry and manufacturing industry on high-quality economic development--the empirical research on 283 cities at the prefecture level and above,” *China Business and Market*, vol. 35, no. 9, pp. 22–31, 2021.
- [52] F. Yan and T. S. Wang, “Professional agglomeration and cooperative agglomeration of logistics industry and manufacturing industry and regional economic growth,” *Enterprise Economy*, vol. 40, no. 4, pp. 88–97, 2021.
- [53] A. Charnes, W. W. Cooper, and E. Rhodes, “Measuring the efficiency of decision making units,” *European Journal of Operational Research*, vol. 3, no. 4, pp. 339–444, 1979.
- [54] K. Tone, “A slacks-based measure of super-efficiency in data envelopment analysis,” *European Journal of Operational Research*, vol. 143, no. 1, pp. 32–41, 2002.
- [55] J. J. Chen and J. J. Chen, “The research on the Co-location between producer services and manufacturing: the empirical analyses based on the 69 cities and regions in Zhejiang province,” *China Industrial Economics*, vol. 6, pp. 141–150, 2011.
- [56] J. Tobin, “Estimation of relationships for limited dependent variables,” *Econometrica*, vol. 26, no. 1, pp. 24–36, 1958.
- [57] J. Zhang, G. Y. Wu, and J. P. Zhang, “The estimation of China’s provincial capital stock: 1952-2000,” *Economic Research Journal*, vol. 10, pp. 35–44, 2004.
- [58] Z. J. Wu and N. J. Wu, “Research on the measurement, decomposition and influencing factors of green economic efficiency in the Yangtze River economic belt: based on super-efficiency SBM-ML-tobit model,” *Urban Problems*, vol. 1, pp. 52–62, 2021.
- [59] L. L. Ding, L. Zhu, and G. S. He, “Measurement and influencing factors of green total factor productivity of marine economy in China,” *Forum on Science and Technology in China*, vol. 2, pp. 72–78, 2015.
- [60] X. Gao, “Government efficiency: the big problem in China’s public management,” *Public Administration and Policy Review*, vol. 1, pp. 55–62, 2020.

Research Article

How Does the Electronic Products Retailer Transform Operational Modes Considering Consumer Preferences for Leasing?

Gaidi Tian , Chunfa Li , and Dongdong Li 

School of Management, Tianjin University of Technology, Tianjin 300384, China

Correspondence should be addressed to Chunfa Li; chunfali@163.com

Received 31 May 2022; Revised 14 August 2022; Accepted 29 August 2022; Published 20 September 2022

Academic Editor: Conghu Liu

Copyright © 2022 Gaidi Tian et al. This is an open access article distributed under the Creative Commons Attribution License, which permits unrestricted use, distribution, and reproduction in any medium, provided the original work is properly cited.

Consumer interest in renting brand-new electronic products has increased recently. Some retailers started to lease them, but they remarkably depreciate shortly after leasing. If their rental income cannot bring in enough profit, should a retailer lease them? This paper uses consumer preferences for leasing to describe their rental utility. It develops an analytical framework to study how the retailer selects operational modes. In a supply chain consisting of a manufacturer and a retailer, three different operational modes are analyzed: pure selling (S), pure leasing (L), and hybrid selling-leasing (SL). Results mainly show that when consumer preferences for leasing exceed a certain threshold, both the manufacturer's and the retailer's profits can be increased if the retailer transforms the business operational mode from S to SL/L. When consumer preferences for leasing are within a certain range, the retailer's profits can be increased if the operational mode is transformed from S/L to SL. This happens as both consumers' lease and purchase requirements for electronic products are met after the transformation. The wholesale price, leasing price, selling price, and the manufacturer's profit all rise in the SL mode as consumer preference for leasing rises, but the retailer's profit falls. Only if the retailer cooperates with the manufacturer can the operational mode be transformed from S/L to SL when consumer preferences for leasing are lower, and the coordination contract can achieve Pareto improvement in the profits of both the manufacturer and the retailer.

1. Introduction

The enormous market for electronic products accelerated the growth of the retail sector. In 2020, the size of the consumer electronics market exceeded 1 trillion USD, and 8% annual growth is anticipated from 2021 to 2027 (<https://www.gminsights.com/industry-analysis/consumer-electronics-market>, retrieved on 27 May 2022). Ceconomy, as a retailer specializing in selling electronic products to downstream consumers, ranks ninth among German family businesses with sales of 22.1 billion euros (<https://www.163.com/dy/article/F5VB842V0518WSO6.html>, retrieved on 27 May 2022). Additionally, retail sales of electronic products make up a sizable portion of those of the world-renowned online retailers Amazon and JD.com. Electronic-related sales account for more than half of JD.com platform's revenue and 44% of Amazon's revenue (<https://www.chinairn.com/hyzz/20200605/140556382.shtml>, retrieved

on 27 May 2022). Retailers must be responsive to market changes due to the enormous volume of sales of electronic products in order to maintain their competitive advantage and boost profits.

In recent years, leasing has gained popularity as a circular business model. Numerous rental platforms have appeared; for instance, “Renrenzu” and Alibaba’s “Zhima Credit” both introduced product leasing services that decreased the use cost and purchase risk for consumers. With the rapid replacement of electronic products, the improvement of network credit mechanisms, the application of digital technology, and the implementation of intelligent logistics systems, consumers have shown a greater interest in renting electronic products. The lease of electronic products is becoming more and more popular, and conventional electronics retailers are facing tremendous challenges.

Conventional electronics retailers can meet market challenges by undergoing rapid transformation. In addition

to selling electronic products, Dixintong, electronics retailer in China, has started to provide leasing services, offering hybrid selling and leasing of electronic products on its platform (https://www.thepaper.cn/newsDetail_forward_1720419, retrieved on 27 May 2022). JD has also launched various product leasing websites for individuals and businesses (https://www.ce.cn/cysc/tech/gd2012/201909/17/t20190917_33166817.shtml, retrieved on 27 May 2022). Retailers can also turn into pure renters. However, completely giving up the selling option of electronic goods and offering only leasing services requires a significant adjustment on the part of the retailer.

In the real world, electronic products are updated very quickly. When retailers provide leasing service, consumers who prefer using the newest electronic products can choose to rent and only use them for the duration of the leasing period. Electronic products, in contrast to other goods, have a short lifespan [1]. For instance, 80% of consumers use their phones for less than two years [2]. They have a relatively long leasing period. For example, most retailers offer new phone leases for up to a year and beyond (<https://shop.ee.co.uk/>, retrieved on 8 Aug. 2022). Due to its lengthy lease time, they significantly depreciate after leasing, and the renters are the ones who gain the most from their value.

Therefore, this paper mainly considers the following situation: a retailer who purchases electronic products from a manufacturer only leases new electronic products for a certain leasing term. Products are returned to the retailer who receives their residual value when the lease expires. Consumer leasing preferences are used to describe their rental utility during a certain leasing period. In view of the above-mentioned practical challenges faced by retailers of electronic products, the following questions are explored:

- (1) How do electronics retailers transform their operational modes considering consumer preferences for leasing? Will they transform to pure leasing or hybrid selling-leasing?
- (2) How do consumer preferences for leasing impact the retailer's transformation of operational modes, prices, demand, profit, and consumer surplus of electronic products supply chains?
- (3) How do retailers cooperate with upstream manufacturers when they implement the operational modes transformation? What are the impacts of their cooperation on retailers' transformation and supply chains' efficiency?

To address the aforementioned questions, this study uses a Stackelberg game model framework that includes a manufacturer, a retailer, and consumers who have the same preferences for leasing electronic products in a given leasing period. The manufacturer provides its electronic products to the retailer, who then decides the operational mode: pure selling (S), pure leasing (L), or hybrid selling-leasing (SL). After obtaining the equilibrium solutions, the impact of consumer preferences for leasing and the residual value of the electronic product on these solutions are investigated. The retailer's optimal choices under the three modes are then

discussed, followed by a numerical analysis. Moreover, the retailer's hybrid selling-leasing mode transformation under cooperation with the manufacturer is analyzed, and a "wholesale price discounts and revenue sharing" coordination contract is also investigated.

It was found that leasing can increase the demand for electronic products whether it is a pure leasing mode or a hybrid selling-leasing mode. Therefore, when consumer preferences for leasing exceed a certain threshold, both the manufacturer's and the retailer's profits can be increased if the retailer transforms its operational mode from S to SL/L. When consumer preferences for leasing are within a certain range, the retailer's profits can be increased if the operational mode is transformed from S/L to SL. Adding a leasing/selling channel to a strictly selling/leasing mode gives consumers more options and gives retailers a new revenue stream. As consumer preference for leasing increases, selling and leasing prices as well as the manufacturer's profits all rise in the SL mode, while the retailer's profits fall. On the other hand, leasing prices and the manufacturer's and the retailer's profits all rise in the L mode. When consumer preferences for leasing are lower, only if the retailer cooperates with the manufacturer can the operational mode be transformed from S/L to SL. Using a "wholesale price discounts and revenue sharing" contract might attract the manufacturer to cooperate and achieve Pareto improvement in the profits of both the manufacturer and the retailer.

The remainder of this article is organized as follows. Section 2 reviews the related literature. Section 3 details about the assumptions and the three modes that the retailer may consider when selling the electronic products provided. In Section 4, equilibrium results of the three models are compared, and the product price, market demand, and corporate profits are analyzed. A numerical analysis is presented in Section 5. In Section 6, an integration model and a coordination contract as an extension are outlined. Section 7 concludes this article. All proofs are provided in the Appendix.

2. Literature Review

The related literature to this article includes the following three streams: (i) selling versus leasing, (ii) the product leasing channel, and (iii) consumer preferences for leasing.

2.1. Selling Versus Leasing. When consumers buy products, they pay for the right to own them, but when they rent, they only pay for the right to use them. Pure selling, pure leasing, or hybrid selling-leasing mode selection of a monopoly manufacturer are discussed in numerous academic works. Yu et al. [3] compared per-use rentals with sales from a durable goods manufacturer, where there is a vertical differentiation between leased and brand-new products. They found that the degree of vertical difference between products significantly affects the choice of selling, leasing, or hybrid selling-leasing mode. Consumers may have financial limitations and are sensitive to products' prices. The model established by Li et al. discussed this issue and found that

manufacturers offer products to consumers at low prices through leasing, which expands the market coverage and creates price discrimination [4]. Gilbert et al. [5] analyzed how per-use rentals and sales differentiate consumers within the framework of a hybrid selling-leasing model. They found that sales allow a firm to discriminate according to consumers' usage frequencies, and rentals allow it to discriminate according to their realized valuation. Bhaskaran and Gilbert [6] study how complementary products influence manufacturers' choice to lease or sell their products. Another popular area of research is the sale of digital goods via subscription (leasing) or perpetual (selling) [7–9]. Liu et al. [10] considered green product design in the comparison of manufacturers' various lease modes. In a hybrid selling-leasing mode, manufacturers combined selling and leasing to create discriminatory pricing, which attracts potential price-sensitive customers. In contrast to the above-mentioned articles on the choice of selling or leasing modes made by manufacturers, this paper shifts the research perspective to explore how retailers directly facing consumers in the downstream supply chain make selling or leasing choices.

The choices of selling or leasing modes are different in a duopoly market structure. Tang and Deo [11] analyzed the leasing price and duration competition between two retailers that only offer lease services. The model of Chau and Schulz [12] depicts two manufacturers supplying goods to the market through their own intermediaries. Manufacturers can decide whether to sell or lease their products to intermediaries, and intermediaries can also decide whether to lease or sell their goods to consumers. Desai and Purohit [13] are the first to analyze the durable goods market in which both manufacturers adopt the hybrid leasing and selling strategy. Wang et al. [14] extends this issue by exploring six scenarios in which the two manufacturers adopt pure selling, pure leasing, or hybrid selling-leasing modes. In contrast to previous studies, our analysis focuses on the increasingly popular retailer's choice to sell or lease products and analyzes the leader-follower game relationship between a manufacturer and a retailer considering consumer preferences for leasing.

2.2. Product Leasing Channel. Direct product leasing is not only available from professional renters but also from retailers and manufacturers. Manufacturers may encounter numerous rental channel structures. Bhaskaran and Gilbert [15] studied whether producers offer goods to consumers through intermediaries and compared whether products are offered through selling or leasing. They find that manufacturers are more willing to invest in product durability when offering leasing services. Xiong et al. [16] studied the implementation of product leasing and sales in both manufacturers' direct selling and distribution channels and found that leasing products provided by manufacturers through direct selling channels may lead to the late withdrawal of product dealer. Bhaskaran and Gilbert [17] studied the competition between dealers when a manufacturer leases and sells its goods through multiple dealers, and one of their interesting findings is that the

manufacturer prefers to use leasing-brokering arrangement. Kalantari et al. [18] discussed pricing policies by a manufacturer that sells its products online and whether these policies motivate a retailer as an independent part to enter the market to provide selling and leasing options through a brick store. Additionally, numerous studies investigated the channel problem of leased used products in the secondary market [19–23]. In contrast to previous studies, this paper analyzes the reality of retailers' leasing products while considering consumer preferences for leasing in order to analyze the selling or leasing mode selection through the model and offer recommendations for retailers to better make their decisions.

2.3. Consumers' Preferences for Leasing. The difference between a leasing mode and a selling mode is not only the form of ownership of the product but also the extent to which consumers accept the leasing. Depicting consumers' reactions to product leasing is an important part of the research on product leasing. Yu et al. [3] analyzed the pricing of products and rental services in a market where consumers can buy products or pay for per-use rental services. They found that leasing has three effects on consumers as compared to purchase. First, unlike a one-time payment for a purchase, a consumer is required to pay for per-use rental services. Second, the consumer obtains the consumer-side benefits from ownership (CBO) under the purchase mode and loses the negative utility of finding the lease item under the lease model. In addition, the repeated use of leased products results in vertical differences in the quality of sold products. Li et al. [4] distinguished between sold products and leased products by describing that the product for leasing is devalued compared to the unused one and the degree of condition differentiation between products for leasing and unused products for selling occurring as an exogenous variable. They held that consumers without capital constraint can freely choose between the selling or leasing channel, while those with capital constraint can only lease the product. They also mentioned two interactions between consumers and leases: the decrease in the lease product value and the restrictions on the choice of leasing and selling under capital constraint. Gilbert et al. [5] used a similar model to describe the relationship between consumer utility and usage rate. For electronic products, there are differences in consumer acceptance of product leases. The leased products are older, and the short-term lease needs to change the consumption habits of consumers. There are also troubles in data preservation. Therefore, despite the fact that some consumers prefer product leasing, this preference is less common than consumers' directly purchasing goods. Hence, similar to the two above-mentioned studies, we describe the low utility caused by product rental as consumer preference for leasing and analyze the impact of leasing preference degree on consumer leasing behavior. Li et al. [24] believed that due to the low service level of the platform and the psychological gap caused by nonownership of products, the perceived value of lease products will undoubtedly be lower than that of retail products. This value

perception factor and owners' maintenance costs can influence the operating mode of original equipment manufacturers. Jalili and Pangburn [25] also agreed that a rental only offers a fraction of the utility that full ownership would. When consumers face significant value uncertainty, rentals also provide a mechanism for consumers to discover whether they like a product.

Existing studies on the choice of enterprise leasing and selling modes all focus the mode selection of manufacturers who directly deal with consumers [3–5, 24, 25], or they focus on the retailers mode selection without considering different leasing preferences of consumers [11–14]. In the electronic products industry, the rise in consumer acceptance of leasing has brought new opportunities for retailers to transform to leasing modes. There is no literature examining the effects of retailers' pure leasing, pure selling, and hybrid selling-leasing mode in light of customers' various leasing preferences. Therefore, we model and analyze the important challenges faced by retailers in their transition to leasing, which will provide theoretical reference for retailers' leasing transition.

3. Problem Description and Modeling

3.1. Problem Description. Consider an electronic product supply chain consisting of a manufacturer, a retailer, and consumers with the same leasing preferences [25]. In this supply chain, the manufacturer (M) wholesales electronic products to the retailer (R), and only the retailer sells or leases new electronic products to consumers. The retailer has three alternative operational modes as shown in Figure 1: pure selling (S), pure leasing (L), and hybrid selling-leasing (SL) [16]. In the S mode, electronic products are sold to consumers directly. In the L mode, electronic products are leased to consumers directly. In the SL mode, electronic products are sold and leased to consumers who choose how to obtain the products based on their utility.

There is a Stackelberg game between the manufacturer and the retailer. The manufacturer produces the electronic products and provides them to the retailer. Assume that the unit manufacturing cost of the electronic product is c . The manufacturer, as the leader, decides the wholesale price of the electronic product as w [26, 27]. Assume that the manufacturer will be able to immediately respond to the entire product demand in the market, and there will be no shortage or overproduction of the electronic product [12]. The retailer has three options for delivering electronic goods to customers after receiving them from the manufacturer. In the mode S , the selling price of the electronic product is p^S . In the L mode, the leasing price of the electronic product is r^L . In the SL mode, the selling price of the electronic product is p^{SL} , and the leasing price of the electronic product is r^{SL} . Assume that when the retailer offers a lease service, the item is only leased for a certain leasing period [28]. When the lease expires, all the leased goods are returned, and their residual value is obtained [29]. This paper denotes the residual value as r_e for a product that has been leased and returned.

Assume that the total market size is 1, and consumers value the purchased product as v , uniformly distributed over the range $[0,1]$ [25]. It is also assumed that the leasing period of the product is less its lifespan. When consumers rent products, they cannot enjoy their full value and must return them on time, but they can take advantage of some additional rental services, such as repair and maintenance services. Therefore, there may be a discount or a raise on the value of the leased product as compared to the purchased product. Consumers value the leased product as αv , and α ($\alpha \geq 0$) is used to denote consumer preferences for leasing. A similar assumption can be seen in recent studies of product leasing [3–5]. The value of α is affected by numerous factors, such as manufacturer's product replacement speed, retailer's rental service level, consumers' acceptance of leasing, and others [2, 8, 24]. $\alpha = 0$ represents the situation where consumers consider the value of the leased product is zero. Therefore, according to consumer utility theory [30], the utility that a consumer obtains by purchasing a product at price p^i is $U_s = v - p^i$, and the utility that a consumer obtains by leasing a product at price r^i is $U_l = \alpha v - r^i$, $i \in [S, L, SL]$. Consumers choose to purchase or lease products according to the principle of utility maximization. Assume that $v_l = \{v|U_l(v) = 0\}$, $v_s = \{v|U_s(v) = 0\}$, and $v_{sl} = \{v|U_s(v) = U_l(v)\}$, which implies that both v_l , v_s , and v_{sl} are functions of p and r . In the S mode, consumers can only choose to purchase goods or not, consumers in $v \in [v_s, 1]$ are buyers who purchase the product, and consumers in $v \in [0, v_s)$ do not purchase the product. In the L mode, consumers can only choose to lease or not to lease the product, consumers in $v \in [v_l, 1]$ are renters who lease, and consumers in $v \in [0, v_l)$ do not lease the products. In the SL mode, a consumer can decide whether to buy, lease, or do neither; consumers in $v \in [0, v_l)$ do not buy or lease products, consumers in $v \in [v_l, v_{sl})$ choose to lease the product, and consumers in $v \in [v_{sl}, 1]$ choose to purchase the product. According to Refs. [31, 32], in the S mode, the consumers' purchasing demand for the electronic product is $D_s^S = 1 - p^S$, and the retailer's wholesale demand for the electronic product is $D^S = D_s^S$; in the L mode, the consumers' leasing demand for the electronic product is $D_l^L = 1 - (r^L/\alpha)$, and the retailer's wholesale demand for the electronic product is $D^L = D_l^L$; in the SL mode, if $\alpha > 1$, consumers will only choose to rent, and the retailer will only choose to lease. This scenario is the same as the L mode. In the SL mode, if $0 \leq \alpha \leq 1$, consumers' purchasing demand for the electronic product is $D_s^{SL} = 1 - (p^{SL} - r^{SL}/1 - \alpha)$, consumers' leasing demand $D_l^{SL} = ((p^{SL} - r^{SL}/1 - \alpha) - (r^{SL}/\alpha))$, and the retailer's wholesale demand is $D^{SL} = D_s^{SL} + D_l^{SL}$. Figure 2 illustrates the market segmentation. The profits of the manufacturer and the retailer are π_M^i, π_R^i , $i \in [S, L, SL]$.

3.2. Pure Selling Mode (S). In the S mode, the manufacturer first determines the wholesale price of the electronic product, and then the retailer determines the selling price accordingly. The Stackelberg game model can be established as

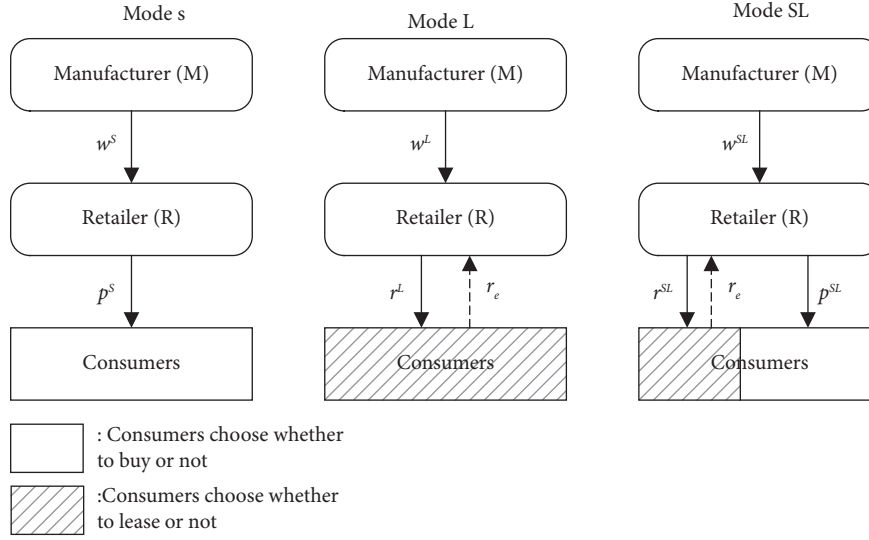


FIGURE 1: Retailer's three alternative operational modes.

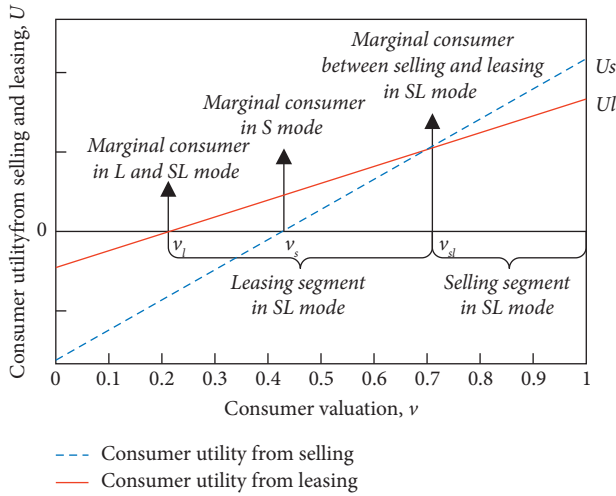


FIGURE 2: Consumers' utility from leasing and selling and market segmentation.

$$\begin{aligned} \max_{w^S} \pi_M^S &= (w^S - c)D_s^S, \\ \text{s.t. } \max_{p^S} \pi_R^S &= (p^S - w^S)D_s^S. \end{aligned} \quad (1)$$

Backward induction is adopted to solve this problem, and the equilibrium results are presented in Lemma 1.

Lemma 1. *In the S mode, the equilibrium wholesale and sales prices of the electronic product are $w^{S*} = (1 + c/2)$ and $p^{S*} = (3 + c/4)$. The equilibrium wholesale and purchasing demand for the electronic product are $D^{S*} = D_s^{S*} = (1 - c/4)$. The equilibrium profit of the manufacturer and the retailer are $\pi_M^{S*} = ((1 - c)^2/8)$ and $\pi_R^{S*} = ((1 - c)^2/16)$.*

3.3. Pure Leasing Mode (L). In the L mode, the manufacturer first determines the wholesale price of the electronic product, and the retailer then determines the leasing

price accordingly. The Stackelberg game model can be established as

$$\begin{aligned} \max_{w^L} \pi_M^L &= (w^L - c)D_l^L, \\ \text{s.t. } \max_{r^L} \pi_R^L &= (r^L + r_e - w^L)D_l^L. \end{aligned} \quad (2)$$

Backward induction is adopted to solve this problem, and the equilibrium results are presented in Lemma 2.

Lemma 2. *In the L mode, the equilibrium wholesale and leasing prices of the electronic product are $w^{L*} = (\alpha + c + r_e/2)$ and $r^{L*} = (3\alpha + c - r_e/4)$. The equilibrium wholesale and leasing demand of the electronic product are $D^{L*} = D_l^{L*} = (\alpha + r_e - c/4\alpha)$. The equilibrium profit of the manufacturer and the retailer are $\pi_M^{L*} = ((\alpha + r_e - c)^2/8\alpha)$ and $\pi_R^{L*} = ((\alpha + r_e - c)^2/16\alpha)$.*

In order to guarantee the existence of non-negative demand and equilibrium solution, the condition $\alpha \geq c - r_e$ needs to be satisfied. This means that when consumer preferences for leasing are large enough, the retailer's products can be leased.

Observation 1. In the L mode (i) as α increases, D_l^{L*} , r^{L*} , w^{L*} , π_M^{L*} , and π_R^{L*} also increase and (ii) as r_e increases, D_l^{L*} , w^{L*} , π_M^{L*} , and π_R^{L*} increase, but r^{L*} decreases.

Results in Observation 1 state that in the L mode, the leasing demand, wholesale price, leasing price, and profits of both the manufacturer and the retailer, all rise as the consumer preferences for leasing increase. The leasing demand, wholesale price, and profits of both the manufacturer and the retailer, all decrease as the residual value of a leased-returned product decreases, but the leasing price increases; that is, the residual value of the electronic products significantly depreciates after leasing; in order to reduce the operating risk for the leasing business, the retailer should raise the lease pricing, and the leasing demand will be reduced.

3.4. Hybrid Selling-Leasing Mode (SL). In the SL mode, the retailer provides consumers with electronic products by both selling and leasing. The manufacturer first determines the wholesale price of the goods, and the retailer then determines the leasing and selling prices. The Stackelberg game model can be established as

$$\begin{aligned} \max_{w^{\text{SL}}} \pi_M^{\text{SL}} &= (w^{\text{SL}} - c)(D_l^{\text{SL}} + D_s^{\text{SL}}), \\ \text{s.t. } \max_{p^{\text{SL}}, r^{\text{SL}}} \pi_R^{\text{SL}} &= (p^{\text{SL}} - w^{\text{SL}})D_s^{\text{SL}} + (r^{\text{SL}} + r_e - w^{\text{SL}})D_l^{\text{SL}}. \end{aligned} \quad (3)$$

The equilibria result is derived by backward induction, which is summarized in Lemma 3.

Lemma 3. *In the SL mode, the equilibrium wholesale price is $w^{\text{SL}*} = (\alpha + c + r_e/2)$, selling and leasing prices are $r^{\text{SL}*} = (3\alpha + c - r_e/4)$ and $p^{\text{SL}*} = (2 + \alpha + c + r_e/4)$, respectively. The equilibrium wholesale, leasing demand, and purchasing demand are $D^{\text{SL}*} = (\alpha + r_e - c/4\alpha)$, $D_l^{\text{SL}*} = (\alpha^2 - (1 - c - r_e)\alpha - (c - r_e)/4\alpha(1 - \alpha))$, and $D_s^{\text{SL}*} = (1 - \alpha - r_e/2(1 - \alpha))$, respectively. The profits of the manufacturers and the retailer are $\pi_M^{\text{SL}*} = ((\alpha + r_e - c)^2/8\alpha)$ and $\pi_R^{\text{SL}*} = (3\alpha^3 + (2c + 6r_e - 7)\alpha^2 + (3r_e^2 + 2r_e c - 6r_e - c^2 - 2c + 4)\alpha + (c - r_e)^2/16\alpha(1 - \alpha))$, respectively.*

To guarantee the existence of non-negative demand, the condition $\alpha_0 \leq \alpha \leq \alpha_1$ ($\alpha_0 = (1 - c - r_e + \sqrt{c^2 + 2cr_e + r_e^2 + 2c - 6r_e + 1})/2$, $\alpha_1 = 1 - r_e$) needs to be satisfied. In other words, there is a range of consumer preferences for leasing. Within this range, retailers are able to attract customers to both lease and make purchases (we ignore the corner solutions of SL mode and only analyze the interior solution in detail because the corner solution of SL mode will degenerate into S mode and L mode, which we have modeled in the previous two sections).

Observation 2. In the SL mode, as α increases, (i) $D^{\text{SL}*}$, $D_l^{\text{SL}*}$, $w^{\text{SL}*}$, $r^{\text{SL}*}$, $\pi_M^{\text{SL}*}$, and $p^{\text{SL}*}$ increase, (ii) $D_s^{\text{SL}*}$ and $\pi_R^{\text{SL}*}$ decrease.

Observation 2 shows that in the SL mode, when consumer preferences for leasing increase, the leasing demand increases but the purchasing demand decreases. Additionally, the total wholesale demand, the wholesale price, the leasing price, and the manufacturer's profits all rise, while the retailer's profits fall. This can be taken to mean that retailers cannot directly benefit from the rise in consumer preferences for leasing once their operational mode is changed from S to SL. Therefore, they generally lack the motivation to promote the leasing business. For example, after "Jingxiao zu" and "Guomei zuzu" launched the mobile phone leasing business (<https://prom.gome.com.cn/html/prodhtml/topics/201709/30/2461678680.html>, retrieved on 27 May 2022), they did not carry out leasing publicity on their platform websites and APP clients to guide customers to change their consumption concepts. Unlike retailers, manufacturers are always able to benefit from the increase in consumer preferences for leasing and are therefore more willing to promote leasing business.

Observation 3. In the SL mode, as r_e increases, (i) $D^{\text{SL}*}$, $D_l^{\text{SL}*}$, $w^{\text{SL}*}$, $p^{\text{SL}*}$, and $\pi_M^{\text{SL}*}$ increase, (ii) $D_s^{\text{SL}*}$ and $r^{\text{SL}*}$ decrease, and (iii) $\pi_R^{\text{SL}*}$ first decreases and then increases.

As shown in Observation 3, in the SL mode, the leasing demand for leased-returned electronic products increases as their residual value increases, while the purchasing demand decreases. However, as the total wholesale demand increases, wholesale and sales prices increase, the lease price decreases, and the manufacturer's profits increase. If the residual value of the leased-returned electronic product is larger than a certain threshold, the retailer's profits monotonously increase with the residual value. It is generally believed that retailers who offer mobile phones to customers through both selling and leasing will earn more profits if they lease or sell phones with higher residual values. However, since a higher wholesale price is typically associated with a larger residual value of the leased-returned electronic product, retailers who offer mobile phones to consumers through both selling and leasing may experience a decline in profits if they advise customers to lease mobile phones with higher residual value unless the residual value is greater than a certain threshold.

4. Comparisons of Equilibrium Results

This section compares the equilibrium results of the retailer's three alternative operational modes. Some analytical results are first derived by comparing the equilibrium price, demand, and profit. The equilibrium consumer surpluses are calculated and compared afterwards. The related conclusions are then analyzed and explained (These conclusions are only meaningful when $\alpha_0 \leq \alpha \leq \alpha_1$. Because in order to guarantee that the coexistence of leasing and purchasing demand for the electronic product and the retailer's hybrid selling-leasing business transformation make sense, condition $\alpha_0 \leq \alpha \leq \alpha_1$ needs to be satisfied).

Proposition 1. *The equilibrium price has the following properties: (i) $w^{\text{S}*} \geq w^{\text{SL}*} = w^{\text{L}*}$, (ii) $p^{\text{S}*} \geq p^{\text{SL}*} \geq r^{\text{SL}*} = r^{\text{L}*}$, and (iii) in the SL mode, define the portion of the selling price that exceeds the leasing price as $\Delta_0 = p^{\text{SL}*} - r^{\text{SL}*}$, which decreases as α increases, and increases as r_e increases.*

Proposition 1 (i) shows that in L and SL modes, wholesale prices of the electronic product are the same, which are lower than the wholesale prices in the S mode. For retailers only selling the electronic product, manufacturers should set relatively high wholesale prices. Proposition 1 (ii) shows that compared with the S mode, in the SL mode, the selling price is lower, which can be understood as that retailers should lower the selling price once their operational mode transforms from S to SL in order to prevent the leasing business from having a greater impact on the selling business. In S and SL modes, leasing prices are the same, and the retailer's leasing pricing is only related to the production cost, the residual value of leased-returned electronic product, and consumer preferences for leasing but has nothing to do with the operational modes. Proposition 1 (iii) shows that the larger the consumer preferences for leasing, the smaller the differences between leasing and selling prices, and the price difference increases with the rise of the residual value.

Brands such as Huawei, Apple, and other new 5G high-end smartphones have a large residual value and a significant price difference between leasing and selling prices. Therefore, these smartphones attract more customers to lease them.

Proposition 2. *The equilibrium demand has the following properties: (i) $D^{S*} \leq D^{SL*} = D^{L*}$, (ii) $D_s^{SL*} > D_s^{S*}$ when $\alpha < \alpha_2$, and $D_s^{SL*} \leq D_s^{S*}$ when $\alpha_2 \leq \alpha$, and (iii) $D_i^{SL*} \leq D_i^{L*}$. ($\alpha_2 = (1 + c - 2r_e/1 + c)$).*

Proposition 2 (i) shows that in SL and L modes, the wholesale demand for electronic products is relatively larger. The expansion of leasing business by retailers can boost the market's wholesale demand for electronic products. Proposition 2 (ii) shows that when consumer preferences for leasing are higher than α_2 , the purchasing demand for the electronic product will increase after the retailer's operational mode is transformed from S to SL. This shows that leasing has a certain promotion and erosion effect on selling. When consumer preferences for leasing are lower than a certain threshold, the promotion effect is greater than the erosion

effect. Otherwise, the erosion effect will be greater than the promotion effect, and the purchasing demand for the electronic product will decrease. Proposition 2 (iii) shows that in the L mode, the leasing demand for the electronic product is larger.

Proposition 3. *The equilibrium profits have the following properties:*

- (i) *Comparing manufacturer profits of different modes, there are conditions such as*
 - (i) $\pi_M^{S*} > \pi_M^{SL*} = \pi_M^{L*}$ when $\alpha_0 \leq \alpha < \alpha_3$,
 - (ii) $\pi_M^{S*} = \pi_M^{SL*} = \pi_M^{L*}$ when $\alpha = \alpha_3$,
 - (iii) $\pi_M^{S*} < \pi_M^{SL*} = \pi_M^{L*}$ when $\alpha_3 < \alpha \leq \alpha_1$.
- (ii) *Comparing retailer profits of different modes, there are conditions such as*
 - (i) $\pi_R^{SL*} > \pi_R^{S*} > \pi_R^{L*}$ when $\alpha_0 \leq \alpha < \alpha_3$,
 - (ii) $\pi_R^{SL*} > \pi_R^{L*} = \pi_R^{S*}$ when $\alpha = \alpha_3$,
 - (iii) $\pi_R^{SL*} > \pi_R^{L*} > \pi_R^{S*}$ when $\alpha_3 < \alpha \leq \alpha_1$.

$$\left(\alpha_3 = \frac{c^2 - 2r_e + 1 + \sqrt{c^4 - 4c^2r_e - 2c^2 + 8r_e c - 4r_e + 1}}{2} \right). \tag{4}$$

Comparison results of the manufacturer's profits under different modes are shown in Proposition 3 (i). In S and SL modes, the manufacturer's profits are the same. When consumer preferences for leasing are higher than α_3 , the manufacturer's profit is larger in S and SL modes. Otherwise, the manufacturer's profit is larger in the S mode. Comparison results of the retailer's profits under different modes are shown in Proposition 3 (ii). In the SL mode, the dual needs of consumers for leasing or purchasing the electronic product are met, and the retailer has the highest profit; when consumer preferences for leasing are less than α_3 , the retailer's profit is the smallest in the L mode; otherwise, the retailer's profit is the smallest in the S mode. Results demonstrate that when consumer preferences for leasing are within a certain range, after electronic products retailers' operational mode transforms from S/L to SL, retailer's profits increase. However, the manufacturer's profits also increase only when consumer preferences for leasing exceed a certain threshold within a certain range.

The equilibrium consumer surpluses in S, L, and SL modes are $CS^{S*} = \int_{p^{S*}}^1 (v - p^{S*})dv = ((1 - c)^2/32)$, $CS^{L*} = \int_{(r^{L*}/\alpha)}^1 (\alpha v - r^{L*})dv = ((\alpha + r_e - c)^2/32\alpha)$, and $CS^{SL*} = \int_{(r^{SL*}/\alpha)}^{(p^{SL*} - r^{SL*}/\alpha)} (p^{SL*} - r^{SL*}/\alpha)dv + \int_{(p^{SL*} - r^{SL*}/\alpha)}^1 (v - p^{SL*})dv = (3\alpha^3 + (2c + 6r_e - 7)\alpha^2 + (3r_e^2 + 2r_e c - 6r_e - c^2 - 2c + 4)\alpha + (c - r_e)^2/16\alpha(1 - \alpha))$, respectively.

Proposition 4. *The equilibrium consumer surpluses have the following properties:*

- (i) $CS^{SL*} > CS^{S*} > CS^{L*}$ when $\alpha_0 \leq \alpha < \alpha_3$,
- (ii) $CS^{SL*} > CS^{L*} = CS^{S*}$ when $\alpha = \alpha_3$,
- (iii) $CS^{SL*} > CS^{L*} > CS^{S*}$ when $\alpha_3 < \alpha \leq \alpha_1$.

Proposition 4 shows that in the SL mode, the dual consumer demand for leasing or purchasing the electronic products are met, and the equilibrium consumer surplus is the largest. When consumer preferences for leasing are less than α_3 , the equilibrium consumer surplus is the smallest in the L mode. Otherwise, it is the smallest in the S mode. Therefore, after electronic products retailers' operational mode transforms from S/L to SL, consumers can also benefit from having the choice of leasing or purchasing.

5. Numerical Analysis

To further understand the influence of the different parameters, the following numerical experiments that compare the equilibrium results of the above three alternative operation modes are designed.

5.1. Impact of Consumers' Preferences for Leasing. Without loss of generality, we set the production cost $c = 0.3$, and the residual value of leased-returned electronic product $r_e = 0.2$ [33]. According to Lemma 3 in Section 3.4,

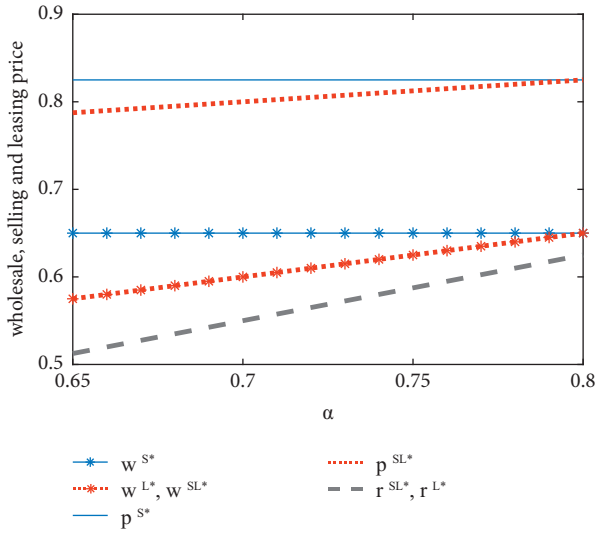


FIGURE 3: Impact of preferences on wholesale, selling, and leasing prices.

α is defined to be in the range $[0.65, 0.8]$ (In the SL mode, when $\alpha < 0.65$, no customers will choose to rent the products. When $\alpha > 0.8$, no customers will choose to purchase the products. Only when $0.65 \leq \alpha \leq 0.8$, some customers will choose to rent the products while other customers will choose to purchase the products.). The results are shown in Figures 3–7.

Figure 3 illustrates the selling, leasing, and wholesale prices of the electronic product under the three alternative operation modes. In the S mode, the wholesale price of the electronic product is higher. In SL and L modes, the wholesale and leasing prices of the electronic product are the same and increase with consumer preferences for leasing. After a retailer’s operational mode transforms from S to SL/L, the manufacturer reduces the wholesale price of the electronic product, and the retailer reduces the selling price. In the S mode, while consumer preference for leasing increases, leasing and selling prices of the electronic product increase, but the leasing and selling price gap narrows.

Figures 4 and 5 illustrate the wholesale demand, purchasing and leasing demands under the three alternative operation modes. In SL and L modes, the wholesale demand for the electronic product is relatively larger, consumer preferences for leasing increases, and the wholesale and leasing demands for the electronic product increase. When consumer preference for leasing is in the range $(0.65, 0.69]$, the purchasing demand for electronic product increases after the retailer’s operational mode transforms from S to SL/L.

Figure 6 shows that in SL and L modes, the manufacturer’s profits are the same. In the S mode, it is more profitable for the manufacturer when consumer preference for leasing is in the range $[0.65, 0.67)$. In SL and L modes, it is more profitable for the manufacturer when consumer preference for leasing is in the range $(0.67, 0.8]$. Figure 7 illustrates that in the SL mode, it is more profitable for the retailer when consumer preferences for leasing is in the range $(0.67, 0.8]$. The retailer can make maximum profits when consumer preference for leasing is 0.65. In the L mode,

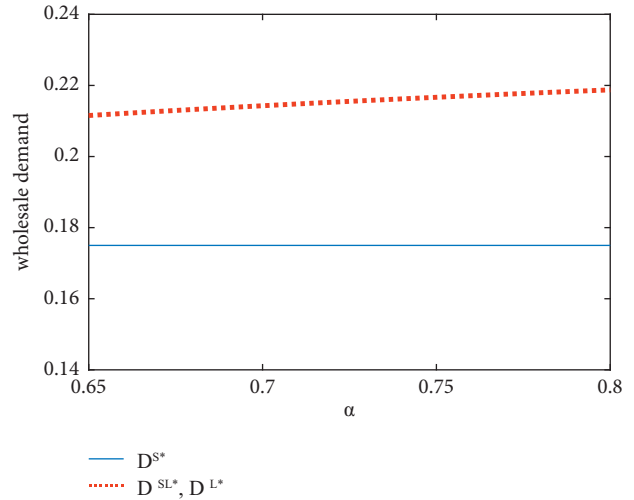


FIGURE 4: Impact of preferences on wholesale demand.

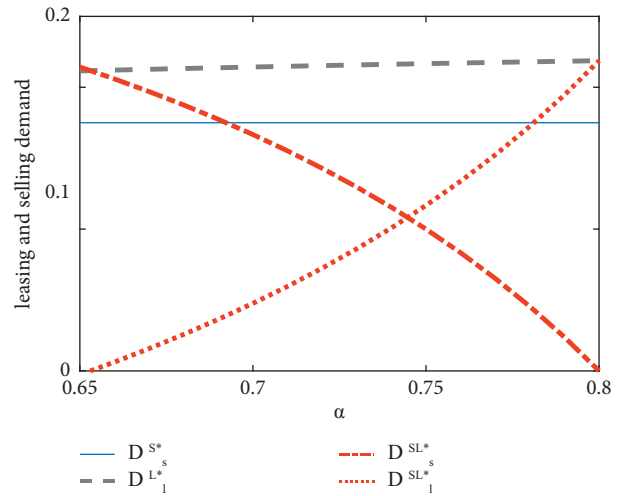


FIGURE 5: Impact of preferences on selling and leasing demand.

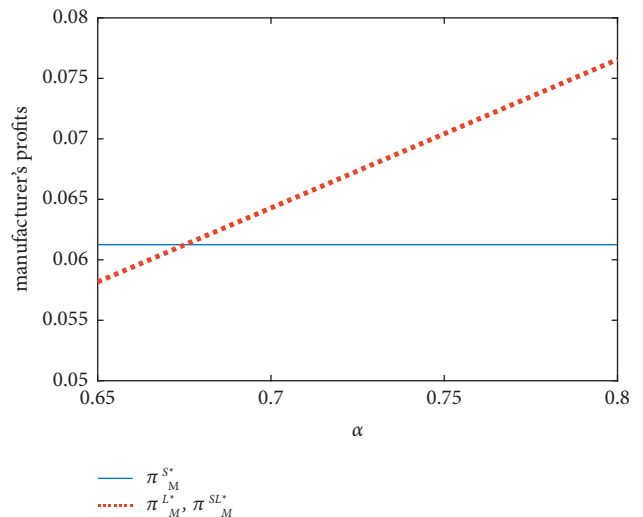


FIGURE 6: Impact of preferences on manufacturer’s profits.

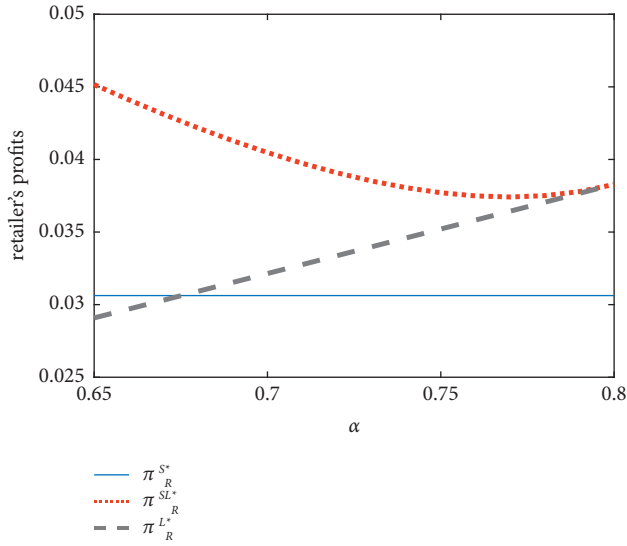


FIGURE 7: Impact of preferences on retailer's profits.

the retailer's profit is the smallest when consumer preference for leasing is in the range $[0.65, 0.67)$. In the S mode, the retailer's profit is the smallest when consumer preference for leasing is in the range $(0.67, 0.8]$. When consumer preferences for leasing increase, retailer profits decrease in the SL mode and increase in the L mode.

5.2. Impact of the Residual Value. The residual value of the leased-returned electronic product has a significant impact on the retailer's leasing decision, which is analyzed using numerical examples in this section. Let $c = 0.3$ and $\alpha = 0.7$ [25, 33]. In order to ensure the analysis is meaningful, according to Lemma 3, the condition that electronic products selling and purchasing demand exist simultaneously is $r_e \in [0.18, 0.3]$ (In the SL mode, when $r_e < 0.18$, no customers will choose to rent the products. When $r_e > 0.3$, no customers will choose to purchase the products. Only when $0.18 \leq r_e \leq 0.3$, some customers will choose to rent the products while other customers will choose to purchase the products.), then the equilibrium results under the three alternative operation modes are shown in Figures 8–13.

Figure 8 shows the relationship between the equilibrium wholesale, leasing, and selling prices with the residual value of the leased-returned electronic product. As the residual value increases, the wholesale price in the SL/L mode is also appropriately increased, but the wholesale price in the S mode is not affected. As the residual value increases, the leasing price gradually decreases, the selling prices in the S mode gradually increase, and the gap between leasing and selling prices gradually increases.

Figures 9 and 10 show the relationship between the manufacturer's equilibrium wholesale demand and the retailer's equilibrium leasing and purchasing demands with the residual value of leased-returned electronic product, respectively. As the residual value increases, the wholesale demand in the SL/L mode also gradually increases, but the wholesale demand in the mode S is not affected by the

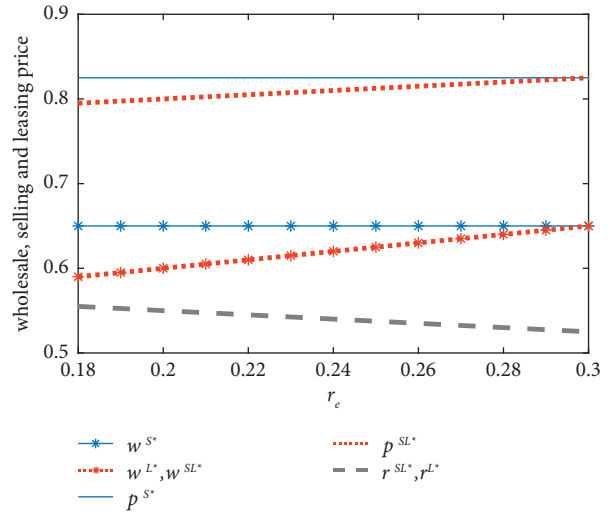


FIGURE 8: Impact of the residual value on wholesale, selling, and leasing prices.

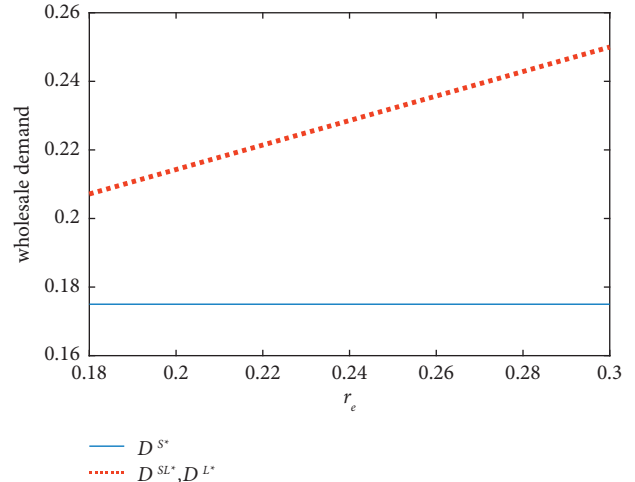


FIGURE 9: Impact of the residual value on wholesale demand.

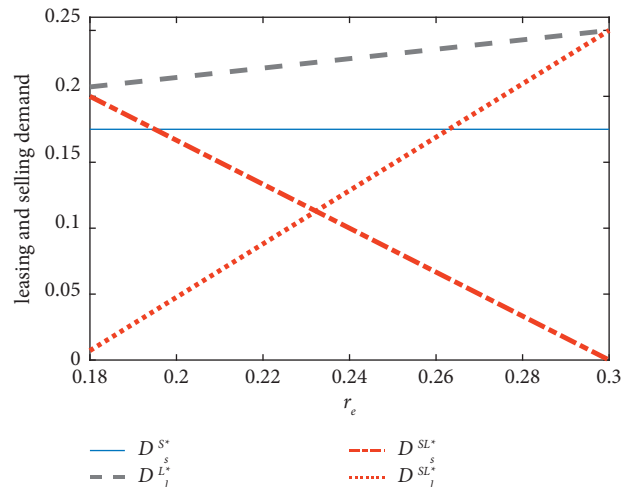


FIGURE 10: Impact of the residual value on selling and leasing demand.

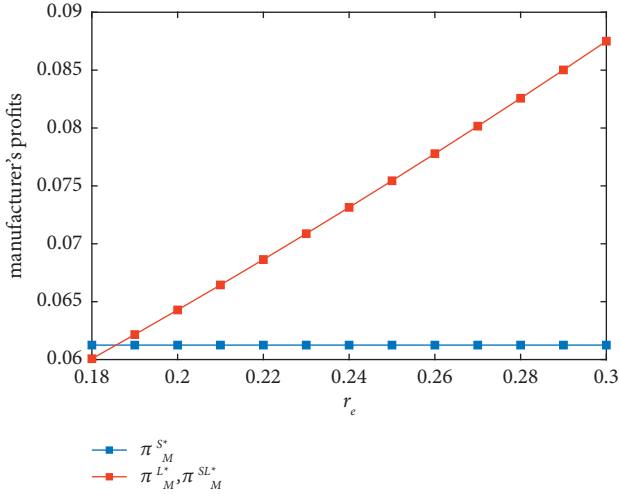


FIGURE 11: Impact of the residual value on manufacturer's profits.

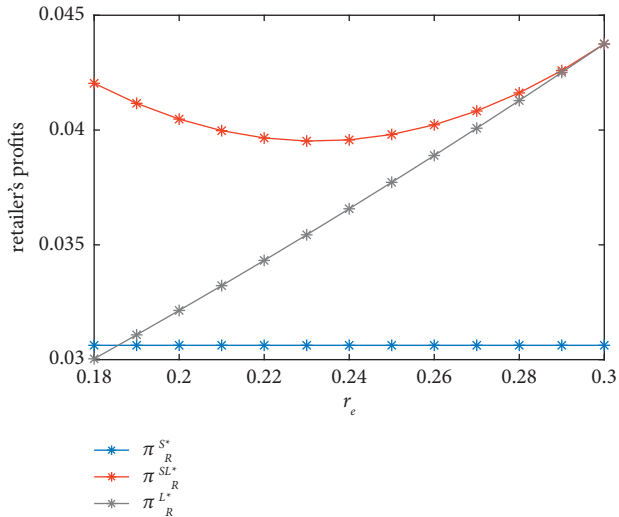


FIGURE 12: Impact of the residual value on retailer's profits.

residual value. As the residual value increases, the leasing demand gradually increases, and the purchasing demand in the SL mode gradually decreases.

Figures 11 and 12 show the relationship between the manufacturer's and retailer's equilibrium profits with the residual value of the leased-returned electronic product, respectively. As the residual value increases, the manufacturer's equilibrium profits in the SL/L mode gradually increase. Therefore, if manufacturers increase the residual value by modular design of electronic products, their equilibrium profits increase in the SL/L mode. As the residual value increases, the retailer's equilibrium profit first increases and then decreases in the SL mode, while the retailer's equilibrium profit increases in the L mode.

5.3. Consumer Surplus. In this section, the impact of leasing preferences and residual value on consumer surplus is examined. The same parameter settings are used as in the two previous sections. The results are shown in Figure 13.

As shown in Figure 13, there is a similar change trend between the consumer surplus and the retailer's profits, and the calculation shows that the consumer surplus is always half the retailer's profits. Therefore, the retailer's three leasing models cannot increase the acquisition of consumer surplus, and the retailer's increased profits after the operation model transformation depends entirely on the change of market size.

6. Extensions

The previous sections have discussed three alternative operational modes of electronic product retailers when the manufacturer and retailer make the decentralized decision. Results show that it is profitable for the retailer to transform the operational mode from S/L to SL when consumer preferences for leasing are within a certain range because both the consumer lease and purchase requirements are met after the transformation. If the retailer cooperates with the manufacturer and they make a centralized decision, the double marginal effect of the supply chain can be eliminated, the leasing and selling prices can be reduced, the conflicts in the leasing and selling market can be alleviated, and the overall profits of the supply chain can be improved. Samsung has partnered with "Xianghuanji" to launch a mobile phone leasing service in China. In Germany, Samsung and Grover conducted a mobile phone leasing pilot. The following constructs a cooperative selling-leasing model and designs a combined contract coordination pricing mechanism of "wholesale price discounts and revenue sharing" in order to achieve the cooperation between the manufacturer and retailer.

6.1. Cooperative Selling-Leasing Mode (C). In the C mode, the leasing and selling prices are determined with the objective of maximizing the profit in the supply chain. Let the total profit function of the supply chain be π^C ; thus, the following optimal decision model can be established:

$$\begin{aligned} \max_{p^C, r^C} \pi^C = & (p^C - c) \left(1 - \frac{p^C - r^C}{1 - \alpha} \right) \\ & + (r^C + r_e - c) \left(\frac{p^C - r^C}{1 - \alpha} - \frac{r^C}{\alpha} \right). \end{aligned} \quad (5)$$

Lemma 4. In the C mode, when $\alpha_4 \leq \alpha \leq \alpha_1$, the leasing and purchasing markets of the electronic product coexist. The equilibrium leasing and selling prices of the electronic product are $r^{C*} = (\alpha + c - r_e/2)$ and $p^{C*} = (1 + c/2)$. The equilibrium profit of the supply chain is $\pi^{C*} = (2\alpha^2 c - \alpha c^2 + 2\alpha c r_e - \alpha^2 - 2\alpha c + c^2 - 2c r_e + r_e^2 + \alpha/4(1 - \alpha)\alpha) \cdot (\alpha_4 = 1 - (r_e/c))$.

Proposition 5. In the C mode, there are (i) $\alpha_4 < \alpha_0$, (ii) $p^{S*} > p^{C*}$ and $\pi^{S*} < \pi^{C*}$ when $\alpha_4 \leq \alpha < \alpha_0$, and (iii) $p^{SL*} > p^{C*}$, $r^{SL*} > r^{C*}$, $\pi^{SL*} < \pi^{C*}$ when $\alpha_0 \leq \alpha \leq \alpha_1$.

Proposition 5 states that the range of consumer preferences for leasing in the coexistence of selling-leasing

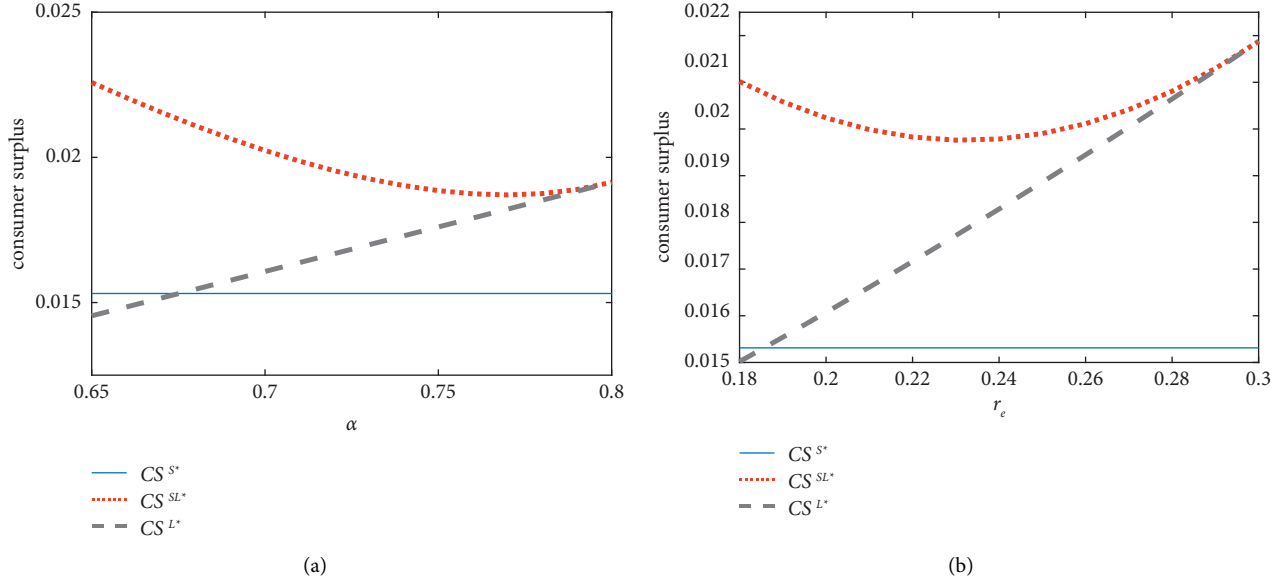


FIGURE 13: Impact of preferences and the residual value on consumer surplus.

markets is larger in the C mode than it is in the S mode, which is advantageous for the transformation of the selling-leasing business in the supply chain of electronic products. When $\alpha_4 \leq \alpha < \alpha_0$, the leasing market does not exist in the SL mode, while the leasing and selling markets coexist in the C mode. When $\alpha_0 \leq \alpha \leq \alpha_1$, the leasing and selling markets coexist in the SL/C mode, the leasing and selling prices of electronic products are lower, and the supply chain's profits are larger.

6.2. Coordination Contract. In order to make the profits of the supply chain operating in the mode SL equal to the

profits when operating in the C mode, a coordinated pricing mechanism of “wholesale price discounts and revenue sharing” combination contract is designed. Let this combination contract signed by electronic products manufacturer and retailer be $(f, \phi, w^{SC}, p^{SC}, r^C)$, f is the manufacturer's wholesale price discount, ϕ is the retailer's revenue sharing ratio, w^{SC} is the wholesale price, p^{SC} and r^{SC} are the selling and leasing prices under the contract, and the revised decision model becomes as follows:

$$\begin{aligned} \max_{w^{SC}} \pi_M^{SC} &= (w^{SC} f - c) \left(1 - \frac{r^{SC}}{\alpha}\right) + \left((p^{SC} - w^{SC}) \left(1 - \frac{p^{SC} - r^{SC}}{1 - \alpha}\right) + (r^{SC} + r_e - w^C) \left(\frac{p^{SC} - r^{SC}}{1 - \alpha} - \frac{r^{SC}}{\alpha}\right)\right) \phi, \\ \text{s.t. } \max_{p^{SC}, r^{SC}} \pi_R^{SC} &= \left((p^{SC} - w^{SC} f) \left(1 - \frac{p^{SC} - r^{SC}}{1 - \alpha}\right) + (r^{SC} + r_e - w^{SC} f) \left(\frac{p^{SC} - r^{SC}}{1 - \alpha} - \frac{r^{SC}}{\alpha}\right)\right) (1 - \phi). \end{aligned} \quad (6)$$

Backward induction is adopted to solve the equilibrium. The optimal response function of the retailer is $p^{SC*} = (1 + w^{SC} f/2)$ and $r^{SC*} = (\alpha - r_e + w^{SC} f/2)$. Let $p^{SC*} = p^{C*}$ and $r^{SC*} = r^{C*}$, then we obtain that $w^{SC*} = (\alpha + c + r_e/2)$ and $f^* = (2c/\alpha + c + r_e)$, and the coordination of supply chain is realized.

Lemma 5. Under the coordination contract, when $\alpha_4 \leq \alpha \leq \alpha_1$, the leasing and purchasing markets of the

electronic product coexist. The equilibrium wholesale, leasing and selling prices are $w^{SC*} = (\alpha + c + r_e/2)$, $r^{SC*} = (\alpha + c - r_e/2)$, and $p^{SC*} = (1 + c/2)$, respectively.

Proposition 6. When $\alpha_4 \leq \alpha < \alpha_0$ and $\phi_0 < \phi^* < \phi_1$, or $\alpha_0 \leq \alpha \leq \alpha_1$ and $\phi_2 < \phi^* < \phi_3$, in the coordinated pricing mechanism of portfolio contract $(f^*, \phi^*, w^{SC*}, p^{SC*}, r^{SC*})$, the profits of manufacturers and distributors can obtain Pareto improvement:

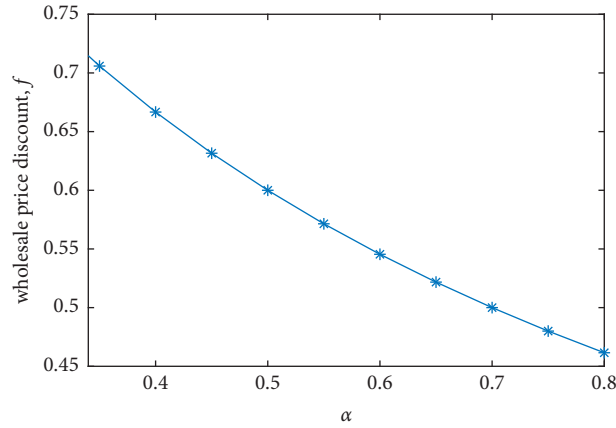


FIGURE 14: Impact of preferences on wholesale price discount.

$$\left(\begin{array}{l} \phi_0 = \frac{\alpha(1-\alpha)(1-c)^2}{2(2\alpha^2c - \alpha c^2 + 2\alpha cr_e - \alpha^2 - 2\alpha c + c^2 - 2cr_e + r_e^2 + \alpha)} \\ \phi_1 = \frac{\alpha^2c^2 + 6\alpha^2c - 5\alpha c^2 + 8\alpha cr_e - 3\alpha^2 - 6\alpha c + 4c^2 - 8cr_e + 4r_e^2 + 3\alpha}{4(2\alpha^2c - \alpha c^2 + 2\alpha cr_e - \alpha^2 - 2\alpha c + c^2 - 2cr_e + r_e^2 + \alpha)} \\ \phi_2 = \frac{(1-\alpha)(c-r_e-\alpha)^2}{2(2\alpha^2c - \alpha c^2 + 2\alpha cr_e - \alpha^2 - 2\alpha c + c^2 - 2cr_e + r_e^2 + \alpha)} \\ \phi_3 = \frac{3(1-\alpha)(c-r_e-\alpha)^2}{4(2\alpha^2c - \alpha c^2 + 2\alpha cr_e - \alpha^2 - 2\alpha c + c^2 - 2cr_e + r_e^2 + \alpha)} \end{array} \right). \quad (7)$$

Proposition 6 shows that the design of the “wholesale price discounts and revenue sharing” combination contract increases the range of consumer leasing preferences that the leasing and selling markets coexist, promotes the transformation of the retailer’s rental and sale business, and realizes the Pareto improvement of manufacturer’s and retailer’s profits.

The coordination contracts between the electronic product manufacturer and retailer are analyzed. The coordination contract is further analyzed through numerical simulation. The production cost is set to $c = 0.3$, and the residual value $r_e = 0.2$ [33]. According to Proposition 6, let the consumer preferences for leasing α be in the range of $[0.34, 0.8]$. Under the coordination contracts, the changes of wholesale price discount and selling-leasing revenue sharing ratio are shown in Figures 14 and 15, respectively.

Figure 14 shows that the wholesale price discount parameter of the combination contract decreases as consumer preferences for leasing increase. The areas marked in grey in Figure 15 are the areas where both the manufacturer and the retailer can obtain Pareto improvement through revenue sharing, and the upper bound and interval range of revenue sharing ratio parameters increase with the increase of consumer preferences for leasing. Therefore, under this set of parameters, the coordination contract between the

manufacturer and the retailer can achieve Pareto improvement when the revenue sharing ratio is roughly 0.6.

Observation 4. (i) As r_e increases, α_0 , α_1 , α_2 , α_3 , and α_4 decrease; (ii) Define $\Delta_1 = \alpha_1 - \alpha_0$, and $\Delta_2 = \alpha_1 - \alpha_4$. As r_e increases, Δ_1 and Δ_2 increase.

Observation 4 shows that when r_e increases, preference thresholds (α_0 , α_1) of retailer’s SL mode transformation decrease, preference threshold (α_2) of a drop in purchasing demand decreases, threshold (α_3) of an increase in the manufacturer’s profit decreases, and preference thresholds (α_4 , α_1) of retailer’s C mode transformation decrease, and $[\alpha_0, \alpha_1]$ and $[\alpha_4, \alpha_1]$ are preference spaces of retailer’s SL and C mode selection. When r_e increases, preference spaces of retailer’s SL and C mode selection (Δ_1, Δ_2) increase. In order to make more profit, Proposition 3 shows that when $\alpha_0 \leq \alpha \leq \alpha_1$, the retailer should choose the SL mode, whereas when $\alpha > \alpha_1$, the retailer should choose the L mode. Combined with Proposition 3, Observation 4 can be deeply interpreted as when r_e increases, retailers are more likely to lease electronic products in order to make more profit. This explains why retailers prefer to offer rental service for Apple’s new phones (because their residual value is higher). If retailers lease electronic products with higher residual value, their purchasing demand is more likely to be negatively affected. If the

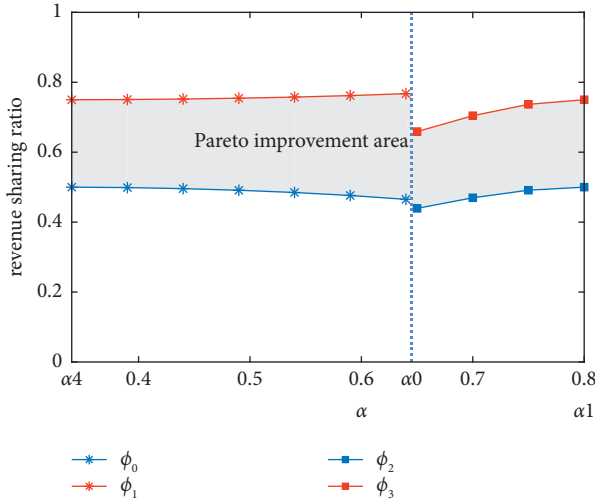


FIGURE 15: Impact of preferences on revenue sharing.

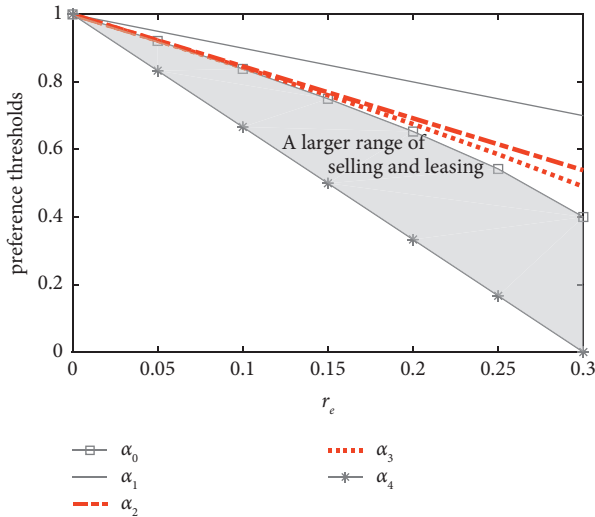


FIGURE 16: Impact of the residual value on preference thresholds.

electronic products' residual value is higher, manufacturers' profit is more likely to be positively affected.

The production cost is also set to $c = 0.3$ [33]. According to Observation 4, preference thresholds ($\alpha_0, \alpha_1, \alpha_2, \alpha_3, \alpha_4$) are shown in Figure 16.

Figure 16 shows that when r_e increases, $\alpha_0, \alpha_1, \alpha_2, \alpha_3,$ and α_4 decrease, and Δ_1 and Δ_2 increase. As r_e increases, the range of consumer leasing preferences that the leasing and selling markets coexist becomes larger, and if the retailer cooperates with the manufacturer, the range of consumer leasing preferences that the leasing and selling markets coexist becomes larger. In a word, the increase of residual value, as well as supply chain cooperation, can promote the retailer's hybrid selling-leasing business transformation.

7. Conclusion

Electronics retailers can turn into purely rental businesses; they can stop selling their goods and limit their services to

renting them out to customers. They can also open up the leasing option to consumers while maintaining their original sales business. In this study, considering consumer preferences for leasing, electronics retailer's three alternative operational modes were compared: pure selling, pure leasing, and hybrid selling-leasing. Our study primarily focused on how consumer preferences for leasing affect retailers' operational selection. Additionally, the consumer surplus and upstream manufacturer profits were analyzed. Furthermore, a cooperative hybrid selling-leasing mode was examined and a "wholesale price discounts and revenue sharing" coordination contract based on the hybrid selling-leasing mode was designed.

The retailer's selection was analyzed using a mathematical model and numerical examples. The key findings can be summarized as follows: (1) For the retailer, the pure leasing mode is better than the pure selling mode as long as the consumer preferences for leasing are not very low, but the hybrid selling-leasing mode is always the best when the consumer's leasing preferences are within a certain range; (2) for the manufacturer, the hybrid selling-leasing mode is always the same as the pure leasing mode, and the leasing mode is always better than the selling mode, as long as the consumer preference for leasing is not too low; (3) the hybrid selling-leasing mode is always beneficial to both retailers and consumers when consumer preferences for leasing are within a certain range because it offers numerous choices to customers. Therefore, when the leasing preference and residual value are not small, the manufacturer has no incentive to prevent the retailer from transforming its operational mode; (4) in the hybrid selling-leasing mode, the wholesale, selling, and leasing prices increase, the manufacturer's profits increase, but the retailer's profits decrease, as the consumer preferences for leasing increase; (5) the use of "wholesale price discounts and revenue sharing" contracts can promote the retailer's hybrid selling-leasing business transformation and achieve Pareto improvement in both the retailer's and the manufacturer's profits; (6) the increase of residual value, as well as supply chain cooperation, can promote the retailer's hybrid selling-leasing business transformation.

On the other hand, it is noteworthy to mention that this study has some limitations. First, a monopoly market with only one manufacturer and one retailer was considered. This setting is in line with the practice that JD controls the majority of online market share of Apple's iPhones. However, it may be interesting to incorporate the competition between multiple manufacturers and retailers. Second, a retailer that only leases new electronic products in a certain leasing period was considered. This setting is in line with the practice that Dixintong leases only new mobile phones for one year, but other retailers also lease second-hand electronic products and offer leasing services with varying lease terms, so future research can incorporate these factors as well. Third, this study focuses on retailer's operational mode transformation considering consumer preferences for leasing and residual value of the leased-returned electronic product. Considering how retailers get the residual value is also an interesting problem to investigate through releasing,

through resale, or simply through recycling. Finally, faced with the risk-averse behavior of consumers and retailers, the optimal pricing strategy for retailers is also worth studying.

Appendix

Proof of Lemma 1. Backward induction is used to derive the equilibrium outcomes. In the S mode, the retailer's profit is $\pi_R^S = (p^S - w^S)D_s^S = (p^S - w^S)(1 - p^S)$. $(\partial^2 \pi_R^S / \partial^2 p^S) = -1 < 0$, so the retailer's profit is concave in p^S . According to the first-order conditions, we have $p^{S*} = (1 + w^S/2)$. Substituting p^{S*} to the manufacturer's profit function, we have $\pi_M^S = (1 - w^S)(w^S - c)$ and $(\partial^2 \pi_M^S / \partial^2 w^S) = -1 < 0$, so the manufacturer's profit is concave in w^S . According to the first-order conditions, we have $w^{S*} = (1 + c/2)$. Then the equilibrium outcomes in the S mode can be derived immediately. \square

Proof of Lemma 2. Backward induction is used to derive the equilibrium outcomes. In the L mode, the retailer's profit is $\pi_R^L = (r^L + r_e - w^L)D_l^L = (r^L + r_e - w^L)(1 - (r^L/\alpha))$. $(\partial^2 \pi_R^L / \partial^2 r^L) = -1 < 0$, so the retailer's profit is concave in r^L . According to the first-order conditions, we have $r^{L*} = (\alpha - r_e + w^L/2)$. Substituting r^{L*} to the manufacturer's profit function, we have $\pi_M^L = ((\alpha + r_e - w^L)(w^L - c)/2\alpha)$, $(\partial^2 \pi_M^L / \partial^2 w^L) = -1 < 0$, so the manufacturer's profit is concave in w^L . According to the first-order conditions, we have $w^{L*} = (\alpha + c + r_e/2)$. Then the equilibrium outcomes in the L mode can be derived immediately. \square

Proof of Lemma 3. Backward induction is used to derive the equilibrium outcomes. In the SL mode, the retailer's profit is $\pi_R^{SL} = (p^{SL} - w^{SL})D_s^{SL} + (r^{SL} + r_e - w^{SL})D_l^{SL} = (p^{SL} - w^{SL})(1 - (p^{SL} - r^{SL}/1 - \alpha)) + (r^{SL} + r_e - w^{SL})((p^{SL} - r^{SL}/1 - \alpha) - (r^{SL}/\alpha))$. The π_R^{SL} Hessian matrix about r^{SL} and p^{SL} is H , and $H = \begin{pmatrix} (\partial^2 \pi_R^{SL} / \partial^2 r^{SL}) & (\partial^2 \pi_R^{SL} / \partial r^{SL} \partial p^{SL}) \\ (\partial^2 \pi_R^{SL} / \partial p^{SL} \partial r^{SL}) & (\partial^2 \pi_R^{SL} / \partial^2 p^{SL}) \end{pmatrix}$. $(\partial^2 \pi_R^{SL} / \partial^2 r^{SL}) = (-2/\alpha(1 - \alpha)) < 0$ and $|H| = \begin{vmatrix} (-2/\alpha(1 - \alpha)) & (2/1 - \alpha) \\ (2/1 - \alpha) & (-2/1 - \alpha) \end{vmatrix} > 0$. So the retailer's profit is concave in r^{SL} and p^{SL} . According to the first-order conditions, we have $r^{SL*} = (\alpha - r_e + w^L/2)$ and $p^{SL*} = (1 + w^{SL}/2)$. Substituting r^{SL*} and p^{SL*} to the manufacturer's profit function, manufacturer's profit is concave in w^{SL} . According to the first-order conditions, we have $w^{SL*} = (\alpha + c + r_e/2)$. Then the equilibrium outcomes in the SL mode can be derived immediately. \square

Proof of Observation 1

$$\begin{aligned} \frac{\partial w^{L*}}{\partial \alpha} & \\ \frac{\partial r^{L*}}{\partial r_e} &= -\frac{1}{4} < 0, \\ \frac{\partial D^{L*}}{\partial r_e} &= \frac{\partial D_l^{L*}}{\partial r_e} = \frac{1}{4\alpha} > 0, \\ \frac{\partial \pi_M^{L*}}{\partial r_e} &= \frac{\alpha + r_e - c}{4\alpha} > 0, \\ \frac{\partial \pi_R^{L*}}{\partial r_e} &= \frac{\alpha + r_e - c}{8\alpha} > 0, \\ \frac{\partial w^{L*}}{\partial r_e} &= \frac{1}{2} > 0, \\ \frac{\partial r^{L*}}{\partial \alpha} &= \frac{3}{4} > 0, \\ \frac{\partial D^{L*}}{\partial \alpha} &= \frac{\partial D_l^{L*}}{\partial \alpha} = \frac{1}{4} > 0, \\ \frac{\partial \pi_M^{L*}}{\partial \alpha} &= \frac{(\alpha + r_e - c)(\alpha - r_e + c)}{8\alpha^2} > 0, \\ \frac{\partial \pi_R^{L*}}{\partial r_e} &= \frac{(\alpha + r_e - c)(\alpha - r_e + c)}{16\alpha^2} > 0. \end{aligned} \tag{A.1}$$

Proof of Observation 2. When $\alpha_0 \leq \alpha \leq \alpha_1$, $(\partial D^{SL*} / \partial \alpha) = (c - r_e/4\alpha^2) > 0$, $(\partial D_l^{SL*} / \partial \alpha) = ((c + r_e)\alpha^2 + (-2c + 2r_e)\alpha + c - r_e/4\alpha^2(1 - \alpha)^2) > 0$, $(\partial D^{SL*} / \partial \alpha) = (-r_e/2(1 - \alpha)^2) < 0$, $(\partial w^{SL*} / \partial \alpha) = (1/2) > 0$, $(\partial p^{SL*} / \partial \alpha) = (1/4) > 0$, and $(\partial r^{SL*} / \partial \alpha) = (3/4) > 0$, then $\pi_M^{SL*} = (w^{SL*} - c)D^{SL*}$, then w^{SL*} and D^{SL*} increase with α , so π_M^{SL*} increases with α because $(\partial \pi_R^{SL*} / \partial \alpha) = (\nabla/16\alpha^2(1 - \alpha)^2)$, where $\nabla = -3\alpha^4 + 6\alpha^3 + (-c^2 + 2r_e c + 3r_e^2 - 3)\alpha^2 + 2(c - r_e)^2\alpha - (c - r_e)^2$, so $(\partial \nabla / \partial c) = -2(1 - \alpha)^2(c - r_e) < 0$, ∇ decreases as c increases. $\nabla = -3\alpha^4 + 6\alpha^3 - 3\alpha^2$ is maximum when $c = 0$, and $-3\alpha^4 + 6\alpha^3 - 3\alpha^2 < 0$, $(\partial \pi_R^{SL*} / \partial \alpha) < 0$, so π_R^{SL*} decreases as α increases. \square

Proof of Observation 3

$$\begin{aligned}
 & \frac{\partial w^{SL*}}{\partial r_e} \\
 & \frac{\partial p^{SL*}}{\partial r_e} = \frac{1}{4} > 0, \\
 & \frac{\partial r^{SL*}}{\partial r_e} = -\frac{1}{4} < 0, \\
 & \frac{\partial D^{SL*}}{\partial r_e} = \frac{1}{4\alpha} > 0, \\
 & \frac{\partial D_l^{SL*}}{\partial r_e} = \frac{1+\alpha}{4\alpha(1-\alpha)} > 0, \\
 & \frac{\partial D_s^{SL*}}{\partial r_e} = \frac{-1}{2(1-\alpha)} < 0, \\
 & \frac{\partial \pi_M^{SL*}}{\partial r_e} = \frac{\alpha+r_e-c}{4\alpha} > 0, \\
 & \frac{\partial \pi_R^{SL*}}{\partial r_e} = \frac{(3\alpha+1)r_e+3\alpha^2+c\alpha-3\alpha-c}{8\alpha(1-\alpha)}, \\
 & \text{when } r_e < -\frac{3\alpha^2+c\alpha-3\alpha-c}{3\alpha+1}, \\
 & \frac{\partial \pi_R^{SL*}}{\partial r_e} < 0, \\
 & \text{when } r_e > -\frac{3\alpha^2+c\alpha-3\alpha-c}{3\alpha+1}, \\
 & \frac{\partial \pi_R^{SL*}}{\partial r_e} > 0.
 \end{aligned} \tag{A.2}$$

Proof of Proposition 1

- (i) $w^{SL*} = w^{L*} = (\alpha + r_e + c/2)$, $w^{SL*} - w^{S*} = (\alpha + r_e + c/2) - (1 + c/2) = (\alpha + r_e - 1/2)$, and because $\alpha \leq \alpha_1 = 1 - r_e$, we have $\alpha + r_e - 1 \leq 0$, so $w^{S*} \geq w^{SL*} = w^{L*}$.
- (ii) $r^{SL*} = r^{L*} = (3\alpha + c - r_e/4)$, $p^{SL*} - p^{S*} = (2 + \alpha + c + r_e/4) - (3 + c/4) = (\alpha + r_e - 1/4) \leq 0$, so $p^{S*} \geq p^{SL*} \geq r^{SL*} = r^{L*}$.
- (iii) $\Delta_0 = p^{SL*} - r^{SL*} = (1 - \alpha + r_e/2)$, $(\partial \Delta_0 / \partial \alpha) = -(1/2) < 0$, and $(\partial \Delta_0 / \partial r_e) = (1/2) > 0$. \square

Proof of Proposition 2

- (i) As shown in Lemma 1 and Proposition 1, $(r^{SL*} / \alpha) \leq p^{SL*} \leq p^{S*}$, i.e., $1 - p^{S*} \leq 1 - p^{SL*} \leq 1 - (r^{SL*} / \alpha)$, and because $D^{S*} = 1 - p^{S*}$, $D^{SL*} = D^{L*} = 1 - (r^{SL*} / \alpha)$, so $D^{S*} \leq D^{SL*} = D^{L*}$.

- (ii) $D_s^{SL*} - D_s^{S*} = (1 + c - 2r_e - (1 + c)\alpha/4(1 - \alpha))$, and let $1 + c - 2r_e - (1 + c)\alpha = 0$, so $\alpha_2 = (1 + c - 2r_e/1 + c)$, $\alpha_0 < \alpha_2 < \alpha_1$ can be obtained by comparison; if $\alpha_0 \leq \alpha < \alpha_2$, then $D_s^{SL*} > D_s^{S*}$; if $\alpha = \alpha_2$, then $D_s^{SL*} = D_s^{S*}$; if $\alpha_2 \leq \alpha < \alpha_1$, then $D_s^{SL*} < D_s^{S*}$.
- (iii) $D_l^{L*} - D_l^{SL*} = (\alpha + r_e - c/4\alpha) - (\alpha^2 - (1 - c - r_e)\alpha - (c - r_e)/4\alpha(1 - \alpha)) = (1 - \alpha - r_e/2(1 - \alpha)) \geq 0$, so $D_l^{SL*} \leq D_l^{L*}$. \square

Proof of Proposition 3

- (i) $\pi_M^{SL*} = \pi_M^{L*}$, $\pi_M^{SL*} - \pi_M^{S*} = (\alpha^2 + (-c^2 + 2r_e - 1)\alpha + (c - r_e)^2/8\alpha)$, and define $\alpha^2 + (-c^2 + 2r_e - 1)\alpha + (c - r_e)^2 = 0$, so $\alpha_3 = (c^2 - 2r_e + 1 + \sqrt{c^4 - 4c^2r_e - 2c^2 + 8r_e c - 4r_e + 1/2})$, so if $\alpha_0 \leq \alpha < \alpha_3$, then $\pi_M^{S*} > \pi_M^{SL*} = \pi_M^{L*}$; if $\alpha = \alpha_3$, then $\pi_M^{S*} = \pi_M^{SL*} = \pi_M^{L*}$; and if $\alpha_3 < \alpha \leq \alpha_1$, then $\pi_M^{S*} < \pi_M^{SL*} = \pi_M^{L*}$.
- (ii) $\pi_R^{SL*} - \pi_R^{S*} = (3\alpha^3 + (c^2 + 6r_e - 6)\alpha^2 + (3r_e^2 + 2r_e c - 6r_e - 2c^2 + 3)\alpha + (c - r_e)^2/16\alpha(1 - \alpha)) \geq 0$, and π_R^{SL*} decreases as α increases; when $\alpha = 1 - r_e$, π_R^{SL*} takes the minimum value, and when $\alpha = 1 - r_e$, $\pi_R^{SL*} - \pi_R^{S*} = (r_e^2(1 - c)^2/16\alpha(1 - \alpha)) \geq 0$, so $\pi_R^{SL*} \geq \pi_R^{S*}$; $\pi_R^{SL*} - \pi_R^{L*} = ((\alpha + r_e - 1)^2/4(1 - \alpha)) \geq 0$, so $\pi_R^{SL*} \geq \pi_R^{L*}$; if $\pi_R^{L*} - \pi_R^{S*} = ((\alpha + r_e - c)^2/16\alpha) - ((1 - c)^2/16) = (\alpha^2 + (-c^2 + 2r_e - 1)\alpha + (c - r_e)^2/16\alpha)$, define $\alpha^2 + (-c^2 + 2r_e - 1)\alpha + (c - r_e)^2 = 0$, so $\alpha_3 = (c^2 - 2r_e + 1 + \sqrt{c^4 - 4c^2r_e - 2c^2 + 8r_e c - 4r_e + 1/2})$; so when $\alpha_0 \leq \alpha < \alpha_3$, then $\pi_R^{SL*} > \pi_R^{S*} > \pi_R^{L*}$; when $\alpha = \alpha_3$, then $\pi_R^{SL*} > \pi_R^{L*} = \pi_R^{S*}$; when $\alpha_3 < \alpha \leq \alpha_1$, then $\pi_R^{SL*} > \pi_R^{L*} > \pi_R^{S*}$. \square

Proof of Proposition 4. The proof of Proposition 4 is the same as the proof of Proposition 3. \square

Proof of Proposition 5

- (i) $\alpha_0 - \alpha_4 = (1 - c - r_e + \sqrt{c^2 + 2cr_e + r_e^2 + 2c - 6r_e + 1}/2) - (1 - (r_e/c)) = (c\sqrt{c^2 + 2cr_e + r_e^2 + 2c - 6r_e + 1} - c^2 - cr_e - c + 2r_e/2c) > 0$.
- (ii) When $\alpha_4 \leq \alpha < \alpha_0$, $p^{S*} - p^{C*} = (1 - c/4) > 0$, then $\pi^{C*} - \pi^{S*} = ((-3c^2 - 2c + 1)\alpha^2 + (-1 + 7c^2 - 8r_e c + 2c)\alpha - 4(c - r_e)^2/16(-1 + \alpha)\alpha) > 0$.
- (iii) When $\alpha_0 \leq \alpha \leq \alpha_1$, then $p^{SL*} - p^{C*} = (\alpha + r_e - c/4) > 0$, $r^{SL*} - r^{C*} = (\alpha + r_e - c/4) > 0$, and $\pi^{C*} - \pi^{SL*} = ((\alpha + r_e - c)^2/16\alpha)$. \square

Proof of Proposition 6. Under the coordination mechanism $(f^*, \phi^*, w^{SC*}, p^{C*}, r^{C*})$, the profit of the electronic product supply chain reaches the level of centralized decision-making. When $\alpha_4 \leq \alpha < \alpha_0$, leasing markets that do not exist at the time of decentralized decision-making arise at the time of centralized decision-making. Therefore, in order to facilitate the selling-leasing cooperation between the retailer and the manufacturer, the combination contract shall

guarantee $\pi_M^{SC*} > \pi_M^{S*}$ and $\pi_R^{SC*} > \pi_R^{S*}$. From this calculation, the value range of available ϕ is $\phi_0 < \phi^* < \phi_1$. When $\alpha_0 \leq \alpha \leq \alpha_1$, the portfolio contract is approximately guaranteed to $\pi_M^{SC*} > \pi_M^{SL*}$ and $\pi_R^{SC*} > \pi_R^{SL*}$. From this calculation, the value range of available ϕ is $\phi_2 < \phi^* < \phi_3$. $\phi_0 = (\pi_M^{S*}/\pi_M^{SC*}) = (\alpha(1-\alpha)(1-c)^2/2(2\alpha^2c - \alpha c^2 + 2\alpha cr_e - \alpha^2 - 2\alpha c + c^2 - 2cr_e + r_e^2 + \alpha))$, $\phi_1 = 1 - (\pi_R^{S*}/\pi_R^{SC*}) = (\alpha^2c^2 + 6\alpha^2c - 5\alpha c^2 + 8\alpha cr_e - 3\alpha^2 - 6\alpha c + 4c^2 - 8cr_e + 4r_e^2 + 3\alpha/4(2\alpha^2c - \alpha c^2 + 2\alpha cr_e - \alpha^2 - 2\alpha c + c^2 - 2cr_e + r_e^2 + \alpha))$, $\phi_2 = (\pi_M^{SL*}/\pi_M^{SC*}) = ((1-\alpha)(c-r_e-\alpha)^2/2(2\alpha^2c - \alpha c^2 + 2\alpha cr_e - \alpha^2 - 2\alpha c + c^2 - 2cr_e + r_e^2 + \alpha))$, and $\phi_3 = 1 - (\pi_R^{SL*}/\pi_R^{SC*}) = (3(1-\alpha)(c-r_e-\alpha)^2/4(2\alpha^2c - \alpha c^2 + 2\alpha cr_e - \alpha^2 - 2\alpha c + c^2 - 2cr_e + r_e^2 + \alpha))$. \square

Proof of Observation 4

- (i) $(\partial\alpha_0/\partial r_e) = (-\sqrt{r_e^2 + (2c-6)r_e + (c+1)^2} + r_e + c - 3/2\sqrt{r_e^2 + (2c-6)r_e + (c+1)^2}) < 0$, $(\partial\alpha_1/\partial r_e) = -1 < 0$, $(\partial\alpha_2/\partial r_e) = (-2/1+c) > 0$, $(\partial\alpha_3/\partial r_e) = -1 - ((c-1)^2/\sqrt{(c-1)^2(c^2+2c-4r_e+1)}) < 0$, and $(\partial\alpha_4/\partial r_e) = -1$.
- (ii) $\Delta_1 = \alpha_1 - \alpha_0$, $\Delta_2 = \alpha_1 - \alpha_4$ $(\partial\Delta_1/\partial r_e) = (-\sqrt{r_e^2 + (2c-6)r_e + (c+1)^2} - r_e - c + 3/2\sqrt{r_e^2 + (2c-6)r_e + (c+1)^2}) > 0$, and $(\partial\Delta_2/\partial r_e) = (1-c/c) > 0$. \square

Data Availability

The simulation data used to support the findings of this study are included within the article.

Conflicts of Interest

The authors declare that they have no conflicts of interest.

Acknowledgments

This research was funded by the National Social Science Foundation of China (Grant no. 18BJY009).

References

- [1] Q. Tan, X. Zeng, W. L. Ijomah, L. Zheng, and J. Li, "Status of end-of-life electronic product remanufacturing in China," *Journal of Industrial Ecology*, vol. 18, no. 4, pp. 577–587, 2014.
- [2] A. Raihanian Mashhadi, A. Vedantam, and S. Behdad, "Investigation of consumer's acceptance of product-service-systems: a case study of cell phone leasing," *Resources, Conservation and Recycling*, vol. 143, no. 4, pp. 36–44, 2019.
- [3] Y. Yu, Y. Dong, and X. Guo, "Pricing for sales and per-use rental services with vertical differentiation," *European Journal of Operational Research*, vol. 270, no. 2, pp. 586–598, 2018.
- [4] J. Li, H. Wang, Z. Deng, W. Zhang, and G. Zhang, "Leasing or selling? The channel choice of durable goods manufacturer considering consumers' capital constraint," *Flexible Services and Manufacturing Journal*, vol. 34, no. 2, pp. 317–350, 2021.
- [5] S. M. Gilbert, R. S. Randhawa, and H. Sun, "Optimal per-use rentals and sales of durable products and their distinct roles in price discrimination," *Production and Operations Management*, vol. 23, no. 3, pp. 393–404, 2014.
- [6] S. R. Bhaskaran and S. M. Gilbert, "Selling and leasing strategies for durable goods with complementary products," *Management Science*, vol. 51, no. 8, pp. 1278–1290, 2005.
- [7] Y. Dou, Y. J. Hu, and D. J. Wu, "Selling or leasing? Pricing information goods with depreciation of consumer valuation," *Information Systems Research*, vol. 28, no. 3, pp. 585–602, 2017.
- [8] K. Jia, X. Liao, and J. Feng, "Selling or leasing? Dynamic pricing of software with upgrades," *European Journal of Operational Research*, vol. 266, no. 3, pp. 1044–1061, 2018.
- [9] J. Zhang and A. Seidmann, "Perpetual versus subscription licensing under quality uncertainty and network externality effects," *Journal of Management Information Systems*, vol. 27, no. 1, pp. 39–68, 2010.
- [10] J. Liu, M. Wan, W. Jiang, and J. Zhang, "How does leasing affect green product design?" *Mathematical Problems in Engineering*, vol. 2019, no. 8, Article ID 5780342, 16 pages, 2019.
- [11] C. S. Tang and S. Deo, "Rental price and rental duration under retail competition," *European Journal of Operational Research*, vol. 187, no. 3, pp. 806–828, 2008.
- [12] N. N. Chau and S. A. Schulz, "Selling versus leasing of durable goods: the impact on marketing channels," *Journal of Marketing Channels*, vol. 21, no. 1, pp. 4–17, 2014.
- [13] P. S. Desai and D. Purohit, "Competition in durable goods markets: the strategic consequences of leasing and selling," *Marketing Science*, vol. 18, no. 1, pp. 42–58, 1999.
- [14] X. H. Wang, L. F. Xie, Q. Dong, H. L. Liu, Y. P. Huang, and Z. S. Liu, "A game-theory analysis of optimal leasing and selling strategies of durable goods in duopoly markets," *Canadian Social Science*, vol. 11, no. 4, pp. 127–135, 2015.
- [15] S. R. Bhaskaran and S. M. Gilbert, "Implications of channel structure and operational mode upon a manufacturer's durability choice," *Production and Operations Management*, vol. 24, no. 7, pp. 1071–1085, 2015.
- [16] Y. Xiong, W. Yan, K. Fernandes, Z. K. Xiong, and N. Guo, "'Bricks vs. Clicks': the impact of manufacturer encroachment with a dealer leasing and selling of durable goods," *European Journal of Operational Research*, vol. 217, no. 1, pp. 75–83, 2012.
- [17] S. R. Bhaskaran and S. M. Gilbert, "Implications of channel structure for leasing or selling durable goods," *Marketing Science*, vol. 28, no. 5, pp. 918–934, 2009.
- [18] S. S. Kalantari, M. Esmaeili, and A. A. Taleizadeh, "Selling by clicks or leasing by bricks? A dynamic game for pricing durable products in a dual-channel supply chain," *Journal of Industrial and Management Optimization*, no. 1, pp. 1–32, 2021.
- [19] V. V. Agrawal, M. Ferguson, L. B. Toktay, and V. M. Thomas, "Is leasing greener than selling?" *Management Science*, vol. 58, no. 3, pp. 523–533, 2012.
- [20] V. Agrawal, A. Atasu, and S. Ülkü, "Leasing, modularity, and the circular economy," *Management Science*, vol. 67, no. 11, pp. 6782–6802, 2021.
- [21] N. Aras, R. Güllü, and S. Yürülmez, "Optimal inventory and pricing policies for remanufacturable leased products," *International Journal of Production Economics*, vol. 133, no. 1, pp. 262–271, 2011.
- [22] P. Desai and D. Purohit, "Leasing and selling: optimal marketing strategies for a durable goods firm," *Management Science*, vol. 44, pp. 19–34, 1998.

- [23] D. Purohit and R. Staelin, "Rentals, sales, and buybacks: managing secondary distribution channels," *Journal of Marketing Research*, vol. 31, no. 3, pp. 325–338, 1994.
- [24] Y. Li, X. Bai, and K. Xue, "Business modes in the sharing economy: how does the OEM cooperate with third-party sharing platforms?" *International Journal of Production Economics*, vol. 221, no. 3, pp. 1–17, 2020.
- [25] M. Jalili and M. S. Pangburn, "Pricing joint sales and rentals: when are purchase-conversion discounts optimal?" *Production and Operations Management*, vol. 29, no. 12, pp. 2679–2695, 2020.
- [26] K. Li, T. Zhou, and B. Liu, "The comparison between selling and leasing for new and remanufactured products with quality level in the electric vehicle industry," *Journal of Industrial and Management Optimization*, vol. 17, no. 3, pp. 1505–1529, 2021.
- [27] L. Li, J. Chen, and S. Raghunathan, "Recommender system rethink: implications for an electronic market-place with competing manufacturers," *Information Systems Research*, vol. 29, no. 4, pp. 1003–1023, 2018.
- [28] R. El-Yaniv, R. Kaniel, and N. Linial, "Competitive optimal on-line leasing," *Algorithmica*, vol. 25, no. 1, pp. 116–140, 1999.
- [29] K. Dress, S. Lessmann, and H. J. Von Mettenheim, "Residual value forecasting using asymmetric cost functions," *International Journal of Forecasting*, vol. 34, no. 4, pp. 551–565, 2018.
- [30] P. Coto-Millán, *Theory of Utility and Consumer Behaviour: A Comprehensive Review of Concepts, Properties and the Most Significant Theorems*, Physica-Verlag HD, Berlin, Germany, 2003.
- [31] J. Lin, L. Zhou, V. L. Spiegler, M. M. Naim, and A. Syntetos, "Push or pull? The impact of ordering policy choice on the dynamics of a hybrid closed-loop supply chain," *European Journal of Operational Research*, vol. 300, no. 1, pp. 282–295, 2022.
- [32] J. Huang, M. Leng, and M. Parlar, "Demand functions in decision modeling: a comprehensive survey and research directions," *Decision Sciences*, vol. 44, no. 3, pp. 557–609, 2013.
- [33] G. Ferrer and J. M. Swaminathan, "Managing new and remanufactured products," *Management Science*, vol. 52, no. 1, pp. 15–26, 2006.

Research Article

Data-Driven Green Development Efficiency of Regional Sci-Tech Finance: A Case Study of the Yangtze River Delta

Yuan Wang,^{1,2} Hongjun Liu ,¹ Shuling Zhou,¹ Fan Liu,¹ Yaliu Yang ,¹ Juan Zhu,¹ and Yi Xu^{1,2}

¹Business School, Suzhou University, Suzhou 234000, China

²Center for International Education, Philippine Christian University, Manila 1004, Philippines

Correspondence should be addressed to Hongjun Liu; sxylhj@ahszu.edu.cn

Received 13 June 2022; Revised 10 July 2022; Accepted 15 July 2022; Published 29 August 2022

Academic Editor: A. M. Bastos Pereira

Copyright © 2022 Yuan Wang et al. This is an open access article distributed under the Creative Commons Attribution License, which permits unrestricted use, distribution, and reproduction in any medium, provided the original work is properly cited.

Green development is an important connotation of high-quality development and is one of the goals of scientific and technological innovation. This study constructs a data-driven measurement model of the green development efficiency of regional sci-tech finance, measures the green development efficiency of sci-tech finance by using the super-slack-based measure model, and deeply analyses and evaluates the changes in green development efficiency of regional sci-tech finance by calculating Malmquist index. This study calculates the green development efficiency of sci-tech finance in the Yangtze River Delta. Results show that the green development efficiency of sci-tech finance in the Yangtze River Delta is on the rise as a whole and maintains an efficient state, but differences are observed between provinces and cities. This study provides theoretical and methodological support for the evaluation of the green development efficiency of regional sci-tech finance and serves as reference for policy makers and researchers of sci-tech finance.

1. Introduction

1.1. Background. Under the background of the increasing pressure on global resources and the deterioration of the ecological environment, the United Nations Conference on environment and development proposed the “concept of sustainable development.” Then, major economies around the world vigorously implement the “Green Deal” to determine a new economic development model with the “green” relationship between long-term stable growth, resource consumption, and environmental protection. The European Commission issued the European Green agreement in December 2019, aiming to build a modern economic system in which economic growth is decoupled from resource consumption. In March 2020, the European Commission issued the action plan for the new circular economy. The core content is applying the concept of the circular economy throughout the product life cycle to reduce resource consumption. The US federal government headed by Obama adopted the “Green Deal” to promote the

circular economy, encourage relevant technological innovation, and rely on science and technology to promote the coordinated development of the environment and economy. Since 2017, with the high-quality transformation of China’s economic growth momentum from factor investment driven to innovation driven, China’s economy has developed from high-speed to high-quality development. The implementation of green development strategy through technological innovation has become a key measure to achieve the goal of sustainable development [1]. Green development needs scientific and technological support in a wide range of fields, and innovation has become the leading force for countries to accelerate green transformation and improve resource efficiency. The adoption and dissemination of innovation by enterprises are the key pillar of the national resource efficiency strategy and the development of circular economy [2].

Scientific and technological innovation begins with technology, and success depends on capital. Sci-tech finance cooperates the two elements of scientific and technological

innovation and modern finance, serves scientific and technological innovation through modern finance, and then promotes scientific and technological progress. Sci-tech finance promotes innovative development, combines with green development, and brings economic and environmental returns at the same time. Comprehensively and effectively improving the green development efficiency of sci-tech finance is an important means of sustainable economic development and is the guarantee of high-quality economic development.

1.2. Literature Review. Green development is a green concept and connotation. It is a mode of economic growth and social development aimed at efficiency, harmony, and sustainability. Its essence is the coordination and unity of economy, population, resources, and environment [3]. Therefore, measuring the efficiency level of green development and exploring the influencing factors of green development have become the focus of scholars. Green development efficiency is the key index to measure green development. It can comprehensively evaluate the resource utilisation efficiency and resource and environmental consumption in economic development. Scholars mainly measure the efficiency of green development through data envelopment analysis (DEA) model [4], slack-based measure (SBM) model [5], super-SBM model [6], and SBM-DEA model [7]. However, the traditional DEA model ignores relaxation variables and cannot sort and distinguish the efficiency values of effective decision-making units at the same frontier. The super-SBM model and undesirable SBM model are widely used because they can effectively solve these limitations [8]. Scholars have explored the effects on green development from the aspects of environmental regulation [9], scientific and technological innovation, research and development (R&D) investment [10], industrial structure [11], urbanisation and marketisation [12], energy [13], foreign investment [14], financial development [15], manufacturing [16], and machine processes [17].

Green development needs the support of technological innovation. Yin et al. pointed out that technological innovation plays important strategic roles in green growth [18]. Zhang and Liu believed that advancing ahead in both technical conversion and scientific innovation efficiency should be the best path of green development [19]. Feng et al. proposed that financial development is an important driving force for promoting green technology innovation [20]. Fang and Shao [21] and Wang [22] reached the same conclusion in their research. Ye et al. research showed that the positive effect of the finance on green development by supporting green technology innovation is significant in eastern China [6]. However, Wang and Wang pointed out that insufficient investment in scientific and technological innovation is an important bottleneck factor limiting green development [23].

Sci-tech finance is the key to solve the investment in scientific and technological innovation. Sci-tech finance can optimise the allocation of resources, promote more capital flow to science and technology innovation enterprises or

R&D institutions, and provide financial guarantee for green innovation [24], so as to alleviate their financing constraints [25] and improve the efficiency of green innovation by shortening the innovation cycle, dispersing or reducing innovation risks [26]. Large financing capacity can promote the formation of capital, make capital large-scale, and then promote the improvement of regional green innovation efficiency. As two systems [27], the combination effect of sci-tech finance affects the level of scientific and technological innovation [28]. Chen et al. studied the integration efficiency of sci-tech finance in Heilongjiang Province and found that financial structure and scientific and technological innovation affect and restrict each other, and a win-win relationship is observed between scientific and technological innovation and financial capital [29]. Research on the efficiency of sci-tech finance has become the focus to further promote the high-quality integration of financial industry and science and technology industry. Scholars mainly establish different evaluation index systems to measure the efficiency of sci-tech finance through DEA model [30, 31] and cat-o-c and cat-o-v models [32]. Li and Wen estimated the allocation efficiency of scientific and technological financial resources in 27 provinces and regions in China and considered that the overall allocation efficiency does not reach the effective state of resource allocation [33]. Qi et al. measured the allocation efficiency of scientific and technological financial resources in Hubei Province and found that the problem of low allocation efficiency of scientific and technological financial resources in Hubei Province is the low value of pure technical efficiency and small effect on scale efficiency [34]. Empirical research shows that the efficiency level of sci-tech finance is affected by the government and its policies, venture capital companies [35], human capital [36], infrastructure environment, education funds [37], the proportion of direct financing, and the incubation capacity of science and technology business incubators [38]. Da Fonseca, RS pointed out that the governments continue to play a critical and determining role in science, technology, and innovation financing whether through financial incentives, fiscal incentives, or a mix of both.

1.3. Study Limitations. On the basis of the analysis of the above research results, domestic and foreign scholars have made great progress in the research of sci-tech finance and green innovation efficiency. However, some limitations are still observed as follows: (1) Sci-tech finance investment improves the production efficiency of enterprises, forms industrialised economic achievements, and plays a positive role in reducing energy consumption and pollution emission in the production process and improving the ecological environment. Therefore, the evaluation index of sci-tech financial efficiency must be further improved, so as to objectively evaluate the efficiency of sci-tech finance. (2) The traditional DEA model ignores the relaxation variable, cannot sort and distinguish the efficiency value of the same frontier effective decision-making unit, and ignores the key variable of undesirable output, leading to the distortion of the efficiency measurement results of sci-tech finance, and

cannot reflect the green innovation effect of sci-tech finance. Therefore, a data-driven efficiency evaluation model with undesirable output must be built. (3) Correctly evaluating the efficiency level of regional sci-tech finance, showing the effect of sci-tech finance in promoting green economic development, revealing the influencing factors of green development of sci-tech finance, and providing targeted opinions are of great practical importance for improving the use efficiency of sci-tech financial resources and realising green economic development.

1.4. Theoretical Value and Practical Importance. This study establishes a new evaluation model of the green development efficiency of regional sci-tech finance and takes the Yangtze River Delta (YRD) as an example. This research has theoretical and practical importance. Theoretical significance includes measuring the green development efficiency of sci-tech finance from the perspective of data-driven and further improving the theoretical research content of sci-tech finance. The efficiency index system of sci-tech finance established in this study includes economic output and knowledge output and considers the output of ecological environment. A more comprehensive index system is helpful to measure the efficiency of sci-tech finance more objectively. The data-driven evaluation method is helpful to reveal the influencing factors of the efficiency of sci-tech finance more scientifically and accurately. It expands the research scope of sci-tech finance. Practical significance includes analysing the main factors affecting the green development efficiency of sci-tech finance and providing a feasible path for the green transformation and upgrading of science and technology enterprises through data-driven evaluation. These processes can provide policy suggestions for national policy makers to optimise the external environment of sci-tech finance and realise the coordinated development of economy and ecology under the green development background of regional economy. They also provide direction for financial institutions to further optimise the allocation of sci-tech financial resources, reform financial services, and provide research reference for relevant researchers.

1.5. Overview. The framework of this study to achieve the above research objectives is as follows: the first part is the introduction. The second part is the method, which mainly includes data-driven data collection, data model, data analysis, and application. The third part is the case analysis. Taking the YRD as an example, this study calculates the green development efficiency of sci-tech finance in three provinces and one city in the YRD and decomposes the total factor productivity (TFP). The fourth part is the conclusion.

2. Methods

This part introduces the data-driven green development efficiency measurement of regional sci-tech finance, including method process, data collection, data model, data analysis, and application.

2.1. Method and Process. As the initiative of scientific and technological innovation, sci-tech finance is the key factor to accelerate the green development of economy. Measuring the green development efficiency of sci-tech finance is of great importance to regional sustainable development. How to effectively and objectively measure the efficiency of green development is the focus of evaluating the effectiveness of the allocation of sci-tech financial resources. This study uses the super-SBM model and Malmquist index to investigate the current situation of the green development efficiency of regional sci-tech finance and proposes policy suggestions to improve the green development efficiency of sci-tech finance and implement the concept of green development as shown in Figure 1.

2.2. Evaluation Index. The selection of input and output indicators determines the scientificity and accuracy of efficiency evaluation to measure the green development efficiency of sci-tech finance. Following the principle of representativeness and availability, this study draws lessons from Li (2019) and Zhao (2020) by focusing on the input and output of sci-tech finance. Twelve important indicators with high interpretation of input and output are selected to establish the evaluation system of the green development efficiency of sci-tech finance. The details are shown in Table 1.

In accordance with the factors, the investment resources of sci-tech finance can be divided into three aspects: policy input, personnel input, and capital input. This study selects personnel input and capital input as the primary indicators of sci-tech finance input because the policy input is difficult to quantify. The input indexes of sci-tech finance are based on the views of Zhao et al. [39, 40], R&D personnel equivalent to full-time equivalent are selected for personnel input, and R&D internal expenditure, financial sci-tech expenditure, and financial market support are selected for capital input. Financial market capital support includes bank credit, venture capital, science and technology insurance, and other capital market capital sources. The financial market supports scientific and technological innovation through scientific and technological loans of financial institutions, securities markets, venture capital, scientific and technological insurance, and others. The support of the financial market in science and technology innovation is mainly the science and technology loans of financial institutions. Therefore, this study selects the proportion of regional loans in deposits to reflect the support of funds in the financial market for science and technology innovation.

Sci-tech finance aims to promote scientific and technological development, promote the transfer and transformation of scientific and technological achievements, and accelerate the formation of industrialisation. Therefore, the direct output of sci-tech finance includes economic benefits and intellectual property rights. According to Qi et al. [34, 41], the economic output indicators are the turnover of technology market, the sales revenue of new high-tech products, and the operating revenue of high-tech industry. The three indicators are the direct expression of the

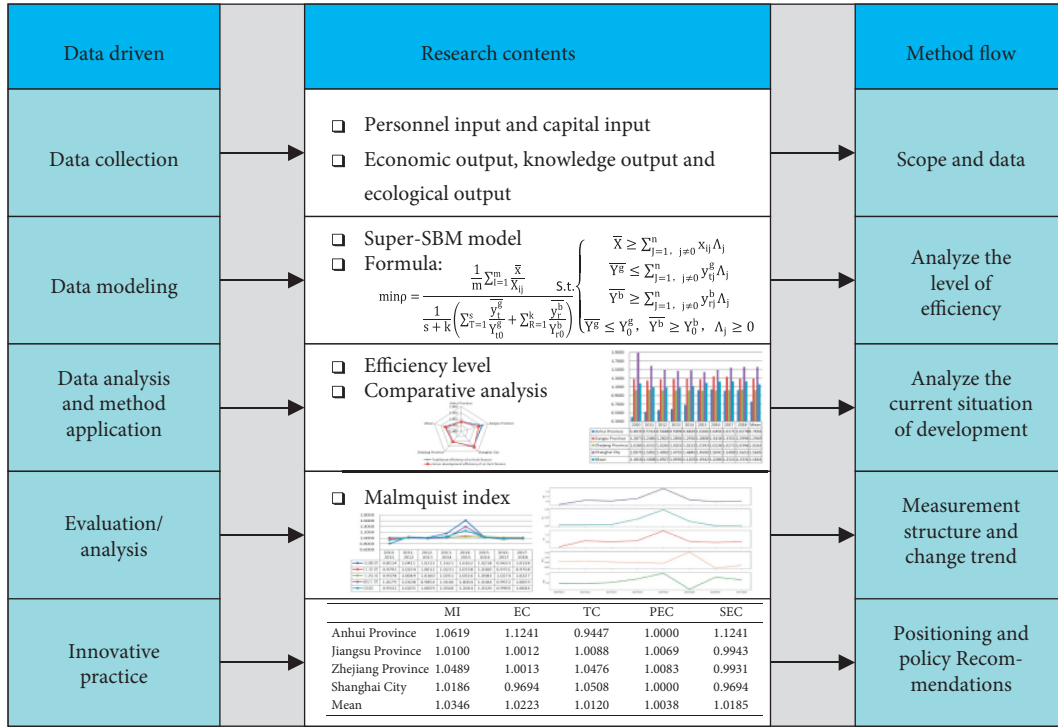


FIGURE 1: Method flow.

TABLE 1: Input-output indicators of the green development efficiency of regional sci-tech finance.

	Primary index	Secondary index	Tertiary index
Input in sci-tech finance	Input index	Personnel input	Full-time equivalent of R&D personnel (x1) R&D internal expenditure (x2)
		Capital input	Financial sci-tech expenditure (x3) Financial market support (x4)
Output in sci-tech finance	Expected output index	Economic output	Technology market turnover (y1) Sales revenue of high-tech new products (y2) Operating income of high-tech industry (y3) Number of invention patents authorised (y4)
		Knowledge output	The main retrieval tools include scientific and technological papers (y5)
	Undesirable output index	Ecological output	Waste water (y6) Waste gas (y7) Waste residue (y8)

transformation of scientific research achievements into money and reflect the economic benefits of sci-tech finance to a certain extent. The main retrieval tools for knowledge output include scientific papers and invention patent authorisation as secondary indicators. Sci-tech financial input is bound to be accompanied by undesirable output, such as effectively reducing energy consumption and pollution emissions in the production process. This study selects waste water, waste gas, and waste residue as the undesirable output index.

On the basis of the reliability and availability of data, this study collects and arranges the panel data of sci-tech finance input and output in Anhui Province, Zhejiang Province,

Jiangsu Province, and Shanghai from 2010 to 2018. All data are derived from China Statistical Yearbook [42] and the statistical yearbook of three provinces and one city in the YRD [43–46]. The data of 2016 and 2018 are obtained through the arithmetic average method due to the lack of the operating income data of high-tech industry in 2017.

2.3. Data Modelling

2.3.1. Super-SBM Model with Undesirable Output. DEA is a nonparametric efficiency analysis method proposed by famous American operational research scientists Charnes,

Cooper, and Rhodes. It can be used to evaluate the relative efficiency of multiple decision-making units (DMUs) with multiple inputs and outputs. DEA can decompose the original complex system into submodules, so as to explore the low efficiency of submodules. Combined with the insufficient output, the key crux of the low efficiency of the total system can be found. However, the traditional DEA model ignores the relaxation variables, radial deviation, and the influence of external environment, thereby making the measured efficiency deviate from the actual efficiency. Tone put the relaxation variable into the objective function and proposed a nonradial SBM model with undesirable output based on the relaxation variable [47]. However, the traditional SBM model cannot distinguish and sort multiple equally effective units. Thus, Tone proposed the super-SBM model [48] in 2002 to solve this problem. Compared with other DEA models, super-SBM model has obvious advantages. Firstly, super-SBM model solves the problem of nonzero relaxation of input or output that cannot be solved by the traditional DEA model and considers the relaxation variable as much as possible when calculating efficiency. Secondly, the super-SBM model allows the efficiency value to be greater than or equal to 1. When there are multiple

effective DUMs, they can be sorted. Therefore, the super-SBM model can achieve the complete evaluation and sorting of DUMs. Referring to this method, this study selects the super-SBM model to measure the green development efficiency of regional sci-tech finance.

The basic principle is as follows: suppose that n DMUs are found, and m inputs, s expected outputs, and k undesirable outputs are obtained for each DMU. Assuming that the input, expected output, and undesirable output vectors of each DMU are expressed as $x \in R^m$, $y^g \in R^s$, and $y^b \in R^k$, respectively, the matrix can be defined as follows:

$$\begin{cases} X = (x_1, \dots, x_n) \in R^{m \times n} \\ Y^g = (y_1^g, \dots, y_n^g) \in R^{s \times n} \\ Y^b = (y_1^b, \dots, y_n^b) \in R^{k \times n} \end{cases} \quad (1)$$

Suppose $x > 0$, $y^g > 0$, and $y^b > 0$; the production possibility set is defined as follows: $p = \{(x, y^g, y^b) | x \geq X\lambda, y^g \leq Y^g\lambda, y^b \geq Y^b\lambda, \lambda \geq 0\}$.

The super-SBM model with undesirable output can be obtained as follows:

$$\min \rho = \frac{1/m \sum_{i=1}^m (\bar{x}/X_{ij})}{1/s + k \left(\sum_{t=1}^s (\bar{y}_t^g/Y_{t0}^g) + \sum_{r=1}^k (\bar{y}_r^b/Y_{r0}^b) \right)} \quad (2)$$

$$\text{s.t.} \begin{cases} \bar{X} \geq \sum_{j=1, j \neq 0}^n x_{ij} \lambda_j \\ \bar{Y}^g \leq \sum_{j=1, j \neq 0}^n y_{tj}^g \lambda_j \\ \bar{Y}^b \leq \sum_{j=1, j \neq 0}^n y_{rj}^b \lambda_j \\ \bar{Y}^g \leq Y_0^g, \bar{Y}^b \geq Y_0^b, \lambda_j \geq 0, \\ i = 1, 2, \dots, m; j = 1, 2, \dots, n; t = 1, 2, \dots, s; r = 1, 2, \dots, k. \end{cases} \quad (3)$$

ρ is the calculated green development efficiency value of sci-tech finance. When $0 < \rho < 1$, the green development efficiency of regional sci-tech finance is in an invalid state. When $\rho \geq 1$, the green development efficiency of regional sci-tech finance is in an effective state, and the greater the ρ value, the greater the green development efficiency of sci-tech finance, and the higher the green development level of sci-tech finance.

2.3.2. Malmquist Index. The green development efficiency of sci-tech finance calculated by the super-SBM model is a static description, and Malmquist model can dynamically analyse the changes in the green development of sci-tech finance. Therefore, this study selects Malmquist index model

to supplement and improve the analysis of the efficiency of sci-tech finance.

Malmquist productivity index was proposed by Malmquist, a Swedish scholar. Subsequently, some scholars applied it to measure productivity change. The construction of Malmquist index is based on the distance function. The change in technical efficiency is analysed from a dynamic point of view through the comparison of distance functions. Therefore, the Malmquist productivity index from period t to period $t + 1$ is as follows:

$$\begin{aligned} MI &= M_i(x^t, y^t, x^{t+1}, y^{t+1}) = (M^t \times M^{t+1})^{1/2} \\ &= \left(\frac{D_i^t(x^{t+1}, y^{t+1})}{D_i^t(x^t, y^t)} \times \frac{D_i^{t+1}(x^{t+1}, y^{t+1})}{D_i^{t+1}(x^t, y^t)} \right)^{1/2}. \end{aligned} \quad (4)$$

MI reflects the changes in total factor productivity in the green development of sci-tech finance. $MI > 1$ indicates that the green development efficiency of sci-tech finance is improved. $MI < 1$ indicates that the green development efficiency of sci-tech finance decreases. $MI = 1$ indicates that the green development efficiency of sci-tech finance remains unchanged.

The use of Malmquist index to analyse the green development efficiency of regional sci-tech finance can also

decompose the total factor productivity, so as to further observe whether the investment decision of sci-tech finance is correct or not and explore the reasons for the differences in resource allocation efficiency. Total factor productivity (TFP) is decomposed into technical progress change index (TC) and technical efficiency change index (EC), and EC is further decomposed into the product of pure technical efficiency index (PEC) and scale efficiency index (SEC).

$$\text{Total Factor Productivity (TFP)} = \text{Technical Efficiency (EC)} \times \text{Technical Progress (TC)}, \quad (5)$$

$$\text{Technical Efficiency (EC)} = \text{Pure Technical Efficiency (PEC)} \times \text{Scale Efficiency (SEC)}. \quad (6)$$

EC is used to measure the efficiency change in a DMU. $EC > 1$ indicates that the efficiency of DMU is improved, whereas $EC < 1$ indicates that the efficiency of DMU is reduced. TC is used to measure the technical change in a DMU from t period to $t + 1$ period.

2.4. Data Analysis and Application. This research is based on the measurement of the green development efficiency of regional sci-tech finance driven by data. The specific data analysis and application are as follows:

Firstly, we construct the input-output index of the green development of regional sci-tech finance, calculate the green development efficiency of regional sci-tech finance by using the super-SBM model, and analyse its change trend.

Secondly, we use the super-SBM model to calculate the efficiency of regional sci-tech finance (excluding undesirable output) and compare it with the green development efficiency of regional sci-tech finance.

Thirdly, we use the Malmquist index to analyse the dynamic changes in green total factor productivity of regional sci-tech finance and identify the main factors affecting the improvement of green development efficiency of regional sci-tech finance in accordance with the decomposition of the green total factor productivity of regional sci-tech finance.

Finally, we propose policy suggestions to improve the green development efficiency of regional sci-tech finance in accordance with the above analysis.

The steps are shown in Figure 2.

3. Case Study

This study takes the YRD as an example, collects and sorts out the data in accordance with the input-output indicators of the green development of regional sci-tech finance, and measures and evaluates the green development efficiency of sci-tech finance in the YRD by using the super-SBM model and Malmquist index to prove the effectiveness of the proposed method.

3.1. Case Study Background. The YRD includes Shanghai, Jiangsu Province, Zhejiang Province, and Anhui Province. The YRD is one of the regions with the most active economic development, the highest degree of openness, and the strongest innovation ability in China. It is also a major strategic growth pole of China's economic development. In 2020, the gross domestic product (GDP) of the YRD ranked fifth in the world. In 2021, the GDP of the YRD reached 27.6 trillion Yuan, accounting for 24% of China's total economy. The high-speed economic growth and high-quality development of the YRD promote the construction of China's modern economic system and help the YRD become the growth pole of the global economy, which is of great importance to the high-quality development of the world economy.

Under the integrated development strategy of the YRD, scientific and technological innovation, as one of the driving forces of economic development, is extremely important. Strengthening the integration of regional innovation in the YRD and building a science and technology innovation community in the YRD have a strong demand for sci-tech finance. However, the development of the YRD is restricted by resources and environment, so the green development of sci-tech finance in the YRD has high research value.

3.2. Results

3.2.1. Measurement of Sci-Tech Financial Efficiency in the YRD. This study uses Maxdea Ultra 7.0 software to calculate the green development efficiency of sci-tech finance in the YRD from 2010 to 2018 without considering the output lag. In the follow-up research, this study chooses to measure the green development efficiency of regional sci-tech finance under the condition of constant return to scale. Some of the results are shown below.

In accordance with the green development efficiency value, the green development level can be defined, and the green development efficiency level can be analysed vertically. Green development efficiency value greater than or equal to 1 indicates extremely high efficiency. Green development efficiency value greater than 0.6 indicates high efficiency. Green development efficiency value less than 0.6 indicates

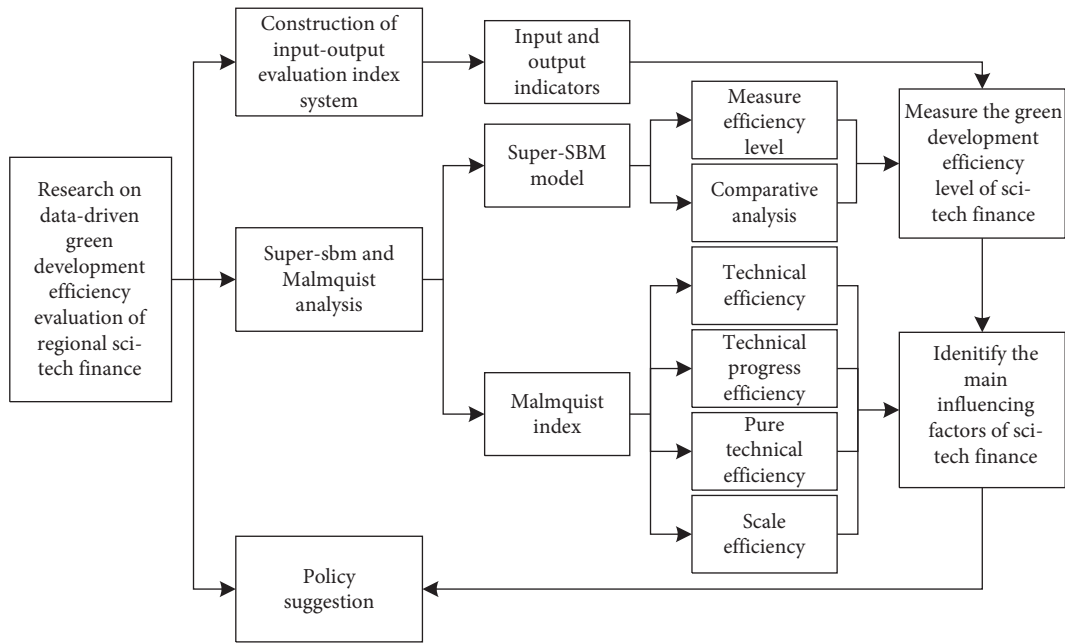


FIGURE 2: Data analysis and application.

low efficiency. As shown in Figure 3, from 2010 to 2018, the average green development efficiency of sci-tech finance in three provinces and one city in the YRD reached high efficiency. The green development efficiency of sci-tech finance in Zhejiang, Jiangsu, and Shanghai fluctuated and is greater than 1. The efficiency value of the green development of sci-tech finance in Anhui Province is in a rapid rising stage from 2010 to 2016, whereas it is in a volatile rise from 2016 to 2018. On the whole, the overall green development level of sci-tech finance in Anhui Province improved significantly.

In comparison, Anhui Province has the highest degree of improvement in the green development efficiency of sci-tech finance, from 0.4031 in 2010 to 1.0278 in 2018, an increase of 0.6247. Jiangsu Province and Zhejiang Province are relatively stable and have been in a state of high efficiency. Shanghai showed a slow downward trend in the green development efficiency of sci-tech finance, which decreased by 0.5575 from 2.0075 in 2010 to 1.45 in 2015 and reached the lowest level in 2015. This finding indicated that although the utilisation efficiency of sci-tech financial resources remained efficient, the utilisation capacity of resources decreased. From 2015 to 2018, the green development efficiency value of sci-tech finance in Shanghai increased slightly but did not reach the previous level.

On the whole, significant differences are observed in the green development efficiency of sci-tech finance among the three provinces and one city in the YRD. Shanghai has the highest green development efficiency of sci-tech finance, followed by Jiangsu Province, Zhejiang Province, and Anhui Province. As the largest economic centre in China, Shanghai has a high level of economic development. Its industries are mainly modern manufacturing and high-tech industries. Therefore, the green development efficiency of sci-tech finance is extremely high. The investment in sci-tech finance

in Jiangsu Province ranks first in the YRD. However, the ability of scientific and technological innovation is weaker than that in Shanghai because the secondary industry is the leading industry in Jiangsu Province. Anhui Province is relatively late in development than Jiangsu and Zhejiang, and its scientific and technological innovation ability is weak, resulting in the low efficiency of the green development of sci-tech finance. However, in recent years, the economy of Anhui Province has developed rapidly, resulting in the rapid improvement of the green development efficiency of sci-tech finance.

3.2.2. Comparative Analysis. To deeply understand the green development efficiency level of regional sci-tech finance, this study performs a comparative analysis between the green development efficiency of sci-tech finance considering ecological output and the traditional sci-tech finance efficiency without considering undesirable output, as shown in the figure below.

From Figure 4, we can see that in general, the green development efficiency of sci-tech finance considering environmental pollution in Anhui Province, Jiangsu Province, and Zhejiang Province is lower than that without environmental pollution. This shows that the emission of environmental pollutants, such as “three wastes,” is one of the reasons affecting the efficiency level of regional sci-tech finance. This condition indicates that distortion occurs in the evaluation of sci-tech finance efficiency without considering environmental pollution. By contrast, significant differences are observed in the effects of environmental factors on the efficiency of sci-tech finance in three provinces and one city in the YRD. Jiangsu Province is the most affected, followed by Zhejiang Province and Anhui Province, and Shanghai is unaffected. The main reason is that the tertiary industry in

Shanghai accounts for about 80% of the industrial structure, and the industry is also dominated by modern manufacturing and high-tech industries. Shanghai has a high technology transformation effect and is relatively leading in promoting environmental improvement through technological innovation. The secondary industry is the leading industry in Jiangsu Province, and its environmental protection ability is weaker than that of Shanghai. Therefore, the efficiency of sci-tech finance is obviously affected by environmental factors.

3.2.3. Dynamic Evolution of the Green Development Efficiency of Sci-Tech Finance in the YRD. This study uses the panel data of three provinces and one city from 2010 to 2018 and applies the Malmquist index model to further explore the change in the green development efficiency of sci-tech finance over time. These processes are performed to more comprehensively analyse the development trend of sci-tech finance in the YRD. The Malmquist index and its decomposition value of three provinces and one city in the YRD are calculated on Maxdea Ultra 7.0 software. The calculation results are as follows.

As shown in Figure 5, on the whole, the average value of MI in the YRD fluctuates around 1, indicating that the overall efficiency of the green development of sci-tech finance in the YRD is unstable. Specifically, from 2010 to 2015, the green development efficiency of sci-tech finance in the YRD was in an upward trend, peaked in 2015, decreased, and exhibited an inflection point in 2017. The technical efficiency of sci-tech finance in the YRD during the study period is greater than 1, and the technical progress index is less than 1 in 2011, 2013, and 2017 by further decomposing MI. This finding shows that the convergence between the progress of technical efficiency and the change in MI is higher.

As shown in Figure 6, from the perspective of three provinces and one city, from 2010 to 2018, the dynamic efficiency of science and technology finance in Anhui Province improved the fastest, with an average increase of 6.19%, followed by Zhejiang Province, with an average growth rate of 4.89%, and Jiangsu Province and Shanghai have an average growth rate of less than 2%. This finding shows that Jiangsu Province and Shanghai have been growing slowly due to the high efficiency of the green development of sci-tech finance and the less room for progress than Anhui Province and Zhejiang Province. Anhui Province and Zhejiang Province have lagged behind Jiangsu Province and Shanghai in economy and technology. In recent years, the national YRD regional strategy has greatly improved their economic development level, industrial structure, and resource allocation. Therefore, the green development efficiency of sci-tech finance has been improved rapidly.

The further decomposition of the index of three provinces and one city shows that the reasons for the rapid growth of the green development efficiency of sci-tech finance in Anhui Province and Zhejiang Province are different. The driving force for the rapid growth of the green development efficiency of sci-tech finance in Anhui Province

is the technical efficiency ($EC = 1.1241$), contributing a growth rate of 12.41%, and the driving force of Zhejiang Province is the technical progress ($TC = 1.0476$), contributing a growth rate of 4.76% compared with the technical efficiency ($EC = 1.0013$).

To sum up, this study uses the super-SBM model with undesirable output and Malmquist index to explore the characteristics of the green development efficiency of sci-tech finance in three provinces and one city in the YRD from 2010 to 2018 from the two dimensions of time series dynamic evolution and influencing factors and draws the following conclusions: (1) The green development efficiency of sci-tech finance in the YRD shows an upward trend as a whole, but the efficiency of sci-tech finance in three provinces and one city is different. Shanghai, Jiangsu Province, and Zhejiang Province have maintained high efficiency, whereas Anhui Province has developed rapidly from low efficiency to high efficiency. (2) The emission of environmental pollutants is one of the reasons affecting the efficiency of regional sci-tech finance. (3) On the whole, except for 2010–2011 and 2016–2017, the Malmquist index is greater than 1. The changes in technological progress and technological and financial efficiency are the same, but the speed of the technological progress of three provinces and one city is different. Anhui Province has made rapid progress and gradually narrowed the efficiency gap in sci-tech finance with other provinces and cities.

3.3. Policy Suggestions. On the basis of the above research conclusions, the policy suggestions to optimise the efficiency of financial resource allocation and further improve the green development efficiency of sci-tech finance in the YRD are proposed as follows.

3.3.1. Further Improve Scientific and Technological Innovation. In accordance with Table 2, the average green development efficiency of sci-tech finance in Shanghai is 1.5695, and the average green development efficiency of sci-tech finance in Anhui Province is 0.7656. The main reason for such a large difference is that Shanghai's scientific and technological innovation ability exceeds that of Anhui Province and is in the centre of the YRD. Therefore, we must improve the ability of regional science and technology innovation to improve the green development efficiency of regional sci-tech finance. On the one hand, scientific and technological innovation promotes the adjustment of industrial structure, so as to promote the development of high-tech industries, especially low-carbon industries, and help further control the emission of pollutants. On the other hand, technological progress brings sustainable and rapid economic development, which helps to promote the efficiency of sci-tech finance. The government should support enterprises to further improve scientific and technological innovation and technology and abandon or upgrade enterprises with high pollution and high investment whilst increasing the support of scientific and technological innovation investment. The investment of sci-tech finance must focus on the rational allocation of energy and the

TABLE 2: Average Malmquist index and its decomposition in three provinces and one city.

	MI	EC	TC	PEC	SEC
Anhui Province	1.0619	1.1241	0.9447	1.0000	1.1241
Jiangsu Province	1.0100	1.0012	1.0088	1.0069	0.9943
Zhejiang Province	1.0489	1.0013	1.0476	1.0083	0.9931
Shanghai City	1.0186	0.9694	1.0508	1.0000	0.9694
Mean	1.0346	1.0223	1.0120	1.0038	1.0185

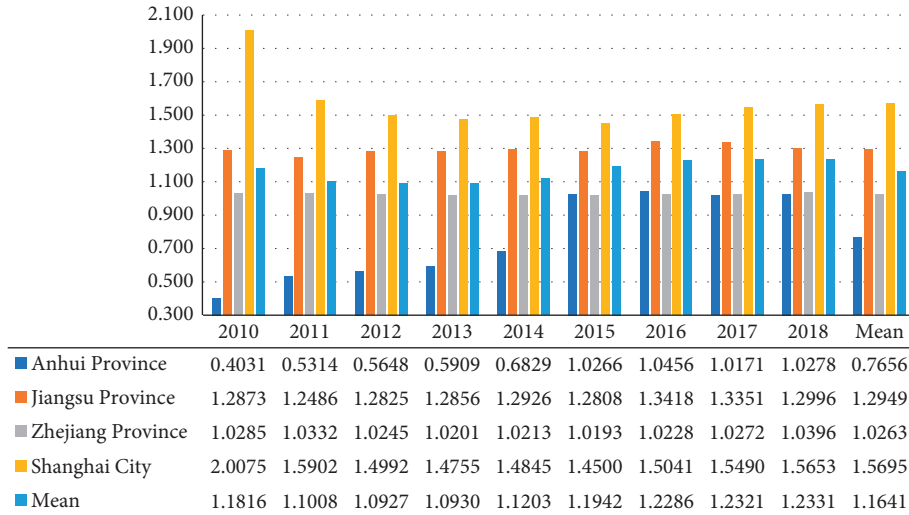


FIGURE 3: Efficiency value of the green development of sci-tech finance in the YRD, 2010–2018.

protection of ecological environment, so as to truly realise the high-quality development of economy.

3.3.2. Promote the Construction of a Regional Ecological Integrated Governance System. In accordance with Figure 7, undesirable outputs reduce the green development efficiency of regional sci-tech finance. Therefore, to improve the green development efficiency of regional sci-tech finance and achieve a win-win situation in regional economic development and ecological environment, we must improve the expected output and reduce the total amount of undesirable output. Ecological problems have the characteristics of diffusion and externality, and it is inevitable to promote the construction of a regional ecological integrated governance system. Based on firmly establishing the concept of green development, we should establish a unified and authoritative regional ecological supervision organization, formulate unified environmental testing standards and environmental law enforcement, and fully mobilize the enthusiasm of the public, social organizations, and enterprises to participate in ecological construction (see Figures 3–6).

3.3.3. Seek Common Ground Whilst Reserving Differences in Regional Management. From the above analysis, the reasons for promoting the efficiency growth of the green development of sci-tech finance in regional provinces and cities are different. The driving force for the rapid growth of the green development efficiency of sci-tech finance in Anhui Province

depends on the technical efficiency ($EC = 1.1241$), the driving force of Zhejiang Province and Shanghai is the technological progress (TC is 1.0476 and 1.0508, respectively), and a small gap is observed between the technical efficiency and the contribution of technological progress in Jiangsu Province. Based on the different resource endowments and scientific and technological innovation capabilities of provinces and cities, we should emphasize the scientific and technological level and scientific and technological innovation capability and pay attention to the differentiation of regional sci-tech financial management at the current stage to achieve regional green development. For example, Anhui provincial government should focus on accelerating technological efficiency, whilst Zhejiang Province and Shanghai should focus on improving the level of technological progress.

3.4. Discussion and Management Enlightenment. Compared with the existing literature [34, 35], this study has the following advantages. Firstly, this study further improves the evaluation index of regional sci-tech financial efficiency. On the basis of the traditional sci-tech financial efficiency evaluation index, this study adds ecological output as undesirable output, which can more objectively evaluate the effects of regional sci-tech financial investment on scientific and technological innovation and ecological environment. Secondly, the super-SBM model and Malmquist index are used to measure the green development efficiency of regional sci-tech finance and analyse the level and timing changes in

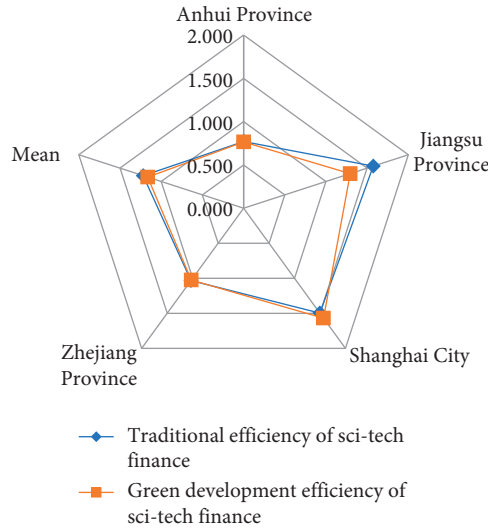


FIGURE 4: Comparative analysis of the efficiency of sci-tech finance in the YRD.

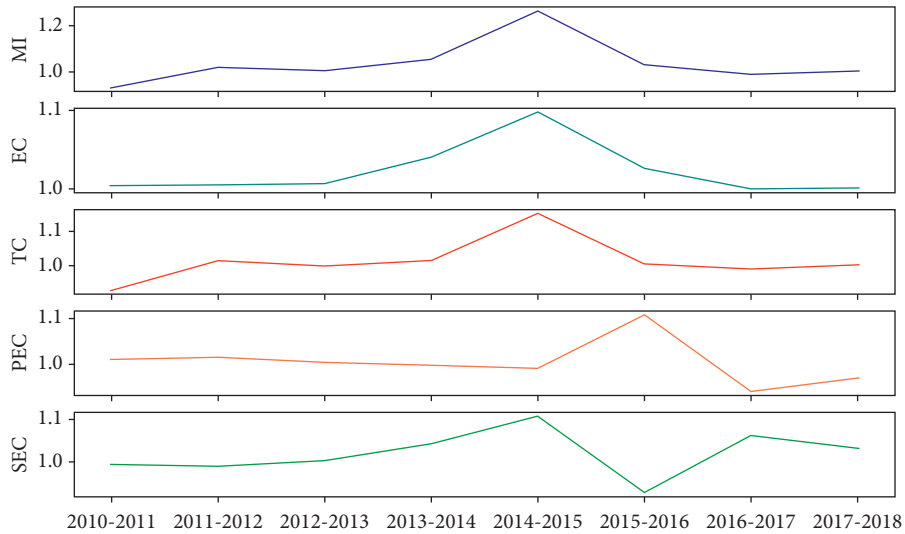


FIGURE 5: Malmquist index and its efficiency decomposition in the YRD, 2010–2018.

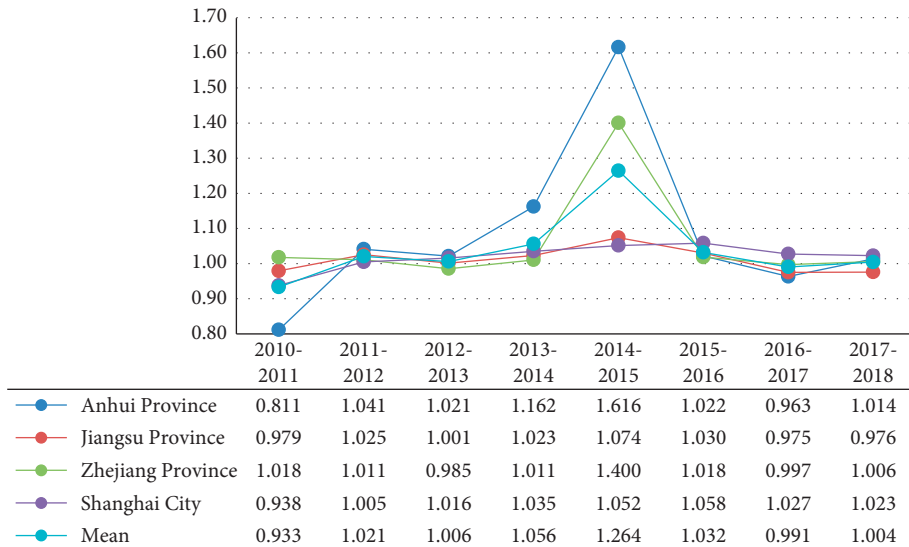


FIGURE 6: Malmquist index in three provinces and one city, 2010–2018.

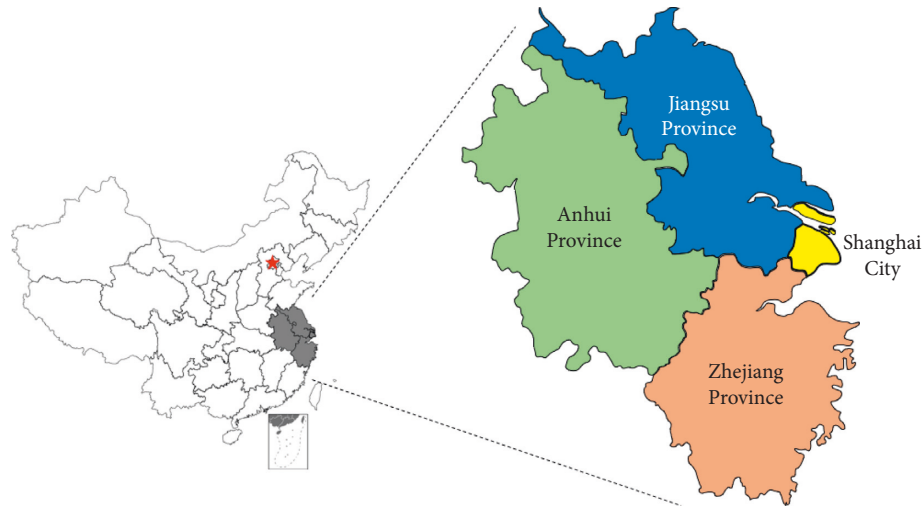


FIGURE 7: Yangtze river delta.

the green development efficiency of sci-tech finance. The evaluation of sci-tech finance efficiency is more objective and comprehensive, which is helpful to provide scientific decision-making basis. Finally, this study proposes some suggestions to improve science and technology innovation technology and improve the regional green development governance system to realise the sustainable development of economy and environment from the perspective of sci-tech finance, so as to make the decision more targeted.

On the basis of the above research and conclusions, we obtain the following management enlightenment.

- (1) Under the background of green economic development, regional differences require a set of scientific and reasonable measurement and evaluation index system of regional scientific, technological, and financial efficiency. It is conducive to grasp the situation of sci-tech finance promoting scientific and technological innovation and to understand the effects of scientific and technological financial resource investment on the ecological environment.
- (2) The measurement and evaluation of the green development efficiency of regional sci-tech finance must start from the dynamic and static aspects, so as to better grasp and understand the current situation and development trend of regional sci-tech finance and provide a scientific basis for the formulation of sci-tech finance policies in the future.
- (3) In the context of big data, we can diagnose and find problems through the establishment of models for data analysis, thereby helping to drive the scientificity of decision-making. Therefore, research of regional sci-tech finance should fully utilise big data and analyse the innovation effect and ecological effect of sci-tech finance more scientifically through data driving.

4. Conclusion

Sci-tech finance is the key driving force to promote the high-quality integrated development of regional economy and an important factor to realise the sustainable development of economy and environment. Therefore, the efficiency of sci-tech finance and the efficiency of financial capital allocation must be further improved, and the deep integration of finance and science and technology industry must be promoted. This study proposes a data-driven measurement and evaluation method of the green development efficiency of regional sci-tech finance, which is calculated by the super-SBM model, is analysed by Malmquist index, and provides targeted suggestions.

The main innovations of this study are as follows: (1) this study constructs the measurement index of the green development efficiency of regional sci-tech finance. The input index of the index system consists of four input indexes: R&D personnel converted into full-time equivalent, internal expenditure of R&D funds, government science and technology expenditure, and financial market fund support, which cover the main sources of sci-tech finance. The output index consists of direct output and undesirable output, where the direct output consists of economic benefits and intellectual property rights, and the three waste indexes are selected for the undesirable output. The input-output evaluation index system of the green development efficiency of sci-tech finance is more comprehensive, and the evaluation of the efficiency of sci-tech finance is more reliable. (2) This study constructs a data-driven evaluation of the green development efficiency of regional sci-tech finance. The evaluation process is more objective, and the evaluation results are more credible. (3) The time series measurement and influencing factor analysis of the green development efficiency of regional sci-tech finance can comprehensively analyse the changes in the green development efficiency of regional sci-tech finance, so as to provide a scientific decision-making basis for the formulation of sci-tech finance policies.

However, this study has some deficiencies: the selection of indicators of the green development efficiency of sci-tech finance needs to be further improved. The effects of sci-tech financial input on the ecological environment depend on the existence of undesirable output and environmental input factors, such as energy consumption and water resource consumption.

The evaluation of the green development efficiency of regional sci-tech finance is a complex study. In the future research, we will more comprehensively evaluate the dynamic changes in the green development efficiency of sci-tech finance from the perspective of time sequence and space, further improve the input-output index system of sci-tech finance, and build a complete sci-tech finance system, so as to explore the path for promoting the deep integration of finance and scientific and technological innovation from a more diversified perspective to promote high-quality integrated development of regional economy.

Data Availability

The data used to support the findings of this study are included within the article.

Conflicts of Interest

The authors declare no conflicts of interest.

Acknowledgments

This research was funded by the following projects: Excellent Youth Fund Project of Suzhou University (2013xqrw010); Key Scientific Research Project of Suzhou University (2019ydz13); Research Project of Humanities and Social Sciences of Anhui Provincial Department of Education in 2020 (sk2020a0531); Research Project of Humanities and Social Sciences of Anhui Provincial Department of Education in 2019 (sk2019a0527); Research Project of Humanities and Social Sciences of Anhui Provincial Department of Education in 2021 (sk2021a0092); Support Program for Outstanding Young Talents in Colleges and Universities of Anhui Provincial Department of Education in 2021 (gxyqZD2021039); Innovation Team of Suzhou University (2018kytd02); and Research Platform Project of Suzhou University (2019yfk20).

References

- [1] H. Y. Huang, F. R. Wang, M. L. Song, T. Balezentis, and D. Streimikiene, "Green innovations for sustainable development of China: Analysis based on the nested spatial panel models," *Technology in Society*, vol. 65, Article ID 101593, 2021.
- [2] G. Cainelli, A. D'Amato, and M. Mazzanti, "Resource efficient eco-innovations for a circular economy: Evidence from EU firms," *Research Policy*, vol. 49, no. 1, Article ID 103827, 2020.
- [3] N. P. Jiang and R. K. Xiang, "Some problems of green economic development in China," *Contemp Econ Res*, vol. 2, no. 2, pp. 50–54, 2013.
- [4] F. Chao, W. Miao, C. L. Guan, and B. H. Jian, "Green development performance and its influencing factors: A global perspective," *Journal of Cleaner Production*, vol. 144, pp. 323–333, 2017.
- [5] F. D. Qiu, Y. Chen, J. T. Tan, J. B. Liu, Z. Y. Zheng, and X. L. Zhang, "Spatial-temporal Heterogeneity of green development efficiency and its influencing factors in growing Metropolitan Area: A case study for the Xuzhou Metropolitan Area," *Chinese Geographical Science*, vol. 30, no. 2, pp. 352–365, 2020.
- [6] T. F. Ye, X. L. Xiang, X. Y. Ge, and K. L. Yang, "Research on green finance and green development based eco-efficiency and spatial Econometric Analysis," *Sustainability*, vol. 14, no. 5, p. 2825, 2022.
- [7] H. Li, F. He, and G. J. Deng, "How does environmental regulation promote technological innovation and green development? New Evidence from China," *Polish Journal of Environmental Studies*, vol. 29, no. 1, pp. 689–702, 2019.
- [8] G. Li, Y. Zhou, F. Liu, and T. Wang, "Regional differences of manufacturing green development efficiency considering undesirable outputs in the Yangtze River economic belt based on super-SBM and WSR system methodology," *Frontiers in Environmental Science*, vol. 8, Article ID 631911, 2021.
- [9] R. Wang, "The influence of environmental regulation on the efficiency of China's regional green economy based on the GMM model," *Polish Journal of Environmental Studies*, vol. 29, no. 3, pp. 2395–2402, 2020.
- [10] S. T. Kim, G. L. Cho, S. D. Lee, and B. Lim, "An Analysis on the economic performance of industrial R&D investments to Achieve green growth strategy," *Journal of Korean Economy Studies*, vol. 29, no. 2, pp. 5–50, 2011.
- [11] G. F. Liang, D. J. Yu, and L. F. Ke, "An empirical study on dynamic evolution of industrial structure and green economic growth—based on data from China's Underdeveloped Areas," *Sustainability*, vol. 13, no. 15, p. 8154, 2021.
- [12] M. L. Zhang and B. Z. Li, "How to design regional characteristics to improve green economic efficiency: a fuzzy-set qualitative comparative analysis approach," *Environmental Science and Pollution Research*, vol. 4, pp. 6125–6139, 2022.
- [13] V. Tawiah, A. Zakari, and F. F. Adedoyin, "Determinants of green growth in developed and developing countries," *Environmental Science and Pollution Research*, vol. 29, pp. 39227–39242, 2021.
- [14] D. S. Yu, X. P. Li, J. J. Yu, and H. Li, "The impact of the spatial agglomeration of foreign direct investment on green total factor productivity of Chinese cities," *Journal of Environmental Management*, vol. 290, no. 290, Article ID 112666, 2021.
- [15] T. H. Li and G. K. Liao, "The Heterogeneous impact of financial development on green total factor productivity," *Frontiers in Energy Research*, vol. 8, 2020.
- [16] S. Jia, Q. H. Yuan, J. X. Lv, Y. Liu, D. W. Ren, and Z. W. Zhang, "Therblig-embedded value stream mapping method for lean energy machining," *Energy*, vol. 138, pp. 1081–1098, 2017.
- [17] S. Jia, W. Cai, C. H. Liu et al., "Energy modeling and visualization analysis method of drilling processes in the manufacturing industry," *Energy*, vol. 228, no. 228, Article ID 120567, 2021.
- [18] K. D. Yin, R. C. Zhang, X. Jin, and L. Yu, "Research and optimization of the Coupling and coordination of environmental regulation, technological innovation, and green development," *Sustainability*, vol. 14, no. 1, p. 501, 2022.

- [19] J. X. Zhang and R. C. Liu, "Evolution of urban green innovation efficiency under environmental regulations: A case study of Xi'an," *Chinese Journal of Urban and Environmental Studies*, vol. 08, no. 03, Article ID 2050015, 2020.
- [20] S. L. Feng, R. Zhang, and G. X. Li, "Environmental decentralization, digital finance and green technology innovation," *Structural Change and Economic Dynamics*, vol. 61, pp. 70–83, 2022.
- [21] Y. Fang and Z. Q. Shao, "Whether green finance can effectively moderate the green technology innovation effect of Heterogeneous environmental regulation," *International Journal of Environmental Research and Public Health*, vol. 19, no. 6, p. 3646, 2022.
- [22] X. Y. Wang, "Research on the impact mechanism of green finance on the green innovation performance of China's manufacturing industry," *Managerial and Decision Economics*, vol. 2, no. 2, 2022.
- [23] Y. Wang and X. M. Wang, "Analysis on green development level and restricting factors of Lanzhou-Xining urban Agglomeration development Zone," *Areal Research and Development*, vol. 40, no. 4, pp. 32–38, 2021.
- [24] M. X. Zhang, S. J. Wei, and X. Y. Zhu, "Science and technology finance: from concept to theoretical system," *China Soft Science*, vol. 4, pp. 31–42, 2018.
- [25] C. H. Yu, X. Q. Wu, D. Y. Zhang, S. Chen, and J. S. Zhao, "Demand for green finance: Resolving financing constraints on green innovation in China," *Energy Policy*, vol. 2021, Article ID 112255, 2021.
- [26] K. X. Meng and Q. H. Yan, "Green finance and investment structure optimization of enterprise eco-innovation," *Studies in Science of Science*, vol. 35, no. 12, pp. 1886–1895, 2017.
- [27] M. K. Shi and L. Y. Yu, "Cooperative efficiency measurement of China's provincial science financial system based on network data envelopment analysis and its time-spatial differences," *Journal of Shanghai University. Natural Science Edition*, vol. 26, no. 6, pp. 1015–1025, 2020.
- [28] L. Y. Ma and X. M. Li, "Does science and technology finance policies promote regional innovation? Quasi - natural Experiment based on the Pilot policy of combining science and technology with finance," *China Soft Science*, vol. 12, pp. 30–42, 2019.
- [29] T. T. Chen, S. L. Zhang, and F. N. Zhang, "An empirical study on the integration efficiency of science and technology finance in Heilongjiang Province Based on Projection Pursuit Model," in *Proceedings of the International Conference on Robots & Intelligent System (ICRIS)*, pp. 644–649, IEEE, Sanya, China, November 2020.
- [30] P. Adamovsky and V. Gonda, "Differences in efficiency of national innovation systems of Slovakia and selected EU countries," *Politická Ekonomie*, vol. 67, no. 2, pp. 181–197, 2019.
- [31] J. F. Zhao, X. Deng, L. Shen, C. R. Huang, and C. J. Chen, "Performance evaluation of Guangdong province technology finance based on DEA model," *Application of Intelligent Systems in Multi-modal Information Analytics*, vol. 1233, pp. 96–104, 2020.
- [32] M. A. Karadayi and Y. Ekinci, "Evaluating R&D performance of EU countries using categorical DEA," *Technology Analysis & Strategic Management*, vol. 31, no. 2, pp. 227–238, 2019.
- [33] J. X. Li and X. N. Wen, "Research on the relationship between the Allocation efficiency and influencing factors of China's science and technology finance," *China Soft Science*, no. 1, pp. 164–174, 2019.
- [34] B. Q. Qi, Z. C. Chen, and H. Ao, "Comparative study on the Allocation efficiency of science and technology financial resources in Hubei province," in *Proceedings of the 4th International Conference on Management Engineering, Software Engineering and Service Sciences*, pp. 140–146, ICMSS, January 2020.
- [35] R. S. Da Fonseca and A. P. Veloso, "The Practice and future of financing science, technology, and innovation," *Foresight and STI Governance*, vol. 12, no. 2, pp. 6–22, 2018.
- [36] C. C. Zhang, "Factors influencing the Allocation of regional sci-tech financial resources based on the multiple Regression model," *Mathematical Problems in Engineering*, pp. 1–9, 2021.
- [37] W. Han, P. Wang, Y. Jiang, and H. Han, "Nonlinear influence of financial technology on regional innovation capability: based on the Threshold effect Analysis of human capital," *Sustainability*, vol. 14, no. 2, p. 1007, 2022.
- [38] Y. N. Chen, X. Li, and W. Li, "Analysis on Determinants and Spatiotemporal Heterogeneity of science and technology innovation efficiency at Chinese provincial level," *China Soft Science*, no. 4, pp. 137–149, 2021.
- [39] D. Zhao, H. Ao, and M. Y. Yu, "Research on the Allocation efficiency of sci-tech finance in Hubei province," *International Conference on E-Business, Information Management and Computer*, no. 9, pp. 140–144, 2020.
- [40] X. W. Wang, M. L. Xie, and Y. Q. Tian, "Calculation of technology finance efficiency and influencing factor Analysis in digital economy Era," *Science and Technology Management Research*, no. 2, pp. 61–69, 2022.
- [41] L. Shen and W. X. Fan, "The spatial Spillover effect of Port development on economic openness: research based on two-Regime spatial Durbin model," *Management Review*, vol. 33, no. 1, pp. 44–53+67, 2021.
- [42] National Bureau of Statistics, "National Bureau of Statistics," 2022, <http://www.stats.gov.cn/tjsj/ndsj>.
- [43] Anhui Provincial Bureau of Statistics, "Anhui provincial Bureau of Statistics," 2022, <http://tj.ah.gov.cn/ssah/qwfbjd/tjnj/index.html>.
- [44] Jiangsu Provincial Bureau of Statistics, "Jiangsu provincial Bureau of Statistics," 2022, <http://tj.jiangsu.gov.cn/col/col83749/index.html>.
- [45] Zhejiang Provincial Bureau of Statistics, "Zhejiang provincial Bureau of Statistics," 2022, <http://tj.zj.gov.cn/col/col1525563/index.html>.
- [46] Shanghai Bureau of Statistics, "Shanghai Bureau of Statistics," 2022, <https://tj.sh.gov.cn/tjnj/index.html>.
- [47] K. Tone, "A slacks-based measure of efficiency in data envelopment analysis," *European Journal of Operational Research*, vol. 3, pp. 498–509, 2001.
- [48] K. Tone, "A slacks-based measure of super-efficiency in data envelopment analysis," *European Journal of Operational Research*, vol. 143, no. 1, pp. 32–41, 2002.

Research Article

Sensor Optimization for Variation Diagnosis in Multistation Assembly Processes

Kang He ^{1,2} Xiaobiao Li ^{1,2} Fei Sun ^{1,2} Quan Yang^{1,2} Bo Wu ^{1,2} and Chao Meng ²

¹High-End Micro-Nano Grinding Equipment School-Enterprise Collaborative Innovation Engineering Center, Suzhou University, Suzhou 234000, China

²Anhui Root Industrial Co Ltd., Suzhou 234000, China

Correspondence should be addressed to Xiaobiao Li; szjzxx2022@126.com

Received 3 May 2022; Revised 15 June 2022; Accepted 5 July 2022; Published 2 August 2022

Academic Editor: Wei Cai

Copyright © 2022 Kang He et al. This is an open access article distributed under the Creative Commons Attribution License, which permits unrestricted use, distribution, and reproduction in any medium, provided the original work is properly cited.

Appropriate sensor deployment is the key to the efficient diagnosis of product variation. Yet, optimizing sensor placement in complex manufacturing systems remains challenging. We propose a variation propagation analysis (VPA)-based sensor deployment strategy for variation diagnosis in multistation assembly processes. A state-space model is employed to analyze the influences of fixture faults and workpiece dimensional deviations on assembly variation. Based on matrix transformation, the assembly variation propagation characteristics are quantified and a VPN-based causal graph is constructed to represent the causality between assembly variation and sensor measurement. To ensure the diagnosability of over-tolerance of assembly variation (OAV) and the economics of the sensor system, an optimal sensor deployment scheme is presented. It uses the enhanced shuffled frog-leaping algorithm to minimize the OAV unobservability per unit cost and the sensor cost under the constraint of detectability. Finally, the effectiveness of the proposed approach is illustrated by a case study of sensor deployment for variation diagnosis in a multistation automobile differential assembly process.

1. Introduction

In the multistation assembly processes used in current manufacturing industries, variation diagnosis is an important issue that remains to be solved. In product assembly processes, condition monitoring based on distributed sensor networks (DSNs) is an effective and reliable way to ensure the assembly quality of product parts. In multistation assembly processes, fixture failure is the main source of dimensional variation in assembled parts [1], especially in the automotive and aerospace industries, where about 70% of product assembly variations are caused by fixture failure [2]. Therefore, in multistation assembly processes, an effective, real-time strategy is needed to monitor the sources of variation that cause product assembly quality defects, so as to effectively diagnose and control product variation.

In complex multistation assembly processes, product variation diagnosability depends on the ability of sensors to determine abnormal states in the system [3]. However, this is constrained by many aspects, such as the assembly process,

the sensor characteristics and arrangement, and the characteristics of the variation sources. Improper sensor placement may fail to provide sufficient and accurate data, thereby reducing the diagnostic capabilities of the system. Although a saturated sensor arrangement can effectively overcome this, it may produce a large amount of irrelevant or conflicting data, increasing the difficulty of data processing [1] and reducing system diagnosability. For this reason, there has been much research on optimizing sensor arrangements for condition monitoring during assembly processes.

Initial sensor placement strategies for variation diagnosis mainly focused on single-station placement. Khan et al. [4] proposed an optimized sensor arrangement for fault identification in automobile body assembly fixtures. The fixture design specification was incorporated into the sensor field plan to optimize the sensor arrangement for single-fixture fault diagnosis and reduce the variation in automobile body assembly. They also proposed a multilayer, two-step, and hierarchical optimized sensor arrangement based on Computer Aided Design (CAD) assembly data for multifixture

fault diagnosis during stamped part assembly processes, which improved the multifixture fault diagnosability by maximizing the minimum single-fixture diagnosis vector norm [5]. Liu et al. [6] proposed a causal network approach to characterize the causal relationship between assembly variation sources and measurement features. Based on a causal network, they used information entropy to evaluate the sensitivity of measurement features to the source of assembly variation. Then, a sensor optimization algorithm was used to obtain the minimum number of features and optimal sensor arrangement for fully identifying the sources of assembly variation. Li et al. [7] proposed a grey relational analysis (GRA)-based quantitative causal diagram (QCD) sensor allocation strategy, which considers the influence of the propagation of fault risks. Fault-to-sensor and fault-to-fault causal relationships are expressed by the QCD and the propagation coefficients of fault risk, which are calculated by GRA. However, they only considered sensors of a single type. He et al. [8, 9] proposed a quantitative fuzzy bipartite graph model to characterize the causal relationship between sensors and fault/assembly variation sources. The sensor layout is optimized for condition monitoring of a single-station and multistep manufacturing process by efficiently integrating sensor and fault/variation source features into cause-and-effect diagrams. However, this approach is limited by the single-station sensor layout and a lack of systematic analysis of the inherent causal relationships between various fault/variation sources.

Compared with local single-station sensor arrangements, multistation arrangements based on distributed sensing at the system level have received increasing attention. Based on matrix transformation of a state-space model, Ding et al. [1] analyzed the transmissibility of variation between stations and the variation diagnosability of single stations. They then derived a corresponding performance measurement index for variation diagnosis in multistation assembly processes. However, the characteristic differences between sensors were ignored. Yu et al. proposed a novel approach that integrates statistical analysis with domain knowledge. The relationships between key control and product characteristics are revealed by a variation propagation model. The fault diagnosis problem is transformed into a search for a sparse solution to abnormal variance changes in process faults. Based on the non-negative property of a covariance matrix, a Bayesian hierarchical model was developed to allow sparse estimation of the variance in underdetermined multistage assembly processes [10]. Shukla et al. [11] presented a novel method of sensor allocation for multistation assembly processes. It minimizes the effect of noise on sensor placement by maximizing the determinant of a Fischer information matrix. The state-space method is used to simulate the variation propagation pertaining to the transfer of parts within a multistation assembly process. The influence of sensor coupling noise was added to an optimization objective function, and a chaotic embedded fast simulated annealing algorithm (CEFSA) was proposed to optimize the objective function. An optimal sensor arrangement with minimal noise impact was obtained. Ren and Ding [12] proposed a distributed sensor

placement strategy to maximize assembly variation diagnosability in multistation assembly processes. They defined a sensitivity index to characterize the diagnostic capability of sensor networks and employed a data-mining-guided evolutionary approach for the nonlinear optimization of sensor layouts. However, only sensors of the same type were considered. Bastani et al. [13] proposed an optimal sensor layout method based on compressive sensing for fault diagnosis in multistation assembly processes. It is based on the ability of compressed sensing theory to deal with indeterminate equations by seeking the minimum average cross-correlation coefficient to maximize the system fault diagnosability. Liu and Shi [14] proposed a sensor arrangement method for real-time system fault diagnosis based on distributed sensor networks. They used a Bayesian network to determine the causal relationships between system faults and sensor measurements. The sensor placement problem was transformed into a sensor set coverage problem to minimize the system cost and meet the diagnosability constraints. Finally, the optimal sensor arrangement was obtained via an intelligent searching algorithm of minimum placement subsets. Using a discrete-time nonlinear state-space model, Qu et al. [15] developed a more accurate multistation assembly process variation propagation model, which provides a mathematical representation for process-oriented positioning reference system design. They proposed a design parameter model that includes a positioning reference system and established the quantitative relationship between key control characteristics and key product characteristics. Shukla et al. [16] proposed an optimal sensor placement method based on key product features for product quality variation diagnosis in multistation assembly processes. Firstly, a genetic algorithm is used to maximize the number of key feature points, and then a search method is used to further optimize the sensor network to obtain its optimal arrangement. Although, the concept of key quality characteristics was proposed, there was no analysis of the internal correlations between them.

It can be seen from the above literature that whether a single- or multistation sensor arrangement strategy is used, variation diagnosis in assembly variation transmission, causal model construction, and multiobjective optimization still have the following problems that the present study aimed to solve the following:

- (1) Although many studies have considered variation transfer characteristics in multistation assembly processes, the inherent correlations between the variation source characteristics and the assembly process, as well as the influences of sensor and variation source characteristics on multistation sensor arrangements, still require further analysis and improvement.
- (2) In multistation assembly processes, the status information provided by different types of sensors and variation source features influences the network diagnosis accuracy. Effectively integrating such information into causal models has received little attention in research on multistation sensor optimal arrangement.

- (3) The optimization of sensor arrangements for multistation assembly variation diagnosis is currently limited to single-objective optimization approaches. The introduction of an effective intelligent optimization algorithm into a multiobjective optimization approach warrants further research.

2. Sensor Layout Methodology

2.1. Multistation Assembly Variation Propagation Analysis (VPA). Multistation assembly refers to a process where products/parts are assembled at multiple stations. For example, the assembly of automobile main reducers, bodies in white, and engines are completed at multiple stations. In the assembly process, positioning pins and NC positioning blocks are widely used for precise positioning during workpiece assembly. The 3-2-1 fixture and rigid part assumptions are made in the derivation. For rigid parts, the 3-2-1 principle is the most common layout method [17]. It mainly includes locating pins P_1 limited to four degrees of freedom, a locating pin P_2 restricted to two degrees of freedom, and an NC block restricted in a single direction. At each assembly station, a fixture failure can directly cause assembly misalignment, producing an error declination $\Delta\alpha_{P_{2,1}}$. If the fixture is excessively worn, the positioning point is moved from P_2 to $P_{2,2}$, resulting in a deviation angle $\Delta\alpha_{P_{2,2}}$. In some special cases, if the workpiece itself has a dimensional deviation, such as in the size of a positioning hole, the resulting deviation angle $\Delta\alpha_{P_{2,1}}$ is equivalent to the deviation angle $\Delta\beta_{P_2}$, as shown in Figure 1.

To effectively describe the evolution of the variation information in the multistation assembly process and reveal the causal relationship between this information and sensor measurements, a state-space model is used to characterize the multivariate input and output relationship of the assembly variation information flow [17], as shown in Figure 2. The model is as follows:

$$\begin{aligned} X_k &= A_{k-1}X_{k-1} + B_kU_k + e_k, \\ U_k &= F_{k,i} + P_{k,j}, \\ Y_k &= C_kX_k + w_k, \end{aligned} \quad (1)$$

$i, j, k \in \{1, 2, \dots, N\}$,

where k is the station index and N is the number of stations. The product dimensional state, which describes random dimensional deviations, is denoted as $X_k \in \mathfrak{R}^{n_k \times 1}$ ($k = 1, 2, \dots, N$). $U_k \in \mathfrak{R}^{v_k \times 1}$ ($k = 1, 2, \dots, N$) represents the variation information introduced at station k . $F_{k,i} \in \mathfrak{R}^{v_k \times 1}$ and $P_{k,j} \in \mathfrak{R}^{v_k \times 1}$ describe the variation information introduced by the i^{th} fixture failure and j^{th} workpiece dimensional deviation, respectively. Product measurements at the station are included in $Y_k \in \mathfrak{R}^{m_k \times 1}$. However, if Y_k is not specifically measured, then $C_k = 0$. v_k, μ_k, γ_k respectively represent the dimensions of its vector. Additional process variation, including unmodeled higher-order terms, is represented by e_k . Sensor noise, denoted by w_k , is a vector of uncorrelated random variables with zero means. A_k is known as a dynamic matrix that characterizes assembly reorientation during part

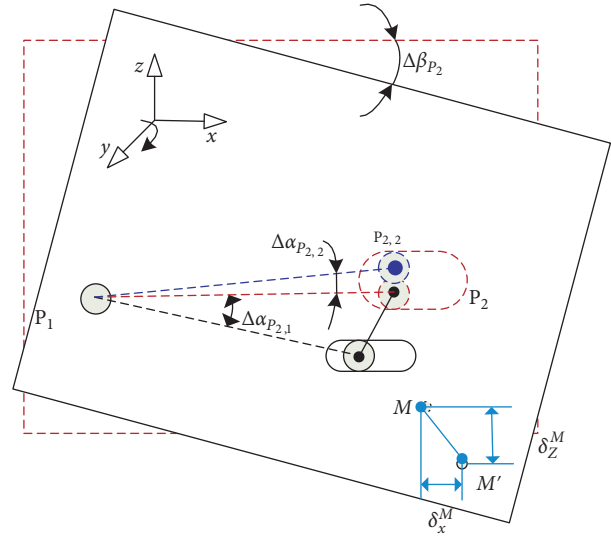


FIGURE 1: Assembly deviation due to locating pin P_2 .

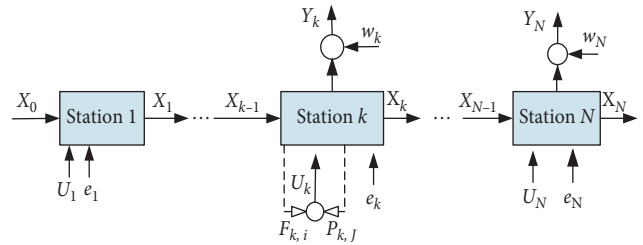


FIGURE 2: Multistation assembly variation information flow.

transfer between stations. B_k is an input matrix that determines how fixture failure and workpiece dimensional deviation affect the product assembly variation state at station k . C_k is an observation matrix that includes sensor deployment information [17]. A detailed analysis of a multistation system modeled by equation (1) was reported in [1]. The recursive expression in equation (1) can be formulated into an input-output relation as

$$\begin{aligned} X_k &= A_{k-1}X_{k-1} + B_kU_k + e_k \\ &= \prod_{j=k-1}^{i-1} A_j X_{i-1} + \begin{bmatrix} B_k \\ \prod_{j=k-1}^{k-1} A_j B_{k-1} \\ \prod_{j=k-1}^{k-2} A_j B_{k-2} \\ \vdots \\ \prod_{j=k-1}^i A_j B_i \end{bmatrix} \begin{bmatrix} U_k \\ U_{k-1} \\ U_{k-2} \\ \vdots \\ U_i \end{bmatrix} + \begin{bmatrix} I \\ \prod_{j=k-1}^{k-1} A_j \\ \prod_{j=k-1}^{k-2} A_j \\ \vdots \\ \prod_{j=k-1}^i A_j \end{bmatrix} \begin{bmatrix} e_k \\ e_{k-1} \\ e_{k-2} \\ \vdots \\ e_i \end{bmatrix} \\ &= G_{i-1 \rightarrow k} X_{i-1} + \begin{bmatrix} G_{k \rightarrow k} B_k \\ G_{k-1 \rightarrow k} B_{k-1} \\ G_{k-2 \rightarrow k} B_{k-2} \\ G_{k-3 \rightarrow k} B_{k-3} \\ \vdots \\ G_{i \rightarrow k} B_i \end{bmatrix} \begin{bmatrix} U_k \\ U_{k-1} \\ U_{k-2} \\ U_{k-3} \\ \vdots \\ U_i \end{bmatrix} + \begin{bmatrix} G_{k \rightarrow k} \\ G_{k-1 \rightarrow k} \\ G_{k-2 \rightarrow k} \\ G_{k-3 \rightarrow k} \\ \vdots \\ G_{i \rightarrow k} \end{bmatrix} \begin{bmatrix} e_k \\ e_{k-1} \\ e_{k-2} \\ e_{k-3} \\ \vdots \\ e_i \end{bmatrix}, \end{aligned} \quad (2)$$

where a state transition matrix for a state-space approach may be defined as $G_{i \rightarrow k} = \left\{ \prod_{j=k-1}^i A_j, \text{ when } i \leq k-1; I, \text{ when } i = k \right\}$. The linear input-output relations between the observation vector Y_k and variation sources U_k is illustrated based on the SOVA model, as shown in (1) [17]. The input-output model is

$$S_i \longrightarrow Y_{1 \rightarrow k} = Z_{1 \rightarrow k} U_{1 \rightarrow k} + \Theta_{1 \rightarrow k}, \quad (3)$$

where S_i indicates that the i^{th} sensor is installed at the k^{th} station. $\Delta_{1 \rightarrow k}$ indicates the accumulated error information at the k^{th} station ($\Delta = Y, U$). $\Theta_{1 \rightarrow k}$ represents the independent noise source accumulated at the k^{th} station, $\Theta_{1 \rightarrow k} = \sum_{i=1}^k C_k G_{j \rightarrow k} e_i + w_k$. The coefficient of the first term in equation (2), $Z_{1 \rightarrow k}$, can be defined as

$$Z_{1 \rightarrow k} = \begin{bmatrix} C_1 B_1 & 0 & 0 & 0 \\ C_2 G_{1 \rightarrow 2} B_1 & C_2 B_2 & \dots & 0 \\ C_3 G_{1 \rightarrow 3} B_1 & C_3 G_{2 \rightarrow 3} B_2 & \dots & 0 \\ C_4 G_{1 \rightarrow 4} B_1 & C_4 G_{2 \rightarrow 4} B_2 & \dots & 0 \\ \vdots & \vdots & \vdots & \vdots \\ C_k G_{1 \rightarrow k} B_1 & C_k G_{2 \rightarrow k} B_2 & \dots & C_k B_k \end{bmatrix}. \quad (4)$$

According to equations (2) and (3), whether the sensor S_i should be arranged at station k or not is closely related to the matrix $G_{i \rightarrow k} B_i$. After $\pi(\bullet)$ matrix transformation [1], $\pi(G_{i \rightarrow k} B_i)$ can be obtained, whose rank $R_{i \rightarrow k} = \text{Rank}\{\pi(G_{i \rightarrow k} B_i)\}$ represents the number of assembly variation sources transmitted from station i to station k . Assuming that there are v_i workpiece/part assemblies at station i , the assembly variation transfer rate from station i to station k is $R_{i \rightarrow k}/3v_i$. When the number of workpieces/parts is joined at station i and the coordinates of the positioning pins are known, it is easy to obtain the assembly variation transfer coefficient [18]. If v_i independent workpieces/parts are assembled at the i^{th} station, the variation transfer coefficient from station i to station k , $c_{i \rightarrow k}$, can be expressed as

$$c_{i \rightarrow k} = \begin{cases} 0.667 v_i = 2, R_{k-1 \rightarrow k} = 4, \\ 0.833 v_i = 2, R_{k-1 \rightarrow k} = 5, \\ 1 v_i \geq 3, \text{ or } i = k. \end{cases} \quad (5)$$

To objectively evaluate the system diagnostic capability, it is crucial to effectively integrate the assembly variation and sensor characteristics (especially of heterogeneous sensors) into the sensor layout optimization process [3]. Here, the failure mode effect analysis (FMEA) of 6Sigma is used to effectively quantify the characteristics of the sensor and assembly variation source itself, such as the occurrence rate (f) of over-tolerance of assembly variation (OAV). The causal analysis tool of 6 Sigma is used based on VPA to build a causal model of sensor measurement and multistation assembly variation.

2.2. Optimal Sensor-Distribution Strategy. The reliability of the diagnostic network is not only restricted by the assembly process, but also by the characteristics of the sensor and the

source of assembly variation itself. To match the assembly variation source node with the sensor node, it is necessary to minimize the unobservability of the OAV of the entire system; that is, to minimize the probability that sensor failure and OAV occur at the same time [3]. This also minimizes the sensor layout cost [7]. The detectability of assembly variation is taken as the constraint condition. Mathematically, this can be expressed as

$$\text{Min: } U = \frac{\sum_{k=1}^N \sum_{i=1}^M [\log(f_{k,i}) + \sum_{j=1}^m (d_{i,j} \times \log(\text{Pr}_{k,j}) \times x_j)]}{\sum_{k=1}^N \sum_{j=1}^m c_{k,j} x_j},$$

$$\text{Min: } C = \sum_k \sum_j c_{k,j} x_j,$$

Subject to:

$$\left(\sum_{j \in S} d_{i,j} x_j \right) | \forall i \in X > 0. \quad (6)$$

These equations mean that an OAV is only unable to be observed when it occurs at the moment of sensor failure. Here, U is the OAV unobservability index per unit cost, C is the system layout cost, $f_{k,i}$ is the OAV occurrence probability, $\text{Pr}_{k,j}$ is the sensor failure probability, $d_{i,j}$ is the entry of a binary bipartite matrix ($d_{i,j} = 1$ if the OAV affects sensor S_j or is zero otherwise), and x_j and $c_{k,j}$ are decision variables related to how many j^{th} sensors need to be used, and their price, respectively. We notice that the primary objective is the OAV unobservability index per unit cost (U). The system layout cost (C) is the secondary objective function that needs to be minimized under the constraints of detectability. The proposed approach to direct sensor deployment is shown in Figure 3.

3. Results and Discussion

To illustrate the proposed sensor deployment approach for multistation assembly system diagnosis, a case study of an automobile differential assembly process is presented below.

An automobile differential assembly line (Figure 4) owned by the project team was used to demonstrate the proposed sensor deployment approach. Optimization of the sensor arrangement was carried out for this multistation assembly process. Figure 5 shows the assembly process. Four stations are analyzed, of which three parts are joined at Station 1, which has an assembly variation transfer coefficient $c_{1 \rightarrow k} = 1, 1 < k \leq 4$. At Station 2, two parts are joined, and their 4-DOF positioning pins have the same Z -coordinate, which means $R_{k-1 \rightarrow k} = 4$. Therefore, its assembly variation transfer coefficient is $c_{2 \rightarrow k} = 0.667, 2 < k \leq 4$. Similarly, at Station 3, the assembly variation transfer coefficient is $c_{3 \rightarrow k} = 0.833, 3 < k \leq 4$. Station 4 is the end inspection station. Based on variation propagation analysis of the above assembly process, a VPA-based causal diagram was constructed (Figure 6). Among them, $X_k (k = 1, 2,$

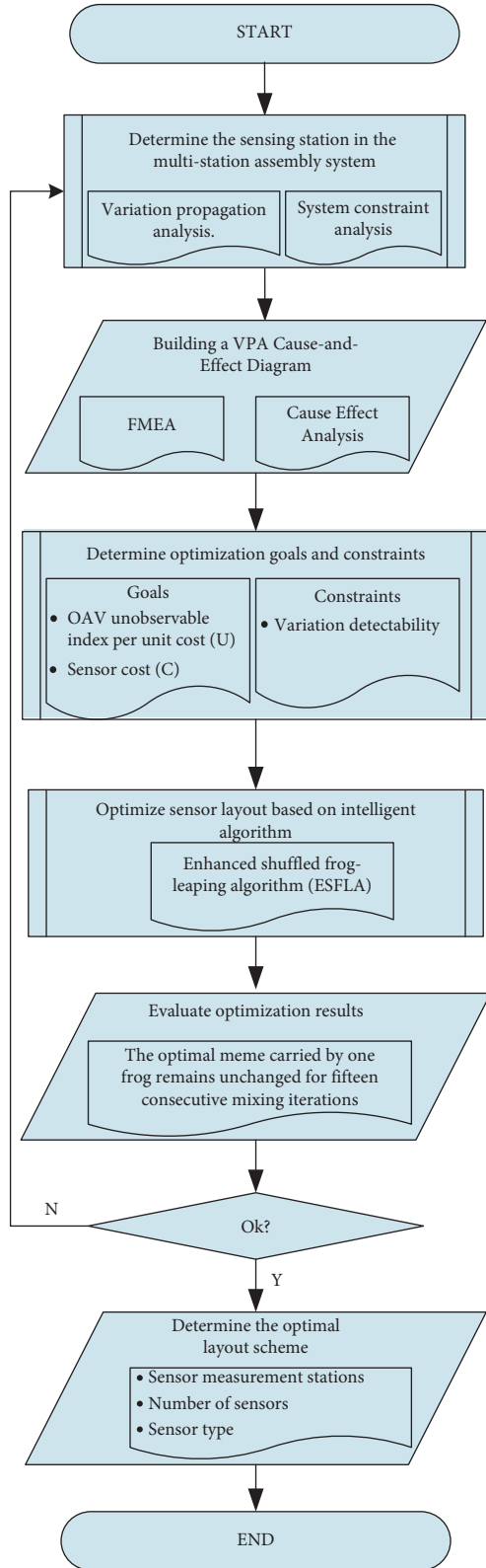


FIGURE 3: VPA-based approach to optimizing sensor layout in multistation assembly processes.

..., 4) denotes the accumulated assembly variation information at the k^{th} station, $F_{i,j}$ is the fixture fault information introduced when the j^{th} part is joined at the i^{th} station, and



FIGURE 4: Automobile differential assembly stations.

$P_{i,j}$ is the workpiece dimensional deviation information introduced, when the j^{th} workpiece is joined at the i^{th} station. Table 1 shows the sensor features and assembly variation characteristics based on FMEA.

The final design of an optimized sensor arrangement must be based on a systematic analysis of operability and economy [19]. To this end, the enhanced shuffled frog-leaping algorithm (ESFLA) is adopted to minimize the OAV unobservability per unit cost, thereby improving the diagnosability and economy of the sensor network system. Here, the “sensor layout position” refers to the position of the assembly variation feature to be detected, rather than the physical position of the sensor actually installed [1]. For the convenience of comparison, a backward propagation (BP)-based sensor layout strategy [1, 11, 12, 18], end-of-line (EOL) sensing, and saturated sensing are also discussed. The optimization variables are exactly the same for all four compared optimization schemes and were derived from the sensor and assembly variation characteristics (Table 1) and their causal relationship based on VPA (Figure 6). In addition, the basic parameters of the ESFLA were as follows. Number of memplexes $m_g = 50$, number of frogs in each memplex $n_g = 60$, number of frogs in a submemplex $q_g = 50$, iteration number within each submemplex $L_{\max} = 30$, and maximum step size $S_{\max} = 1$. The convergence criteria are met if at least one frog carries the “best memetic pattern so far” for fifteen consecutive shuffles. The results are shown in Table 2.

It can be seen from Table 2 that compared with the other three sensor placement strategies, the proposed VPA-based causal graph achieves a lower OAV unobservability index per unit cost (U) and a lower network placement cost (C), demonstrating better system diagnosability and economy.

The BP-based sensor deployment for multistation assembly variation diagnosis takes into account the transfer characteristics of assembly variations between different stations but ignores the influences of the sensor and assembly variation characteristics on the optimization of the sensor distribution. Therefore, BP-based sensing has a higher OAV unobservability index per unit cost ($U_{BP} = -0.0017 > U_{VPA} = -0.0021$) and a higher network placement cost ($C_{BP} = 2700 > C_{VPA} = 2000$).

The traditional EOL sensor deployment approach ignores the assembly variation propagation characteristics between different stations during the assembly process. This

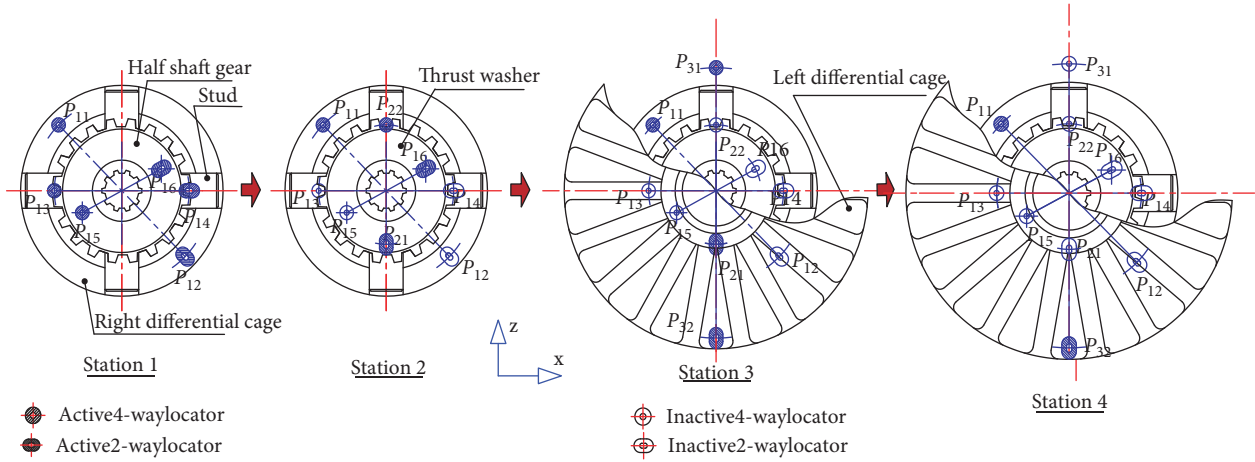


FIGURE 5: Automobile differential assembly sequence.

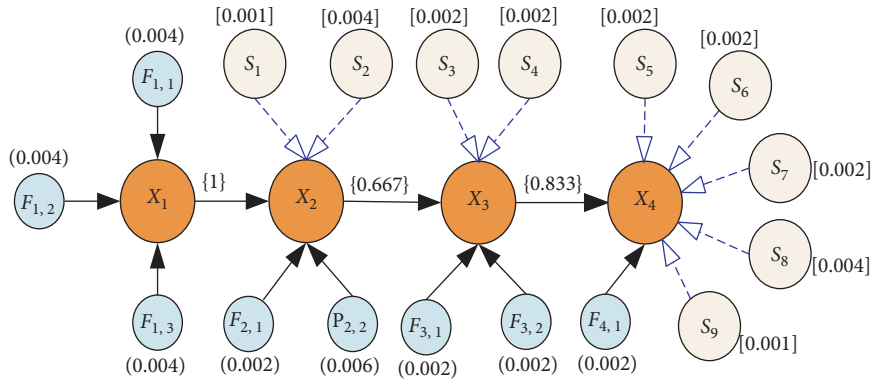


FIGURE 6: VPA-based causal diagram.

TABLE 1: Assembly variations and sensors used in the differential assembly process.

Sensor candidates	Sensor failure rate (P_r , %)	Sensor cost (C, \$)	Part candidate	Possible variations	OAV occurrence rate (f , %)
Displacement sensor S_1	0.1	200	Fixture $F_{2,1}$	Excessive wear	0.2
Thickness sensor S_2	0.4	400	Thrust washer $P_{2,2}$	Thickness deviation	0.6
Displacement sensor S_3	0.2	300	Left diff. cage $F_{3,1}/F_{3,2}$	Fixture failure	0.2
Displacement sensor S_4	0.2	300	Left diff. cage $F_{3,1}/F_{3,2}$	Fixture failure	0.2
Displacement sensor S_5	0.2	300	Right diff. cage $F_{1,1}$	Fixture failure	0.4
Displacement sensor S_6	0.2	300	Stud $F_{1,2}$	Fixture failure	0.4
Displacement sensor S_7	0.2	300	Half-shaft gear $F_{1,3}$	Fixture failure	0.4
Thickness sensor S_8	0.4	400	Thrust washer $P_{2,2}$	Thickness deviation	0.6
Displacement sensor S_9	0.1	200	Left diff.cage/fixture $F_{4,1}$	Excessive wear	0.2

is because the assembly variations generated at Stations 2 and 3 cannot be propagated to the end station (Station 4), while Stations 2 and 3 lack sensor arrangements ($S_1 \sim S_4$). Therefore, the assembly variations generated at Stations 2

and 3 cannot be detected by the system, so system diagnosability cannot be ensured. In addition, the traditional EOL sensor deployment has a high unit OAV unobservability index per unit cost ($U_{EOL} = -0.0005 > U_{VPA} =$

TABLE 2: Comparison of various approaches to automobile differential assembly.

Approach	Sensors selected	OAV unobservability index per unit cost (U)	Cost utilized ($C/\$$)
VPA-based causal graph	$\{S_1, S_2, S_3, S_5, S_6, S_7, S_9\}$	-0.0021	2000
BP-based sensing	$\{S_1, S_2, S_3, S_4, S_5, S_6, S_7, S_8, S_9\}$	-0.0017	2700
EOL sensing	$\{S_5(3), S_6(3), S_7(3), S_8(3), S_9(3)\}$	-0.0005	4500
Saturated sensing	$\{S_1(3), S_2(3), S_3(3), S_4(3), S_5(3), S_6(3), S_7(3), S_8(3), S_9(3)\}$	-0.0012	8100

-0.0021), so it cannot ensure the economy of the sensor system.

In industrial applications, to maximize OAV diagnosability, the corresponding sensors are usually arranged at each potential source of assembly variation, resulting in sensor saturation. Here, considering the actual system, *saturation deployment* refers to installing three sensors at each station, which can effectively reduce information loss. However, due to its high OAV unobservability index per unit cost ($U_{Saturate} = -0.0012 > U_{VPA} = -0.0021$), high sensor deployment cost ($C_{Saturate} = 8100 > C_{VPA} = 2000$), and the difficulty of processing massive sensor datasets in the later stage, the diagnosis efficiency and economy of multistation assembly variation are further weakened. This is also the fundamental reason why the sensor network needs to be optimally deployed.

4. Conclusions

Optimal sensor deployment is an important issue in detecting multistation assembly variation. The accurate and efficient collection of sensor signals is also a new challenge. The contributions of this paper are three-fold:

- (1) Based on a state-space model, the influences of fixture faults and workpiece dimensional deviations on multistation assembly variation were analyzed. By matrix transformation of the state-space model, the inherent characteristics of variation propagation between stations were quantified.
- (2) Based on the analysis of the multistation assembly variation process, a VPA-based causal graph was proposed to characterize the causal relationship between sensor measurements and multistation assembly variations. The key characteristics of the sensors and assembly variations were quantified using the 6Sigma tool and effectively fused into a causal graph.
- (3) A multiobjective optimization model was proposed that (1) minimizes the OAV unobservability index per unit cost (U) and sensor layout cost (C) as its optimization objective, (2) takes detectability as the constraint condition, and (3) is optimized by the ESFLA. A case study of sensor deployment for variation diagnosis in an automobile differential multistation assembly process was conducted. It shows that compared with BP-based, traditional EOL, and saturation sensor layout strategies, the

proposed VPA-based causal graph strategy can (1) obtain a lower OAV unobservability index per unit cost and (2) a lower sensor layout cost, and (3) ensure multistation assembly variation diagnosability and sensor deployment economy.

Data Availability

Data are contained within the article.

Conflicts of Interest

The authors declare no conflicts of interest.

Acknowledgments

This work was supported in part by the Natural Science Foundation of Anhui Province under Grant 2108085ME172, in part by the 2020 Suzhou Science and Technology Plan Project: Development of Nano-pesticide Insecticide Grinding Equipment, in part by the Suzhou University key project under Grant 2021yzd02, in part by the Corporate-Funded R&D Projects under Grant 2022xhx122, 2021xhx023, 2021xhx022, 2021xhx024, and 2021xhx025, in part by the Suzhou College Teacher Application Ability Development Workstation under Grant 2018XJYY01, 2020XJYY03, in part by the Suzhou University Scientific Research Platform Project under Grant 2020ykf14 and 2020ykf13, in part by the Doctoral Scientific Research Foundation of Suzhou University under Grant 2020BS004, and in part by the School-Enterprise Collaborative Innovation Engineering Center Of High-End Micro-Nano Grinding Equipment under Grant 2021XJPT19ZC.

References

- [1] Y. Ding, P. Kim, D. Ceglarek, and J. Jin, "Optimal sensor distribution for variation diagnosis in multistation assembly processes," *IEEE Transactions on Robotics and Automation*, vol. 19, no. 4, pp. 543–556, 2003.
- [2] Y. K. Fu, G. Yang, H. Ma, H. Chen, and B. Zhu, "Statistical diagnosis for quality-related faults in BIW assembly process," *IEEE Transactions on Industrial Electronics*, p. 1, 2022.
- [3] Z. Wu, S. J. Hsieh, and J. Li, "Sensor deployment based on fuzzy graph considering heterogeneity and multiple-objectives to diagnose manufacturing system," *Robotics and Computer-Integrated Manufacturing*, vol. 29, no. 1, pp. 192–208, 2013.
- [4] A. Khan, D. Ceglarek, J. Shi, J. Ni, and T. C. Woo, "Sensor optimization for fault diagnosis in single fixture systems: a

- methodology,” *Journal of Manufacturing Science and Engineering*, vol. 121, no. 1, pp. 109–117, 1999.
- [5] A. Khan and D. Ceglarek, “Sensor optimization for fault diagnosis in multi-fixtured assembly systems with distributed sensing,” *Journal of Manufacturing Science and Engineering*, vol. 122, no. 1, pp. 215–226, 2000.
- [6] Y. Liu, X. Luan, and H. Liu, “Feature selection and sampling uncertainty analysis for variation sources identification in the assembly process online sensing,” *International Journal of Advanced Manufacturing Technology*, vol. 92, no. 5-8, pp. 2777–2785, 2017.
- [7] Y. Li, N. Y. Lu, J. T. Shi, and B. Jiang, “A quantitative causal diagram based optimal sensor allocation strategy considering the propagation of fault risk,” *Journal of the Franklin Institute*, vol. 358, no. 1, pp. 1021–1043, 2021.
- [8] K. He, M. Jia, and Q. Xu, “Optimal sensor deployment for manufacturing process monitoring based on quantitative cause-effect graph,” *IEEE Transactions on Automation Science and Engineering*, vol. 13, no. 2, pp. 963–975, 2016.
- [9] K. He, M. Jia, L. Zhu, and Z. Zhao, “Sensor deployment for variation diagnosis considering heterogeneity in single-station multi-step assembly processes,” *International Journal of Advanced Manufacturing Technology*, vol. 94, no. 9-12, pp. 3889–3901, 2018.
- [10] D. Yu, J. Guo, Q. Zhao, D. Zhao, and J. Hong, “Fault diagnosis for underdetermined multistage assembly processes via an enhanced Bayesian hierarchical model,” *Journal of Manufacturing Systems*, vol. 58, pp. 280–290, 2021.
- [11] N. Shukla, M. K. Tiwari, and R. Shankar, “Optimal sensor distribution for multi-station assembly process using chaos-embedded fast-simulated annealing,” *International Journal of Production Research*, vol. 47, no. 1, pp. 187–211, 2009.
- [12] Y. Ren and Y. Ding, “Optimal sensor distribution in multi-station assembly processes for maximal variance detection capability,” *IIE Transactions*, vol. 41, no. 9, pp. 804–818, 2009.
- [13] K. Bastani, Z. J. Kong, W. Huang, and Y. Zhou, “Compressive sensing-based optimal sensor placement and fault diagnosis for multi-station assembly processes,” *IIE Transactions*, vol. 48, no. 5, pp. 462–474, 2016.
- [14] K. Liu and J. Shi, “Objective-oriented optimal sensor allocation strategy for process monitoring and diagnosis by multivariate analysis in a Bayesian network,” *IIE Transactions*, vol. 45, no. 6, pp. 630–643, 2013.
- [15] X. Qu, X. Li, Q. Ma, and X. Wang, “Variation propagation modeling for locating datum system design in multi-station assembly processes,” *International Journal of Advanced Manufacturing Technology*, vol. 86, no. 5-8, pp. 1357–1366, 2016.
- [16] N. Shukla, D. Ceglarek, and M. K. Tiwari, “Key characteristics-based sensor distribution in multi-station assembly processes,” *Journal of Intelligent Manufacturing*, vol. 26, no. 1, pp. 43–58, 2015.
- [17] J. Jin and J. Shi, “State space modeling of sheet metal assembly for dimensional control,” *Journal of Manufacturing Science and Engineering*, vol. 121, no. 4, pp. 756–762, 1999.
- [18] X. Lai, Z. Tian, and Z. Lin, “A simplified method for optimal sensor distribution for process fault diagnosis in multistation assembly processes,” *Journal of Manufacturing Science and Engineering*, vol. 130, no. 5, pp. 051002–051014, 2008.
- [19] B. Li, “Model and algorithm of innovation performance evaluation for coordination of supply and demand based on wireless sensor network,” *EURASIP Journal on Applied Signal Processing*, vol. 2021, no. 1, p. 108, 2021.

Research Article

DEM Investigation of Discrete Heat Transfer Behavior of the Grinding Media in Ball Mills

Zixin Yin ^{1,2}, Nan Wang ^{1,2} and Tongqing Li ³

¹School of Mechanical and Electronic Engineering, Suzhou University, Suzhou 234000, China

²Suzhou University Technology and Research Center of Engineering Tribology, Suzhou University, Suzhou234000, China

³School of Mechanical Engineering, Jiangsu Ocean University, Lianyungang 222005, China

Correspondence should be addressed to Zixin Yin; yzxszu@126.com and Nan Wang; szxywn@126.com

Received 29 March 2022; Accepted 31 May 2022; Published 30 July 2022

Academic Editor: Ardashir Mohammadzadeh

Copyright © 2022 Zixin Yin et al. This is an open access article distributed under the Creative Commons Attribution License, which permits unrestricted use, distribution, and reproduction in any medium, provided the original work is properly cited.

This study presented a numerical model for the quantitative assessment of the heat transfer behavior of grinding media inside a ball mill. Effects of various mill speeds, grinding media filling, and the number of lifters on heat transfer were studied and verified by comparing the experimental results and the numerical simulations calculated by DEM (Discrete Element Method). The results show that the heat transfer of grinding media has a strong sensitivity to the variation of the mill speed, grinding media filling, and the number of lifters. The optimum grinding conditions for heat transfer behavior can be determined in terms of the temperature field of the grinding media. The maximum temperature rise of grinding media occurs at a range from 70% to 80% of critical speed. The maximum average temperature of grinding media up to 295.057 K appears at the grinding media filling 25% and the number of lifters 12. Subsequently, validation experiments are carried out to validate the numerical simulation results. The experimental results are closer to the simulation results, indicating the reasonability of the heat transfer model.

1. Introduction

Ball mills are widely used in many industrial fields for grinding and crushing granular materials, such as the mineral, chemical, and pharmaceutical industries [1–4]. It is dependent on the lifters to lift the grinding media to a specific level of energy and the balls then cataract and cascade, and in consequence, collide with each other, resulting in particles breakage. As a very complicated system, ball mills are typically high-energy and inefficient equipment because of the environment itself. To this end, it is worth attempting to reduce the energy consumption of the ball mill by any means [5].

The charge motion, liner wear, and particle breakage behavior in ball mills have been attracted considerably further attention [6–8]. These outstanding results provide a sound foundation for optimizing mill performance and reducing energy consumption. In the grinding process, bulk ore particles in the grinding process lead to elevated temperatures of the milling environment. This in turn will influence the particle breakage behavior and the energy consumption of the

ball mills, such as tantalum ore particles. However, there are comparatively few studies on heat transfer in conjunction with particle collisions in ball mills. One of the challenges involved in understanding the heat transfer is the approach to determining the temperature distribution of the grinding media in ball mills.

Heat transfer in granular materials is a common phenomenon, and it affects a wide variety of applications ranging from food products to building materials. The phenomenon of heat transfer inside a rotating drum is widely encountered in areas ranging from food products to building materials. In recent years, alternative methodologies have been used to study the heat transfer phenomena, including kinetic theory [9], continuum approaches [10–13], and DEM simulation [14–17]. Chaudhuri et al. [18] used the method of experimentation and DEM simulation to examine the flow, mixing, and mass and heat transport in rotary calciners. Alumina and copper were used to understand the effect of particle flow and heat transfer on the calcination performance. The results showed that the material with higher thermal conductivity

warmed up faster in experiments and DEM simulations. Xie et al. [19] investigated the heat transfer inside a drum mixer by coupling the DEM simulation with a conductive heat transfer model. The DEM simulation showed that the specific heat transfer coefficient of the particle flow increased with the increasing rotating speed but decreased with the amounts and heights of the lifters. Komossa et al. [20] investigated the heat transfer in an indirectly heated tumbling drum. The particle movement and heat transfer showed a good agreement between the DEM simulation and the experiment. Gui and Fan [21] used the DEM simulation with a thermal conduction model to investigate the effects of the rotation speed and the wave number on the heat transfer. The wavy drums raised the heat transfer process higher than a circular drum for a lower rotation speed. Figueroa et al. [22] applied various evaluation methods to examine the interaction between heat transfer and particle load behavior. A continuum model was used to study the relationship between temperature contours and mixing patterns. Oschmann et al. [23] derived a novel particle-wall heat transfer coupling algorithm from resolving the heat transfer due to particle-wall contact and inner wall heat conduction. Li et al. [24] studied the heat transfer of granular material in a rotary drum. The results showed that increasing rotational speed can intensify heat transfer to a certain degree, and the average temperature of granular materials increases with the number of flights and decreases the fill level. These above-mentioned studies have provided an understanding of the heat transfer phenomena of granular materials. The drums and granular materials are preheated before grinding and mixing, which is completely different from the grinding process of ball mills. In addition, the heat generated by the granular particle collision is not taken into account.

This paper provides a novelty DEM heat transfer model to investigate the multibody collision in the ball mills. The effects of the mill speed, grinding media filling, and the number of lifters on the temperature field of grinding media are further studied. A laboratory-scale ball mill is employed to perform measurements and validate numerical results.

2. Heat Transfer Model

The heat transfer involved within the particles includes thermal convection, thermal radiation, and thermal conduction, as shown in Figure 1. To quantitatively describe the discrete heat transfer behavior of the grinding media in ball mills, the thermal conduction, and collisional heat of the heat transfer model are considered while the convection and the radiation are being ignored [19]. In this model, the following assumptions are considered:

- (1) The ball mill temperature remains unchanged, and there is no thermal exchange between the particles and the geometry
- (2) The heat generated due to friction can be neglected
- (3) Only the heat transfer in the particle flow due to the contact conduction and collision effect is considered, and the interstitial gas is neglected
- (4) The thermal-physical properties of the grinding media and the iron ore are constant

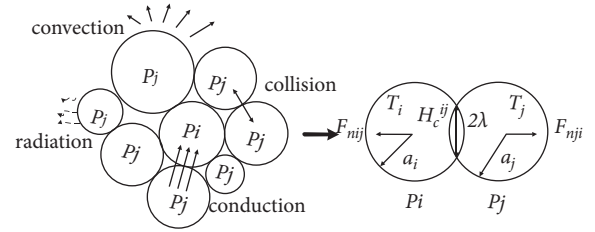


FIGURE 1: Schematic of heat transfer.

In the DEM simulation software, the granular materials are considered as a collection of frictional inelastic spherical particles. A nonlinear Hertz–Mindlin no-slip model is employed to solve the contact force between colliding particles. In DEM simulations, the forces and torques acting on a particle i can be expressed as follows:

$$\begin{aligned} m_i a_i &= \sum F, \\ I_i \theta_i &= \sum M, \end{aligned} \quad (1)$$

where m_i , I_i , a_i , and θ_i are, respectively, the mass, moment of inertia, acceleration, and angular acceleration of particle i ; $\sum F$ and $\sum M$ are the total force and torque applied on particle i , respectively.

The normal contact and tangential contact forces between particles i and j can be described as follows:

$$\begin{aligned} F_n &= -K_n \Delta x + C_n v_n \\ F_t &= \min \left\{ u F_n, K_t \int v_t dt + C_t v_t \right\}. \end{aligned} \quad (2)$$

where K_n and K_t are the normal and tangential stiffness, respectively; Δx is the amount of overlap; v_n and v_t are the normal and tangential relative velocity, respectively; C_n and C_t are the normal and tangential damping coefficient, respectively; u is the friction coefficient.

The C_n depends on the coefficient of restitution ϵ , which is given by the following equation:

$$C_n = -2 \ln(\epsilon) \frac{\sqrt{m_{ij} K_n}}{\sqrt{\pi^2 + \ln^2(\epsilon)}}, \quad (3)$$

where $m_{ij} = m_i m_j / (m_i + m_j)$.

The total heat dissipation of the particle I can be written as follows:

$$Q_i = m_i C_i \frac{dT_i}{dt} = \sum_{j=1}^N (H_c^{ij} (T_i - T_j) + Q_c^{ij}). \quad (4)$$

The H_c^{ij} is a function of the compression force, which refers to the ability of two materials in contact to transfer heat through their mutual interface, which can be expressed as follows [25]:

$$H_c^{ij} = 2k_p \lambda = \frac{4k_{p1} k_{p2}}{k_{p1} + k_{p2}} \left[\frac{3F_n a^*}{4E^*} \right]^{1/3}, \quad (5)$$

where C_i is the specific heat capacity of particle i , T_i and T_j are the temperatures of particle i and j , respectively, H_c^{ij} is

TABLE 1: Ball mill parameters.

Parameters	Test 1	Test 2	Test 3
Mill speed ψ (of critical speed)	50%, 60%, 70%, 80%, 90%, 100%	75%	75%
Grinding media filling J	25%	10%, 15%, 20%, 25%, 30%, 35%	25%
Number of lifters n	12	12	0, 8, 12, 16

the heat transfer coefficient between particles i and j with j varying from 1 to the contact number N , k_p is the thermal conductivity of the granular media, λ represents the contact radius, F_n is the normal force, a^* is the equivalent radius, and E^* is the effective Young's modulus.

The Q_c^{ij} is the heat dissipation by particle collision, which can be expressed as follows:

$$Q_c^{ij} = k\beta E_{ij}, \quad (6)$$

where k refers to the proportional coefficient of collision loss energy converted into internal energy, $k = 0.97$ [26, 27], β is the heat flux distribution coefficient, and E_{ij} is the collision loss energy.

3. Materials and Methods

In this paper, the laboratory-scale ball mill of 520 mm diameter and 260 mm length is employed to investigate the effects of mill speed, grinding media filling, and the number of lifters on the temperature field of the grinding media. The ball mill parameters and its DEM simulation parameters are listed in Tables 1 and 2 [27].

4. DEM Simulation Results and Discussions

4.1. Effect of Mill Speed. Mill speed is one of the vital parameters in ball mills, and it is normally specified as a fraction of critical speed. It determines whether the load behavior is predominantly the cascading regime, the cataracting regime, or the centrifuging regime. Figure 2 shows the effect of mill speed on the temperature field of the grinding media. As shown in Figure 2, significant differences in the temperature field of the grinding media can be observed at different mill speeds. The difference in the colors refers to the temperature of the grinding media, red for the highest temperature and blue for the lowest. As the mill speed is increased from 50% to 100%, a larger amount of grinding media are lifted, and the load behavior has changed from the cataracting regime to the centrifuging regime. This result indicates a dependency of the temperature field of the grinding medium on the loading behavior.

In addition, the load behavior remains nearly unchanged at the mill speed of 50% to 60%, whereby the grinding media is being increasingly lifted to a higher position at mill speeds of 70% to 80%. The temperature field is accordingly altered. As the mill speed reaches 90%–100%, the outermost layer of the grinding media undergoes centrifugation, while the inner layer moves with a cascading regime, exhibiting a significant temperature difference. This is due to a larger amount of grinding media being lifted, reducing heat transfer and contact behavior. In summary, mill speed has a significant effect on

heat transfer, and the change in the temperature field of grinding media indicates the intensity of charge motion.

To quantify the effect of mill speed on the temperature field of the grinding media, the particle numbers at different temperatures are performed, as shown in Figure 3. The results show that the maximum particle number corresponds to the grinding media temperatures for various mill speeds are 298.043 K, 298.048 K, 298.055 K, 298.057 K, 298.049 K, and 298.021 K, respectively. In addition, the average temperature of grinding media increases first and then decreases with mill speed. With a mill speed of 50% of the critical speed, the range of grinding media temperatures is relatively more minor due to the lower mill speed, which leads to the grinding media in cascading motion. With a mill speed of 60% of critical speed, the range of grinding media temperatures is much greater than that at $\psi = 50\%$. The grinding media temperature distribution of the grinding media is dispersed, and the grinding media temperature increases. This changes because the grinding media is lifted and mixed. With a mill speed of 70% of the critical speed, most grinding media is concentrated at a higher temperature. The range of temperatures is minimal compared with the other condition of the mill speeds. This indicates that the mill speed significantly affects the grinding media temperature rise. With a mill speed of 80% of critical speed, there is a similar tendency to at $\psi = 70\%$, but the main change is that the grinding media temperature is marginally lower. However, at a higher speed of $\psi = 90\%$ –100%, the grinding media is trapped between lifters and progressively deviates to the centrifugal motion, resulting in the wide distribution of grinding media temperature. The above-given cases indicate that the mill speed affects the load behavior and the temperature rise, and the maximum grinding media temperature rise is between $\psi = 70\%$ –80%.

4.2. Effect of Grinding Media Filling. The particle breakage process is performed by falling grinding media in ball mills. The crushing and the grinding intensity of the ore particles are dependent on the grinding media amount and velocity. The grinding media filling is a significant operating factor affecting particle breakage and load behavior [28]. The amount of grinding media in the ball mill affects the load behavior and the heat transfer. The current research mainly involves observing the heat transfer phenomenon of the particles by heating the rotating body. However, there has been no reporting on the variation of the temperature field of grinding media with different grinding media fillings. To understand the interrelation between the grinding media filling and the temperature field of grinding media, for the ball mill, grinding media fillings for six levels between $J = 10\%$ and $J = 35\%$ are selected, as shown in Figure 4. All the

TABLE 2: DEM simulation parameters.

Parameters		Value
Grinding media	Size (mm)	30
	Initial temperature (K)	298
	Poisson's ratio	0.30
	Specific heat capacity (J/kg * K)	598.60
	Thermal conductivity (W/m * K)	55.90
	Thermal diffusion coefficient (cm ² /s)	0.12
	Density (kg/m ³)	7850
Coefficient of restitution	Grinding media—grinding media	0.75
	Grinding media—wall	0.45
Coefficient of rolling friction	Grinding media—grinding media	0.01
	Grinding media—wall	0.01

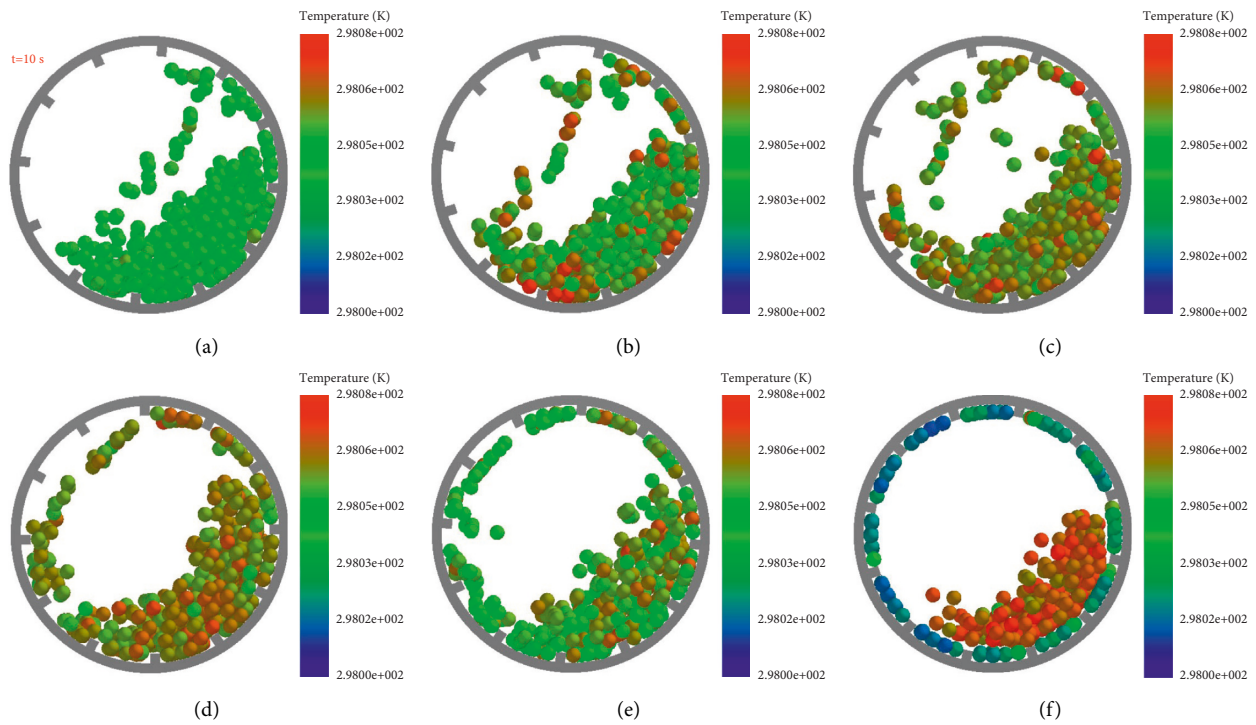


FIGURE 2: Effect of mill speed on the temperature field of grinding media. (a) $\psi = 50\%$. (b) $\psi = 60\%$. (c) $\psi = 70\%$. (d) $\psi = 80\%$. (e) $\psi = 90\%$. (f) $\psi = 100\%$.

load behavior shows that the toe and shoulder angles of the grinding media remain almost unchanged, but the significant difference is the cascading free surface. The grinding media distribution presents obviously two parts of cataracting and cascading. More grinding media is lifted, and the amount of grinding media cascading down from the bulk of grinding media increases with the grinding media filling. At $J = 10\% - 15\%$, the grinding media mainly have a green color. As the grinding media filling increases from 20% to 35%, it is clearly displayed that the red grinding media are more than that of the lower grinding media filling. However, the temperature field of grinding media only changes slightly.

Figure 5 shows the average grinding media temperature variation for different grinding media fillings, which

corresponds to the temperature field of grinding media in Figure 4. As the ball mill motion tends toward a steady state, the average grinding media temperature increases to a maximum value at $J = 25\%$, decreasing from $J = 30\%$ to $J = 35\%$. The average temperatures of grinding media are 298.051 K, 298.053 K, 298.056 K, 298.057 K, 298.057 K, and 298.055 K. The temperature field of grinding media under higher grinding media filling is more inhomogeneous than that of a lower grinding media filling. The reason for this is that the collision frequency and the contact number increase with the grinding media filling, so the grinding media temperature rises increases. As the grinding media filling continues to increase, the bulk of the grinding media is very close to the center of the mill and contributes little to the

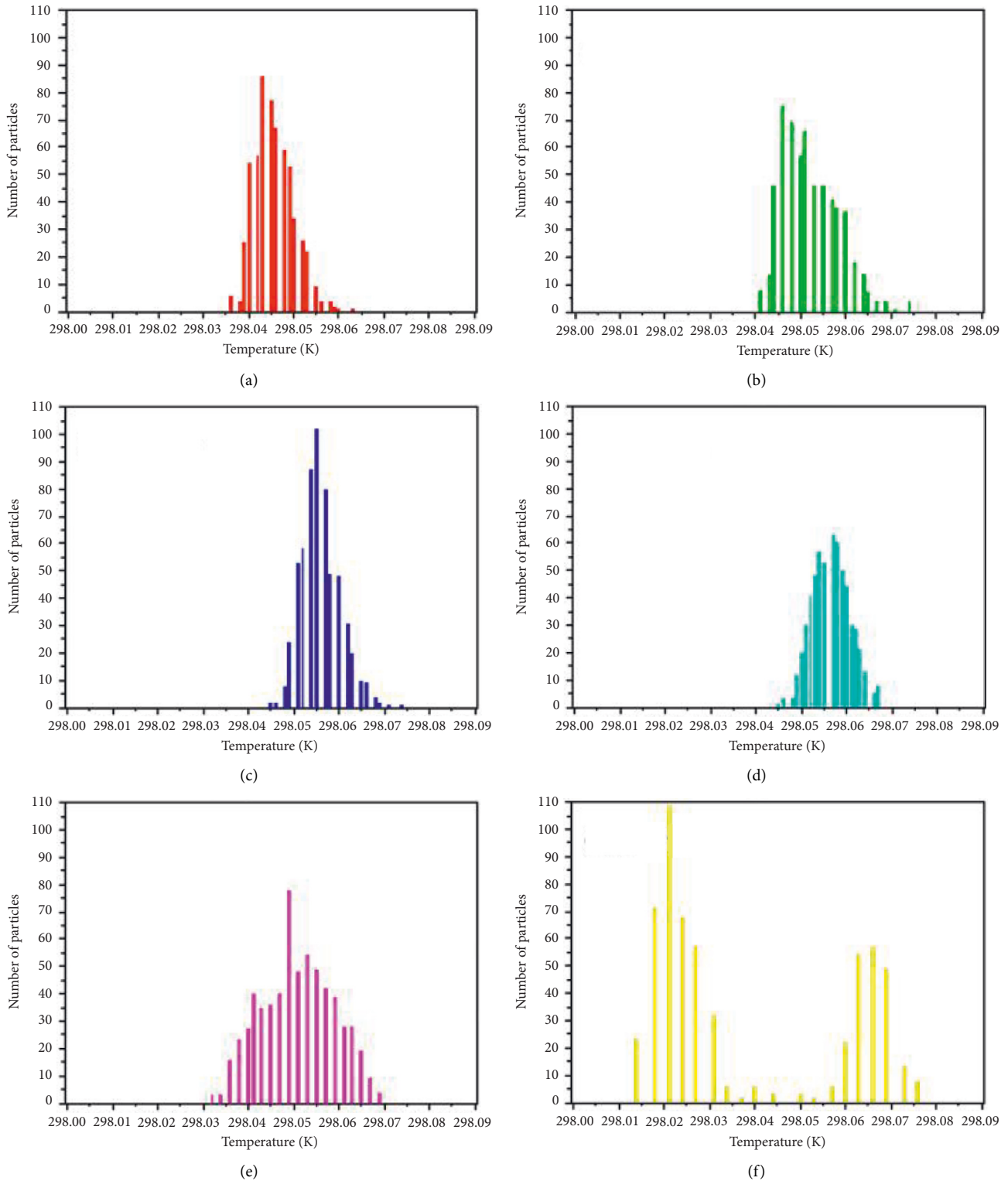


FIGURE 3: The distributions of grinding media temperatures for different mill speeds. (a) $\psi = 50\%$. (b) $\psi = 60\%$. (c) $\psi = 70\%$. (d) $\psi = 80\%$. (e) $\psi = 90\%$. (f) $\psi = 100\%$.

grinding media being off-center. Therefore, the grinding media contributes little to the temperature rise. This result indicates that the grinding media temperature varies slightly with the increase of the grinding media filling.

4.3. *Effect of Number of Lifters.* Lifters are generally used to raise grinding media to transfer the energy from a mill to a load. The distribution of the lifters around a mill shell is an essential factor that affects the grinding and crushing

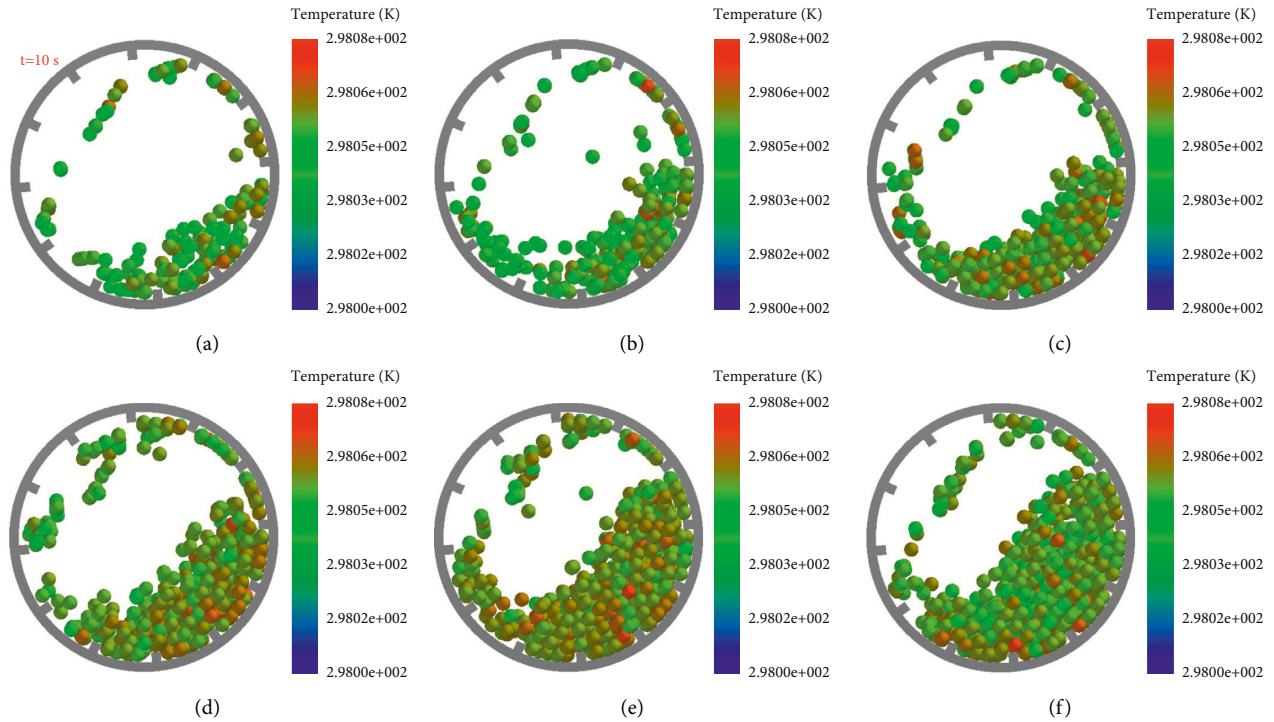


FIGURE 4: Effect of grinding media filling on the grinding media temperature field. (a) $J=10\%$. (b) $J=15\%$. (c) $J=20\%$. (d) $J=25\%$. (e) $J=30\%$. (f) $J=35\%$.

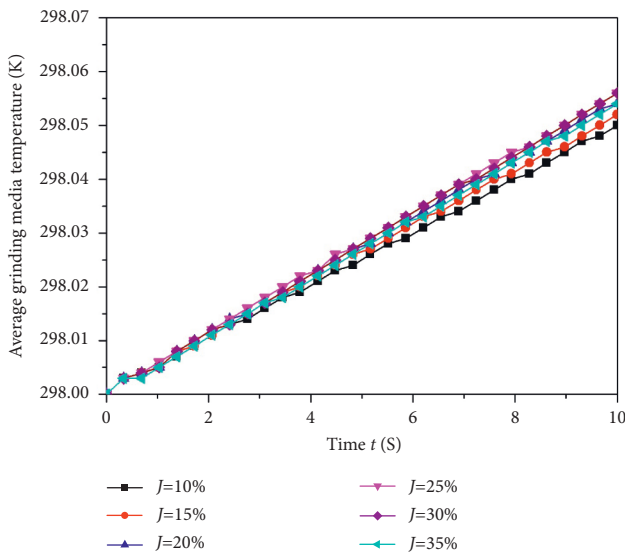


FIGURE 5: The distributions of grinding media temperatures for different grinding media fillings.

efficiency. To understand the interrelation between the number of lifters and the temperature field of grinding media, for the ball mill, the number of lifters for four levels is selected to be between $n=0$ and $n=16$, as shown in Figure 6. The results showed that the shoulder angle of grinding media increases with the number of lifters. However, the temperature field of grinding media revealed that the heat transfer increases first and then decreases. With the number of lifters $n=0$, all the grinding media is located in the cascading regime, and the

grinding media is piled together to grind each other. The temperature field of grinding media is more uniform. With the number of lifters $n=8$, a fraction of grinding media is lifted, but the distribution of the grinding media temperature field changes relatively minor compared with $n=0$. With the number of lifters $n=12$, increasing the number of lifters cause more grinding media to be lifted, and the temperature field of grinding media shows the highest temperature rise. This is because the lifter hinders the sliding motion of the grinding media and promotes the cataracting movement. With the number of lifters $n=16$, the excessive number of lifters increases the slippage between grinding media. This indicates that the distance between two lifters restricts the sliding motion and accelerates the cataracting movement.

Figure 7 shows the distribution of the grinding media temperature field for the different number of lifters, which corresponds to Figure 6. It can be seen that the maximum particle number corresponding to the temperatures of grinding media are 298.048 K, 298.051 K, 298.057 K, and 298.056 K, respectively. The average temperature of grinding media reaches a maximum value of 295.057 K at $n=12$. However, the average temperature of grinding media reaches a minimum value of 298.047 K at $n=0$. These results indicated that increasing the number of lifters can improve heat transfer.

5. Comparison with DEM Simulation and Experiment

The laboratory-scale ball mill with two detachable acrylic plates is employed to validate the established heat transfer model. As shown in Figure 8, the experimental setup consists

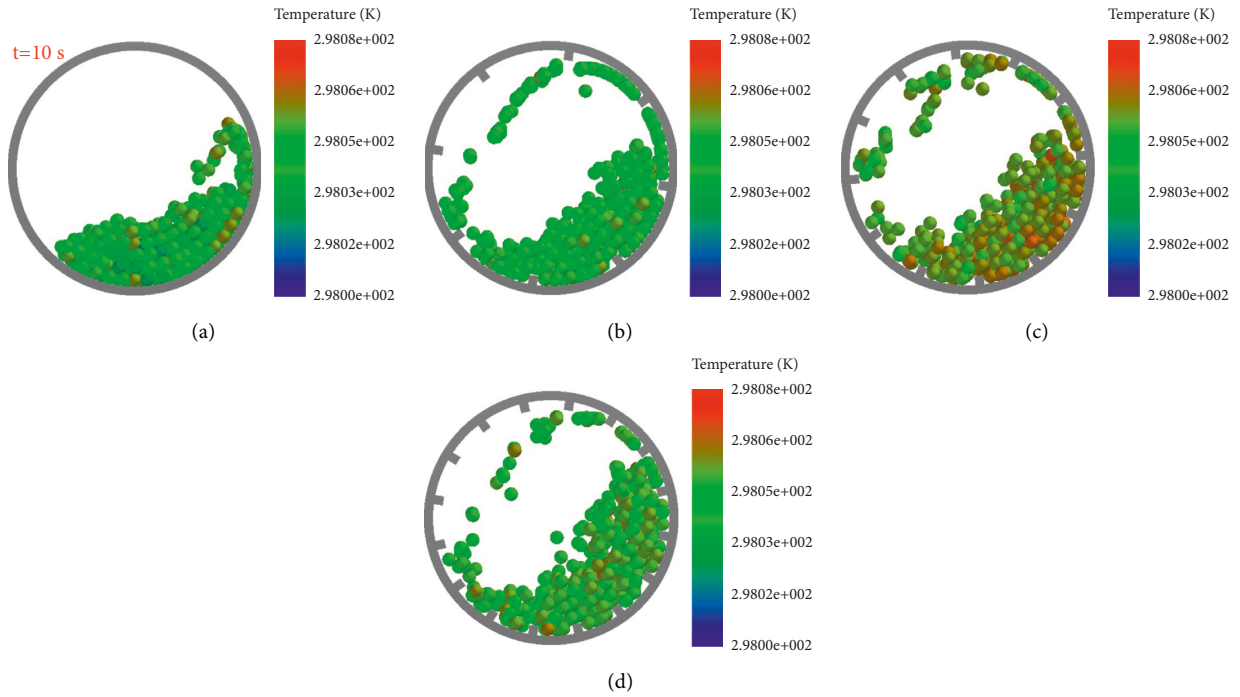


FIGURE 6: Effect of the number of lifters on grinding media temperature field. (a) $n = 0$. (b) $n = 8$. (c) $n = 12$. (d) $n = 16$.

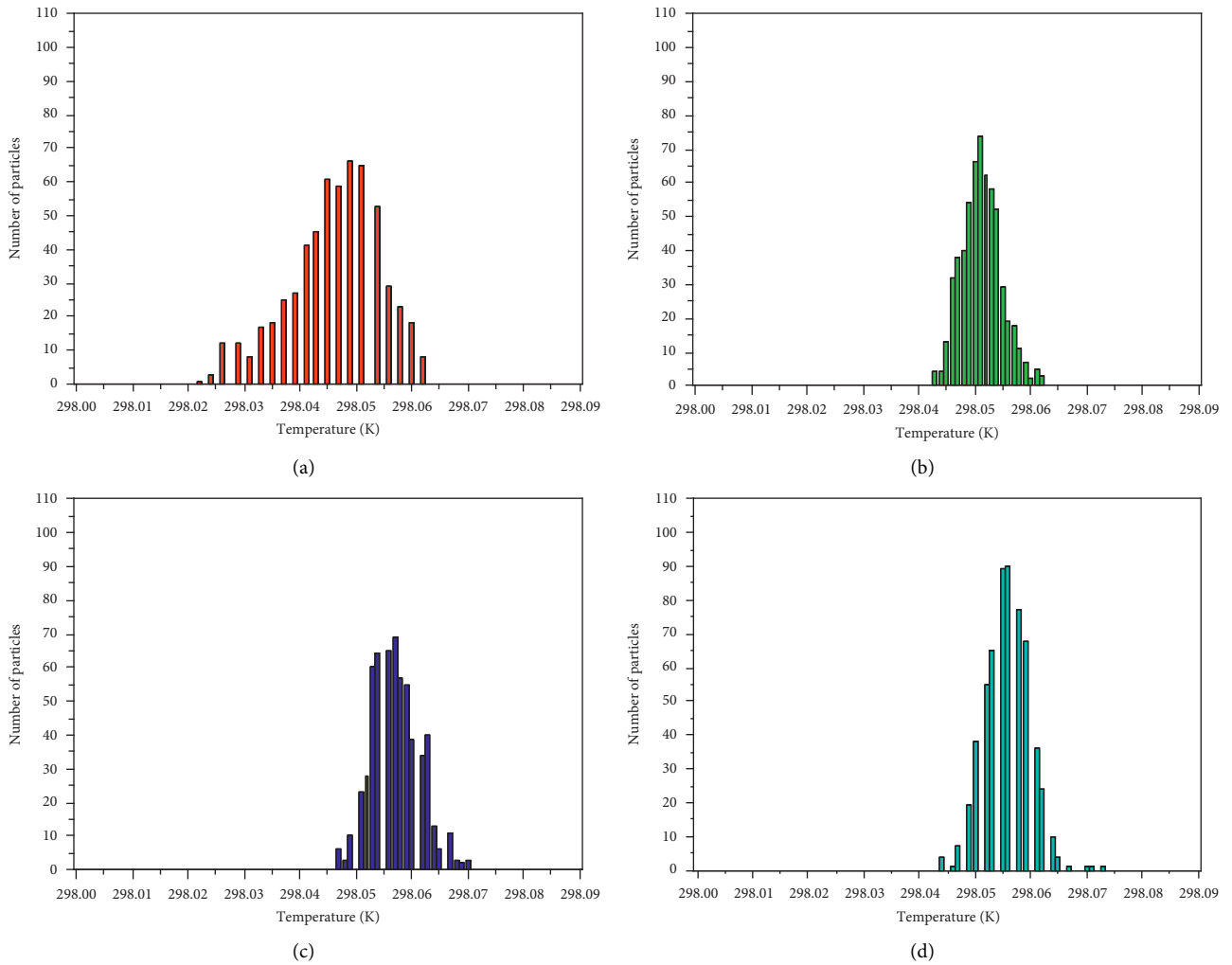


FIGURE 7: The distributions of grinding media temperature for different numbers of lifters. (a) $n = 0$. (b) $n = 8$. (c) $n = 12$. (d) $n = 16$.

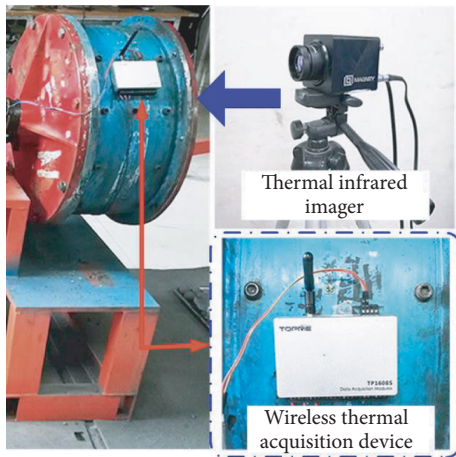


FIGURE 8: Laboratory-scale ball mill.

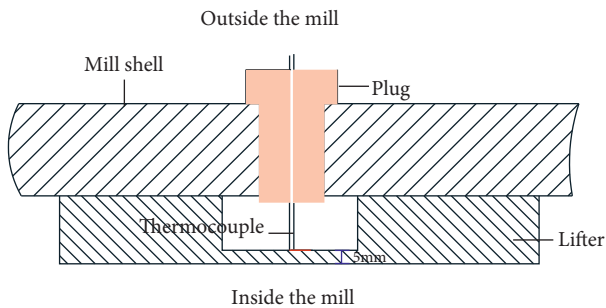


FIGURE 9: Schematic diagram of thermocouple installation.

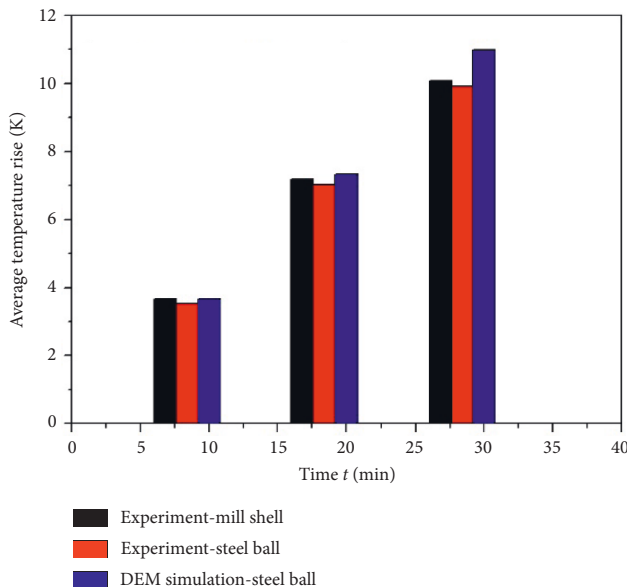


FIGURE 10: Comparison of temperature rise between DEM simulation and experiment.

of a wireless thermal device and a thermal infrared imager. A high-precision wireless thermal acquisition device is used to measure the mill shell temperature. The measuring accuracy

is 0.2% and can realize the online temperature measurement. The mill shell temperature was measured by the thermocouple and the installation method of the thermocouple on the mill shell as shown in Figure 9. A combination of contact and noncontact methods is used to determine the emissivity of the steel ball. The results show an emissivity of 0.96 for the steel balls. The thermal infrared imager is used to measure the temperature of the steel ball, with a measuring accuracy of 2%. In the experiments, the ball mill is stopped at pre-determined intervals to open the mill shell quickly and then photograph the steel ball using a thermal infrared imager. The grinding durations are $t = 0$ min, $t = 10$ min, $t = 20$ min, and $t = 30$ min.

One set of validation tests is used to validate the numerical simulations. The experiments are carried out with a mill speed of 75% of the critical speed, a grinding media filling of 25%, and a steel ball size of 30 mm. Figure 10 shows the average temperature rise of the steel ball for the DEM simulations and the experimental results. Since the DEM simulation time is limited, the results are calculated proportionally. As shown in Figure 10, the DEM simulation results agree with the experimental results, despite the former being slightly higher. The primary reason for this discrepancy is that the temperature dissipation produced by mill shutdown is ignored. In addition, only the temperature on the surface of the grinding media is measured by the thermal infrared imager, which makes this error acceptable. In summary, the rationality of the numerical model of heat transfer is well validated by the experimental results.

6. Conclusions

This study mainly investigates the effect of the mill speed, grinding media filling, and the number of lifters on the discrete heat transfer behavior of grinding media in ball mills. In DEM simulations, the temperature field of grinding media and the load behavior is susceptible to the mill speed, grinding media filling, and the number of lifters. The average temperature of the grinding media firstly increases and then decreases with the increased mill speed, grinding media filling, and the number of lifters. Consequently, the developed heat transfer model is well-validated, and the temperature field of the grinding media is in good agreement with the experimental results, indicating the reasonableness and reliability of the model. The numerical models of heat transfer provide an opportunity to optimize the movement and mixing of granular materials sensitive to temperature.

Data Availability

The data used to support the findings of this study are included within the article.

Conflicts of Interest

The authors declare that there are no conflicts of interest.

Authors' Contributions

The authors wish to thank Yin for conceiving and designing the schemes; Wang and Li performed the experiments and analyzed the data.

Acknowledgments

This study was supported by the Doctoral Scientific Research Foundation of Suzhou University (Grant no. 2020BS004) and the National Natural Science Foundation of China (Grant no. 51475458). The authors also wish to thank the Natural Science Foundation of the Jiangsu Higher Education Institutions of China (Grant no. 19KJB440004), the Natural Science Research Project in Universities of Anhui Province in China (Grant no. KJ2021A1115), and the Nature Science Research Key Project of Suzhou University (Grant no. 2019yzd03).

References

- [1] G. W. Delaney, P. W. Cleary, R. D. Morrison, S. Cummins, and B. Loveday, "Predicting breakage and the evolution of rock size and shape distributions in Ag and SAG mills using DEM," *Minerals Engineering*, vol. 50-51, no. 5, pp. 132-139, 2013.
- [2] N. S. Weerasekara, M. S. Powell, P. W. Cleary et al., "The contribution of DEM to the science of comminution," *Powder Technology*, vol. 248, no. 248, pp. 3-24, 2013.
- [3] M. Yahyaei and S. Banisi, "Spreadsheet-based modeling of liner wear impact on charge motion in tumbling mills," *Minerals Engineering*, vol. 23, no. 15, pp. 1213-1219, 2010.
- [4] Z. X. Yin, Y. X. Peng, Z. C. Zhu, Z. Yu, and T. Li, "Impact load behavior between different charge and lifter in a laboratory-scale mill," *Materials*, vol. 10, no. 8, p. 882, 2017.
- [5] C. H. Liu, W. Cai, M. Y. Zhai, G. Zhu, C. Zhang, and Z. Jiang, "Decoupling of wastewater eco-environmental damage and China's economic development," *Science of the Total Environment*, vol. 789, Article ID 147980, 2021.
- [6] P. W. Cleary and R. D. Morrison, "Understanding fine ore breakage in a laboratory scale ball mill using DEM," *Minerals Engineering*, vol. 24, no. 3-4, pp. 352-366, 2011.
- [7] Y. X. Peng, T. Q. Li, Z. C. Zhu, S. Zou, and Z. Yin, "Discrete element method simulations of load behavior with mono-sized iron ore particles in a ball mill," *Advances in Mechanical Engineering*, vol. 9, no. 5, Article ID 168781401770559, 2017.
- [8] T. Q. Li, Y. X. Peng, Z. C. Zhu et al., "Multi-layer kinematics and collision energy in a large-scale grinding mill-the largest semi-autogenous grinding mill in China," *Advances in Mechanical Engineering*, vol. 8, no. 12, Article ID 168781401668137, 2016.
- [9] V. V. R. Natarajan and M. L. Hunt, "Kinetic theory analysis of heat transfer in granular flows," *International Journal of Heat and Mass Transfer*, vol. 41, no. 13, pp. 1929-1944, 1998.
- [10] E. E. Michaelides, "Heat transfer in particulate flows," *International Journal of Heat and Mass Transfer*, vol. 29, no. 2, pp. 265-273, 1986.
- [11] J. R. Ferron and D. K. Singh, "Rotary kiln transport processes," *AIChE Journal*, vol. 37, no. 5, pp. 747-758, 1991.
- [12] C. A. Cook and V. A. Cundy, "Heat transfer between a rotating cylinder and a moist granular bed," *International Journal of Heat and Mass Transfer*, vol. 38, no. 3, pp. 419-432, 1995.
- [13] M. L. Hunt, "Discrete element simulations for granular material flows: effective thermal conductivity and self-diffusivity," *International Journal of Heat and Mass Transfer*, vol. 40, no. 13, pp. 3059-3068, 1997.
- [14] Y. Kaneko, T. Shiojima, and M. Horio, "DEM simulation of fluidized beds for gas-phase olefin polymerization," *Chemical Engineering Science*, vol. 54, no. 24, pp. 5809-5821, 1999.
- [15] J. Li and D. J. Mason, "A computational investigation of transient heat transfer in pneumatic transport of granular particles," *Powder Technology*, vol. 112, no. 3, pp. 273-282, 2000.
- [16] W. L. Vargas and J. J. McCarthy, "Unsteady heat conduction in granular materials[J]," *Mrs Proceedings*, vol. 627, no. 5, pp. 1052-1059, 2000.
- [17] I. Skuratovsky, A. Levy, and I. Borde, "Two-dimensional numerical simulations of the pneumatic drying in vertical pipes," *Chemical Engineering and Processing: Process Intensification*, vol. 44, no. 2, pp. 187-192, 2005.
- [18] B. Chaudhuri, F. J. Muzzio, and M. S. Tomassone, "Experimentally validated computations of heat transfer in granular materials in rotary calciners," *Powder Technology*, vol. 198, no. 1, pp. 6-15, 2010.
- [19] Q. Xie, Z. B. Chen, Q. F. Hou, A. Yu, and R. Yang, "DEM investigation of heat transfer in a drum mixer with lifters," *Powder Technology*, vol. 314, pp. 175-181, 2017.
- [20] H. Komossa, S. Wirtz, V. Scherer, F. Herz, and E. Specht, "Heat transfer in indirect heated rotary drums filled with mono-disperse spheres: Comparison of experiments with DEM simulations," *Powder Technology*, vol. 286, pp. 722-731, 2015.
- [21] N. Gui and J. R. Fan, "Numerical study of heat conduction of granular particles in rotating wavy drums," *International Journal of Heat and Mass Transfer*, vol. 84, pp. 740-751, 2015.
- [22] I. Figueroa, W. L. Vargas, and J. J. McCarthy, "Mixing and heat conduction in rotating tumblers," *Chemical Engineering Science*, vol. 65, no. 2, pp. 1045-1054, 2010.
- [23] T. Oschmann, M. Schiemann, and H. Kruggel-Emden, "Development and verification of a resolved 3D inner particle heat transfer model for the Discrete Element Method (DEM)," *Powder Technology*, vol. 291, pp. 392-407, 2016.
- [24] M. Y. Li, X. Ling, H. Peng, Z. Cao, and Y. Wang, "An investigation on heat transfer of granular materials in the novel flighted rotary drum," *Canadian Journal of Chemical Engineering*, vol. 95, no. 2, pp. 386-397, 2017.
- [25] V. D. Nguyen, C. Cogné, M. Guessasma, E. Bellenger, and J. Fortin, "Discrete modeling of granular flow with thermal transfer: application to the discharge of silos," *Applied Thermal Engineering*, vol. 29, no. 8-9, pp. 1846-1853, 2009.
- [26] X. X. Duan and Y. J. Cao, *Theory and Practice of ball mill*, Metallurgical Industry Press, Beijing, 1999.
- [27] T. Q. Li, Z. X. Yin, and G. Y. Wu, "Study on heat transfer behavior and thermal breakage characteristic of the charge in ball mills," *Advances in Mechanical Engineering*, vol. 13, no. 3, Article ID 168781402199496, 2021.
- [28] S. Rosenkranz, S. Breitung-Faes, and A. Kwade, "Experimental investigations and modelling of the ball motion in planetary ball mills," *Powder Technology*, vol. 212, no. 1, pp. 224-230, 2011.

Research Article

Mullite Reinforced SiC/Al₂O₃ Composites Prepared by Microwave Sintering Based on Green Manufacturing

Xudan Dang ¹, Shaojie Shi,² Linjun Li,³ Fei Luo,¹ and Zheng Ding¹

¹School of Mechanical Engineering, Henan University of Engineering, Zhengzhou 451191, China

²Finance and Asset Management Division, Henan University of Engineering, Zhengzhou 451191, China

³Engineering Training Centre, Henan University of Engineering, Zhengzhou 451191, China

Correspondence should be addressed to Xudan Dang; dangxudan2011@163.com

Received 15 May 2022; Accepted 27 June 2022; Published 9 July 2022

Academic Editor: Conghu Liu

Copyright © 2022 Xudan Dang et al. This is an open access article distributed under the Creative Commons Attribution License, which permits unrestricted use, distribution, and reproduction in any medium, provided the original work is properly cited.

In the preparation process of composites, the implementation of green manufacturing technology has an important impact on improving material properties and preparation efficiency. The adopting of green manufacturing technology not only greatly reduces the energy consumption but also effectively avoids the environmental pollution. Compared with the traditional material preparation process, the material preparation process for green manufacturing is a new concept and idea. Microwave sintering is such an efficient, clean, and pollution-free preparation process, so it is widely used in the field of material preparation. By microwave sintering, the mullite reinforced SiC/Al₂O₃ composites with different SiC particle size were prepared from the composite powders composed of SiC particles coated with SiO₂, by a sol-gel method and Al₂O₃ particles. The effect of SiC particle size on the microstructure, bulk density, fracture toughness, flexural strength, and thermal shock resistance of SiC/Al₂O₃ composites was studied. The bulk density, fracture toughness, and flexural strength were evaluated by the Archimedes method, single-side notched beam method, and three-point bending method, respectively. The thermal shock resistance of samples was investigated through the combination of water quenching and three-point bending methods. The results showed that with the increase of SiC particle size, the bulk density, fracture toughness, and flexural strength of samples all increased first and then decreased. The bulk density, fracture toughness, flexural strength, and flexural strength retention of SiC(5 μm)/Al₂O₃ composites were better than those of other samples, which were 2.06 g/cm³, 1.98 MPa·m^{1/2}, 63 MPa, and 60%, respectively. The better mechanical properties and thermal shock resistance of SiC(5 μm)/Al₂O₃ composites are due to the formation of bridging mullite whiskers between SiC and Al₂O₃ particles with large length diameter ratio. Therefore, the unique sintering mechanisms of size coupling effect and local thermal aggregation effect in microwave sintering were discussed. The research results can not only provide reference for the preparation process of mullite reinforced SiC/Al₂O₃ composites but also for the wide application of microwave sintering technology.

1. Introduction

With the rapid development of science and technology, the manufacturing industry has also received more development opportunities, which not only creates greater economic value for the society, but also brings more economic benefits to the development of the society [1]. However, with the rapid development of traditional manufacturing industry, problems such as high energy consumption and high pollution gradually appear. The environment-friendly manufacturing process based on green manufacturing has

become the development direction in the future. The green manufacturing of composites is an important innovation and development in the research field of composite preparation technology. Green manufacturing is also known as environmental conscious manufacturing for environment [2, 3]. Low energy consumption green preparation process is also called energy-saving process in general [4]. Compared with traditional material preparation, material preparation based on green manufacturing is a new concept and idea [5]. Microwave sintering is a new method of material sintering process. It has the characteristics of fast heating speed, high

energy utilization rate, high heating efficiency, safety, sanitation, and no pollution. Because the time of microwave sintering is greatly shortened, the energy utilization efficiency is greatly improved. Compared with traditional sintering methods, microwave sintering can achieve high efficiency and energy saving. The rapid sintering characteristics of microwave sintering greatly reduce the use of gas as sintering atmosphere in the sintering process, which not only reduces the cost but also reduces the emission of waste gas and waste heat in the sintering process. As one of the green manufacturing processes, microwave sintering is worthy of its name. At the same time, microwave sintering can improve the microstructure and properties of sintered materials, which has become a new research hotspot in the field of material sintering.

Microwave sintering is a method to realize densification, by coupling the special band of microwave with the basic fine structure of materials to generate heat, and the dielectric loss of materials makes the whole material heated to the sintering temperature. In the 1960s, some researchers proposed to use microwave sintering technology to prepare ceramic materials. After the mid-1980s, there was a climax of microwave sintering ceramics all over the world [6]. So far, researchers have done a lot of research on the preparation of carbide ceramics and oxide ceramics by microwave sintering technology [7, 8]. Because of the excellent high temperature mechanical strength, superior refractoriness, low electrical conductivity, good chemical stability, and good thermal shock resistance, the SiC/Al₂O₃ composites have become a promising candidate for high-temperature applications in the fields of refractory materials, machinery, chemical industry, metallurgy, electronics, and ceramics [9, 10]. However, in the fields of several thermal shocks or applications requiring high toughness, the SiC/Al₂O₃ composites are unsuitable for their brittleness [11, 12]. In order to make the SiC/Al₂O₃ composites tougher, some reinforcing phase is introduced into the composites to overcome their inherent brittleness. Not only the morphology of the reinforcing phase but also the chemical compatibility and thermal expansion match of the reinforcing phase and matrix could influence the preparation process and final properties of SiC/Al₂O₃ composites. The recent research showed that particles and whiskers can greatly improve the strength and toughness of the ceramic matrix composites [13–16]. For whisker reinforced composites, the improvement is due to the changes of the microstructure, interface strengthening, and fracture mechanisms. Mullite whiskers are widely used to enhance the properties of alumina-based composites. The in situ mullite whiskers can be synthesized by coating SiO₂ on SiC particles, which facilitates the reaction between SiO₂ and Al₂O₃ to form mullite whiskers at high temperature. The connections of mullite whiskers improve the interfacial bonding between SiC and Al₂O₃ particles. In addition, the oxidation problem of SiC particles in the sintering process is also solved through the coating of SiO₂ in SiC particles. For SiC/Al₂O₃ composites, many reports indicated that mullite whiskers show attractive bending strength at high temperature, good thermal shock resistance, and excellent chemical compatibility with SiC [17–19]. Thus, due to their excellent

thermal shock resistance, mullite whisker reinforced SiC/Al₂O₃ composites have broad application prospects, especially in refractories.

Using various processing techniques such as pressureless sintering, hot pressing, and microwave sintering, the mullite reinforced SiC/Al₂O₃ composites can be prepared. As an internal and faster technique, microwave sintering has received more attention compared with traditional sintering methods [20–22]. Besides being a green manufacturing process, microwave sintering also has two advantages. One is the volumetric energy absorption without temperature gradient over the entire sample. And the other is some special properties induced by the electromagnetic field [23]. Furthermore, besides the improvement of quality of the composites, the microwave sintering can also bring time and energy savings for its unique heating behavior [24, 25]. In addition to increasing the heating rate, uniform heating, and energy saving, microwave sintering also makes the composites have higher density and mechanical properties [26, 27]. Bodhak studied the sintering of pure mullite and mullite-zirconia composites and the results show that compared with the conventional sintering, the microwave sintering leads to better densification and better mechanical [28].

Nevertheless, so far, there were few reports about the preparation of in situ mullite whisker reinforced SiC/Al₂O₃ composites, especially on the microstructure, properties, and microwave sintering mechanism of the composites. In the present investigation, the SiC/Al₂O₃ composites reinforced by in situ mullite were prepared. In the previous research, the optimum sintering temperature, holding time, volume fraction of SiC particles, and volume fraction of Al₂O₃ particles about the mullite reinforced SiC/Al₂O₃ composites were 1500°C, 30 min, 50%, and 50%, respectively [14]. Therefore, the above sintering parameters were also used here. The effect of SiC particle size on the microstructure and properties of mullite reinforced SiC/Al₂O₃ composites were studied in details. Furthermore, the mechanism of microwave sintered SiC/Al₂O₃ composites were discussed, compared with the conventional sintering.

2. Experimental Method

2.1. Microwave Sintering Equipment. Microwave sintering furnace is the key equipment of microwave sintering. The microwave sintering furnace used in this study was shown in Figure 1. Its model is WXD20S-07 (Nanjing Sanle Microwave equipment) multimode microwave sintering furnace, with a maximum input power of 10 kw, frequency of 2.45 GHz, and resonant cavity mode of TE₆₆₆. The microwave furnace is mainly composed of microwave emission source, microwave conduction system, multimode resonator, microwave detection, feedback system, and infrared temperature measurement system.

In order to quickly complete the sintering and reduce the heat loss of samples in microwave sintering, a thermal insulation structure based on a hybrid heating mode was used to isolate the samples from the external environment [29]. The thermal insulation structure, which was mainly



(a)



(b)

FIGURE 1: The resonant cavity and control panel of microwave sintering equipment uniformity of samples. And at the same time the disadvantages that the temperature of samples close to the SiC rods in the insulation structure was high, and the temperature away from the SiC rods, which was low, was avoided. (a) Resonant cavity (b) Control panel.

composed of insulation layer, aided heaters, and sample bin was shown in Figure 2. The aided heaters and insulation layers were SiC rods placed around and porous mullite plate and mullite fibers, respectively. The porous mullite plates possessed excellent thermal shock resistance and thermal insulation effect. Mullite fibers enhanced the thermal insulation effect, which not only ensured the stability of the temperature change of the samples in heating and cooling stage but also improved the heating uniformity of samples. And at the same time, the disadvantages that the temperature of samples close to the SiC rods in the insulation structure were high and the temperature away from the SiC rods, which was low, was avoided.

2.2. Preparation of SiC/Al₂O₃ Composite Samples. In mullite reinforced SiC/Al₂O₃ composites, the composition of SiC/Al₂O₃ composite powders were 50 vol.% Al₂O₃ and 50 vol.% SiC. The SiC/Al₂O₃ composite powders are composed of Al₂O₃ powders and SiC particles coated on SiO₂. The morphologies of raw powders were characterized by SEM (Czech FEI Company Quanta 250). The Al₂O₃ powders with a mean particle size less than 300 nm were commercially

purchased (Beijing Deke Daojun Technology Co., Ltd), which was shown in Figure 3. In the previous research, it was found that the SiC/Al₂O₃ composites with the SiC particle size of 5 μm had good mechanical properties. Therefore, the SiC particle size of 5 μm was taken as the center, through the increase and decrease of SiC particle size, the influence of SiC particle size changes on the mechanical properties of SiC/Al₂O₃ composites were studied. The SiC raw particles (Henan Haixu Abrasive Co., Ltd.) were commercially purchased and were available in four sizes, which were 1 μm, 5 μm, 50 μm, and 125 μm (Figure 4).

In order to coat SiO₂ on SiC particles, a sol-gel method was used [30]. Through the hydrolyzation of tetraethyl orthosilicate (TEOS), the coating process was carried out. For the sake of solving the agglomeration problem, the SiC particles were suspended in distilled water and treated with the ultrasonic for 30 min. Then, the SiC particles were evenly distributed in distilled water. By controlling the mixing ratio of TEOS and ethanol the SiO₂ with a volume fraction of 10% was coated on SiC particles. During the coating process, a certain amount of TEOS and ethanol were added to the suspension of SiC particles. The mixture was evenly stirred on a magnetic stirrer for 4 h. By citric acid, the pH value of

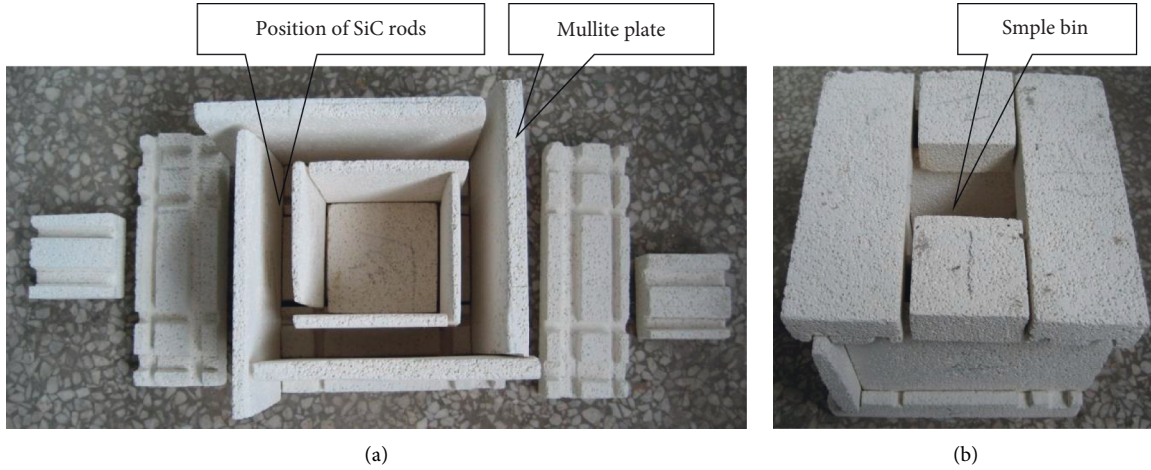


FIGURE 2: The thermal insulation based on hybrid heating mode. (a) Exploded figuer (b) Combination figuer.

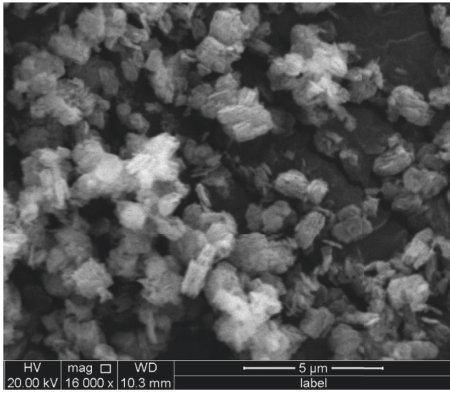


FIGURE 3: SEM image of Al₂O₃ powders.

the suspension was firstly adjusted at about 3. Then, after the TEOS was fully hydrolyzed, the pH value of the suspension was controlled at 9 by dropping ammonia water. A few minutes later, the gel of SiC particles coated on SiO₂ was formed. In a blast drying oven, the gel of coated particles was dried 10 h at 80°C. Later, the coated particles were mixed with Al₂O₃ particles. Figure 5 shows the SEM image of the SiC/Al₂O₃ composite powders, which indicates that the Al₂O₃ particles uniformly mix with the SiC particles coated on SiO₂. In the end, through sol-gel method, the SiC/Al₂O₃ composite powders were prepared. By the reaction between Al₂O₃ and SiO₂, the mullite was formed during microwave sintering.

Next, in a special mould (Figure 6(a)), the SiC/Al₂O₃ composite powders were cold pressed at 3 MPa for 1 min into green compacts (Figure 6(b)). Then, the green compacts were placed in the thermal insulation structure, and sintered in the microwave furnace. By adjusting the input power, the heating rate was controlled. At the same time, the changes between the reflected power and temperature were also detected. With an approximately heating rate of 10°C/min, the green compacts were sintered at 1500°C for 30 min. After that, the samples of SiC/Al₂O₃ composites were slowly

cooled down to room temperature in the furnace at about 15°C/min.

3. Experimental Process

3.1. Bulk Density Test. A high-precision solid-liquid electronic hydrometer (DE-120T, Shenzhen Dahong Meituo density measuring instrument Co., Ltd.) was used to measure the bulk density of SiC/Al₂O₃ composite samples, according to the Archimedes method, with distilled water as immersion medium. The bulk density of SiC/Al₂O₃ composite samples is calculated from the following formula:

$$\rho = \frac{m_1}{m_3 - m_2} \rho_0, \quad (1)$$

where ρ is the bulk density of sample, g/cm³. m_1 , m_2 , and m_3 are the dry weight, suspended weight, and wet weight of sample, respectively. ρ_0 is the density of distilled water, g/cm³.

3.2. Fracture Toughness Test. Fracture toughness refers to the ability of a material to prevent the unstable propagation of macro cracks. It is also a toughness parameter for a material to resist brittle failure. The fracture toughness was measured by single side notched beam method (SENB), with a span of 16 mm [31, 32]. The size of the fracture toughness specimen is 2 mm × 4 mm × 22 mm, and the cross-head speed of universal material testing machine is 0.5 mm/min. The fracture toughness of SiC/Al₂O₃ composite samples is calculated from the following formula:

$$K_{IC} = Y \frac{3PL}{2BW^2} \sqrt{a}, \quad (2)$$

where P is the breaking load of sample, N. L is the span between lower supports, 16 mm. B and W are the width and thickness of sample, 2 mm, 4 mm, respectively. a is the notch depth of sample, 0.8–1.2 mm. Y is a constant [33]. When the ratio of L/W is equal to 4 [34], the value of Y can be calculated by the following formula:

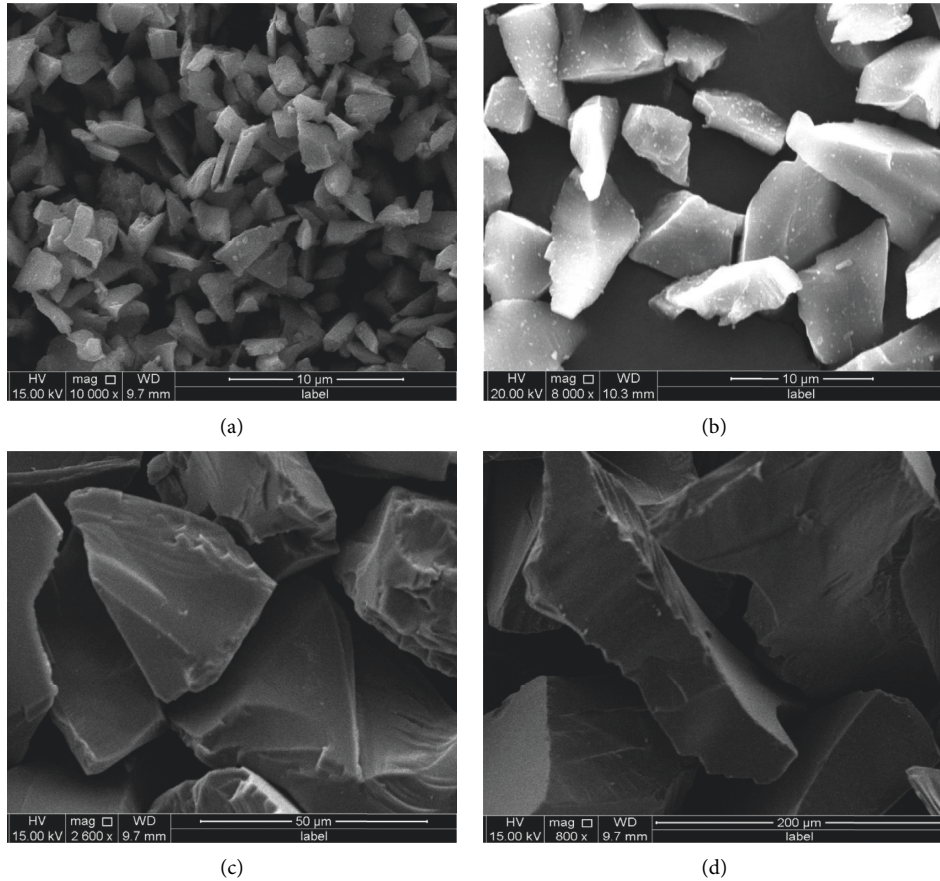


FIGURE 4: SEM images of SiC particles with different particle size. (a) SiC particles of 1 μm. (b) SiC particles of 5 μm. (c) SiC particles of 50 μm. (d) SiC particles of 125 μm.

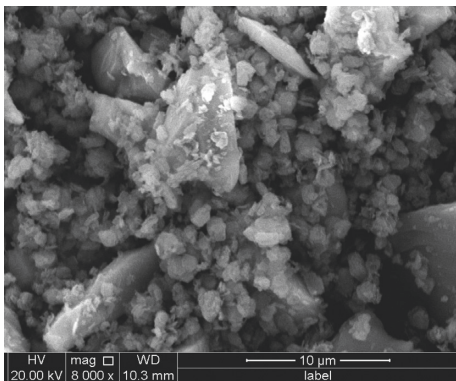


FIGURE 5: SEM image of SiC/Al₂O₃ composite powders.

$$Y = 1.93 - 3.07 \frac{a}{W} + 14.53 \left(\frac{a}{W}\right)^2 - 25.11 \left(\frac{a}{W}\right)^3 + 25.8 \left(\frac{a}{W}\right)^4. \tag{3}$$

3.3. Thermal Shock Resistance Test. Thermal shock resistance refers to the ability of a material to resist damage under rapid temperature changes. The thermal shock resistance is not only one of the important properties of refractories but also

the comprehensive embodiment of mechanical and thermal properties of materials under rapid temperature changes. The thermal shock resistance of mullite reinforced SiC/Al₂O₃ composites was studied by measuring the flexural strength retention of multiple water quenching cycles at 1000°C [35, 36]. For this purpose, the temperature of the heating furnace was raised to 1000°C. After holding for 20 min, the samples with the size of 3 mm × 4 mm × 35 mm were quickly put into the furnace. The thermal cycle process of samples was composed of heat preservation process and quench process. The heat preservation process was that the samples were put into the furnace with a temperature of 1000°C for 15 min. And the quench process was that after the heat preservation process, the samples were immediately water quenched for 5 min. This thermal cycle of heat preservation and quenching was repeated and the selected thermal shock cycles were 0, 5, 10, and 15 times, respectively. There were two main reasons for this choice. One was that according to references, the number of thermal shock cycles given in many references was 0, 5, 10, and 15 times. The other was based on the previous research. In the previous research, the thermal shock resistance cycles were 0, 5, 10, and 15 times. After the thermal shock cycle was completed, the flexural strength was tested on samples by three-point bending method (Figure 7). The three-point bending method was performed using universal testing machines



FIGURE 6: Pressing mould and green compacts of samples. (a) The special mould (b) Green compacts of SiC/Al₂O₃ composites.

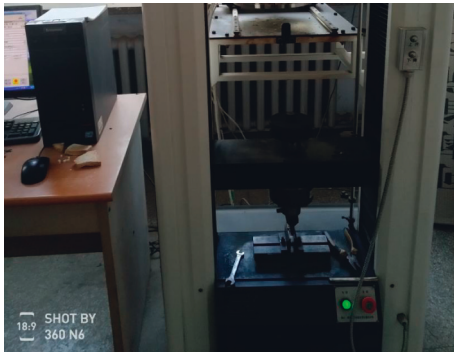


FIGURE 7: Measurement of flexural strength by three-point bending method.

(WD-P4504, Jinan Test Machine Co., Ltd.). The span and cross-head speed were 30 mm and 0.5 mm/min, respectively.

Based on the test values of flexural strength, the flexural strength retention of samples after several thermal cycles was calculated. The flexural strength retention of SiC/Al₂O₃ composites was expressed as R . Under the condition of the same sample composition, R was defined as the ratio of the flexural strength of samples after n times of thermal shock cycles to the flexural strength of samples without thermal shock cycles. The flexural strength retention of samples can be calculated by the following formula:

$$R_n = \frac{\sigma_n}{\sigma_0} \times 100\%, \quad (4)$$

where R is the flexural strength retention. n is the number of thermal cycles. R_0 , R_5 , R_{10} , and R_{15} are the flexural strength retention of samples after 0, 5, 10, and 15 times of thermal cycles, respectively. σ_0 is the flexural strength of samples without thermal shock cycles, and σ_n is the flexural strength of samples after n times of thermal shock cycles.

4. Experimental Results and Analysis

4.1. Experimental Results. The properties of mullite reinforced SiC/Al₂O₃ composites with different SiC particle sizes are listed as Table 1.

The flexural strength of mullite reinforced SiC/Al₂O₃ composites with different SiC particle sizes under different thermal shock cycles are listed as Table 2.

The flexural strength retention of mullite reinforced SiC/Al₂O₃ composites with different SiC particle sizes under different thermal shock cycles are listed as Table 3.

4.2. Analysis of Experimental Results. As we all know, the mechanical properties of ceramic matrix composites are closely related to its microstructure. The SEM images of mullite reinforced SiC/Al₂O₃ composites with different SiC particle sizes after microwave sintering were shown in Figure 8.

It can be clearly seen from Figure 8(a) that there were many pores in the samples of SiC (1 μ m)/Al₂O₃ composites. The SiO₂ coated on SiC particles melted, but did not form a good interface with the surrounding Al₂O₃ particles. The reason was that the selected SiC particle size (1 μ m) was too small to achieve good aggregation. The samples were mainly heated by the aided heaters of SiC rods and the self-heating cannot be well realized. Therefore, the particles grew slowly and the interface between Al₂O₃ and SiO₂ was not good. With the increase of SiC particle size (5 μ m), there were few pores in the composites as shown in Figure 8(b). Through the reaction of SiO₂ and Al₂O₃ particles, the mullite whiskers with large length diameter ratio had been formed and presented a bridge structure through the pores. As a result, the bridging mullite whiskers improve the interface between SiC and Al₂O₃ particles. As can be seen from Figure 8(c), with the continuous increase of SiC particle size (50 μ m) in samples, although the mullite whiskers still existed after microwave sintering, its length diameter ration was small. And there were many pores in SiC (50 μ m)/Al₂O₃ composites. Due to the large size (50 μ m) of SiC particles, the samples can quickly achieve thermal aggregation during microwave sintering, while the rapid outward diffusion of heat cannot be realized, resulting in the formation of many pores. With the further increase of SiC particle size (125 μ m), the mullite whiskers with large length diameter ratio did not form after microwave sintering, as shown in Figure 8(d). The morphology of mullite phase in samples is short rod-like.

TABLE 1: Properties of samples with different SiC particle sizes.

Composites	Bulk density, ρ (g/cm ³)	Fracture toughness, K_{IC} (MPa·m ^{1/2})	Flexural strength, σ_0 (MPa)
SiC (1 μ m)/Al ₂ O ₃	1.76	1.04	30
SiC (5 μ m)/Al ₂ O ₃	2.06	1.98	63
SiC (50 μ m)/Al ₂ O ₃	1.94	1.12	34
SiC (125 μ m)/Al ₂ O ₃	1.88	0.93	29

TABLE 2: Flexural strength of samples under different thermal shock cycles.

Composites	Flexural strength, σ_0 /MPa 0 times	Flexural strength, σ_5 /MPa 5 times	Flexural strength, σ_{10} /MPa 10 times	Flexural strength, σ_{15} /MPa 15 times
SiC (1 μ m)/Al ₂ O ₃	30	16	7	6
SiC (5 μ m)/Al ₂ O ₃	63	38	19	17
SiC (50 μ m)/Al ₂ O ₃	34	19	10	9
SiC (125 μ m)/Al ₂ O ₃	29	14	8	7

TABLE 3: Flexural strength retention of samples under different thermal shock cycles.

Composites	Flexural strength retention, R_0 /%	Flexural strength retention, R_5 /%	Flexural strength retention, R_{10} /%	Flexural strength retention, R_{15} /%
SiC (1 μ m)/Al ₂ O ₃	100	53	23	20
SiC (5 μ m)/Al ₂ O ₃	100	60	30	27
SiC (50 μ m)/Al ₂ O ₃	100	56	29	26
SiC (125 μ m)/Al ₂ O ₃	100	48	28	24

There were also many pores in SiC (125 μ m)/Al₂O₃ composites. Due to the large SiC particle size (125 μ m) and rapid temperature rise of samples, the Al₂O₃ particles and SiO₂ cannot react fully, so, the mullite grains formed had no time to grow. Under the condition of gas-solid two-phase co-existence, the anisotropic growth of mullite grains was limited to a certain extent [37], and the growth rate in all directions was relatively fast, making the mullite phase formed in a short rod-like shape.

The curve of bulk density of mullite reinforced SiC/Al₂O₃ composites with SiC particle size was shown in Figure 9.

It can be observed from Figure 9 that the density of SiC (1 μ m)/Al₂O₃ composites after microwave sintering was relatively small. With the increase of SiC particle size in samples, the bulk density of SiC/Al₂O₃ composites also increased. The bulk density of SiC (5 μ m)/Al₂O₃ composites reached the maximum. The reason was that with the increase of SiC particle size, the better thermal aggregation on the particle surface can be realized. The SiO₂ in samples was melted at high temperature to form a flowing glass phase and fill the pores, so that the porosity of samples was reduced and the density was improved. With the continuous increase of SiC particle size in samples, the bulk density of samples after sintering decreased (Figure 9). The bulk density of SiC (50 μ m)/Al₂O₃ composites was lower than that of SiC (5 μ m)/Al₂O₃ composites after microwave sintering, and the bulk density of SiC (125 μ m)/Al₂O₃ composites decreased further after microwave sintering. Combined with the analysis results of SEM images in Figure 8, the reason for this phenomenon was that the SiC particle size in samples was

too large, the heating rate was too fast, and large amounts of heat accumulated on the particle surface. As a result, the rapid outward diffusion of heat cannot be realized, and the pores formed during the sintering process. Therefore, the porosity of samples was increased, the structure was loose and the bulk density was low. For the bulk density of samples, the reason was the thermal aggregation on the SiC particles. If the thermal aggregation was poor or the thermal aggregation cannot be released in time, the bulk density of SiC/Al₂O₃ composite was relatively low. Overall, with the increase of SiC particle size, the bulk density of SiC/Al₂O₃ composites increased first and then, decreased.

The curve of fracture toughness of mullite reinforced SiC/Al₂O₃ composites with SiC particle size shown in Figure 10.

From Figure 10, it can be seen that the fracture toughness of SiC (1 μ m)/Al₂O₃ composites was relatively low. With the increase of SiC particle size dispersed in samples, the fracture toughness increased. When the SiC particle size increased to about 5 μ m, the fracture toughness of SiC (5 μ m)/Al₂O₃ composites reached the maximum 1.98 MPa·m^{1/2}. This is because the content of mullite whiskers was relatively high, and the mullite whisker connecting phase was formed between the particles, which improved the fracture toughness of the samples. However, when the SiC particle size dispersed in the samples continued to increase, the fracture toughness of SiC (50 μ m)/Al₂O₃ composites and SiC (125 μ m)/Al₂O₃ composites both decreased. The main reason for this phenomenon was that although the mullite was also formed in SiC (50 μ m)/Al₂O₃ composites at high temperature, the growth power of mullite was not enough,

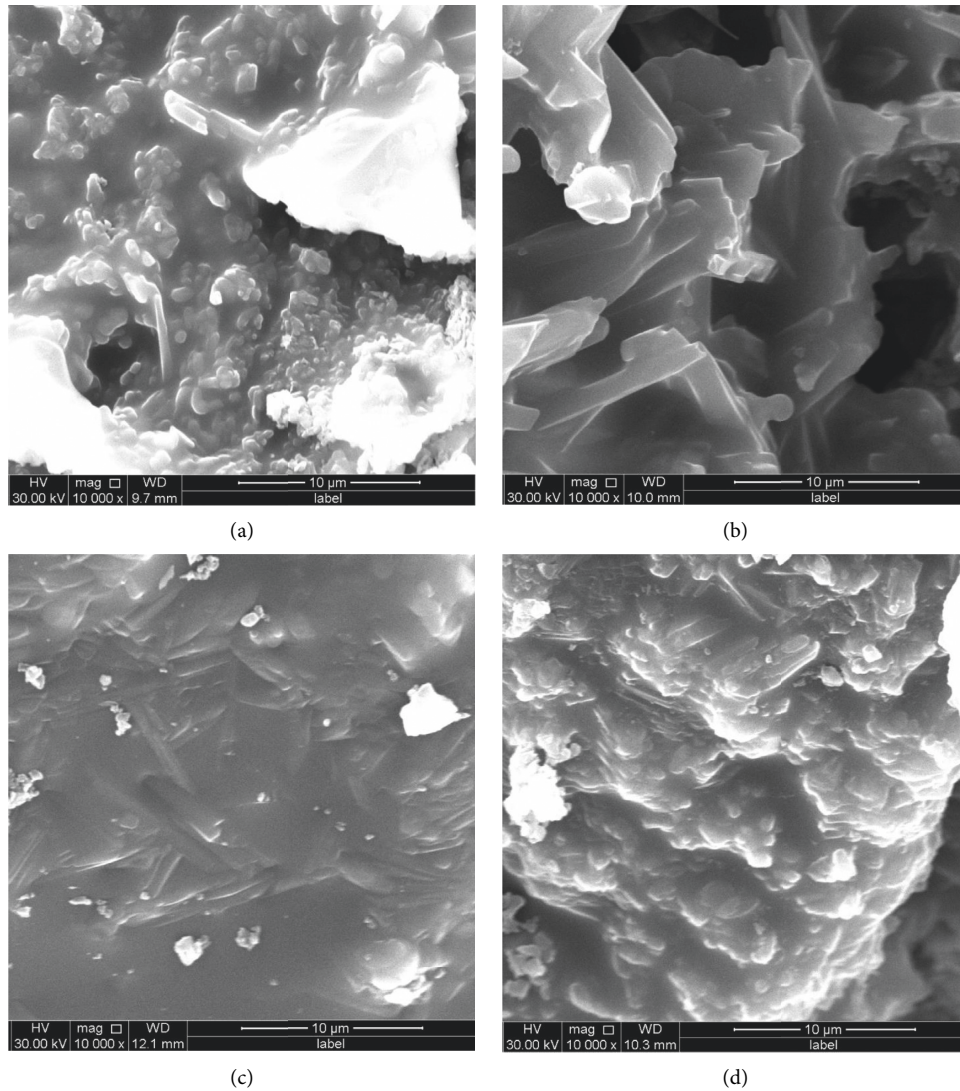


FIGURE 8: SEM images of mullite reinforced SiC/Al₂O₃ composites with different SiC particle sizes. (a) Samples of SiC(1 μm)/Al₂O₃ composites. (b) Samples of SiC(5 μm)/Al₂O₃ composites. (c) Samples of SiC(50 μm)/Al₂O₃ composites. (d) Samples of SiC(125 μm)/Al₂O₃ composites.

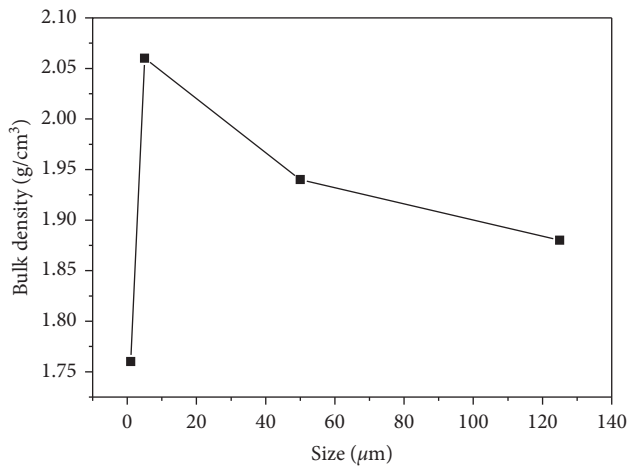


FIGURE 9: Curve of bulk density of samples with SiC particle size.

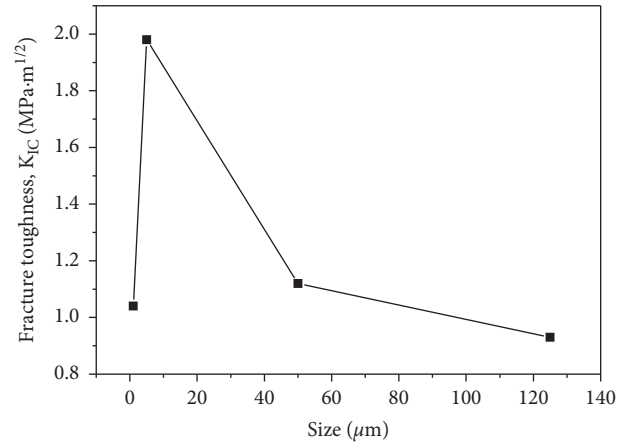


FIGURE 10: Curve of fracture toughness of samples with SiC particle size.

so the mullite whiskers with large length diameter ratio did not form, while the morphology of mullite in SiC (125 μm)/Al₂O₃ composites after microwave sintering was short rod-like and the short rod-like mullite was basically no aspect ratio. Therefore, the mullite whiskers bridging between particles were not formed in SiC (50 μm)/Al₂O₃ composites and SiC (125 μm)/Al₂O₃ composites, so the fracture toughness of these samples was not high. For the fracture toughness, the reason was the formation of mullite whiskers. If there were mullite whiskers with large length diameter ratio, the flexural strength and fracture toughness of samples were high. With the increase of SiC particle size, the fracture toughness of SiC/Al₂O₃ composites also increased first and then decreased.

The curves of flexural strength of mullite reinforced SiC/Al₂O₃ composites with different SiC particle size after 0, 5, 10, and 15 times of thermal cycles were shown in Figure 11. Figure 11 shows the thermal shock resistance of SiC/Al₂O₃ composites.

According to Figure 11, when the four groups of samples were not subjected to thermal shock, the flexural strength of SiC/Al₂O₃ composites increased with the increase of SiC particle size dispersed in the samples. The flexural strength of SiC (5 μm)/Al₂O₃ composites reached the maximum value of 63 MPa. This is mainly due to the synthesis amount of mullite whiskers increased with the increase of SiC particle size, which enhanced the flexural strength of the samples. When the SiC particle size in SiC/Al₂O₃ composites further increased, the flexural strength of samples decreased. The main reason is that when the added SiC particle size was too large (50 μm and 150 μm), the temperature rise of samples was too fast, Al₂O₃ and SiO₂ cannot fully react, and the mullite grains had no time to grow, which reduced the flexural strength of SiC/Al₂O₃ composites. In short, with the increase of SiC particle size, the flexural strength of SiC/Al₂O₃ composites also increased first and then decreased. After 5 times of thermal shock cycles, the flexural strength retention of SiC (125 μm)/Al₂O₃ composites was only 48%, and the flexural strength retentions of SiC (1 μm)/Al₂O₃ composites, SiC (5 μm)/Al₂O₃ composites and SiC (50 μm)/Al₂O₃ composites were 53%, 60%, and 56%, respectively. After 15 times of thermal shock cycles, the flexural strength retention of SiC (1 μm)/Al₂O₃ composites was 20% and the flexural strength retention of SiC (125 μm)/Al₂O₃ composites was 26%. While, the flexural strength retention of SiC (5 μm)/Al₂O₃ composites was 27%. Although, the flexural strength retention of SiC (50 μm)/Al₂O₃ composites was very similar to that of the SiC (5 μm)/Al₂O₃ composites (Table 3), their flexural strength was greatly different. Therefore, the thermal shock resistance of SiC (50 μm)/Al₂O₃ composites was not very good. With the increase of thermal shock cycles, the flexural strength of four groups of SiC/Al₂O₃ composites all decreased. After 5 thermal cycles, the flexural strength of four groups of SiC/Al₂O₃ composites decreased sharply. As the continued increase of thermal shock cycles, the flexural strength of four groups of SiC/Al₂O₃ composites decreased gently. Comparing the above four groups of samples, the SiC (5 μm)/Al₂O₃ composites had good thermal shock resistance. Better thermal shock

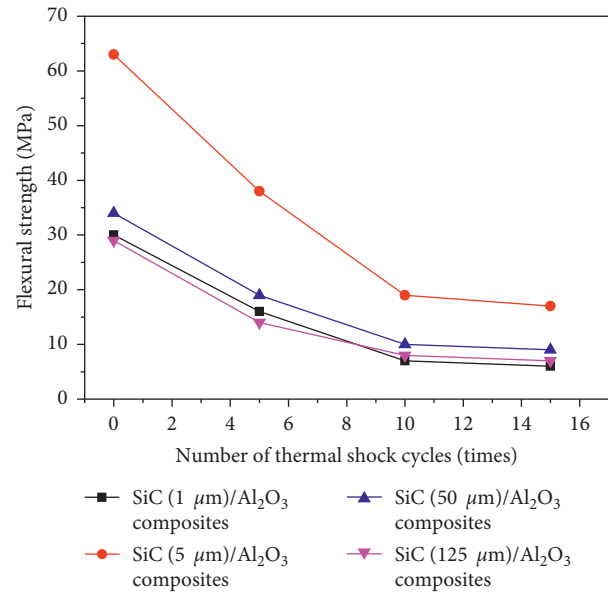


FIGURE 11: Curve of flexural strength of samples with different SiC particle size after several thermal cycles.

resistance of mullite reinforced SiC/Al₂O₃ composites obtained by microwave sintering can be applied to the refractory and heat insulation materials.

Based on the above analysis of microstructure, bulk density, and thermal shock resistance, among the four groups of SiC/Al₂O₃ composites (SiC particle size of 1 μm , 5 μm , 50 μm , and 125 μm), the SiC (5 μm)/Al₂O₃ composites possessed the best comprehensive mechanical properties.

5. Mechanism Analysis of Microwave Sintering

Through analyzing the microstructure and mechanical properties of SiC/Al₂O₃ composites, it can be seen that the morphology of mullite phase was different in different group of samples. The mullite phase was mullite whisker with large length diameter ratio in SiC (5 μm)/Al₂O₃ composites. While, the mullite phase was short rod-like in SiC (1 μm)/Al₂O₃ composites, SiC (50 μm)/Al₂O₃ composites, and SiC (125 μm)/Al₂O₃ composites. It is the morphology of mullite phase that affected the mechanical properties of SiC/Al₂O₃ composites. Through the whisker pullout and whisker bridging, the mullite whiskers toughen the SiC/Al₂O₃ composites. During the fracture process, the whiskers were pulled out and made bridging cracks, so the cracks can be deflected and energy can be absorbed, resulting in the improvement of mechanical properties for SiC/Al₂O₃ composites [38]. In addition to in situ mullite whiskers, the mullite whiskers can also be added externally. But there were some problems with the external mullite whiskers, such as uneven distribution, poor dispersion, difficult sintering, and poor compatibility, with interface and harmful to human body. Compared with the external whisker addition, the situ synthesized mullite whiskers in SiC/Al₂O₃ composites can more effectively toughen the samples because of low cost, better dispersion, and without pollution[39]. For the

formation of mullite whiskers, there existed two mechanisms during the microwave sintering.

One of the reasons for the different morphology of mullite phase was the size coupling effect in microwave sintering. In the initial stage of microwave heating, the temperature rise of SiC/Al₂O₃ composites mainly depended on the local thermal aggregation generated by the coupling of SiC particles and microwave field. When the size of SiC particles dispersed in samples was too small, such as 1 μm, the ability of SiC particles absorbing microwave loss was lower than the ability of particle surface heat diffusion. The good thermal aggregation on the surface of SiC particles cannot be achieved, resulting in slow temperature rise of samples, so the synthesis ability of mullite was limited. When the size of SiC particles dispersed in samples was too large, such as 50 μm and 125 μm, the ability of SiC particles absorbing microwave loss was higher than the ability of particle surface heat diffusion. Although the thermal aggregation on the surface of SiC particles was more, the heat cannot be diffused rapidly, resulting in the slow temperature rise of samples. The more thermal aggregation can promote the reaction of SiO₂ coated on SiC particles and Al₂O₃ to synthesize mullite, but the anisotropic growth of mullite was not obvious [40], and the length and diameter of mullite whiskers were small. In the process of microwave sintering, the ability of SiC particles absorbing microwave loss and the ability of SiC particle surface heat diffusion needed to be balanced so that the mullite grains can grow rapidly along the one-dimensional direction into whiskers with large length diameter ratio. Therefore, there was a critical size (about 5 μm) of SiC particles. When the size of SiC particles dispersed in samples was within the critical size range, the size coupling effect was the most obvious. So, the ability of SiC particles absorbing microwave loss was basically consistent with the ability of particle surface heat diffusion, which made the samples heat up rapidly at low temperature and obtained the mullite whiskers with large length and diameter and bridging between particles.

Another reason for the formation of mullite whiskers during microwave sintering was the local thermal aggregation effect. Because microwave sintering is an integral heating method, this sintering mechanism is a unique feature of microwave sintering. In the conventional sintering method, materials absorbed energy and heated up by means of conduction, convection, and thermal radiation. The sintering mechanism of microwave sintering was completely different from that of conventional sintering. So, in the conventional sintering process, there were no size coupling effect and local thermal aggregation effect. The schematic of mullite growth during microwave sintering and conventional sintering was shown in Figure 12. It can be seen that the mullite growth is different during the two sintering methods [7].

Figure 12(a) shows the growth process of mullite crystal in microwave field. When the SiC/Al₂O₃ composites were prepared by microwave sintering, due to the high SiC dielectric loss, the SiC rods (aided heaters) in the thermal insulation structure absorbed the microwave

energy to generate heat and transfer the heat from outside to inside. At the same time, the SiC particles in samples also preferentially absorbed the microwave energy to make the local instantaneous temperature rise on the SiC particle surface, causing local thermal aggregation effect, and the generated local heat diffused from inside to outside. The local thermal aggregation heated the SiO₂ coated on SiC particles to form a molten of glass phase, which reacted with Al₂O₃ to form mullite. During sintering process, the microwave hybrid heating produced two forms of heat. With the continuous increase of microwave input power, the local thermal aggregation effect was strengthened, which promoted the anisotropic growth of mullite grains, made the mullite grains grew rapidly along one-dimensional direction, and formed the mullite whiskers with large length diameter ratio.

Figure 12(b) shows the growth process of mullite crystal in conventional sintering process. In conventional sintering of SiC/Al₂O₃ composites, the samples are mainly heated by thermal radiation and heat conduction of conventional furnace. The heat was transferred from outside to inside and cannot form the local thermal aggregation effect to make the surface of SiC particles temperature rise instantaneously. This heating method raises the temperature slowly, and the energy dissipates greatly from outside to inside, which causes the less energy use for the synthesis of mullite. Therefore, the growth rate of mullite grains is slow and the anisotropic growth of mullite is not obvious, resulting in the formation of mullite phase with small length diameter ratio.

The SEM images of SiC/Al₂O₃ composites sintered by microwave sintering and conventional sintering were shown in Figure 13.

It can be obviously seen that the morphology of mullite phase in Figure 13(a) is different from Figure 13(b). Compared with the conventional sintering, the greatest advantage of microwave sintering is the local thermal aggregation effect. Because of the thermal aggregation effect, the mullite whiskers formed around the SiC particles. The bridging mullite whiskers with large length diameter ratio only existed in samples prepared by microwave sintering. As shown in Figure 13(b), the SiO₂ coated on SiC particles only melted and reacted with Al₂O₃ to form mullite, but the morphology of mullite was not whiskered. The reason is that the anisotropic growth of mullite is not promoted during conventional sintering. Therefore, the mullite whiskers with large length diameter ratio were not formed.

Due to the different sintering mechanism, the morphologies of mullite phase are different in different sintering methods, resulting in different mechanical properties. The main reasons are the size coupling effect and thermal aggregation effect analyzed above. In addition, compared with the conventional sintering, the microwave sintering can reduce the synthesis temperature of mullite, resulting in energy savings. Moreover, microwave sintering is also a relatively clean, pollution-free, and waste gas free sintering method [41]. Therefore, microwave sintering is a kind of green manufacturing with great potential.

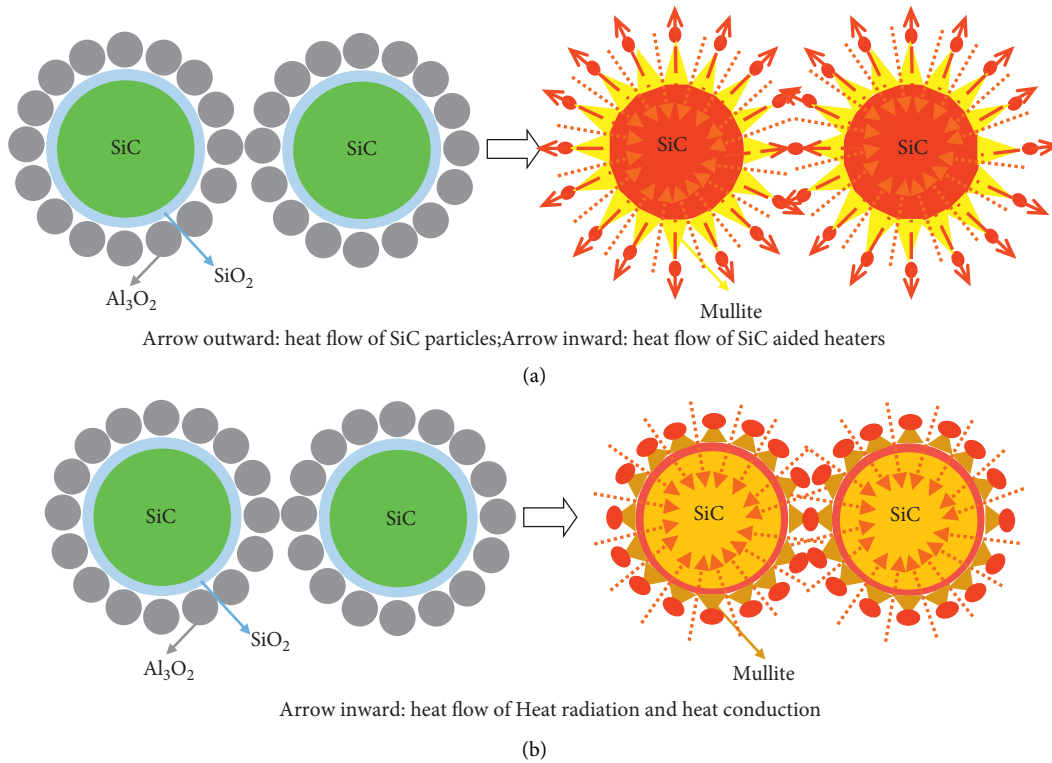


FIGURE 12: Schematic of mullite growth during microwave sintering and conventional sintering. (a) Microwave sintering. (b) Conventional sintering.

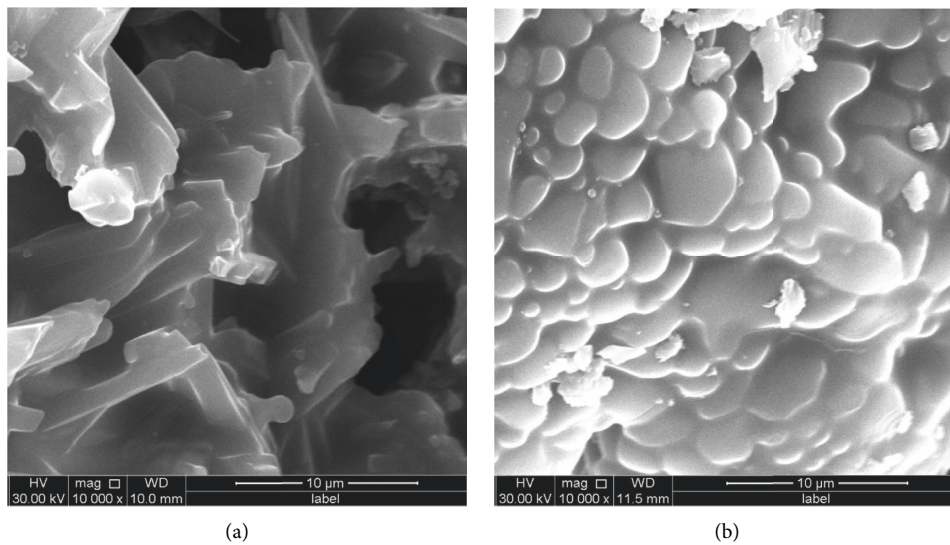


FIGURE 13: SEM images of SiC/Al₂O₃ composites sintered by microwave sintering and conventional sintering (a) Samples of microwave sintering (b) Samples of conventional sintering.

6. Conclusion

(1) Through microwave sintering, the in situ synthesized mullite reinforced SiC/Al₂O₃ composites with different SiC particle size were prepared. The composite powders of samples were composed of SiC particles, coated with SiO₂ by a sol-gel method and Al₂O₃ particles. During microwave sintering, the bridging

mullite whiskers with large length diameter ratio were found in the SiC (5 μm)/Al₂O₃ composites.

(2) With the increase of SiC particle size in samples, the bulk density of SiC/Al₂O₃ composites first increased and then decreased. The bulk density of SiC (5 μm)/Al₂O₃ composites was higher than that of other SiC/Al₂O₃ composites, which reached the maximum value 2.06 g/cm³.

- (3) With the increase of SiC particle size in samples, the fracture toughness and flexural strength of SiC/Al₂O₃ composites also first increased and then decreased. The fracture toughness and flexural strength of SiC (5 μm)/Al₂O₃ composites were higher than those of other SiC/Al₂O₃ composites, which reached the maximum value 1.98 MPa·m^{1/2} and 63 MPa, respectively.
- (4) With the increase of thermal shock cycles, the flexural strength retention of SiC/Al₂O₃ composites with different SiC particle size also decreased. Among the four groups of SiC/Al₂O₃ composites, the flexural strength retention of SiC (5 μm)/Al₂O₃ composites was also higher than those of other SiC/Al₂O₃ composites. After 5, 10, and 15 times of thermal shock cycles, the flexural strength retention of SiC (5 μm)/Al₂O₃ composites were 38%, 19%, and 17%, respectively, which indicated the better thermal shock resistance.
- (5) The morphology of mullite phase were mullite whiskers in SiC (5 μm)/Al₂O₃ composites, which was due to the size coupling effect and thermal aggregation effect in microwave sintering. Based on the size coupling effect and thermal aggregation effect, the anisotropic growth of mullite grains in SiC (5 μm)/Al₂O₃ composites was promoted and the mullite grains grew rapidly along one-dimensional direction during microwave sintering, while the sintering mechanism was heat radiation and heat transfer during conventional sintering, resulting in mullite phase with weak anisotropic growth.

Due to the unique sintering mechanism, the microwave sintering preserves the characteristics of fast speed, clean, and pollution-free, which brings the results of energy savings and environment-friendly. Therefore, microwave sintering is a kind of advanced material preparation process based on green manufacturing.

Data Availability

The data used to support the findings of this study are included within the article.

Conflicts of Interest

The authors declare that they have no conflicts of interest.

Acknowledgments

The authors gratefully acknowledge the financial support from the Science and Technology Project of Henan Province for Tackling Key Problems (182102210030).

References

- [1] X. U. Ni, "Research on manufacturing process and technology of chemical equipment based on the concept of green manufacturing," *Process technology*, no. 15, pp. 236–237, 2020.
- [2] C. Hu, G. Gui, S. Xie, and G. Y. Xiao, "Implementing method of green manufacture oriented material, energy and environment," *Coal Mine Machinery*, vol. 28, no. 3, pp. 107–109, 2007.
- [3] C. Wu, "Analysis of green manufacturing technology in mechanical manufacturing process," *Internal Combustion Engines and Accessories*, no. 3, pp. 150–151, 2021.
- [4] J. Liu, N. Xiao, and L. Zhang, "New mechanical manufacturing technology of green manufacturing," *Internal Combustion Engines and Accessories*, no. 22, pp. 104–106, 2020.
- [5] J. XI, "Research on materials selection for green manufacturing," *Materials Reports*, vol. 23, no. 5, pp. 94–97, 2009.
- [6] S. Fang, *Preparation and Investigation of Mullite Lightweight thermal Insulation Materials by Microwave sintering*, Zhengzhou University (Zhengzhou), Zhengzhou, 2020.
- [7] K. Guan, *Study of the Processing and Mechanisms of Mullite Reinforced Al₂O₃-SiC Composites by Microwave synthesis*, Zhengzhou University (Zhengzhou), Zhengzhou, 2016.
- [8] Liu. Jin, B. Liang, J. Zhang, and Y. Ai, "Research progress on microwave dielectric ceramics prepared via microwave sintering," *Materials Reports*, vol. 36, no. 3, pp. 1–10, 2022.
- [9] H. Zhang, Y. Zhang, B. Wang, and Yang, "Preparation and characterization of continuous alumina based fiber reinforced with orientated mullite whisker," *Chemical Engineering Journal*, vol. 268, pp. 109–115, 2015.
- [10] B. Meng and J. Peng, "Effects of in situ synthesized mullite whiskers on flexural strength and fracture toughness of corundum-mullite refractory materials," *Ceramics International*, vol. 39, no. 2, pp. 1525–1531, 2013.
- [11] O. Ertugrul, R. Dalmis, S. Akpınar, I. M. Kusoglu, and Celik, "Influence of zircon particle size on conventional and microwave assisted reaction sintering of in-situ mullite-zirconia composites," *Ceramics International*, vol. 42, no. 9, pp. 11104–11117, 2016.
- [12] Q. Dang, Y. Ge, and Y. Gao, "Dynamic mechanical properties of Al₂O₃/SiC composite ceramic subjected to impact loading," *Acta Armamentarii*, vol. 43, no. 1, pp. 175–180, 2022.
- [13] B. Fan, W. Li, B. Dai, K. Guan, R. Zhang, and H. Li, "Preparation of mullite whiskers reinforced SiC/Al₂O₃ composites by microwave sintering," *Processing and Application of Ceramics*, vol. 10, no. 4, pp. 243–248, 2016.
- [14] X. Dang, M. Wei, R. Zhang et al., "Crucial effect of SiC particles on in situ synthesized mullite whisker reinforced Al₂O₃-SiC composite during microwave sintering," *Processing and Application of Ceramics*, vol. 11, no. 2, pp. 106–112, 2017.
- [15] C. Lu, *Study on Gelcasting Process of SiC Whisker Toughened Alumina Ceramics*, Shenyang University of Technology (Shenyang), Shenyang, 2021.
- [16] S. Zhang, Y. Feng, X. Gao, Y. Song, F. Wang, and S. Zhang, "Modeling of fatigue failure for SiC/SiC ceramic matrix composites at elevated temperatures and multi-scale experimental validation," *Journal of the European Ceramic Society*, vol. 42, no. 8, pp. 3395–3403, 2022.
- [17] S. Wu and N. Claussen, "Reaction bonding and mechanical properties of mullite/silicon carbide composites," *Journal of the American Ceramic Society*, vol. 77, no. 11, pp. 2898–2904, 2010.
- [18] W. Wang, C. Zhou, G. Liu, and G. Qiao, "Molten salt synthesis of mullite whiskers on the surface of SiC ceramics," *Journal of Alloys and Compounds*, vol. 582, no. 1, pp. 96–100, 2014.

- [19] N. M. Rendtorff, L. B. Garrido, and E. F. Aglietti, "Thermal shock behavior of dense mullite-zirconia composites obtained by two processing routes," *Ceramics International*, vol. 34, no. 8, pp. 2017–2024, 2008.
- [20] X. Pian, B. Fan, H. Chen, B. Zhao, X. Zhang, and R. Zhang, "Preparation of m-ZrO₂ compacts by microwave sintering," *Ceramics International*, vol. 40, no. 7, pp. 10483–10488, 2014.
- [21] D. Żymełka, S. Saunier, D. Goeriot, and J. Molimard, "Densification and thermal gradient evolution of alumina during microwave sintering at 2.45GHz," *Ceramics International*, vol. 39, no. 3, pp. 3269–3277, 2013.
- [22] J. Croquesel, D. Bouvard, J. M. Chaix, C. P. Carry, S. Saunier, and S. Marinel, "Direct microwave sintering of pure alumina in a single mode cavity: grain size and phase transformation effects," *Acta Materialia*, vol. 116, pp. 53–62, 2016.
- [23] M. Xie, J. Shi, G. Chen, and X. Li, "Research progress and prospect of microwave sintering technology," *Powder Metallurgy Industry*, vol. 29, no. 3, pp. 66–72, 2019.
- [24] Z. Yin, J. Yuan, Y. Cheng, and Z. h. Wang, "Research Status of processes and mechanisms of ceramic materials by microwave sintering," *Bulletin of the Chinese Ceramic Society*, vol. 35, no. 5, pp. 1492–1497, 2016.
- [25] D. Xu, C. Fang, Y. Zhan et al., "Effect of two-step microwave sintering on the fracture toughness of alumina ceramics," *Journal of Ceramics*, vol. 39, no. 2, pp. 174–180, 2018.
- [26] H. Yang, X. Zhou, J. Yu, H. Wang, and Z. Huang, "Microwave and conventional sintering of SiC/SiC composites: flexural properties and microstructures," *Ceramics International*, vol. 41, no. 9, pp. 11651–11654, 2015.
- [27] B. Li, L. Xin, J. Cui et al., "Research process in preparation of glass ceramics by microwave sintering," *Materials Reports*, vol. 33, no. Z2, pp. 189–197, 2019.
- [28] S. Bodhak, S. Bose, and A. Bandyopadhyay, "Densification study and mechanical properties of microwave-sintered mullite and mullite-zirconia composites," *Journal of the American Ceramic Society*, vol. 94, no. 1, pp. 146–155, 2011.
- [29] R. Zhang, B. Fan, F. Zhang et al., *Special auxiliary heating and heat preservation device for microwave sintering of oxide composites*, 2012.
- [30] R. Zhang, B. Fan, F. Zhang et al., *A preparation method of mullite reinforced Al₂O₃/SiC composites*, vol. 9, 2015.
- [31] R. Belli, M. Wendler, J. Zorzini, L. H. da Silva, A. Petschelt, and U. Lohbauer, "Fracture toughness mode mixity at the connectors of monolithic 3Y-TZP and LS2 dental bridge constructs," *Journal of the European Ceramic Society*, vol. 35, no. 13, pp. 3701–3711, 2015.
- [32] X. Wang and A. A. Atkinson, "On the measurement of ceramic fracture toughness using single edge notched beams," *Journal of the European Ceramic Society*, vol. 35, no. 13, pp. 3713–3720, 2015.
- [33] J. Wan, M. Zhou, X. S. Yang et al., "Fracture characteristics of freestanding 8wt% Y₂O₃-ZrO₂ coatings by single edge notched beam and Vickers indentation tests," *Materials Science and Engineering A*, vol. 581, no. 5, pp. 140–144, 2013.
- [34] W. F. Brown and J. E. Srawley, *Plane Strain Crack Toughness Testing of High Strength Metallic Materials*, American Society for Testing Materials, Philadelphia, 1966.
- [35] P. Kumar, M. Nath, and A. Ghosh, "Enhancement of thermal shock resistance of reaction sintered mullite-zirconia composites in the presence of lanthanum oxide," *Materials Characterization*, vol. 101, pp. 34–39, 2015.
- [36] M. Nath and H. S. Tripathi, "Thermo-mechanical behavior of Al₂O₃-Cr₂O₃ refractories: effect of TiO₂," *Ceramics International*, vol. 41, no. 2, pp. 3109–3115, 2015.
- [37] J. Zhang, *Preparation, Growth Methenism of Mullite Whiskers and Their Enhancement Effect on Ceramic Matrix composites*, China University of Geosciences, Wuhan, 2012.
- [38] X. Ma, T. Ohtsuka, S. Hayashi, and Z.-e. Nakagawa, "The effect of BN addition on thermal shock behavior of fiber reinforced porous ceramic composite," *Composites Science and Technology*, vol. 66, no. 15, pp. 3089–3093, 2006.
- [39] K. K. Chawla, "Interface engineering in mullite fiber/mullite matrix composites," *Journal of the European Ceramic Society*, vol. 28, no. 2, pp. 447–453, 2008.
- [40] T. Zhang, L. Kong, Z. Du, J. Ma, and S. Li, "Tailoring the microstructure of mechanoactivated Al₂O₃ and SiO₂ mixtures with TiO₂ addition," *Journal of Alloys and Compounds*, vol. 506, no. 2, pp. 777–783, 2010.
- [41] C. Liu, J. Chen, and W. Cai, "Data-Driven remanufacturability evaluation method of waste parts," *IEEE Transactions on Industrial Informatics*, vol. 18, no. 7, pp. 4587–4595, 2022.

Research Article

Pushing Pose Sensing of Underground Mobile Supporting Robot

Nan Wang,¹ Hao Liu,¹ Xiaobiao Li,¹ Meizi Tian,² and Lin Zhang^{2,3} 

¹School of Mechanical and Electronic Engineering, Suzhou University, Suzhou 234000, China

²School of Robot Engineering, Yangtze Normal University, Chongqing 408100, China

³School of Mechanical Engineering, Shanghai Jiao Tong University, Shanghai 200240, China

Correspondence should be addressed to Lin Zhang; lin.zhang_2014@hotmail.com

Received 23 March 2022; Revised 15 April 2022; Accepted 22 April 2022; Published 8 June 2022

Academic Editor: Jorge Cunha

Copyright © 2022 Nan Wang et al. This is an open access article distributed under the Creative Commons Attribution License, which permits unrestricted use, distribution, and reproduction in any medium, provided the original work is properly cited.

The pushing pose of underground mobile supporting robot (MSR), i.e., hydraulic support, is a key factor to measure the straightness of the working face. Therefore, in order to independently complete the pushing process and ensure the straightness requirements of the pushing pose, by considering the pushing displacement of MSR and the pose of the middle groove of the scraper conveyor, this study proposes a fusion evaluation model combined with the least square straightness based on the pushing displacement and the straightness based on the pose of the middle groove. The pose sensing approach is established by estimating the pose of the middle groove and the displacement of MSR, analyzing, and extracting the data characteristics of acceleration signal; the OVR (one-versus-rest) method is used to realize the displacement state pattern recognition of hydraulic support based on SVM (support vector machine). The effectiveness of this approach is verified by building an experimental platform.

1. Introduction

As an important intelligent equipment for fully mechanized mining, mobile supporting robot (MSR, also known as hydraulic support) uses high-pressure emulsion to realize the cyclic actions and provides support and protection for the fully mechanized mining face [1]. The pushing pose of MSR refers to the pose state formed by the middle groove of the scraper conveyor when MSR pushes forward with the working face, pushed and moved periodically [2]. In the process of coal mining, MSR, scraper conveyor, and coal wall need to maintain a certain straightness to ensure the smooth operation of coal mining equipment [3–6]. However, the pushing pose of MSR is the essential factor for the straightness of the working face. Therefore, in order to ensure the good straightness of the working face, it is necessary to study the sensing approach of the pushing pose of MSR and realize the straightness evaluation of the pose of MSR.

At present, the pose sensing approach of MSR mainly depends on the displacement sensor installed in MSR pushing jack. However, approach has large systematic error. At the same time, it is complicated to replace the damaged

sensors because of the poor working conditions and heavy equipment. Thus, it is very necessary to study a new approach to sense MSR pose. Based on the sensing of MSR pose and considering the influencing factors of the change of the middle groove pose, this study established the pushing pose straightness evaluation model based on the pushing displacement and the middle groove pose of the scraper conveyor, which provided the model basis and constraint target for the independent pushing of MSR.

2. Related Work

At present, the sensing approach for pose and straightness of hydraulic support mainly focus on simple on-site pull wire and infrared beam measurement. With the deep integration of intelligent detection technology into coal mine production, the inertial navigation technology [6, 7], Unity3D technology [8–11], and visual technology [12, 13] have been used gradually. Zhang et al. and Chen et al. [3, 14] proposed a pose monitoring method of hydraulic support based on multisensor fusion technology. Yang et al. [15] and Liang et al. [16] used the lidar and inclination sensors to measure the pose of hydraulic support, respectively. Wang et al. [17]

proposed a method for measuring the height and straightness of the hydraulic support group based on point cloud; analyzing the geometric posture of single hydraulic support point cloud, the feature points are selected on each hydraulic support to solve the straightness, which effectively reduce the matching error. Wang et al. [18] realized the continuously adjusted for alignment without the interrupt of longwall face based on the reference target line with absolute direction. In addition, multisoftware cosimulation [19], information fusion [20, 21], and algorithm fusion [22, 23] are used in straightness detection of hydraulic support.

Although the above approaches have been verified by theory and experiment, the environment in the coal mine has lots of dust and the oil circuit on the hydraulic support is complex, resulting in the obstruction of sight and the limited use of indirect measurement technology. Meanwhile, the existing position sensor is installed inside the hydraulic jack with high error. In order to solve these problems, in this study, the IMU (inertial measurement unit) installed on the middle groove of scraper conveyor is used to directly measure the displacement acceleration, and the MS-KF (multisegmental Kalman filter) approach is used to eliminate the accumulation error. By considering the sensing of the hydraulic support pose and the change of middle groove pose, established the pushing pose straightness evaluation model combined the pushing displacement and the middle groove pose, which provided the model basis and constraint target for the independent pushing of the hydraulic support.

3. Pose Sensing Based on Pushing State Recognition

At present, the sensors used by the electrohydraulic control system of MSR in collecting the displacement information are built in the push jack, but this method has sensing error and unfavorable for the installation and maintenance of the sensor. In order to solve these problems, IMU installed on the middle groove of the scraper conveyor is used to directly measure the displacement. However, there is a large time accumulation error in the method of using IMU to collect the acceleration in the process of moving and calculating the pushing displacement through integral processing. Therefore, it is necessary to study more effective error elimination methods to realize the accurate measurement of pushing pose based on IMU.

In the pushing process of MSR, the jack will quickly enter the uniform motion state from the static state, which is called the instantaneous acceleration state. After a period of time, it will quickly enter the static state from the uniform state, which is called the instantaneous deceleration state. The instantaneous acceleration and instantaneous deceleration state are called variable velocity state (VVS). Uniform motion state is called constant velocity state (CVS). Other stages remain at static state which is called zero velocity state (ZVS).

According to the above prior knowledge, the acceleration data in different states are processed in sections: the Kalman filtering method of the variable acceleration model be used in VVS, the Kalman filtering method of the zero acceleration model be used in CVS, and ZVS provides the

reference point of zero velocity update for the whole process of displacement estimation. Compared with the traditional method, it does not use all the data for Kalman filtering calculation, but only uses the data in VVS and CVS periods, so it can reduce the source of cumulative error. In addition, a priori knowledge about velocity and acceleration is added in VVS and CVS periods; the Kalman state space conversion model in the two periods is refined, finally reducing the measurement error.

3.1. Methods. This method recognizes the pushing state with the acceleration signal collected; different Kalman filter state space conversion models are applied in different states; meanwhile, the reference point of ZUPT is provided in the ZVS period, which will reduce the measurement error. In essence, the method is called the multiphased Kalman filter (MS-KF) because of subsection handling a group of acceleration time series with the Kalman filter. The method architecture is shown in Figure 1, and the key technical process is as follows.

3.1.1. Estimation of Middle Groove Pose. The acceleration signal collected by IMU is affected by gravity. In order to remove the influence caused by gravity, we need to obtain the direction of gravity component through pose estimation with the help of gyroscope information output by IMU and then remove the acceleration component caused by gravity. The pose of the middle groove can be estimated by the following formula:

$${}^L_G q_{w,t} = \frac{1}{2} {}^L_G q_{t-1} \otimes {}^L \omega_t, \quad (1)$$

$${}^L_G q_{w,t} = {}^L_G q_{w,t-1} + {}^L_G q_{w,t} \Delta t,$$

where ${}^L \omega_t$ is the angular rate relative to the sensing coordinate system at time t , ${}^L_G q_{t-1}$ is the rotation quaternion of the world coordinate system relative to the sensing coordinate system at time $t-1$, and ${}^L_G q_{w,t}$ is the rotation quaternion of the world coordinate system relative to the sensing coordinate system at t -time.

Through the following formula, the acceleration signal in the sensing coordinate system can be converted into the acceleration signal in the world coordinate system.

$${}^G g' = R({}^L_G q_{w,t}) {}^L \alpha_t. \quad (2)$$

Among them, $R(\cdot)$ converts the pose represented by quaternion into matrix form, and the conversion formula is

$$R(q) = \begin{bmatrix} q_0^2 + q_1^2 - q_2^2 - q_3^2 & 2(q_1 q_2 - q_0 q_3) & 2(q_1 q_3 + q_0 q_2) \\ 2(q_1 q_2 + q_0 q_3) & q_0^2 - q_1^2 + q_2^2 - q_3^2 & 2(q_2 q_3 - q_0 q_1) \\ 2(q_1 q_3 - q_0 q_2) & 2(q_2 q_3 + q_0 q_1) & q_0^2 - q_1^2 - q_2^2 + q_3^2 \end{bmatrix}. \quad (3)$$

Theoretically, the acceleration signal caused by gravity meets the following equation after conversion:

$$R(\Delta q_{acc}) {}^G g_r = {}^G g', \quad (4)$$

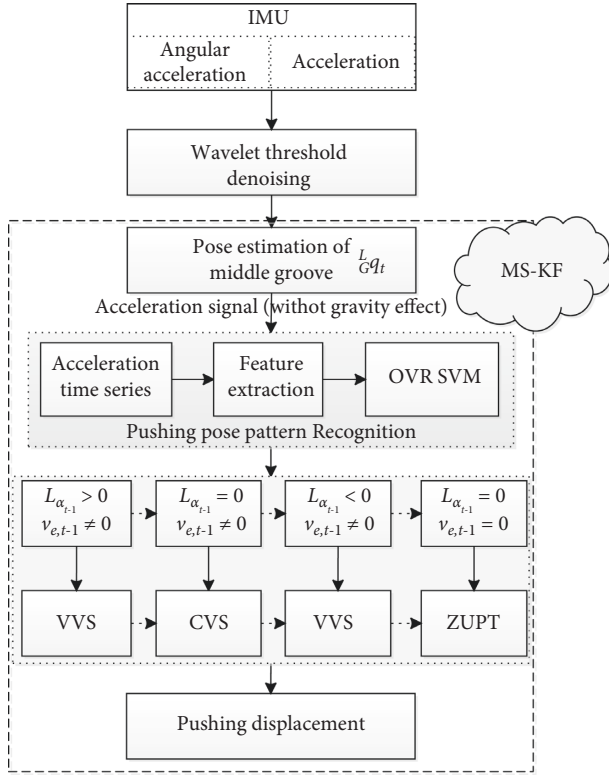


FIGURE 1: Pushing displacement sensing architecture.

where ${}^G g_r$ is the true gravity vector, the theoretical value is ${}^G g_r = [0, 0, g]^T$. In practice, deviation $\Delta \hat{q}_{acc}$ may exist. The final pose can be obtained by quaternion interpolation through SLERP and other methods:

$${}^L_G q_t = {}^L_G q_w \otimes \Delta \hat{q}_{acc}. \quad (5)$$

Through the above steps, it not only can calculate the pose of the middle groove but also can pretreat the acceleration signal, removing the component generated by gravity in the acceleration signal.

3.1.2. Displacement Estimation Based on MS-KF. After the pose estimation of the middle groove, the collected acceleration signals are transformed into the acceleration time series without the influence of gravity, the data characteristics of the acceleration signals are analyzed and extracted, and the SVM is used for training. Finally, the displacement state of the acceleration time series can be recognized by using the trained SVM model.

For acceleration time series under different transition states, MS-KF will use different state space models to estimate the transition displacement. Delimiting the displacement and velocity variables x_t and v_t , respectively, the state space model of VVS section is

$$\begin{bmatrix} x_{e,t} \\ v_{e,t} \\ {}^L a_{e,t} \end{bmatrix} = \begin{bmatrix} I & \Delta t I & I \Delta t^2 / 2 \\ 0 & I & R({}^L_G q_t) \Delta t \\ 0 & 0 & I \end{bmatrix} \begin{bmatrix} x_{e,t-1} \\ v_{e,t-1} \\ {}^L a_{e,t-1} \end{bmatrix} + \begin{bmatrix} 0 \\ -g \Delta t \\ 0 \end{bmatrix} + v_t. \quad (6)$$

Among them, v_t refers to the processing noise. For the acceleration in the CVS period, theoretically, the acceleration should be 0, so the state space model adopted by CVS is

$$\begin{bmatrix} x_{i,t+1} \\ v_{i,t+1} \\ {}^L a_{i,t+1} \end{bmatrix} = \begin{bmatrix} I & \Delta t I & 1/2 I \Delta t^2 \\ 0 & I & R({}^L_G q_t) \Delta t \\ 0 & 0 & 0 \end{bmatrix} \begin{bmatrix} x_{i,t} \\ v_{i,t} \\ {}^L a_{i,t} \end{bmatrix} + \begin{bmatrix} 0 \\ -g \Delta t \\ 0 \end{bmatrix} + v_t. \quad (7)$$

Second, different initial state values need to be set for acceleration time series in different phases when Kalman filtering estimation is carried out. The initial value setting is shown in the following formula:

$$X_t = \begin{cases} X_{e,t} | \{X_{e,0} = 0, P_0 = 0\}, \text{mean}(\{x_i\}) > 0, & x_i \in \text{VVS}, \\ X_{i,t}, & y_i \in \text{CVS}, \\ X_{e,t} | \{X_{e,0} = X_{i,t}, P_0 = 0\}, \text{mean}(\{x_i\}) < 0, & x_i \in \text{VVS}. \end{cases} \quad (8)$$

Among them, X_t is the state variable, $X_t = [x_{i,t}, v_{i,t}, {}^L a_{i,t}]^T$, and $X_{e,0}$ and P_0 are the initial values of state variables and estimation errors in Kalman filter estimation, respectively. MS-KF can be realized with the above steps.

3.2. Feature Extraction and Selection. Before realizing MS-KF, it is necessary to subsection the process of acceleration time series. In order to study the data characteristics of acceleration time series in the process of MSR pushing, the pushing displacement signal and acceleration signal collected in the laboratory environment are collected, as shown in Figures 2(a) and 2(b), respectively, finally getting the schematic diagram of their characteristics with denoising and normalizing the signal, as shown in Figure 2(c). At the beginning of sliding, the positive component of acceleration is large and reaches the average speed of moving jack in a very short time. At the end of sliding, there is a small acceleration change. After the above actions, a sliding process is completed. It is the opposite when moving the support; first, at the beginning of support-moving, the negative component of acceleration is large and then moving at a uniform speed after reaching the average speed of support-moving. At the end of the support-moving, there is a small change, and then, it enters the static state.

MS-KF analysis is based on recognizing the acceleration in VVS, ZVS, and CVS periods. However, when jack is working in the VVS area, the time of accelerating and decelerating is very short, the feature discrimination corresponding to each state is low, and the final recognition effect will be affected. Therefore, it cannot improve the recognition rate through recognizing the state of acceleration signal directly. According to the above analysis of the pushing process, MSR corresponds to the four states of sliding start (S1), pushing end (S2), support-moving start (S3), and support-moving end (S4) in a pushing cycle. VVS corresponds to the area that state transition from one to another. CVS corresponds to the area not only between S1 and S2 but also between S3 and S4. ZVS corresponds to other areas. This method uses the prior knowledge of the transition system in state pattern recognition, which is more efficient and reliable, and the accuracy of final recognition will be improved.

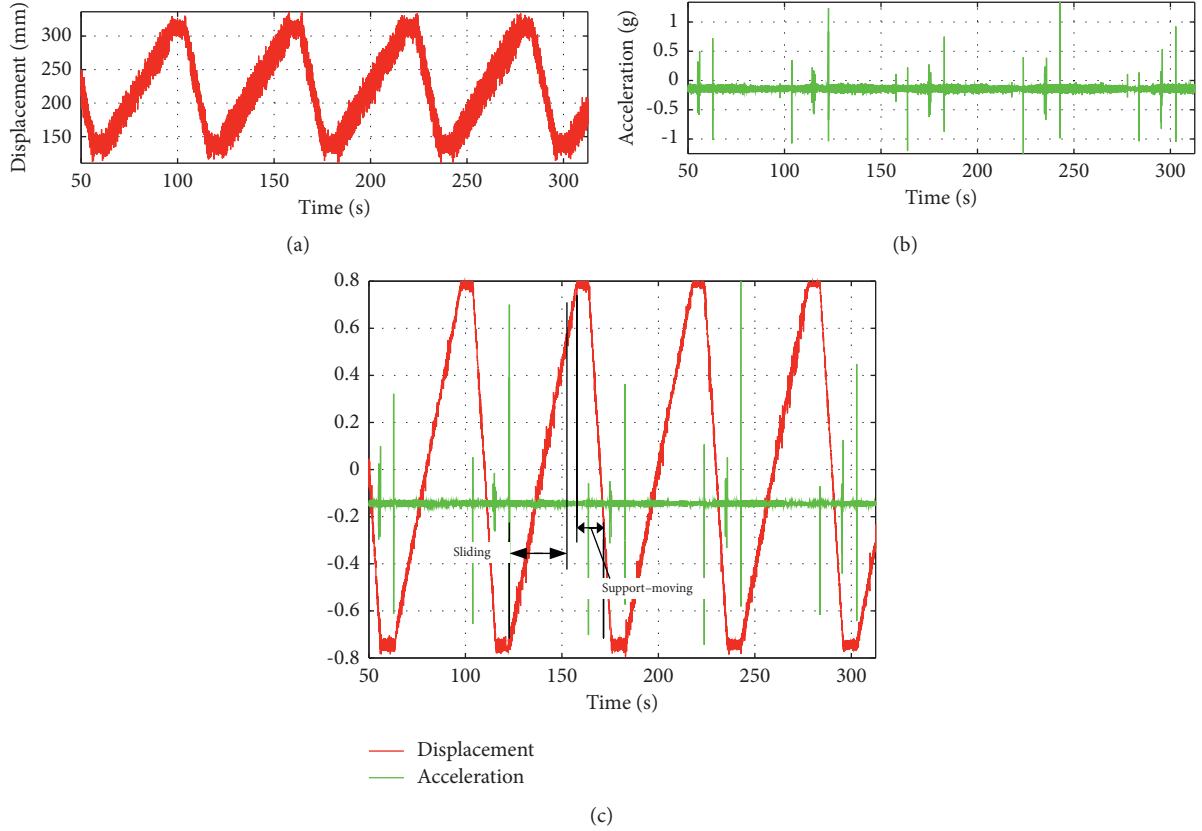


FIGURE 2: Feature samples of acceleration and displacement.

Extracting and selecting effective data features is the premise of pushing state pattern recognition. For the acceleration signal, the features that can be extracted are as follows:

- (1) Average power: describing the vibration intensity of the signal, $x(n)$ is the collected acceleration time series, where n is the length of the time series, $n = 1, 2, 3, \dots, N$. The characteristic value can be calculated according to the following formula:

$$f_1 = \sum_{n=1}^N (x(n))^2. \quad (9)$$

- (2) Sample entropy: measuring the complexity of time series, the specific definition and calculation formula can be carried out according to the method proposed by Richman et al. [24].
- (3) Spectral entropy: quantitative processing the smoothness of spectrum, which is positive correlation with feature show, if the relative power spectrum probability of $x(n)$ is P_k , the spectral entropy can be calculated as follows:

$$f_3 = - \sum_{K=0}^{N/2-1} P_k \ln(P_k). \quad (10)$$

- (4) Mean value: describing the average value of amplitude change of acceleration signal in each area, which can be calculated according to the following formula:

$$f_4 = \frac{1}{N} \sum_{n=1}^N x(n). \quad (11)$$

- (5) Median frequency: a measure used to describe the frequency change. First, calculating the power spectrum corresponding to the acceleration signal and then dividing the power spectrum probability into two parts with equal energy, the detail calculation process as references [25].

- (6) Standard deviation: describing the variation amplitude of acceleration signal, solving according to the following formula:

$$f_6 = \sqrt{\frac{1}{N-1} \sum_{n=1}^N (x(n) - \bar{x})^2}. \quad (12)$$

- (7) Skewness: a asymmetry measure of the vertical distribution near the mean, which is used to describe the asymmetry of acceleration signal when it changes and judge its change direction; the calculation is as follows:

$$f_7 = \frac{\sqrt{N(N-1)}}{N-2} \frac{1/N \sum_{n=1}^N (x(n) - \bar{x})^3}{(1/N \sum_{n=1}^N (x(n) - \bar{x})^2)^{3/2}}. \quad (13)$$

- (8) Kurtosis: reflecting the kurtosis of the square distribution, which is used to describe the amplitude of

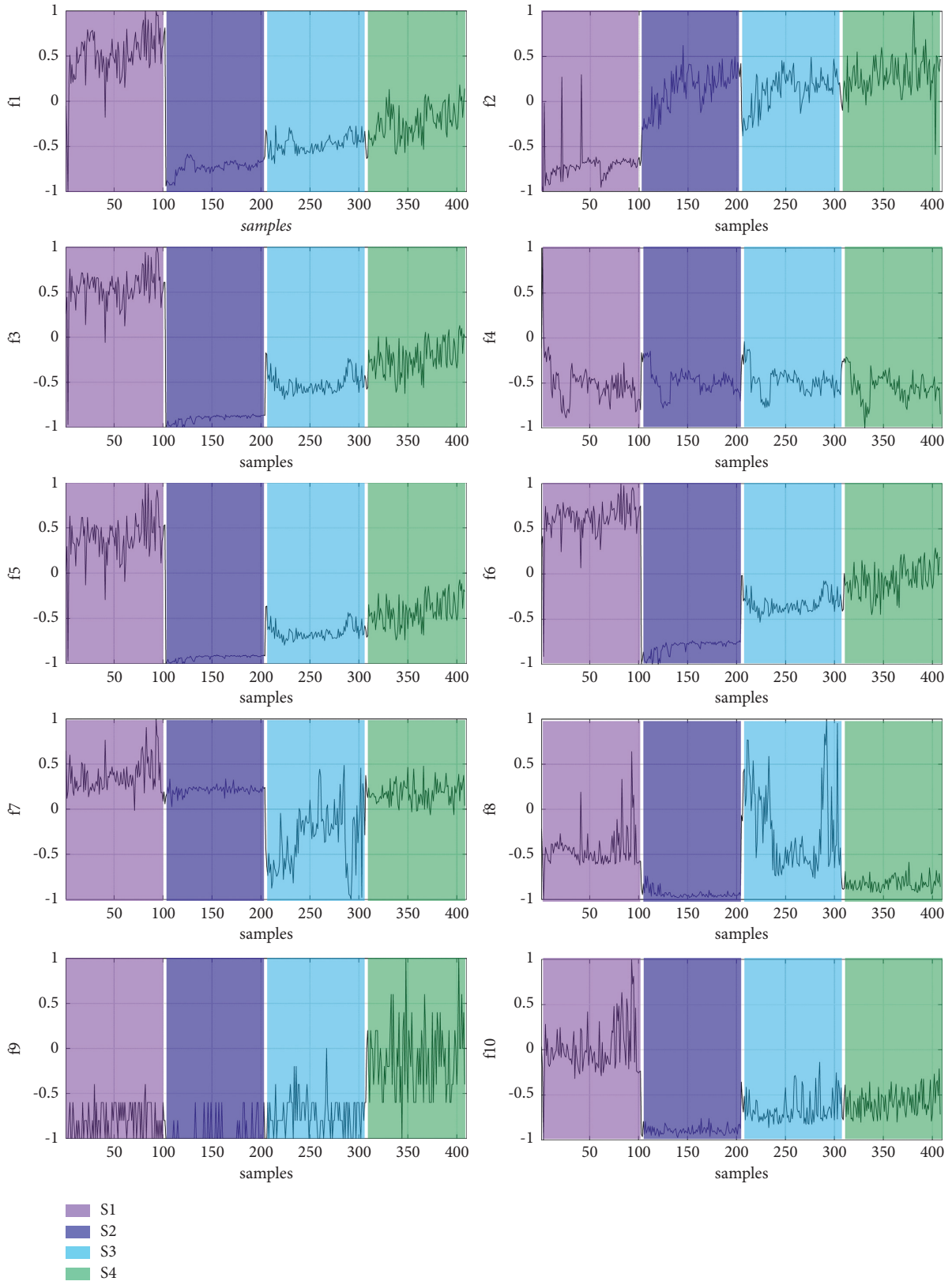


FIGURE 3: Features of samples.

acceleration signal change, the calculation is as follows:

$$f_8 = \frac{N-1}{(N-2)(N-3)} \left((N+1) \frac{1/N \sum_{n=1}^N (x(n) - \bar{x})^4}{(1/N \sum_{n=1}^N (x(n) - \bar{x})^2)^2} - 3(N-1) \right) + 3. \quad (14)$$

(9) Lempel-Ziv: a complex quantification method, reflecting the rate at which new patterns emerge in the time series and the detail calculation process as references [16].

(10) Crest factor: describing the peak sharpness of the signal, the calculation is as follows:

$$f_{10} = \frac{\max(x(n))}{\sqrt{1/N \sum_{n=1}^N (x(n))^2}} \quad (15)$$

Acceleration signals in 102 pushing periods are collected in the laboratory environment; each period corresponds to the acceleration time series $x_i(n)$ of 4 pushing states, $i = 1, 2, 3, \dots, 408$; the length of each time series is 2000, and finally, the eigenvalues corresponding to each acceleration time series are shown as f1–f10 in Figure 3. It can be seen from the figure that all the eigenvalues have a good recognition for the pushing states 1 and 2, but f4 is an exception. Between the pushing states 1 and 4, f4 nearly unchanged, and the boundaries are extremely blurred. Compared with f4, f9 has a good recognition for pushing state 4. When the features f1, f2, f3, and f10 are recognized in the pushing states 2–4, the recognition is low.

The other four eigenvalues, namely, f5–f8, have obvious boundaries for the four pushing states, especially f7 and f8. The consistency of all sample eigenvalues in the same state is very high, but the boundary of sample eigenvalues between different states is very obvious. Therefore, f5–f8 is the best choice among the above features used for pattern recognition of the pushing state. In order to verify the above assumption, first calculating the eigenvalues of all sample data and then arranging and combining all the eigenvalues, the total number of combinations is $\sum_{i=1}^{10} C_{10}^i$. Then, training each combination with SVM, calculating the k -fold cross-validation, and searching the optimal combination of each eigenvalue through the accuracy of the final 10-fold cross-validation, the final calculation results are obtained, as given in Table 1.

It can be seen from the results that the inspection accuracy of six combinations reached 99.8%, meanwhile f5–f8 exist in the six eigenvalue combinations. Considering the complexity of calculation and inspection accuracy, the eigenvalues f5–f8 are selected as the optimal combination, which verify the judgment results of the above eigenvalue selection.

3.3. SVM-Based Pushing State Recognition. Through the extraction and selection of the above feature values, finally, all the time series are converted into the training set (f5, f6, f7, f8) and the corresponding target state set (S1, S2, S3, S4)

TABLE 1: Combination result of the sample features.

f1	f2	f3	f4	f5	f6	f7	f8	f9	f10	CV
				√	√	√	√			0.998
		√	√	√	√	√	√	√		0.998
		√	√	√	√	√	√	√	√	0.998
			√	√	√	√	√			0.998
		√	√	√	√	√	√			0.998
				√	√	√	√	√	√	0.998
					√	√	√	√	√	0.997
					√	√	√	√	√	0.997
√	√	√	√	√	√	√	√	√	√	0.995
			√	√	√	√	√	√	√	0.995
			√	√	√	√	√	√	√	0.995
				√	√	√	√	√	√	0.995
					√	√	√	√	√	0.995
√	√	√	√	√	√	√	√			0.993
...

The values in bold means the best combination considering the cross validation results and the less features used in the algorithm.

of pushing state pattern recognition; it can be trained and predicated according to the training set and the target state set.

SVM is a machine learning method based on statistical theory proposed in the 1990s, which has a good application effect on pattern recognition problems with small samples and high dimensions. It can effectively avoid overfitting and has excellent nonlinear processing ability. By converting it into a convex quadratic programming problem, it can achieve the global optimum. If the given training samples are $(x_1, y_1), (x_2, y_2), \dots, (x_m, y_m)$, in order to transform the input vector from a low-dimensional space x to a high-dimensional space z , first nonlinearly transform the input vector $z = H(x)$, solving weight vector w and offset B , and satisfy the following equation:

$$y_i(w^T \cdot z_i + b) \geq 1 \quad i = 1, 2, \dots, l. \quad (16)$$

The unit vector of the weight vector is the normal direction of the interface. Therefore, the distance between the points close to the interface of the two categories is

$$d(w, b) = \min_{\{x|y=1\}} \frac{z^T \cdot w}{\|w\|} - \max_{\{x|y=-1\}} \frac{z^T \cdot w}{\|w\|}. \quad (17)$$

When the optimal boundary is reached, it should have met $w_o^T \cdot z + b_o = 0$, and the value of w_o meets the requirements of the following formula:

$$d(w_o, b_o) = \frac{2}{\|w_o\|} - \frac{2}{w_o^T \cdot w_o}. \quad (18)$$

So far, the problem of solving the optimal interface is transformed into the following optimization problem:

$$\min H(w) = \frac{1}{2}(w^T \cdot w) + V \cdot \sum_{i=1}^l a_i, \quad (19)$$

$$\text{s.t } y_i(w^T \cdot z_i + B) \geq 1.$$

TABLE 2: Commonly used kernel functions.

Name	Expression	Parameters
Linear kernel	$K(x_i, x_j) = x_i^T x_j$	None
Polynomial kernel	$K(x_i, x_j) = (x_i^T x_j)^d$	$d \geq 1$, polynomial degree
Gaussian kernel	$K(x_i, x_j) = \exp(-\ x_i - x_j\ ^2 / 2\sigma^2)$	$\sigma > 0$, bandwidth
Laplace kernel	$K(x_i, x_j) = \exp(-\ x_i - x_j\ / \sigma)$	$\sigma > 0$
Sigmoid kernel	$K(x_i, x_j) = \tanh(\beta x_i^T x_j + \theta)$	$\beta > 0$ and $\theta < 0$

TABLE 3: Data samples after normalization.

f5	f6	f7	f8	State	f5	f6	f7	f8	State
0.025	0.321	0.648	-0.214	S1	0.302	0.563	0.339	-0.480	S1
0.293	0.417	0.121	-0.579	S1	0.499	0.694	0.302	-0.511	S1
-0.969	-0.911	0.197	-1.000	S1	0.148	0.447	0.422	-0.570	S1
0.248	0.498	0.428	-0.626	S1	0.583	0.751	0.341	-0.566	S1
0.308	0.538	0.358	-0.601	S1	0.411	0.663	0.447	-0.348	S1
...
-0.996	-0.992	0.142	-0.885	S2	-0.944	-0.834	0.202	-0.963	S2
-0.980	-0.937	0.175	-0.945	S2	-0.997	-0.992	0.249	-0.815	S2
-0.953	-0.864	0.246	-0.828	S2	-0.987	-0.955	0.095	-0.823	S2
-0.987	-0.960	0.176	-0.928	S2	-0.937	-0.815	0.231	-0.943	S2
-0.990	-0.970	0.335	-0.739	S2	-0.948	-0.840	0.158	-0.924	S2
...
-0.591	-0.270	-0.489	0.446	S3	-0.627	-0.294	-0.687	0.175	S3
-0.625	-0.301	-0.702	0.039	S3	-0.719	-0.415	-0.592	0.163	S3
-0.475	-0.127	-0.609	0.154	S3	-0.715	-0.409	-0.045	-0.537	S3
-0.656	-0.347	-0.875	0.770	S3	-0.675	-0.354	-0.272	-0.371	S3
-0.637	-0.322	-0.799	0.763	S3	-0.765	-0.486	-0.459	0.070	S3
...
-0.469	-0.109	0.400	-0.708	S4	-0.436	-0.067	0.178	-0.938	S4
-0.525	-0.173	0.250	-0.867	S4	-0.519	-0.158	0.228	-0.924	S4
-0.205	0.155	0.264	-0.804	S4	-0.464	-0.098	0.270	-0.838	S4
-0.124	0.236	0.046	-0.841	S4	-0.147	0.204	0.386	-0.796	S4
-0.440	-0.069	0.144	-0.809	S4	-0.074	0.287	0.092	-0.846	S4
...

Converting the objective function with the Lagrange multiplier algorithm,

$$L(w, b, \lambda) = \frac{1}{2}(w^T \cdot w) + V \cdot \sum_{i=1}^l a_i - \sum_{i=1}^l \lambda_i [y_i(w^T z_i + b) - 1],$$

$$f(z) = \text{sgn}[(w^T \cdot z) + b] = \text{sgn} \left[\sum_{i=1}^l \lambda_i \cdot y_i \cdot (z^T z_i) \right]$$

$$= \text{sgn} \left[\sum_{\text{SupportVector}} \lambda_i \cdot y_i \cdot (z^T z_i) + b \right]. \quad (20)$$

In essence, SVM transforms samples into high-dimensional linear separable space through nonlinear transformation function H and constructs hyperplane to classify and recognize them. This nonlinear transformation function is also called kernel function, which satisfies the Mercer condition, $K(x_i, y_i) = H(x_i) H(y_i)$. Different kernel functions have different effects on SVM performance. The selection of kernel functions includes the selection of type and parameters. The commonly used kernel functions are given in Table 2.

TABLE 4: SVM detection result using different kernel functions.

Kernel function	k-fold	Test accuracy
Linear kernel	0.9938	0.9919
Polynomial kernel	0.9875	1.0000
RBF kernel	0.9939	1.0000
Sigmoid kernel	0.2250	0.2279

In addition to the above common kernel functions, we can also customize the kernel functions. If $K_1(x, x')$ and $K_2(x, x')$ are both kernel functions, we can customize the kernel functions through the following methods:

$$K(x, x') = c \cdot K_1(x, x')$$

$$K(x, x') = f(x) \cdot K_1(x, x') \cdot f(x')$$

$$K(x, x') = \exp[K_1(x, x')]$$

$$K(x, x') = K_1(x, x') + K_2(x, x') \quad (21)$$

$$K(x, x') = K_1(x, x') \cdot K_2(x, x')$$

$$K(x, x') = K_1(\varphi(x), \varphi(x'))$$

$$K(x, x') = x^T \cdot A \cdot x'$$

In this section, the median frequency f5, standard deviation f6, skewness f7, and kurtosis f8 of the acceleration

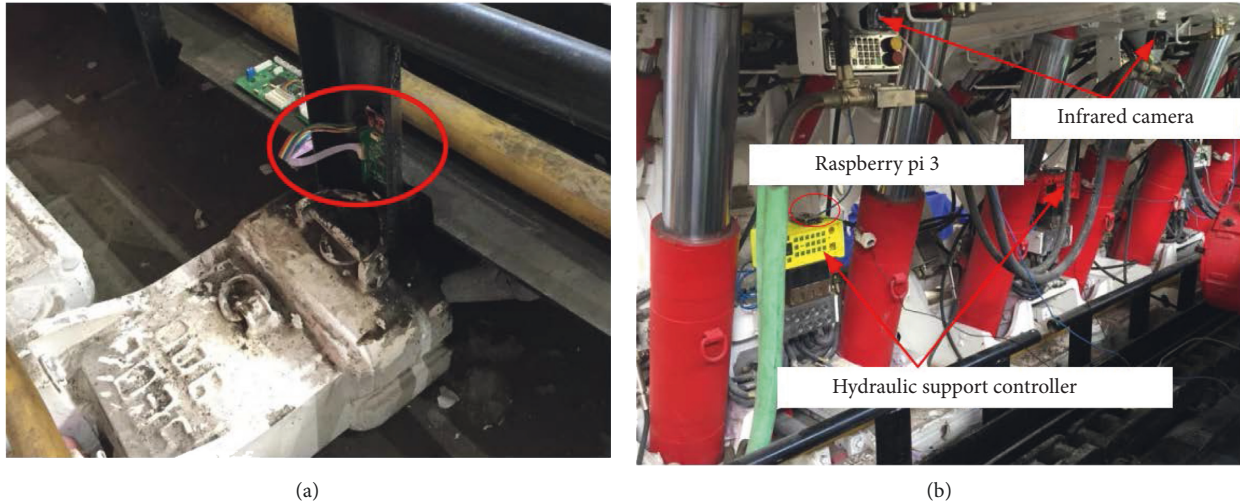


FIGURE 4: IMU sensor installation position and experimental site. (a) IMU sensor installation position. (b) Experimental platform site.

signal are used as the input vectors of SVM, and the OVR method is used to realize the pushing state pattern recognition of MSR based on SVM. After the normalized processing of the acceleration signal collected on-site, the training sample set data obtained are given in Table 3.

Taking 60% of the sample data as the training set and the remaining 40% as the test set, the LibSVM library is used to realize the pushing state pattern recognition program in the MATLAB environment and calculating the k -fold cross test accuracy ($k = 10$) of the training set and the SVM classification results of the test set with different kernel functions. The results are given in Table 4.

It can be seen that RBF kernel function has better recognition accuracy when recognizing the pushing state in SVM, and the average recognition accuracy can reach 99.39%. Therefore, using RBF kernel function can achieve a better SVM classification effect and then realize the pushing state pattern recognition with high accuracy.

4. Experimental Research

4.1. Experimental Platform. Build the pose sensing experimental system of MSR through adding an IMU sensor to the original MSR sensing system. For the higher acquisition frequency and detection accuracy, the ADIS16448 IMU sensor is used for pushing pose sensing, as shown in Figure 4(a). In order to realize the pushing pose sensing, the whole experimental platform includes 4 MSRs, 1 shearer, 1 scraper conveyor, and other equipment. The experimental site is shown in Figure 4(b).

The MSR controller designed in this study is shown in Figure 5. The upper computer is installed with the monitoring software based on openPOWERLINK, which is an open-source industrial ethernet stack implementing the POWERLINK protocol for managing node and controlled node, designed to realize the remote operation of the controller, and the following action of MSR is controlled through POWERLINK. At the same time, the virtual monitoring system of MSR based on Unity3D is designed in

C#.NET platform, which reproduces the pose of the real MSR in real time through the action of the virtual model of MSR with the pose data uploaded by Ethernet; the user interface is shown in Figure 5.

4.2. Experiment and Analysis. The pushing pose of MSR includes the attitude angle and displacement of the middle groove. The attitude angle of the middle groove can be calculated directly according to IMU, but the displacement needs more in-depth research. In order to verify the effectiveness of the pushing sensing method based on pushing state pattern recognition proposed in this study, the IMU sensor is installed on the middle groove of the scraper conveyor to obtain the inertia information in the moving process.

The denoising data samples of acceleration and angular velocity are shown in Figure 6. It can be seen from the figure that four state changes will occur in a cycle. When the state changes, the acceleration and angular velocity will change. According to the change characteristics of acceleration data, the pattern recognition of pushing state can be realized, and then, the acceleration data are processed in phases. Through the structural parameters of MSR, the theoretical sliding and support-moving speeds can be calculated. While, according to the measured displacement, the sliding and support-moving speeds can be calculated as 14.53 mm/s and 35.19 mm/s, respectively. Due to the influence of the current experimental environment and sensor noise, there is a certain error between the measured value and the theoretical value, and the error is given in Table 5.

Conduct the denoised IMU data with time interception, calculate the eigenvalues f_5 , f_6 , f_7 , and f_8 corresponding to the IMU data in each time window, and identify the state in the current time window with the trained SVM model. Each state mode identified in a time window is shown in Figure 7. There is high accuracy in identifying the SVM state with eigenvalues f_5 , f_6 , f_7 , and f_8 , but there are also abnormalities in the case of large vibration. In Figure 7, the recognition

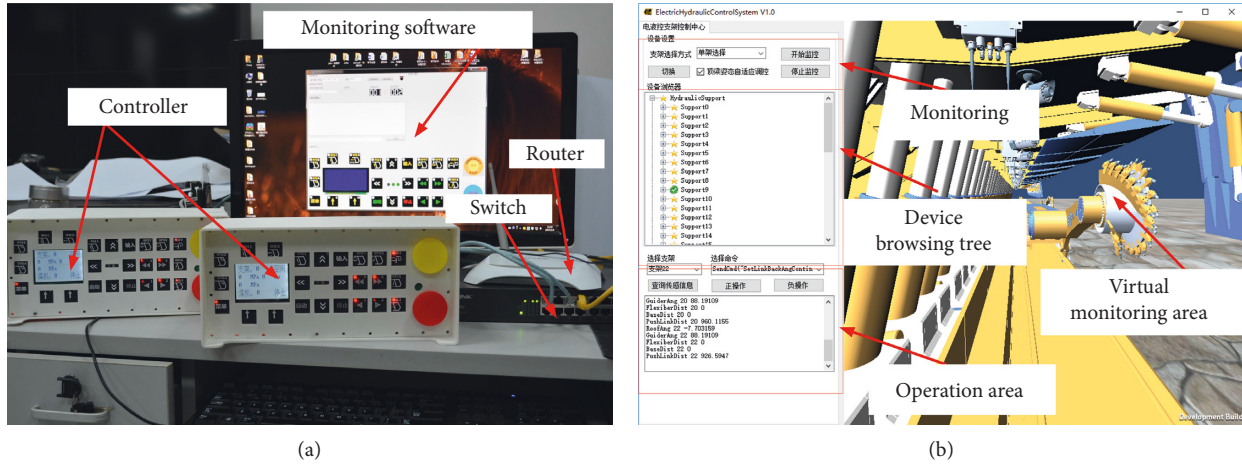


FIGURE 5: Experimental platform for the AFM control system. (a) Autonomous follow-up controller. (b) Virtual monitoring system.

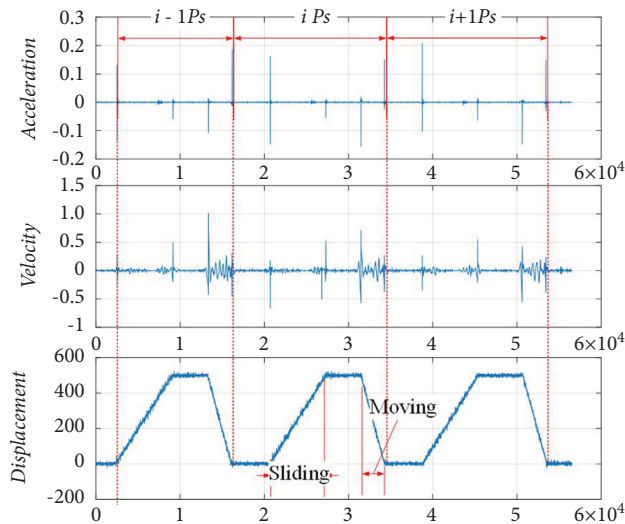


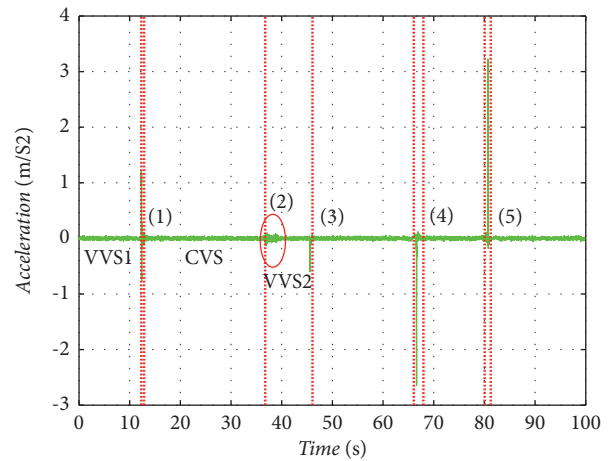
FIGURE 6: Data samples for pushing pose sensing.

rates of the three states of sliding start, support-moving start, and support-moving end are accurate and the corresponding times are (12.53, 13.08), (66.41, 67.24), and (80.27, 81.46), respectively. However, there is a large vibration before the end of sliding, so the recognition rate in this area is low. In order to eliminate the influence of vibration on the pattern recognition of pushing state, it is clustered into the nearest state pattern in the time domain, and the vibration area in the figure is determined as the end of sliding.

According to the pattern recognition results of the pushing state, different IMU data phases are obtained, as shown in Figure 7; phase (1) is the sliding start phase, the sliding speed increases from 0 to the theoretical speed, corresponding to the first VVS phase (VVS1); phase (3) is the sliding end phase, which is the deceleration phase, corresponding to the second VVS phase (VVS2). Between VVS1 and VVS2 is the uniform speed phase, which is the first CVS phase (CVS). For VVS and CVS phase, Kalman filter estimation is performed according to their corresponding state space models, and the results are shown in Figures 8(a)–8(c).

TABLE 5: Pushing velocities.

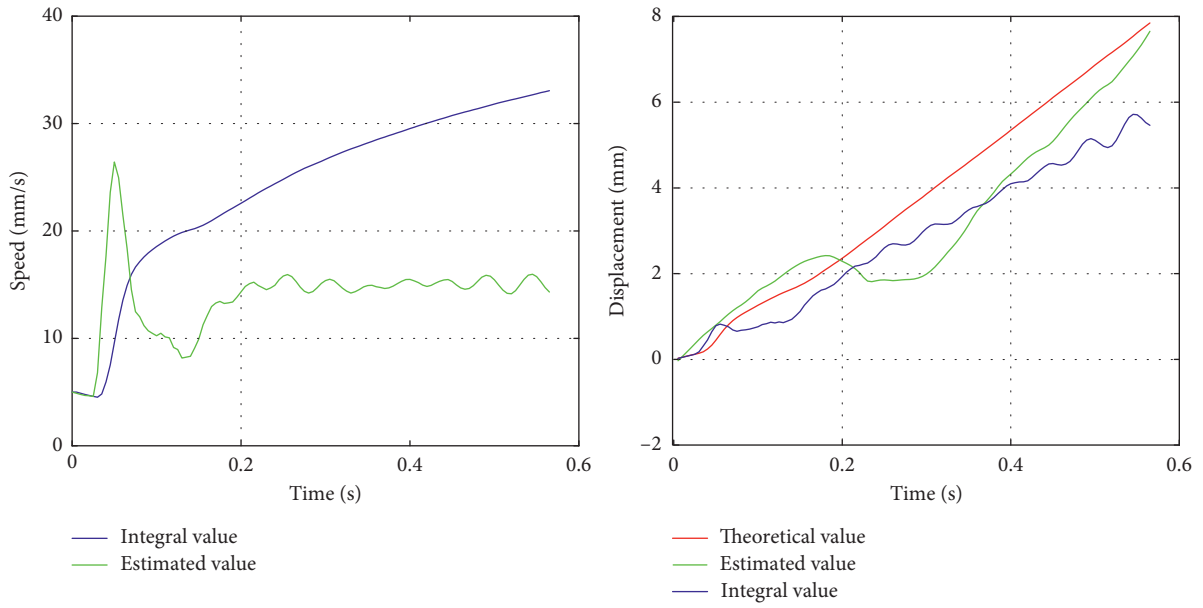
Action	Ground truth (mm/s)	Measurement (mm/s)	Error (%)
Sliding	15.00	14.53	0.13
Support-moving	35.00	35.19	0.54



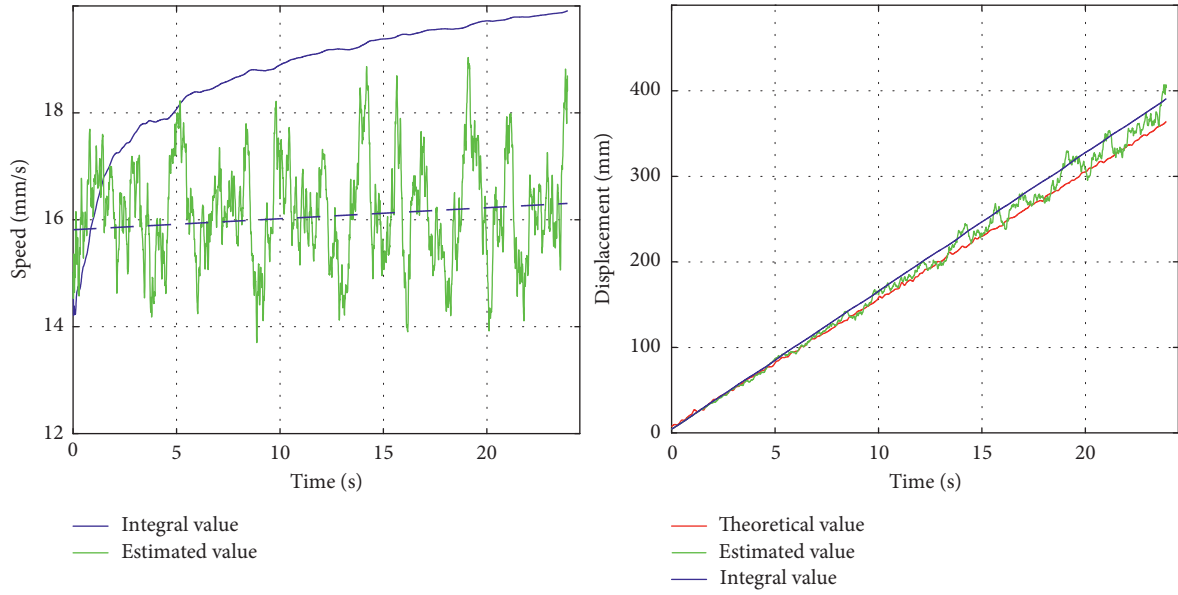
- Segmental point
 (1) Sliding start [2507, 2617];
 (2) Vibration [7399, 7822];
 (3) Sliding end [9141, 9261];
 (4) Moving start [13285, 13448];
 (5) Moving end [16054, 16292]
 Sampling frequency: 200 Hz

FIGURE 7: Recognition result of the pushing state.

In the VVS1 phase, if the integral method is directly adopted, a large cumulative error will occur in the acceleration phase of pushing jack. As shown in Figure 8(a), the final speed obtained by the integral method is more than 30 mm/s, while the theoretical value is only 15 mm/s. The value estimated by IFOA-KF is more accurate, and the final speed is maintained near the theoretical value. Similarly, for



(a)



(b)

FIGURE 8: Continued.

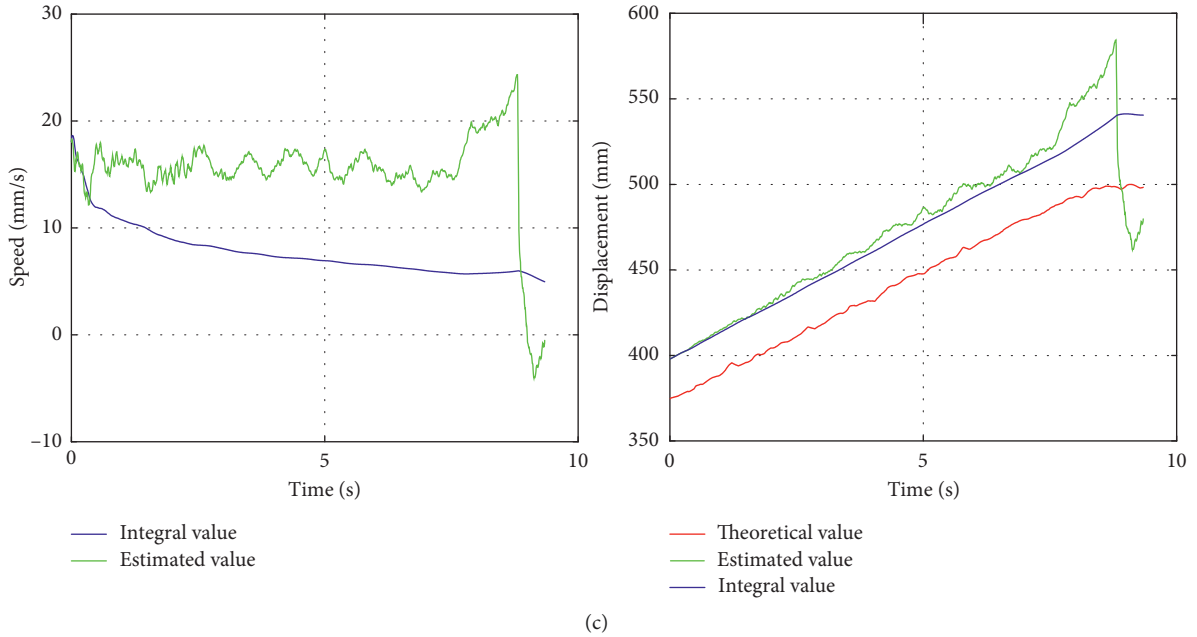


FIGURE 8: Segmental sensing result. (a) VVS1 segment. (b) CVS1 segment. (c) CVS2 segment.

TABLE 6: Error analysis result.

Phase	MSE	
	IFOA-KF method	Integration method
VVS1	0.349	0.581
CVS	5.830	12.442
VVS2	28.218	31.472

the estimation of displacement, the final result of IFOA-KF is closer to the theoretical value, and its mean square error MSE is 1.4615.

In the CVS1 phase, the initial displacement and velocity are determined by VVS1, and its initial condition is $[y_0, v_0, a_0]^T = [5.69, 15.02, 0]^T$. Due to the longtime of this period, the possibility of time cumulative error is greater. As shown in Figure 8(b), theoretically, this phase should move at a uniform speed, and the speed should be maintained at about 15 mm/s; however, the direct integration method produces a large error, resulting in a large displacement error in the final integration. In the VVS2 phase, the initial condition is the end condition of the CVS phase, that is, $[y_0, v_0, a_0]^T = [397.80, 18.01, 0]^T$. The results of integration and estimation are shown in Figure 8(c). The error of velocity and displacement estimated by IFOA-KF is much smaller than that obtained by the direct integration method, and the error analysis results are given in Table 6.

5. Conclusion

By analyzing the composition and characteristics of pushing pose of MSR and middle groove, a fusion evaluation model, which combines the pushing displacement-based least squares straightness and the pushing pose-based straightness of the middle groove, is established for realizing pushing pose alignment. To improve accuracy and reliability in the

straightness evaluation process, a segmented sensing approach based on pushing state pattern recognition is proposed by selecting 4 difference features from typical IMU data features. The selected features are used for SVM training. The trained model can effectively recognize the pushing state pattern of MSR. To test and analyze the feasibility of proposed approach, a pose sensing experiment platform is built, and different motion stages of MSR are verified by experiments. Results show that estimation errors are significantly reduced compared with the traditional algorithm.

Data Availability

The data generated or analyzed during this study are included within the article and are available from the corresponding author upon request.

Conflicts of Interest

The authors declare that they have no conflicts of interest.

Acknowledgments

This work was supported by part of the National Natural Science Foundation of China (52004034), the Science and Technology Research Program of Chongqing Municipal Education Commission (KJQN202101413), Nature Science Research Key Project of Suzhou University (2017ydz14 and 2019ydz03), and the Natural Science Research Project in Universities of Anhui Province in China (KJ2021A1115).

References

- [1] D. L. Wang, X. T. Zeng, G. F. Wang, and R. Li, "Stability of a face guard in a large mining height working face,"

- International Journal of Simulation Modelling*, vol. 20, no. 3, pp. 547–558, 2021.
- [2] X. T. Zeng, G. Y. Meng, and J. H. Zhou, “Analysis on the pose and dynamic response of hydraulic support under dual impact loads,” *International Journal of Simulation Modelling*, vol. 17, no. 1, pp. 69–80, 2018.
 - [3] Y. Zhang, H. Zhang, K. Gao, W. Xu, and Q. Zeng, “New method and experiment for detecting relative position and posture of the hydraulic support,” *IEEE Access*, vol. 7, Article ID 181842, 2019.
 - [4] H. Tu, S. Tu, Y. Yuan, F. Wang, and Q. Bai, “Present situation of fully mechanized mining technology for steeply inclined coal seams in China,” *Arabian Journal of Geosciences*, vol. 8, no. 7, pp. 4485–4494, 2015.
 - [5] A. Boutrid, M. C. Djouamaa, M. Chettibi, A. Bouhedja, and K. Talhi, “Design of a model powered support system in Kenadsa mine (Algeria),” *Journal of Mining Science*, vol. 52, no. 1, pp. 78–86, 2016.
 - [6] K. Gao, W. Xu, H. Zhang, Y. Zhang, Q. Zeng, and L. Sun, “Relative position and posture detection of hydraulic support based on particle swarm optimization,” *IEEE Access*, vol. 8, Article ID 200789, 2020.
 - [7] X. Lu, Z. Wang, H. Yan, L. Si, and C. Tan, “Optimization design of pushing distance estimation of hydraulic support using the Kalman filter with the covariance improvement,” *Advances in Mechanical Engineering*, vol. 11, no. 5, Article ID 168781401985072, 2019.
 - [8] X. Ge, J. Xie, X. Wang, Y. Liu, and H. Shi, “A virtual adjustment method and experimental study of the support attitude of hydraulic support groups in propulsion state,” *Measurement*, vol. 158, Article ID 107743, 2020.
 - [9] S. Li, J. Xie, F. Ren, X. Zhang, X. Wang, and B. Wang, “Virtual straightening of scraper conveyor based on the position and attitude solution of industrial robot model,” *International Journal of Coal Science & Technology*, vol. 8, no. 5, pp. 1149–1170, 2021.
 - [10] S. Li, J. Xie, X. Wang, F. Ren, X. Zhang, and Q. Bao, “Path planning of hydraulic support pushing mechanism based on extreme learning machine and descartes path planning,” *Symmetry*, vol. 13, no. 1, p. 97, 2021.
 - [11] X. Wang, S. Li, and J. Xie, “Straightening method of scraper conveyor driven by robot kinematics and time series prediction,” *Journal of China Coal Society*, vol. 46, no. 2, pp. 652–666, 2021.
 - [12] X. Yang, R. Wang, and H. Wang, “Pose measurement of detection robot IN hydraulic support based on motion process restoration method,” *Journal of Taiyuan University of Technology*, vol. 51, no. 02, pp. 162–170, 2020.
 - [13] X. Zhang, D. Wang, and W. Yang, “Position detection method of hydraulic based on visual measurement,” *Industrial and mining automation*, vol. 45, no. 03, pp. 56–60, 2019.
 - [14] H. Chen, H. Chen, Y. Xu, D. Zhang, Y. Ma, and J. Mao, “Research on attitude monitoring method of advanced hydraulic support based on multi-sensor fusion,” *Measurement*, vol. 187, Article ID 110341, 2022.
 - [15] X. Yang, R. Wang, H. Wang, and Y. Yang, “A novel method for measuring pose of hydraulic supports relative to inspection robot using LiDAR,” *Measurement*, vol. 154, Article ID 107452, 2020.
 - [16] M. Liang, X. Fang, S. Li, G. Wu, M. Ma, and Y. Zhang, “A fiber Bragg grating tilt sensor for posture monitoring of hydraulic supports in coal mine working face,” *Measurement*, vol. 138, pp. 305–313, 2019.
 - [17] B. Wang, J. Xie, X. Wang, S. Liu, and Y. Liu, “A new method for measuring the attitude and straightness of hydraulic support groups based on point clouds,” *Arabian Journal for Science and Engineering*, vol. 46, no. 12, Article ID 11739, 2021.
 - [18] S. Wang, Y. He, and S. Wang, “Study on the alignment method and experiment of scraper conveyor,” *Journal of China Coal Society*, vol. 42, no. 11, pp. 3044–3050, 2017.
 - [19] Z. Meng, Q. Zeng, and L. Wan, “Pose adjusting simulation of hydraulic support based on mechanical-electrical-hydraulic coordination,” *Tehnički Vjesnik*, vol. 25, no. 4, pp. 1110–1118, 2018.
 - [20] J. Xie, X. Wang, Z. Yang, and S. Hao, “Virtual monitoring method for hydraulic supports based on digital twin theory,” *Mining Technology*, vol. 128, no. 2, pp. 77–87, 2019.
 - [21] J. Xie, X. Wang, Z. Yang, and S. Hao, “Attitude-aware method for hydraulic support groups in a virtual reality environment,” *Proceedings of the Institution of Mechanical Engineers - Part C: Journal of Mechanical Engineering Science*, vol. 233, no. 14, pp. 4805–4818, 2019.
 - [22] J. Wang, Z. Wang, J. Xu, C. Tan, and L. Si, “Moving distance measurement for hydraulic support based on fruit fly optimization algorithm,” *Optical Engineering*, vol. 56, no. 1, Article ID 013111, 2017.
 - [23] X. Lu, Z. Wang, C. Tan, H. Yan, L. Si, and D. Wei, “A portable support attitude sensing system for accurate attitude estimation of hydraulic support based on unscented kalman filter,” *Sensors*, vol. 20, no. 19, p. 5459, 2020.
 - [24] J. Wen and Z. Lian, “The communication protocol design of electro-hydraulic control system for hydraulic supports at coal mine,” *Web Information Systems and Mining*, vol. 6987, pp. 73–78, 2011.
 - [25] X. Zhang, P. Xia, Y. B. Cui, Y. Q. Liu, X. X. Liu, and Y. Y. Wang, “Software and hardware design of signal acquisition system about electro-hydraulic control system of hydraulic support,” *Advanced Materials Research*, vol. 889–890, pp. 906–910, 2014.

Research Article

Vision-Based Mobile Manipulator for Handling and Transportation of Supermarket Products

Muhammad Zia Ur Rahman ¹, Muhammad Usman,¹ Adhban Farea ^{2,3}, Nasir Ahmad,¹ Imran Mahmood,¹ and Muhammad Imran¹

¹Department of Mechanical, Mechatronics and Manufacturing Engineering, University of Engineering and Technology Lahore, Faisalabad Campus, Faisalabad 38000, Pakistan

²Department of Civil Engineering, Ibb University, Ibb, Yemen

³Department of Civil Engineering, The University of Lahore, Lahore, Pakistan

Correspondence should be addressed to Muhammad Zia Ur Rahman; ziaurrahman@uet.edu.pk and Adhban Farea; eng.adhban@gmail.com

Received 10 March 2022; Revised 14 April 2022; Accepted 5 May 2022; Published 6 June 2022

Academic Editor: Conghu Liu

Copyright © 2022 Muhammad Zia Ur Rahman et al. This is an open access article distributed under the Creative Commons Attribution License, which permits unrestricted use, distribution, and reproduction in any medium, provided the original work is properly cited.

Robot manipulators are growing more widely employed in the retail market, mostly for warehousing, but automating them in-store logistics processes is still a difficult task. Supermarkets and large retail stores face many challenges: shortages, handling, and placement of a single product on shelves. Various issues needed to be considered to develop a robot which can manipulate products of different sizes, shapes, and weight in limited spaces on shelves. The aim of this article is to design and develop a system to address the issues of shortage, identification, moving, and placements of products in supermarkets by properly incorporating database, camera vision, and line following mobile manipulator. A four-wheeled differential drive mobile robot was designed and developed which has a 5 DOF robotic manipulator on it. The line following technique is used to move it around the warehouse. The barcode recognition technique for the localization of product sections and object detection using SIFT is successfully and efficiently employed. The demonstration of the usefulness of the method was shown by carrying out experiments in a relevant environment which imitates a real supermarket.

1. Introduction

The customer experience and comfort have been improved by the implementation of automation techniques at retail shops. A major example is the Amazon Go shops. On the other hand, automated solutions are still limited in the logistics processes of retail stores of the supermarket industry specifically, in Pakistan. The supermarket industry is widely expanding in Pakistan, while being the fact that it still has not achieved the top-notch advancement. There are many areas of advancement and improvement in it following the problems and complications exist in it. One of those problems is the tracking of products on the shelves which are short as well as to put them right in their place on shelves. As the size of supermarkets and number of products increases, it becomes difficult for humans to manage.

Various commercial mobile robots can be used to monitor shelves for inventory management automatically by choosing diverse technologies, such as radio-frequency identification antennas in the Stockbot or the cameras in the Bossa Nova 2020, Tally 3.0, and LoweBot [1]. Another depalletizing-based automated process uses recent artificial intelligence solutions like the Photoneo Depal [2]. Recently, some control solutions based on artificial intelligence approaches have also been presented [3]. A new depalletizer which was able to manage not only boxes but also varied pallets has been proposed in [4].

The inventory management and unloading solutions are already in the market, whereas other in-store automated processes, such as transporting items from the warehouse to the retail store and shelf restocking, can still be taken as emerging technologies. This is a great demand from retailers

due to the high costs of in-store logistics, up to 60% of the entire functioning store costs [5]. Fierce market competition has led to a decline in profits and high labor costs make it difficult to ensure that there is enough staff to handle all the work in a store [1].

The shelf refill is the most time-taking task with 50% of such of the time is committed in finding the proper slot on the shelf. Very few research literature is available on this particular automation issue such as in [6–8]. Most of the research issues are relevant to the convenience store robotic challenge which was launched by the World Robotic Summit [9]. The solutions are mainly based on the usage of vacuum grippers; therefore, they are applicable only in those situations where pick-and-place and grasp poses are similar. Whereas, the shelf refill objective in an actual environment may require cultured skills of manipulation. The REFILLS (robotic enabling fully integrated logistics lines for super-market) [10] presented a software architecture which implements the shelf replenishment with a comparable speed of human. It also incorporated the KnowRob [11] based task-planning framework.

The current article's contribution is focused on the lower hierarchical level. It comprises of a 7-DOF mobile manipulator prototype that is integrated with a supermarket database system. The proposed system also features a graphical user interface (GUI) for experimentation. A camera vision is also included with the mobile manipulator. As a result of the billing, the supermarket database will be updated. Whenever a product is billed, the system will infer from the database that the product is out of stock. This data will be passed on to the mobile manipulator. After receiving the information, the mobile manipulator will grab the product from the supermarket's warehouse and position it on the shelf where it belongs.

Wireless connection between the database and the mobile manipulator is not used at this time for the sake of simplification. For the purposed system, a laptop will be kept on the mobile manipulator. This laptop will include a database and a graphical user interface. After placing the product in its proper location, the mobile manipulator will also update the database. As a result, the database and the mobile manipulator will be able to communicate in both directions.

1.1. Literature Review. The first steps of any pick-and-place task are object detection and localization. DenseFusion [12] and PoseCNN [13], two of the most current and advanced localization approaches, are nevertheless insufficient for the in-hand maneuvers detailed in this article. The integration of camera vision with a robotic manipulator is a key aspect of our research. Camera vision may be used to identify and regulate the motion of a robotic manipulator, and it can also be used to improve the performance of a robotic manipulator. The proper operation and use of camera vision is fully dependent on determining the point of application. Because determining the point of application, which functions as an input for the system, is required when controlling a robotic manipulator based on its inverse

kinematics. However, it is just necessary to specify the settings and specifications for a robot to automatically classify and stow goods [14, 15].

Other than determining the point of application, another component of camera vision is the scanning of barcodes. This domain also has a substantial amount of work [16]. Numerous strategies for barcode detection using camera vision have been developed over the years [17, 18], and many methods and techniques for improving the barcode detection process have been implemented [19].

A great deal of study has also been done in relation to warehouse and inventory management systems and their various components [20–29]. The design of the mobile robot and mobile manipulator is critical in this project because proper and error-free design leads to the project's error-free operation. Many recent and old publications [15, 30, 31] propose novel techniques to kinematic modelling and comprehensive design of robot manipulators.

The kinematic analysis of robot manipulators is a topic of debate in a number of classic literature [32, 33]. Peter Corke created a software programme and MATLAB library for kinematic and dynamic design and calculations, which has become the industry standard [34]. Koyuncu and Guzel provided a software package called MSG that is used to test the behavior of robot motion [35]. They established a way for solving the kinematics of the *Lynx* 6d of Robot and proposed a method for solving the kinematics of the *Lynx* 6d of Robot. To address the kinematics of the AL5B Robot arm, Qassem et al. proposed a software package [36]. More analysis have been achieved for modeling a 6DOF robotic manipulators using the MATLAB software for the purpose of their design, simulation, and analysis by Iqbal et al., Kumar et al., and Singh et al. [37–39].

2. Methodology

To solve abovementioned problems, we developed a system which incorporates the basic components of the system which are mobile manipulator, microcontroller, database, and GUI in a way to timely track down the shortage of products on shelves. Database carries the information about all the products, their barcodes, their optimum quantity, and their actual quantity in warehouse as well as in supermarkets. The database management system is connected to the billing system in practice. However, for the purpose of simplicity, we developed a GUI in place of billing system. The GUI will be used to reduce the number of products from the database. The reduction in the number of products from GUI, then from database will result in the prompt tracking of short products from shelves. It means the system will no sooner have information of shortage of a product than the billing of that product. However, this is a part of usual supermarket management nowadays.

After the information of shortage, the next step is to assess the availability of that product in the warehouse. It has been mentioned above that database also includes information of barcode all products and the quantity of that product in warehouse. It should be kept in mind that, the shortage here does not imply that the products are also

unavailable in the warehouse. Database will check if the product is available in the warehouse. If its checking results are positive, the system will communicate to the mobile manipulator. Mobile manipulator, which is included by a microcontroller, will be informed by the information of short products and their barcodes.

The locations of different products with different barcodes are known in the warehouse as well as in supermarket by microcontroller. Microcontroller will travel toward that product in the warehouse by tracing down its location. 5 DOF robotic manipulator will pick up that product. The mobile robot will move toward the location of that product in the supermarket. Robotic manipulator will then put that product right on its place on the shelf.

Here, it must be clear that the line following, barcode scanning, and camera vision techniques will be used for mobile robot path planning, section allocation, and product point determination, respectively.

The mobile manipulator will also provide feedback to the microcontroller in the form of feedback sensors. Moreover, after the microcontroller has completed the task of picking and placing the product in its actual place, it will be required to give this information back to PC, i.e., database. In this way microcontroller and mobile manipulator will have mutual communication. Similarly, microcontroller and PC will have mutual communication. Below, Figure 1 represents the block diagram of proposed methodology, and Figure 2 shows the complete 3D model of robotic manipulator.

2.1. Design Calculations

2.1.1. CAD Model

2.1.2. Design of the Mobile Robot. A mobile robot is a four-wheeled vehicle with differential drive. All considerations are made in calculations according to differential drive principles. Design calculations of mobile robot include the velocity and torque calculations of motor, choice of drive mechanism for mobile robot, and its calculations and choice of motors according to above calculations.

2.1.3. Velocity Calculations. Velocity calculations are the calculations of motor angular velocity in context of desired velocity of mobile robot, which is as follows:

$$\begin{aligned} \text{Desired velocity of mobile robot} &= v \\ &= 0.2 \frac{m}{s}, \end{aligned} \quad (1)$$

$$\begin{aligned} \text{Radius of Wheel} &= r \\ &= 0.05m. \end{aligned}$$

We know that,

$$v = r\omega, \quad (2)$$

where, ω is the required angular velocity of motor

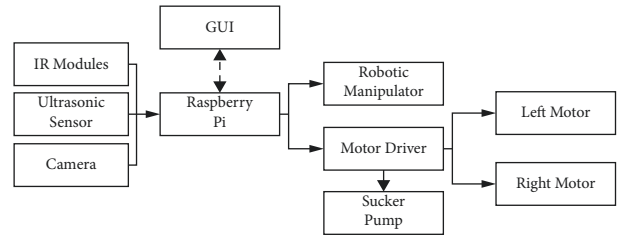


FIGURE 1: Block diagram of the proposed methodology.

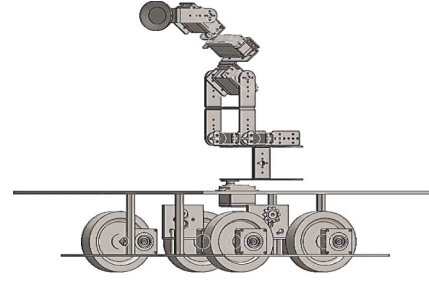


FIGURE 2: Complete 3D model of the prototype.

$$\begin{aligned} \omega &= \frac{v}{r} \\ &= \frac{0.2}{0.05} \\ &= 4Hz. \end{aligned} \quad (3)$$

After unit conversion to RPM:

$$\omega = 240\text{RPM}. \quad (4)$$

It means that both motors of mobile robot should have an angular velocity of 240 RPM or greater.

2.1.4. Torque Calculations for the Mobile Base. In this section, torque requirement of motor will be calculated. For that, we will use the techniques of statics. The first step is to draw a free body diagram.

It can be seen in the free body diagram Figure 3 that the weight of whole mobile manipulator, camera, and laptop is assumed at the center. Due to existence of two motors, these forces are multiplied by 2. Now, we will apply conditions of static systems to evaluate forces:

$$\sum F_Y = 0: 2N_A + 2N_B - mg = 0, \quad (5)$$

$$\sum M_B = 0: -2N_A(133.56) + mg(66.78) = 0. \quad (6)$$

From (16), we have the following:

$$N_A = \frac{mg}{4}. \quad (7)$$

Putting it in (15) results in the below:

$$N_B = \frac{mg}{4}. \quad (8)$$

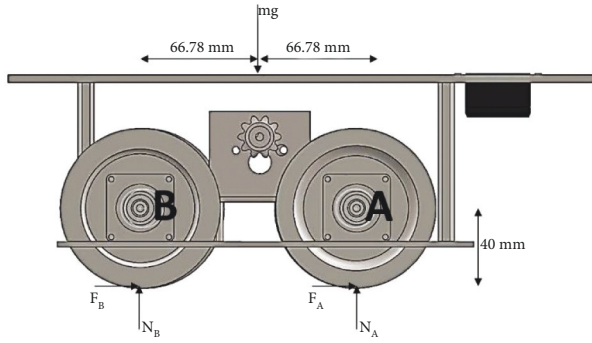


FIGURE 3: FBD of a mobile manipulator.

Which means that both normal forces are equal, i.e.,

$$\begin{aligned} N &= N_A \\ &= N_B \\ &= \frac{mg}{4}. \end{aligned} \quad (9)$$

We know the radius of wheel, so we can find the torque of motor required as follows:

$$\begin{aligned} T &= Nr \\ &= \frac{mgr}{4} \\ &= 6 \times 9.81 \times \frac{0.05}{4} \\ &= 0.735Nm. \end{aligned} \quad (10)$$

It means that both motors must have a torque of at least 1.47 Nm.

2.1.5. Selection of Motors. The choice of motor of the mobile robot is very important in design calculation due to the fact that incorrect choice can lead a great loss in term of cost and performance. We are using DC gear motors due to following reasons:

- (1) DC motors are available with required torque and speed parameters.
- (2) DC motors are preferred over encoded DC motors due to the fact that we do not require high accuracy because we are using line following technique.
- (3) DC gear motors are good for high load and torque applications.

2.1.6. Drive Mechanism. Drive mechanism allows for the proper transmission of power from a powered wheel to a powerless wheel. There are three types of drive mechanisms commonly used:

- (1) Belt drives
- (2) Chain drives

(3) Gear drives

We are using chain mechanism due to following reasons:

- (1) Chain drive offers zero slip unlike belt and gear drives.
- (2) Chain drives are more stable than belt and gear drives.
- (3) Chain drives are highly efficient in power transmission.
- (4) Chain drives are compact in size and easy to install.

2.1.7. Design of a Robotic Manipulator. We are using a 5 DOF robotic arm in our project. All of its joints are revolute. Therefore, it can be said that it is kind of an articulated manipulator.

2.1.8. Torque Calculations. In the articulated manipulator, the torques of the joints having rotations about x -axis are important to find. Due to the downward act of gravitational force (weight) of the links, the links with the rotation about x -axis will have some natural torque. In order to resist the downward force acting on the links plus to lift the payload, the required torques for the motors will be calculated.

To calculate the torques of the motors, the worst condition is considered, i.e., the robotic arm is considered to be placed horizontal. Now, the torque required to lift the corresponding link with load will be maximum as shown in Figure 4.

From the figure, we are only interested to find the maximum torques about points S , E , and R , respectively. Where $W_1, W_2, W_3, W_4, W_5, W_6,$ and W_7 are the masses of the links at different points.

$$\begin{aligned} \text{Maximum Payload} &= A \\ &= 0.15kg, \\ W_1 &= 0.04kg, \\ W_3 &= 0.08kg, \\ W_4 &= 0.02kg, \\ W_6 &= 0.16kg, \\ W_7 &= 0.12kg. \end{aligned} \quad (11)$$

Using second condition of equilibrium, required torque of motor about point 'S' is as follows:

$$\begin{aligned} \tau_s &= (39.8 * 0.15) + (32.3 * 0.12) + (24.8 * 0.16) \\ &\quad + (17.8 * 0.02) + (12.5 * 0.08) + (5.25 * 0.04) \\ &= 15.38kg - cm. \end{aligned} \quad (12)$$

Similarly, required torque of motor about point 'E' is as follows:

$$\begin{aligned} \tau_E &= (29.3 * 0.15) + (21.8 * 0.12) + (14.3 * 0.16) \\ &\quad + (7.3 * 0.02) + (2 * 0.08) = 9.605kg - cm. \end{aligned} \quad (13)$$

For elbow, required torque of motor about point 'R' is as follows:

$$\begin{aligned}\tau_R &= (19.5 * 0.15) + (12 * 0.12) + (4.5 * 0.16) \\ &= 5.085kg - cm.\end{aligned}\quad (14)$$

2.1.9. *Forward Kinematics.* The labeled kinematic diagram of robotic manipulator is shown in Figure 5. The forward kinematics calculations start with the labeling of kinematic diagram according to DH method, basic rules of which are as follows:

- (i) Direction of z -axis is toward of the joint axis.
- (ii) x -axis is parallel to the common normal.

As shown in Table 1, there are four DH-parameters a , d , α and θ . These parameters are designated according to following rules:

- (i) θ_i is the angle from x_{i-1} to x_i along z_{i-1} ; For revolute joint θ_i is variable.
- (ii) d_i is the distance from the intersection of z_{i-1} with x_i to the origin of $(i-1)$ system of axes; For prismatic joint d_i variable.
- (iii) a_i is the shortcut between z_{i-1} and z_i .
- (iv) α_i is the angle from z_{i-1} to z_i along x_i .

The general transformation matrix is as follows:

$$\begin{aligned}T_{i-1}^i &= \begin{bmatrix} c_i & -c_{\alpha_i} \cdot s_i & s_{\alpha_i} \cdot s_i & a \cdot c_i \\ s_i & c_{\alpha_i} \cdot c_i & -s_{\alpha_i} \cdot c_i & a \cdot s_i \\ 0 & s_{\alpha_i} & c_{\alpha_i} & d_i \\ 0 & 0 & 0 & 1 \end{bmatrix}, \\ T_0^1 &= \begin{bmatrix} c_1 & 0 & -s_1 & 0 \\ s_1 & 0 & c_1 & 0 \\ 0 & -1 & 0 & l_1 \\ 0 & 0 & 0 & 1 \end{bmatrix}, \\ T_{12} &= \begin{bmatrix} c_2 & -s_2 & 0 & l_2 \cdot c_2 \\ s_2 & c_2 & 0 & l_2 \cdot c_3 \\ 0 & 0 & 1 & 0 \\ 0 & 0 & 0 & 1 \end{bmatrix}, \\ T_3^2 &= \begin{bmatrix} c_3 & 0 & -s_3 & l_3 \cdot c_l \\ s_3 & 0 & c_3 & l_3 \cdot c_3 \\ 0 & -1 & 0 & 0 \\ 0 & 0 & 0 & 1 \end{bmatrix}, \\ T_3^4 &= \begin{bmatrix} c_4 & 0 & s_4 & 0 \\ s_4 & 0 & -c_4 & 0 \\ 0 & 1 & 0 & l_4 \\ 0 & 0 & 0 & 1 \end{bmatrix}, \\ T_4^5 &= \begin{bmatrix} c_5 & -s_5 & 0 & 0 \\ s_5 & c_5 & 0 & 0 \\ 0 & 0 & 1 & 0 \\ 0 & 0 & 0 & 1 \end{bmatrix}, \\ T_0^5 &= T_0^1 \cdot T_1^2 \cdot T_2^3 \cdot T_3^4 \cdot T_4^5, \\ T_0^5 &= \begin{bmatrix} c_5(c_4(c_1c_2c_3 - c_1s_2s_3) + s_1s_4) - s_5(c_1c_2s_3 + c_4s_3) & c_5(c_4(c_1c_2c_3 - c_1s_2s_3) + s_1s_4) - c_5(c_1c_2s_3 + c_1s_2c_3) & s_4(c_1c_2c_3 - c_1s_2s_3) - s_1c_4 & c_1(l_2c_2 + l_3c_23 - l_4s_23) \\ c_5(c_4(s_1c_2c_3 - s_1s_2s_3) - c_1s_4) - s_5(s_1c_2s_3 + s_1s_2c_3) & c_5(c_4(s_1c_2c_3 - s_1s_2s_3) - c_1s_4) - c_5(s_1c_2s_3 + s_1s_2c_3) & c_1c_4 + s_4(s_1c_2c_3 - s_1s_2s_3) & s_1(l_2c_2 + l_3c_23 - l_4s_23) \\ & (-c_23 \cdot s_5) - (s_23 \cdot c_4 \cdot c_5) & (s_23 \cdot c_4 \cdot c_5) - (c_23 \cdot c_5) & -s_23 \cdot s_4 \cdot l_1 & -l_2s_2 - l_3s_23 - l_4c_23 \\ & 0 & 0 & 0 & 1 \end{bmatrix}.\end{aligned}\quad (15)$$

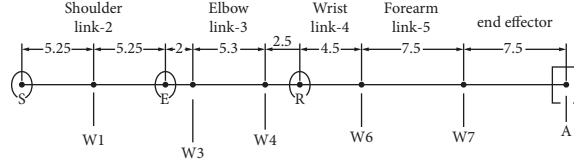


FIGURE 4: FBD of robotic manipulator for torque calculations.

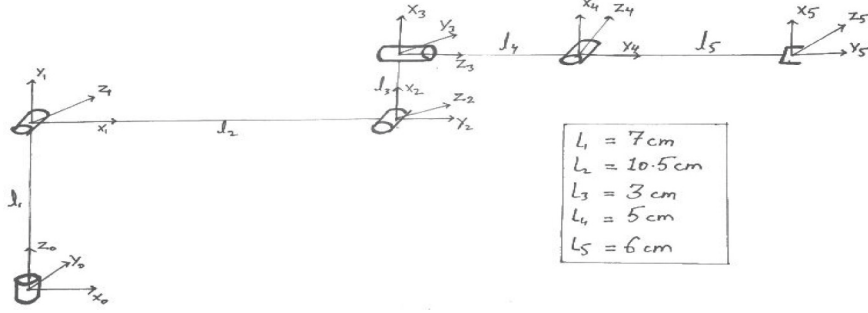


FIGURE 5: Labeled kinematic diagram of the robotic manipulator.

TABLE 1: DH table.

Link	α_i	\mathbf{a}_i	\mathbf{d}_i	θ_i
1	-90	0	l_1	θ_1
2	0	l_2	0	θ_2
3	-90	l_3	0	θ_3
4	90	0	l_4	θ_4
5	0	0	0	θ_5

Gripper's position is defined by the p_5 vector while orientation defined by x_5, y_5, z_5 vectors provided by the forward kinematics:

$$P_5 = \begin{bmatrix} c_1(l_2c_2 + l_3c_{23} - l_4s_{23}) \\ s_1 \begin{pmatrix} l_2c_2 + l_3c_{23} - l_4s_{23} \\ l_1 - l_2s_2 - l_3s_{23} - l_4c_{23} \end{pmatrix} \end{bmatrix}, \quad (16)$$

$$x_5 = \begin{bmatrix} c_5(c_4(c_1c_2c_3 - c_1s_2s_3) + s_1s_4) - s_5(c_1c_2s_3 + c_4s_3) \\ c_5(c_4(s_1c_2c_3 - s_1s_2s_3) - c_1s_4) - s_5(s_1c_2s_3 + s_1s_2c_3) \\ (-c_{23} \cdot s_5) - (s_{23} \cdot c_4 \cdot c_5) \end{bmatrix}, \quad (17)$$

$$y_5 = \begin{bmatrix} c_5(c_4(c_1c_2c_3 - c_1s_2s_3) + s_1s_4) - c_5(c_1c_2s_3 + c_1s_2c_3) \\ c_5(c_4(s_1c_2c_3 - s_1s_2s_3) - c_1s_4) - c_5(s_1c_2s_3 + s_1s_2c_3) \\ (s_{23} \cdot c_4 \cdot c_5) - (c_{23} \cdot c_5) \end{bmatrix}, \quad (18)$$

$$z_5 = \begin{bmatrix} c_1c_2c_3 - c_1s_2s_3 - s_1c_4 \\ s_4(c_1c_4 + s_4(s_1c_2c_3 - s_1s_2s_3) - s_{23}s_4) \end{bmatrix}. \quad (19)$$

2.1.10. Inverse Kinematics. Solution to the inverse kinematics problem is reduced to the calculation of the arguments $\theta_1, \theta_2, \theta_3, \theta_4, \theta_5$ based on the gripper's position and

orientation. These six equations in five unknowns may have no solution, though it is possible to consider it for some instances [40]. Equations (16)–(19) can be rewritten in the following forms:

$$x_5x = c_5(c_4(c_1c_2c_3 - c_1s_2s_3) + s_1s_4) - s_5(c_1c_2s_3 + c_4s_3), \quad (20)$$

$$x_5y = c_5(c_4(s_1c_2c_3 - s_1s_2s_3) - c_1s_4) - s_5(s_1c_2s_3 + s_1s_2c_3), \quad (21)$$

$$x_5z = (-c_{23} \cdot s_5) - (s_{23} \cdot c_4 \cdot c_5), \quad (22)$$

$$y_5x = c_5(c_4(c_1c_2c_3 - c_1s_2s_3) + s_1s_4) - c_5(c_1c_2s_3 + c_1s_2c_3), \quad (23)$$

$$y_5y = c_5(c_4(s_1c_2c_3 - s_1s_2s_3) - c_1s_4) - c_5(s_1c_2s_3 + s_1s_2c_3), \quad (24)$$

$$y_5z = (s_{23} \cdot c_4 \cdot c_5) - (c_{23} \cdot c_5), \quad (25)$$

$$z_5x = s_4(c_1c_2c_3 - c_1s_2s_3) - s_1c_4, \quad (26)$$

$$z_5y = c_1c_4 + s_4(s_1c_2c_3 - s_1s_2s_3), \quad (27)$$

$$z_5z = -s_{23} \cdot s_4, \quad (28)$$

$$P_5x = c_1(l_2c_2 + l_3c_{23} - l_4s_{23}), \quad (29)$$

$$P_5y = s_1(l_2c_2 + l_3c_{23} - l_4s_{23}), \quad (30)$$

$$P_5z = l_1 - l_2s_2 - l_3s_{23} - l_4c_{23}. \quad (31)$$

θ_1 can be evaluated using (29) and (30) straightforwardly:

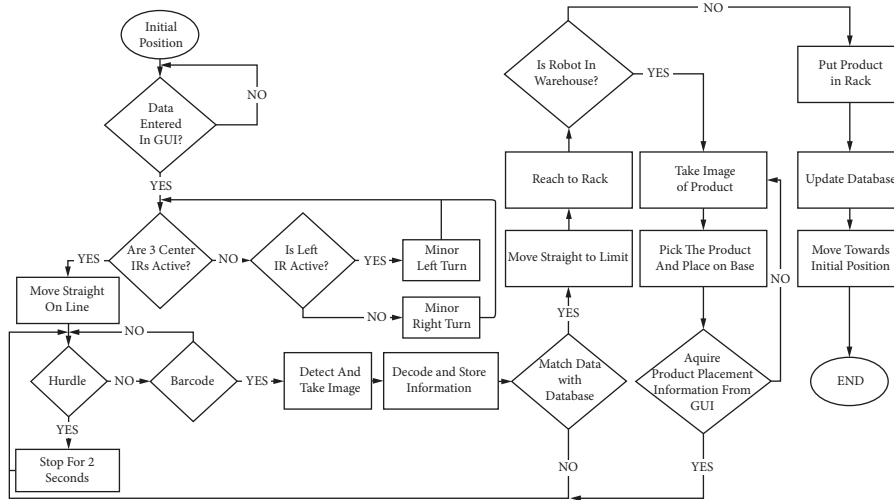


FIGURE 6: Work flow diagram.

$$\theta_1 = \tan^{-1} \frac{P_{5y}}{P_{5x}}. \quad (32)$$

To evaluate θ_2 and θ_3 , we used the geometric method:

$$\theta_2 = 90 - (\varnothing_1 + \varnothing_2), \quad (33)$$

where values of \varnothing_1 and \varnothing_2 can be evaluated as follows:

$$\varnothing_1 = \cos^{-1} \left(\frac{l_3^2 - l_2^2 - r_3^2}{-2l_2r_3} \right),$$

$$\varnothing_2 = \tan^{-1} \left(\frac{r_2}{r_1} \right),$$

$$r_1 = \sqrt{P_x^2 + P_y^2}, \quad (34)$$

$$r_2 = P_z - l_1,$$

$$r_3 = \sqrt{r_1^2 + r_2^2},$$

$$\theta_3 = 180 - \varnothing_3,$$

where

$$\varnothing_3 = \cos^{-1} \left(\frac{r_3^2 - l_2^2 - l_3^2}{-2l_2l_3} \right). \quad (35)$$

From (28),

$$\theta_4 = -\frac{z_{5z}}{s_{23}},$$

$$\theta_5 = \cos^{-1} \left(\frac{y_{5z}}{s_{23}c_4 - c_{23}} \right). \quad (36)$$

2.1.11. Work Flow Diagram. As mentioned in previous sections, all important components and aspects of the project were made functional. Line follower robot, 5 DOF

robotic manipulator, camera vision, GUI, and various peripheral components of these components were significant components of the project. Important portions and systems of the project, such as barcode identification, object detection, and inverse kinematics, were combined with these components. The project was made to function according to the flow diagram illustrated in Figure 6, after all project components and systems were integrated. This flow diagram depicts the project's whole operation after it has been integrated.

3. Experiments and Results

3.1. Development Stages and Final Stage. The development stages and final stage of the proposed model are given in Figures 7 and 8, respectively.

3.2. Implementation of the Barcode Recognition Technique. For section tracking of warehouse and supermarket, we used barcodes as a visual marker. These markers guided the robot toward the location of items. Each section had its different barcode on its front. OpenCV library was used to access the camera. Barcode and QRcode detection and decoding were done by using the pyzbar library with OpenCV. It first reads the image using cv2.imread(). After reading the image, it decodes the image using pyzbar.decode() and extracts the bounding box (x, y) coordinates from the barcode data, enabling us to localize and determine where the barcode in the input image is. It draws a rectangle around the barcode with OpenCV rect function and also puts a decoded text on the image or scene. Our mobile base robotic arm operates on Raspberry Pi B3. We implemented this technique on Raspberry Pi by using a Pi camera. The flowchart in Figure 9 shows the methodology of a barcode recognition technique and results of barcode recognition are shown in Figure 10.

3.3. Object Detection Using SIFT. To overcome the shortage challenges of products in supermarket, we used a vision assisted robotic arm with mobile base. Vision is



FIGURE 7: Development stages of the model.

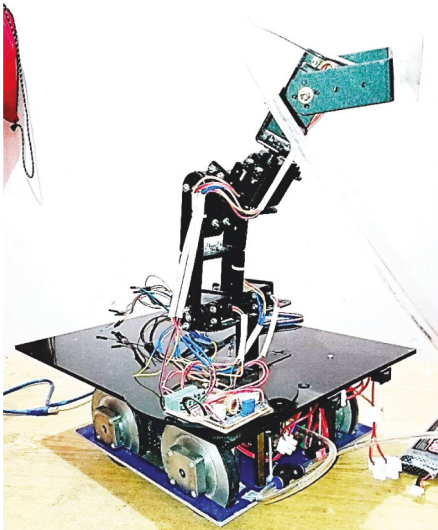


FIGURE 8: Final stage of the model.

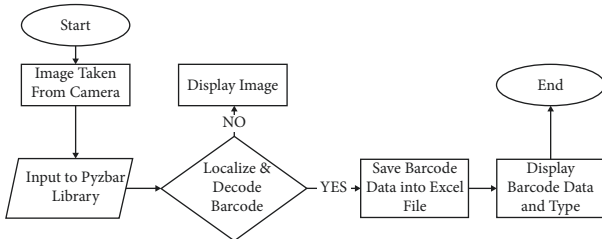


FIGURE 9: Flowchart of methodology of barcode recognition.

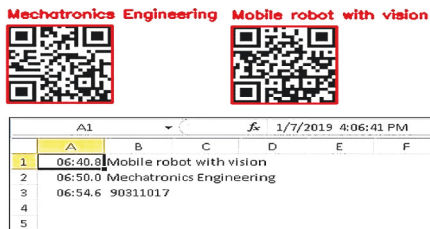


FIGURE 10: Results of barcode recognition.

incorporated with a robotic arm to pick objects from the warehouse and place them in their respective shelves in the supermarket. To detect and recognize different object detection algorithm like SIFT, SURF, and ORB can be used. Scale invariant feature transform (SIFT) is used in our project because it is robust and invariant to scaling and lightning conditions. The flowchart diagram of object detection using SIFT is shown in Figure 11.

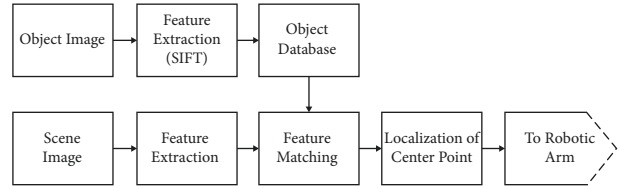


FIGURE 11: Flowchart of object detection using SIFT.

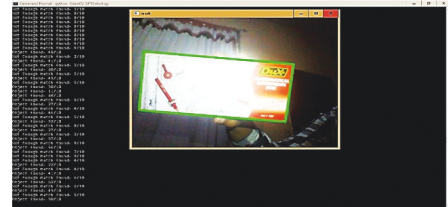


FIGURE 12: Object detection using SIFT before center point calculation.



FIGURE 13: Object detection using SIFT after center point calculation.

To implement the SIFT algorithm in our project, we used openCV version 3.4.2. It is a built in detector in openCV. First, we have to construct a SIFT object using `cv.xfeatures2d.SIFT_create()`. After this, SIFT will detect key points of target object. OpenCV provides `cv2.compute()` which computes the descriptors from the key points. We have key points and descriptors of the target image.

We repeat the same process for the scene image. We get the descriptor vectors of both scene image and target image. Now, we match these two vectors. The minimum Euclidean distance between these two 128 dimensional descriptor vectors will be the best match. For matching brute force and fast library approximation nearest neighbor (FLANN) can be used. The object detection using SIFT before and after center point calculations are given in Figures 12 and 13, respectively.

4. Conclusions

The fixed manipulators on the industry floor have already been developed and established decades ago with great efficiency. The proposed project provided a mobile manipulator which solve many problems faced by today's supermarket and inventory industry. In time placements of products in supermarkets were handled by properly incorporating database, camera vision, mobile manipulator, and Raspberry Pi (Controller). The four-wheeled differential drive mobile robot was designed with line following

capability covered the factory floor area by moving accurately around the warehouse. A 5 DOF robotic manipulator could pick the object effectively with the help of SIFT feature extraction and center point calculation of the object. The barcode recognition technique enabled the identification of product to be placed at right sections in the warehouse. It was done using PYZBAR.

In spite of its good results, many advanced features and desired components could not be introduced due to financial and time limitations.

The future recommendations will likewise focus on addressing the issues. To eliminate interaction with humans on the ground, a line follower robot could be replaced by an overhead transit system. It will significantly increase the speed of the entire operation. There are a variety of additional ways that can be used in this situation. Redevelopment of the product localization process can be done in the future. We urge that additional tests be conducted by replacing the line follower with a SLAM-based navigation system, as we feel that using SLAM-based navigation on a mobile robot can open up new possibilities for the project's functionality.

RFID tags have proven their reliability in the supermarket and product handling applications [41], and they can be used here instead of barcodes to greatly improve results. To improve results, the model of a mobile robot and robotic manipulator can be changed in terms of materials, shape, joints, and actuators. Picking objects in a cluttered environment will be easier with the learning of a robotic manipulator utilizing a neural network. It is the most essential of all future recommendations because it influences the project's main goal.

Aside from these design changes, a significant step forward would be to fully automate this semiautomated system. For example, we used a GUI to perform billing actions in this prototype, but the actual system should be connected to a billing server or database and automatically take inputs from the database. In the future, it is recommended that mobile robots be entirely automated.

Data Availability

There are no explicit data used in the proposed research. All the data are available in the paper.

Conflicts of Interest

The authors declare that they have no conflicts of interest.

References

- [1] R. Bogue, "Strong prospects for robots in retail," *Industrial Robot: The International Journal of Robotics Research and Application*, vol. 46, no. 3, pp. 326–331, 2019.
- [2] "Universal depalletizer." Photoneo, "Accessed: Dec. 2020. [Online]. Available," <https://www.photoneo.com/wp-content/uploads/2020/07/Universal-Depalletizer.pdf>.
- [3] M. Z. U. r. Rahman, M. T. Riaz, M. M. S. A. I. Mahmud, M. Rizwan, and M. A. Choudhry, "The prescribed fixed structure intelligent robust control of an electrohydraulic servo system," *Mathematical Problems in Engineering*, vol. 2022, Article ID 5144602, 12 pages, 2022.
- [4] R. Caccavale, P. Arpentì, G. Paduano et al., "A flexible robotic depalletizing system for supermarket logistics," *IEEE Robotics and Automation Letters*, vol. 5, no. 3, pp. 4471–4476, 2020.
- [5] H. Kuhn and M. G. Sternbeck, "Integrative retail logistics: an exploratory study," *Operations Management Research*, vol. 6, pp. 2–18, 2013.
- [6] J. Winkler, F. B. Benczedi, T. Wiedemeyer et al., "Knowledge-enabled robotic agents for shelf replenishment in cluttered retail environments," in *Proceedings of the 15th International Conference on Autonomous Agents and Multiagent Systems (AAMAS 2016), Singapore*, pp. 1421–1422, May 2016.
- [7] R. Sakai, S. Katsumata, T. Miki et al., "A mobile dual-arm manipulation robot system for stocking and disposing of items in a convenience store by using universal vacuum grippers for grasping items," *Advanced Robotics*, vol. 34, pp. 219–234, 2020.
- [8] S. Okada, N. Koganti, A. Yasuda et al., "Restock and straightening system for retail automation using compliant and mobile manipulation," *Advanced Robotics*, vol. 34, no. 3–4, pp. 235–249, 2020.
- [9] Future convenience store challenge, "World Robotic Summit. Accessed," 2020, <https://worldrobotsummit.org/en/%20wrs2020/challenge/service/fcsc.html>.
- [10] Robotics Enabling Fullyintegrated Logistics Lines for supermarkets, "the REFILLS Project," 2020, <http://www.refills-project.eu/>.
- [11] M. Tenorth and M. Beetz, "Knowrob: a knowledge processing infrastructure for cognition-enabled robots," *The International Journal of Robotics Research*, vol. 32, no. 5, pp. 566–590, 2013.
- [12] C. Wang, D. Xu, Y. Zhu et al., "Densefusion: 6d object pose estimation by iterative dense fusion," in *Proceedings of the 2019 IEEE/CVF Conference on Computer Vision and Pattern Recognition (CVPR)*, pp. 3338–3347, Long Beach, CA, USA, June 2019.
- [13] Y. Xiang, T. Schmidt, V. Narayanan, D. Fox, and PoseCNN, "A Convolutional Neural Network for 6d Object Pose Estimation in Cluttered Scenes," Article ID 00199v3, 2018, <https://arxiv.org/abs/1711.00199>.
- [14] C. J. Lin, J. Shaw, P. C. Tsou, and C. C. Liu, "Vision servo based delta robot to pick-and-place moving parts," in *Proceedings of the IEEE International Conference on Industrial Technology (ICIT)*, March 2016.
- [15] S. Manzoor, R. Ul Islam, A. Khalid, A. Samad, and J. Iqbal, "An open-source multi-DOF articulated robotic educational platform for autonomous object manipulation," *Robotics and Computer-Integrated Manufacturing*, vol. 30, no. 3, pp. 351–362, 2014.
- [16] Z.-Y. Chen and C.-T. Chen, "A remote controlled robotic arm that reads barcodes and handles products," *Inventions*, vol. 3, no. 1, p. 17, 2018.
- [17] K. Pariyar, "Process of detecting barcodes using image processing," *International Journal of Scientific Engineering and Research*, vol. 2, no. 7, 2014.
- [18] S. S. Upasani, A. N. Khandate, A. U. Nikhare, R. A. Mange, and R. V. Tornekar, "Robust algorithm for developing barcode recognition system using webcam," *International Journal of Scientific Engineering and Research*, vol. 7, no. 4, 2016.
- [19] X.-W. Xu, Z. Y. Wang, Y. Q. Zhang, and Y. H. Liang, "A skew distortion correction method for 2D bar code images based on vanishing points," in *Proceedings of the Sixth International*

- Conference on Machine Learning and Cybernetics (ICMLC)*, Hong Kong, Aug2007.
- [20] K. Kamei, K. Shinozawa, T. Ikeda, A. Utsumi, T. Miyashita, and N. Hagita, "Recommendation from robots in a real-world retail shop," in *Proceedings of the International Conference on Multimodal Interfaces and the Workshop on Machine Learning for Multimodal Interaction (ICMI-MLMI)*, Beijing, China, Nov2010.
- [21] R. Li, H. Luo, and Z. Bao, "Based on the Internet of Things the supermarket chain management information system development and safety stock research," in *Proceedings of the 2nd International Conference on Education Technology and Computer (ICETC)*, June2010.
- [22] J. Y. Shiau and M. C. Lee, "A warehouse management system with sequential picking for multi-container deliveries," *Computers & Industrial Engineering*, vol. 58, no. 3, pp. 382–392, 2010.
- [23] B. Yan, Y. Chen, and X. Meng, "RFID technology applied in warehouse management system," in *Proceedings of the ISECS International Colloquium on Computing, Communication, Control, and Management (CCCM)*, Aug2008.
- [24] P. R. Wurman, R. D'Andrea, and M. Mountz, "Coordinating hundreds of cooperative, autonomous vehicles in warehouses," *AI Magazine*, vol. 29, no. 1, p. 9, 2008.
- [25] R. Bogue, "Growth in e-commerce boosts innovation in the warehouse robot market," *Industrial Robot: International Journal*, vol. 43, no. 6, pp. 583–587, 2016.
- [26] A. Causo, Z. H. Chong, R. Luxman, and I. M. Chen, "Visual marker-guided mobile robot solution for automated item picking in a warehouse," in *Proceedings of the IEEE International Conference on Advanced Intelligent Mechatronics (AIM)*. . Sheraton Arabella Park Hotel, July2017.
- [27] B. Chaure and P. Jain, "Development of e-shopping cart with theft control mechanism: No queue," in *Proceedings of the International Conference on Emerging Technological Trends (ICETT)*, Oct2016.
- [28] V. N. Prithvish, S. Agrawal, and J. S. R. Alex, "An IoT-based smart shopping cart using the contemporary barcode scanner Lecture Notes in Electrical Engineering," in *Thalman, D., Subhashini, N., Mohanaprasad, K., Murugan, M. (eds) Intelligent Embedded Systems*, vol. 492, pp. 45–58, Springer, Singapore, 2018.
- [29] X. Shao et al., "Application of a robotic system with mobile manipulator and vision positioning," in *Proceedings of the IEEE International Conference on Advanced Intelligent Mechatronics (AIM)*, Busan, Korea, July 2015.
- [30] T. P. Singh, P. Suresh, and S. Chandan, "Forward and inverse kinematic analysis of robotic manipulators," *International Research Journal of Engineering and Technology (IRJET)*, vol. 4, no. 2, 2017.
- [31] H. A.R. Akkar and A. Najim A-Amir, "Kinematics analysis and modeling of 6 degree of freedom robotic arm from DFROBOT on LabVIEW," *Research Journal of Applied Sciences, Engineering and Technology*, vol. 13, no. 7, pp. 569–575, 2016.
- [32] J. J. Craig, *Introduction to Robotics: Mechanics and Control*, Pearson/Prentice Hall Upper, Saddle River, NJ, USA, 2005.
- [33] M. W. Spong, S. Hutchinson, and M. Vidyasagar, *Robot Modeling and Control*, Wiley, New York, 2006.
- [34] P. Corke, *Robotics, Vision and Control: Fundamental Algorithms In MATLAB® Second, Completely Revised*, Springer, Salmon Tower Building New York City, 2017.
- [35] B. Koyuncu and M. Güzel, "Software development for the kinematic analysis of a lynx 6 robot arm," *International Journal of Computer and Information Engineering (IJCIE)*, vol. 1, no. 6, pp. 1575–2158, 2007.
- [36] M. A. Qassem, I. Abuhadrous, and H. Elaydi, "Modeling and Simulation of 5 DOF educational robot arm," in *Proceedings of the 2nd International Conference on Advanced Computer Control (ICACC)*, March2010.
- [37] J. Iqbal, R. U. Islam, and H. Khan, "Modeling and analysis of a 6 DOF robotic arm manipulator," *Canadian Journal on Electrical and Electronics Engineering*, vol. 3, no. 6, pp. 300–306, 2012.
- [38] K. K. Kumar, D. r. A. Srinath, G. J. anvesh, R. P. sa, and M. suresh, "Kinematic analysis and simulation of 6-DOF KUKAKr5 robot for welding application," *International Journal of Engineering Research in Africa*, vol. 3, no. 2, pp. 820–827, 2013.
- [39] H. Singh, N. Dhillon, and I. Ansari, "Forward and inverse Kinematics Solution for Six DOF with the help of Robotics tool box in matlab," *International Journal of Application or Innovation in Engineering & Management (IJAIEM)*, vol. 4, no. 3, 2015.
- [40] V. N. Iliukhin, K. B. Mitkovskii, D. A. Bizyanova, and A. A. Akopyan, "The modeling of inverse kinematics for 5 DOF manipulator," *Procedia Engineering*, vol. 176, pp. 498–505, 2017.
- [41] G. Roussos, "Enabling RFID in retail," *Computer*, vol. 39, no. 3, pp. 25–30, 2006.

Research Article

Gas Seepage Model and Experiment Based on Bedding Effect of Fractured Coal Body

Kunyun Tian ¹ and Erjian Wei ²

¹School of Resources and Safety Engineering, Henan University of Engineering, Zhengzhou 451191, China

²School of Resource and Environmental Engineering, Wuhan University of Science and Technology, Wuhan 430081, China

Correspondence should be addressed to Kunyun Tian; tky1153@163.com and Erjian Wei; weierjian@wust.edu.cn

Received 24 March 2022; Accepted 15 April 2022; Published 9 May 2022

Academic Editor: Conghu LIU

Copyright © 2022 Kunyun Tian and Erjian Wei. This is an open access article distributed under the Creative Commons Attribution License, which permits unrestricted use, distribution, and reproduction in any medium, provided the original work is properly cited.

Gas drainage is of great significance for the efficient and safe mining in coal mine, in which the coal seam layer bedding has a great influence on it. For obtaining gas permeability characteristics of coal body with the parallel and vertical bedding in fractured coal under the action of stress loading and unloading, experimental research was carried out employing a three-stress-axis simulation device. Experimental results showed that in the stress loading process, the permeability decreased with increasing effective stress; the decrement was initially rapid albeit it slowed later. With the increase of effective stress, the coal sample underwent three stages, namely, crack compaction, elastic deformation, and plastic deformation. In the stress unloading process, the permeability of coal samples increased with decreasing of effective stress, and the increasing trend of permeability was consistent. The degree of fracture compaction of the parallel bedding coal samples after compression was much higher than that of vertical bedding. In the stress-relieved coal seam, gas drainage boreholes should be arranged vertically to the bedding fissure to maximise the gas drainage effect. A group of parallel and vertical bedding gas drainage holes were arranged in the test mine to investigate the drainage effect. Field engineering application also showed that the drilling direction should be perpendicular to the bedding direction as far as possible, so as to improve the gas drainage effect. The research results can provide a reference for the gas drainage borehole layout, thus maximising the gas extraction efficiency and ensuring the sustainability of mine safety production.

1. Introduction

The bedding is widely distributed in the coal seam and determines its stability, especially the gas flow state [1]. The integrity of a coal body is destroyed by bedding fissures; meanwhile, the stress distribution state changes to a great extent [2], and bedding fissures are one of the main controlling factors that determine the strength of a coal body, its deformation, and gas permeability characteristics. Bedding fissures will develop, penetrate, and deform after mining; this has a great influence on the gas seepage and diffusion, directly determining the characteristics of gas migration and accumulation and then greatly affecting the gas drainage of each coal seam. As is known, gas drainage is the most basic technical measure used to control coal mine gas disasters [3], and coal seam permeability is the most important index used

to determine the gas drainage effect [4, 5]. Coal structure is an important index used to determine coal seam permeability. Consequently, gas drainage borehole design, according to the characteristics of different bedding fissures, is essential for improving the gas drainage effect and achieving the best gas drainage.

Research into the influence of coal bedding fissures on permeability has been carried out at home and abroad. Experimental studies of the effect of coal body structure on gas permeability characteristics have been carried out by Huang [6]; research results showed that the effect of coal structure anisotropy on permeability was great and differences in permeability of almost one order of magnitude arose. Research on permeability characteristics of layered natural coal under different loading and unloading has been conducted by Pan et al. [7], and a theoretical model between

fractured coal bedding and the effective stress was established. Using the fluid-solid coupling three-axis servo seepage device with gas coal, a seepage test on two kinds of raw coal samples (parallel and vertical to coal bedding direction) under different stress conditions was carried out by Deng et al. [8]. Results showed that the permeability difference between the two coal samples was mainly caused by the difference of the extent of fracturing in the z -axis direction. Axial effect of multistage loading and unloading on gas seepage in coal body with lower fissure has been conducted by Cen et al. [9], and the results showed that the coal sample goes through three stages of compaction, elastic deformation, and plastic deformation in the process of multistage loading, and the two axial gas permeability decreases with the increase of stress. In the unloading process, the gas permeability in two axial directions was partially recovered. The gas permeability along x -axis of parallel bedding is always greater than that along y -axis of vertical bedding under loading and unloading. A large number of experimental studies on the permeability of coal samples under different bedding conditions have been carried out by Wang et al. [10], Wu et al. [11], and Li et al. [12]; all conclusions showed that coal body bedding affected the permeability characteristics.

All the research results analyse the influence of coal body bedding on gas permeability; these have a certain guiding significance to reasonable gas drainage borehole arrangement. In the actual mining process, a coal body is in a changing stress field [13]. Therefore, it is necessary to examine the gas seepage and failure-deformation characteristics under parallel and vertical bedding directions. For this purpose, large lump coal samples with bedding structures are collected; two different kinds of raw coal samples with parallel and vertical bedding are prepared; and the related research work was carried out in the laboratory. Meanwhile, in order to verify the experimental results, a group of parallel and vertical bedding gas drainage holes were arranged in the test mine to investigate the drainage effect.

2. Experimental Method

2.1. Simulation Experiment System. The independently developed triaxial stress gas permeability simulation experiment device was employed in the experiments, as shown in Figure 1 [14].

2.2. Preparation of Experimental Coal Samples. The coal samples used in this experiment come from the 1,2031 working face in the Xindeng coal mine in Zhengzhou city. The No. 2 coal seam in this coal mine has no obvious geological structural damage in the process of coal forming. This coal seam is a primary structure and is a low-metamorphic rank bituminous coal. The coal seam is mainly horizontally bedded; in addition, the bedding is clearly visible.

The raw samples for the experiment are gained through the following three steps, namely, collection of the large lump coals, coal sample machining in the laboratory, and grinding of the finished product. Collection of the large

lump coal underground involved coring with a rock coring drill along the vertical and parallel to the bedding direction. The grinding of the two ends and the sides of the standard cylindrical samples ensured an unevenness of less than 0.02 mm. Finally, the standard coal sample measured $\Phi 50 \text{ mm} \times 100 \text{ mm}$. The production process of the coal sample was shown in Figure 2.

Two coal samples with parallel bedding were selected, marked as P1 and P2. Meanwhile, the other two coal samples with vertical bedding were selected, marked as V1 and V2. The two types of coal samples are shown in Figure 3.

3. Calculation Method

Initially, the coal body is under a state of static stress (original stress zone). As mining advances, the coal body experiences the process of loading (stress concentration) and unloading (pressure relief belt) [15]. Corresponding to this, the stress loading and unloading path is as follows: under a certain gas pressure (according to the actual situation of the Xindeng coal mine, here, the gas pressure is 0.6 MPa), the axial compression and confining pressure of the coal samples are loaded to 12 MPa; thereafter, confining pressures are unloaded at a uniform rate under constant axial pressure (12 MPa); the rate of confining pressure and axial compression loading and unloading is set to 0.01 MPa/s; and at the same time, the frequency of permeability datum acquisition is set to 5 seconds. Under the same stress loading unloading path, the permeability of parallel and vertical bedding fracture coal samples will be discussed.

Gas flow through the coal samples is collected automatically by the flow meter, and the permeability is calculated from the following formula [16, 17]:

$$k = \frac{2Q_0 P_0 \mu L}{(P_1^2 - P_2^2)A}, \quad (1)$$

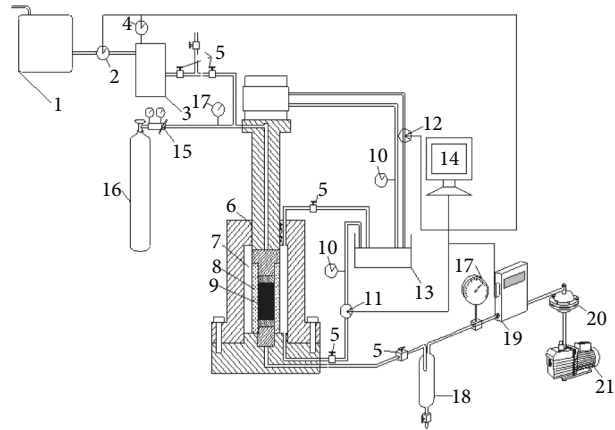
where k is the coal sample permeability, mD; Q_0 is the seepage rate, cm^3/s ; P_0 is the atmospheric pressure at the measuring point, MPa; μ is the gas dynamic viscosity coefficient ($10.8 \times 10^{-6} \text{ Pa s}$); P_1 is the inlet gas pressure (0.6 MPa); P_2 is the outlet gas pressure (0.1 MPa); A is the cross-sectional area of coal samples, cm^2 ; and L is the length of each coal sample, cm. The effective stress of the coal sample is calculated according to the following formula:

$$\sigma_e = \frac{(\sigma_z + 2\sigma_w)}{3} - \frac{(P_1 - P_2)}{2}, \quad (2)$$

where σ_e is the effective stress, σ_z is the axial pressure on the coal sample, σ_w is the confining pressure on the coal samples, P_1 is the inlet gas pressure (0.6 MPa), and P_2 is the outlet gas pressure (0.1 MPa). The specific experimental programme is summarised in Table 1.

4. Experimental Results and Analysis

4.1. Experimental Results. Under the action of stress loading and unloading, the permeability of coal samples with the parallel and vertical bedding are listed in Tables 2 and 3.



(a)



(b)

FIGURE 1: The system and physical figure of triaxial stress gas permeability simulation experiment device: (a) system figure and (b) physical figure. 1 – water tank, 2 – water flow meter, 3 – metering pump, 4 – water pressure gauge, 5 – the valve, 6 – O-ring seal, 7 – pressure chamber, 8 – confining pressure booster aprons, 9 – coal test specimen, 10 – oil pressure gauge, 11 – confining pressure control valve, 12 – axial pressure control valve, 13 – fuel tank, 14 – computer, 15 – pressure release valve, 16 – high pressure gas, 17 – gas pressure gauge, 18 – gas-water separator, 19 – the gas flow meter, 20 – damper, and 21 – vacuum pump.

4.2. *Analysis of Experimental Results.* According to the permeability datum, the permeability and effective stress evolution characteristic curves of coal samples P1, P2, V1, and V2 under the same loading and unloading path are shown in Figure 4.

(1) *In the stress loading process, the gas permeability change trends of the coal samples are similar.* The permeability decrease with increasing effective stress. The permeability of

the P1 and P2 decrease by 84.95% and 84.92%, respectively, when the effective stress reaches 7.75 MPa; meanwhile, the permeability of the V1 and V2 coal samples decrease by 57.30% and 57.25%, respectively. When the effective stress reaches its maximum value of 11.75 MPa, the permeability of the four coal samples fall to 0.00156 mD, 0.00182 mD, 0.00432 mD, and 0.00494 mD, respectively, falling by 98.34%, 98.32%, 75.83%, and 75.97%. P1 and P2 almost lose their permeability capacity. This shows that the four coal

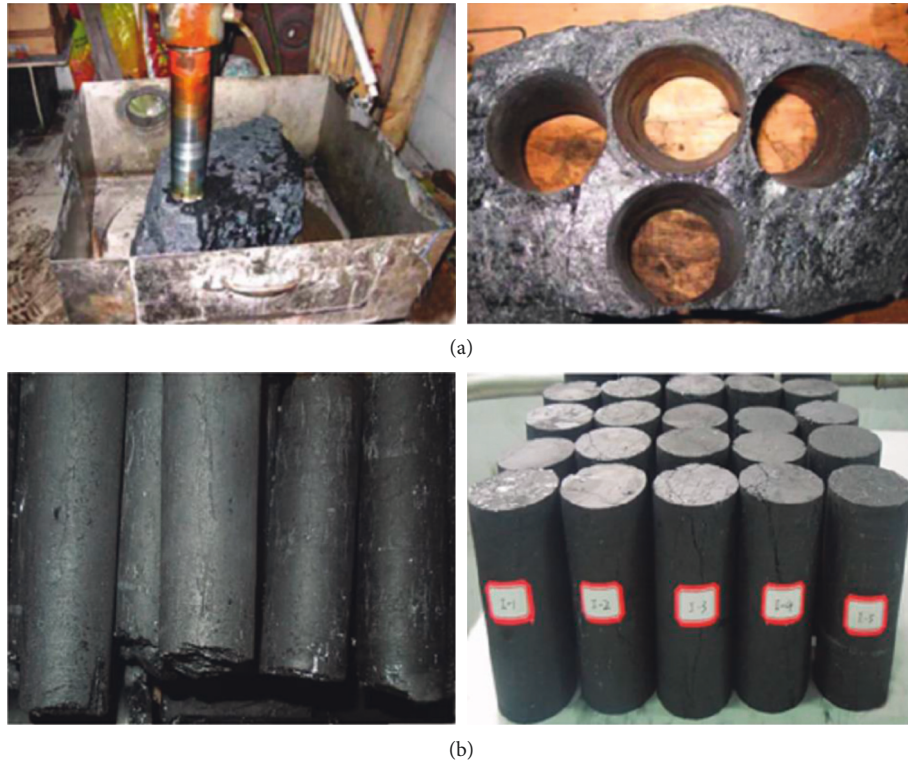


FIGURE 2: Processing and forming of coal samples: (a) machining forming drilling of coal samples and (b) polishing and forming of coal sample.

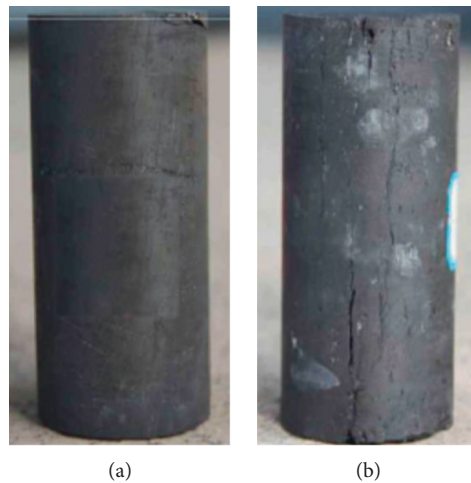


FIGURE 3: Samples with different bedding fracture directions: (a) parallel bedding and (b) vertical bedding.

samples had a significant response to the loading stress in the initial stages of loading. The main reason for this is that cracks are prone to closure under compression, and the permeability decrement is initially rapid albeit it slowed later. The phenomenon could be explained that with the increase of effective stress, the coal sample undergoes three stages [18], namely, crack compaction, elastic deformation, and plastic deformation. When the effective stress is less than 9.75 MPa, the permeability changes rapidly, which can be judged as the coal sample experiencing the first two stages. When the effective stress is greater than 9.75 MPa, the coal

samples enter the plastic deformation stage. The coal samples are gradually compacted, and the permeability become smaller and smaller, and the decrease of permeability gradually become stable, until their permeability were almost lost [19].

The initial gas permeability values of samples P1, P2, V1, and V2 are 0.09396 mD, 0.10814 mD, 0.01787 mD, and 0.02056 mD, respectively, and the ratios of the permeability value of samples with parallel bedding and samples with vertical bedding, namely, k_{0P1}/k_{0V1} and k_{0P2}/k_{0V2} were 5.258 and 5.260, respectively, which indicates that gas is more

TABLE 1: The experimental scheme.

	Inlet gas pressure, P_1 (MPa)	Outlet gas pressure, P_2 (MPa)	Axial compression, σ_z (MPa)	Confining pressure, σ_w (MPa)	Effective stress, σ_e (MPa)
	0.6	0.1	2	2	1.75
	0.6	0.1	4	4	3.75
	0.6	0.1	6	6	5.75
	0.6	0.1	8	8	7.75
Loading process	0.6	0.1	10	10	9.75
	0.6	0.1	12	12	11.75
Unloading process	0.6	0.1	12	12	11.75
	0.6	0.1	12	10	10.42
	0.6	0.1	12	8	9.08
	0.6	0.1	12	6	7.75
	0.6	0.1	12	4	6.42
	0.6	0.1	12	2	5.08

TABLE 2: Permeability of parallel bedding direction coal samples during the loading and unloading process.

	Effective stress, σ_e (MPa)	Permeability, k (mD)			Effective stress, σ_e (MPa)	Permeability, k (mD)	
		Coal sample, P1	Coal sample, P2			Coal sample, P1	Coal sample, P2
Loading process	1.75	0.09396	0.10814	Unloading process	11.75	0.00156	0.00182
	3.75	0.04329	0.04864		10.42	0.00192	0.00243
	5.75	0.02491	0.03096		9.08	0.00262	0.00314
	7.75	0.01414	0.01631		7.75	0.00363	0.00428
	9.75	0.00784	0.01002		6.42	0.00463	0.00528
	11.75	0.00156	0.00182		5.08	0.00511	0.00612

TABLE 3: Permeability of vertical bedding direction coal samples during the loading and unloading process.

	Effective stress, σ_e (MPa)	Permeability, k (mD)			Effective stress, σ_e (MPa)	Permeability, k (mD)	
		Coal sample, V1	Coal sample, V2			Coal sample, V1	Coal sample, V2
Loading process	1.75	0.01787	0.02056	Unloading process	11.75	0.00432	0.00494
	3.75	0.01226	0.01421		10.42	0.00514	0.00591
	5.75	0.00932	0.01072		9.08	0.00565	0.00651
	7.75	0.00763	0.00879		7.75	0.00635	0.00732
	9.75	0.00594	0.00684		6.42	0.00737	0.00841
	11.75	0.00432	0.00494		5.08	0.00866	0.00991

likely to flow along the bedding direction [20]. As seen in Figure 5, the permeability of coal samples P1 and P2 are almost bigger than that of V1 and V2. When the effective stress reaches 11.75 MPa, the permeability of P1 and P2 coal samples become smaller than that of V1 and V2. It can be predicted that with the further increase of stress, the permeability of the parallel bedding coal sample would approach 0.

The relations between permeability and effective stress in the loading process of the four coal samples are obtained through the exponential fitting of permeability evolution characteristics. The relationship between permeability and effective stress is $k = ye^{x\sigma_e}$ (where k is the permeability, σ_e is effective stress, x and y are the fitting coefficients, and R^2 is the correlation coefficient), and the fitting results are shown in Table 4. The fitting coefficients x of coal samples P1 and P2 (-0.3745 and -0.3686) are much smaller than that of V1 and V2 (-0.1353 and

-0.1364), which also fully indicate that the permeability decrease amplitude of parallel bedding is larger than that of vertical bedding.

(2) *In the stress unloading process.* the permeability of the four coal samples increases with decreasing of effective stress, and the increasing trend of permeability is consistent. However, the increasing amplitude is somewhat different. The permeability of the four coal samples (P1, P2, V1, and V2) recover to 168%, 173%, 131%, and 132% of the minimum value, respectively, when the effective stress falls from 11.75 to 9.08 MPa. The permeability increments are 328%, 336%, 200%, and 201% when the effective stress is 5.08 MPa.

In the unloading process, each coal sample has a permeability value corresponding to certain effective stress (11.75 MPa, 1.42 MPa, 9.08 MPa, 7.75 MPa, 6.42 MPa, and 5.08 MPa). The permeability under the same effective stress in the loading process could be calculated through the fitting

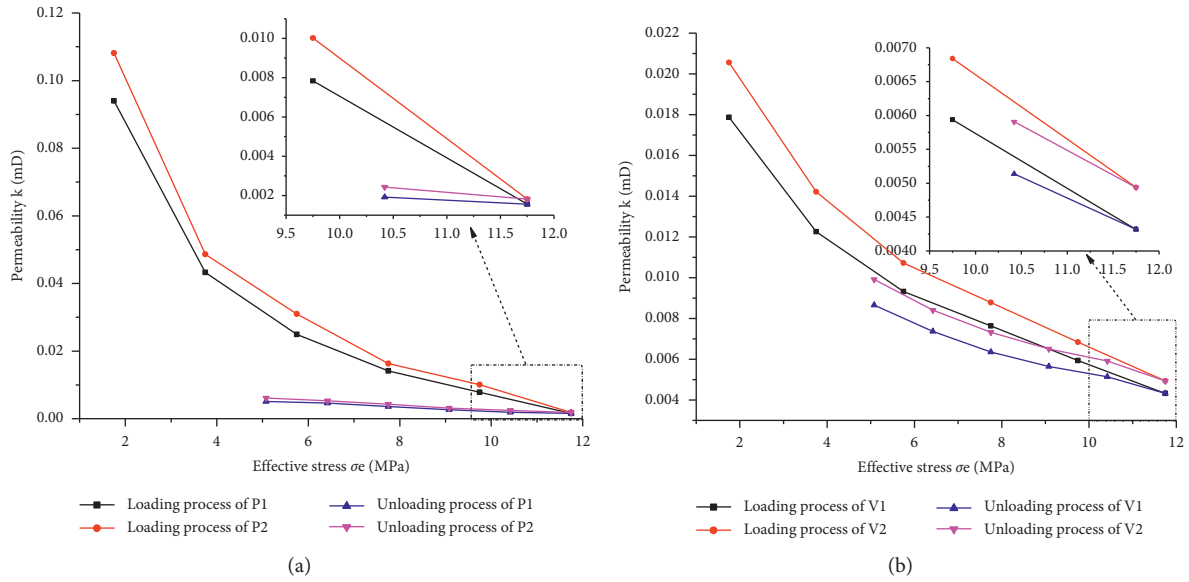


FIGURE 4: Permeability evolution characteristics of coal samples during the loading and unloading process. (a) parallel bedding and (b) vertical bedding.

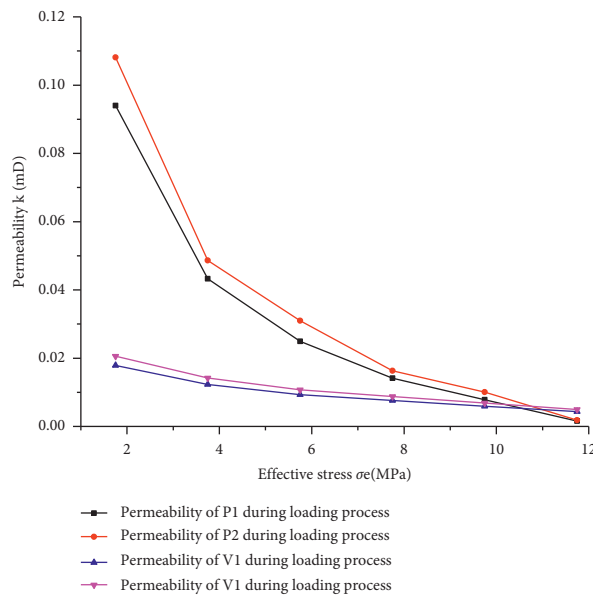


FIGURE 5: Characteristic curve of permeability evolution with effective stress during the stress loading process.

TABLE 4: Fitting results about the relationship between permeability and effective stress during the loading process.

Coal samples	y	x	R^2
P1	0.2013	-0.3740	0.954
P2	0.2299	-0.3686	0.944
V1	0.0214	-0.1353	0.992
V2	0.0247	-0.1364	0.992

formulas corresponding to the coal sample during the loading process (the fitting formulas of the four coal samples were shown in Table 4), and the calculation results are shown in Table 5.

In the unloading process, the permeability of coal samples could not be fully restored to the value of the same

effective stress corresponding to the loading process. In other words, under the same effective stress, there is a certain difference in the permeability of coal samples during the loading and unloading process. This difference reflects the loss of permeability. The larger the loss, the lower the degree

TABLE 5: Calculated permeability value and actual permeability value at the same effective stress.

Effective stress	Calculated permeability value in the loading process				Actual permeability value in the unloading process			
	P1	P2	V1	V2	P1	P2	V1	V2
11.75	0.00249	0.00302	0.00436	0.00500	0.00156	0.00182	0.00432	0.00494
10.42	0.00409	0.00494	0.00523	0.00599	0.00192	0.00243	0.00514	0.00591
9.08	0.00675	0.00809	0.00626	0.00718	0.00262	0.00314	0.00565	0.00651
7.75	0.01109	0.01321	0.00750	0.00861	0.00363	0.00428	0.00635	0.00732
6.42	0.01824	0.02157	0.00898	0.01032	0.00463	0.00528	0.00737	0.00841
5.08	0.03011	0.03534	0.01076	0.01238	0.00511	0.00612	0.00866	0.00991

of permeability recovery, and the higher the anti-sense permeability recovery. The ratio between permeability loss and seepage rate in the loading process could be defined as permeability loss damage rate [21, 22].

The loss rate of coal sample permeability could be used to evaluate the decreased range of coal sample permeability. The higher the damage rate of coal samples permeability, the greater the decrease range of coal samples permeability. The damage rate of coal sample permeability could be calculated according to the following formula [23, 24]:

$$D = \frac{(k_c - k_a)}{k_c} \times 100, \quad (3)$$

where D is the damage rate of coal sample permeability, k_a is the actual permeability value in the unloading process, and k_c is the calculated permeability value in the loading process by the relevant fitting formula. The permeability loss rate of coal sample under the same effective stress is shown in Table 6. The curve of permeability loss rate and effective stress can be drawn according to Table 6, as shown in Figure 6.

As can be seen from Figure 6, the permeability loss rates of the four coal samples increase with the decrease of the effective stress. When the effective stress decrease to 5.08 MPa, the loss rates of the coal sample P1 and P2 are as high as 80%, while the loss rates of the coal sample V1 and V2 are less than 20%. These indicate that the degree of fracture compaction of the parallel bedding coal samples after compression is much higher than that of the vertical bedding coal samples. Even after stress unloading, the degree of fracture recovery is low.

In the process of stress unloading, the change characteristics of permeability with effective stress of the four coal samples are shown in Figure 7. It can be seen that the permeability of the parallel bedding coal samples are always lower than that of the vertical bedding coal samples during the whole unloading process.

(3) *The unloading process of coal samples is not a simple inverse process of the loading process, which can be explained by the deformation of coal sample during stress loading and unloading, as shown in Figure 8.*

The permeability continues to recover with the unloading of effective stress, but the recovery degree of a different coal sample is significantly different. When the maximum loading stress of the coal sample is less than the elastic limitation (A) in the loading stage, there is no plastic damage in the sample, which belongs to the category of elastic deformation. The pores and cracks in the sample can completely be restored after the stress is removed. On the

TABLE 6: Permeability loss rate of coal sample under the same effective stress.

Effective stress	DP1 (%)	DP2 (%)	DV1 (%)	DV2 (%)
11.75	37.22	39.82	1.03	1.14
10.42	53.02	50.78	1.64	1.30
9.08	61.16	61.19	9.81	9.39
7.75	67.28	67.60	15.30	14.97
6.42	74.62	75.52	17.91	18.48
5.08	83.03	82.68	19.54	19.94

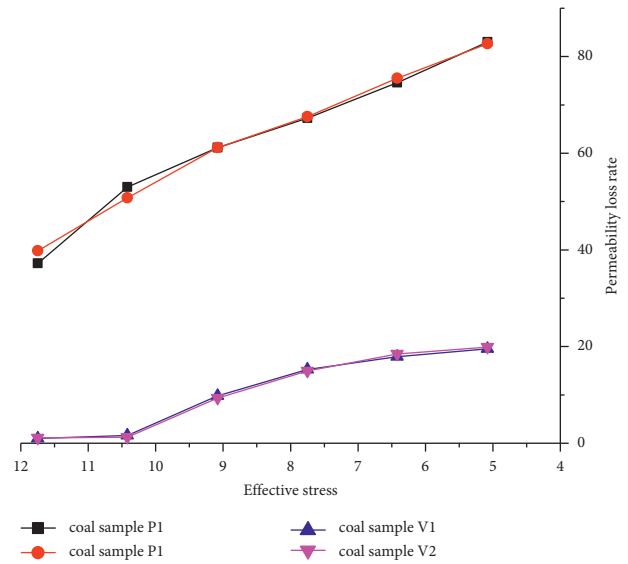


FIGURE 6: Curve of permeability loss rate and effective stress.

contrary, the stress-strain curve will deviate from the curve of the loading process and are unable to return to the origin, as the PC curve shown in Figure 8.

5. Engineering Verification

The test mine is a coal and gas outburst mine. The average thickness of No. 3 coal seam is 6 m; the bedding fissure is developed along the dip direction coal seam; and the gas content of the coal seam reaches 12 m³/t on average, having the characteristics of large outburst risk, low coal seam permeability coefficient, and poor degas effect. According to the “Rules for Prevention and Control of Coal and Gas Outbursts” in China (revised in 2019), two ways of gas predrainage are taken to protect the coal roadway tunneling, including drilling boreholes through the floor rock roadway and along the coal seam [25].

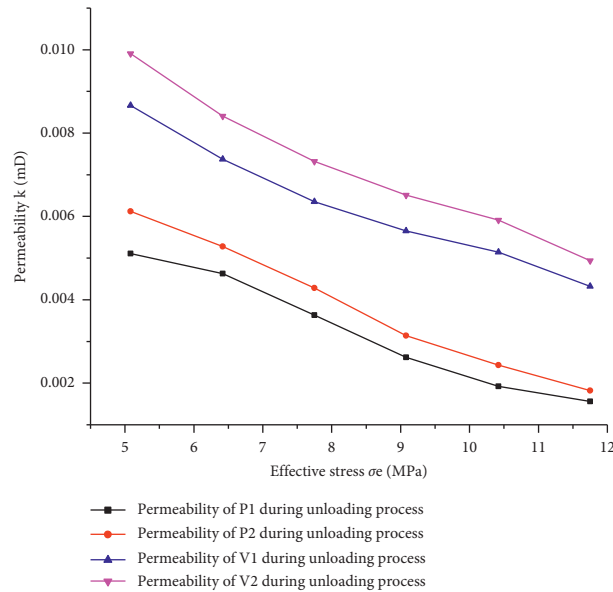


FIGURE 7: Characteristic curve of permeability evolution with effective stress during the stress unloading process.

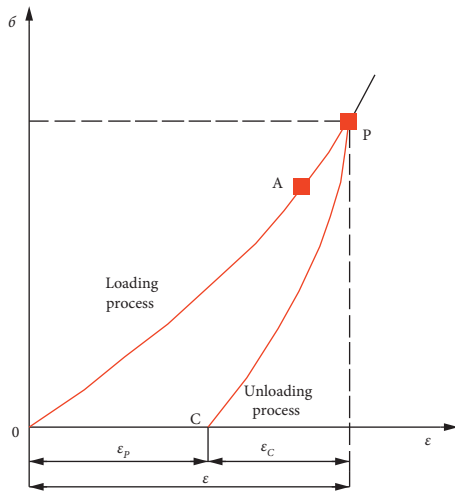


FIGURE 8: Stress-strain curve of coal sample during loading and unloading.

The return air roadway of 11,053 working face has been tunneled through. Before heading into the intake airway of 11,053 working face, drilling boreholes along coal seams in the direction of the intake airway are arranged in the return air roadway; meanwhile, drilling boreholes through coal seams are arranged in the floor rock roadway, as shown in Figure 9.

Arrangement of the two types of drilling is approximately perpendicular and parallel to the direction of bedding, respectively, being regarded as parallel bedding and vertical bedding gas drainage boreholes. With the advance of the driving working face, there will be three zones of stress in front of the working face, namely, pressure relief zone, stress concentration zone, and original stress zone [26]. A group of parallel bedding and vertical bedding gas drainage boreholes were selected to monitor the gas drainage concentration for 40 days. At this time, the gas drainage concentration of the

two groups reflects the permeability of gas along the direction of coal bedding and vertical bedding during stress loading and unloading. The gas drainage concentration of the two groups of boreholes is shown in Table 7. Curves about gas drainage concentration with time of parallel and vertical bedding drilling boreholes are drawn according to the monitored datum, as shown in Figure 10.

According to Figure 10, it can be seen that in the early stage of gas concentration monitoring, the gas drainage concentration of the two groups of drainage holes did not change much, mainly because the in situ stress conditions of the drilling holes did not change, and they were both in the original stress zone. However, the gas concentration of the vertical bedding gas drainage boreholes was always greater than that of the parallel bedding boreholes (sections P_a-P_b and V_a-V_b in Figure 10).

As the roadway moved forward, the stress concentration zone also moved forward, and the stress at the location of the gas drainage hole increased, which was equivalent to loading the coal body [27]. With the increase of loading stress, the permeability of the coal body at the drilling hole became lower and lower, and the gas drainage concentration of the drilling hole also decreased. When the stress was loaded to the peak value, the permeability of the coal seam dropped to the lowest value in the loading process, which reflected that the gas drainage concentration was the lowest (sections P_b-P_c and V_b-V_b in Figure 10). This stage was equivalent to the stress loading stage in the experimental process. It could be seen that the permeability in the vertical bedding direction of the coal body is always greater than that in the parallel bedding direction during the whole loading process.

With the further advance of the tunneling roadway, the stress concentration zone continued to advance, and the stress on the coal body became smaller and smaller [28, 29]. The permeability of coal increased with the stress unloading; the reaction to the gas drainage holes was that the gas drainage concentration was getting higher and higher

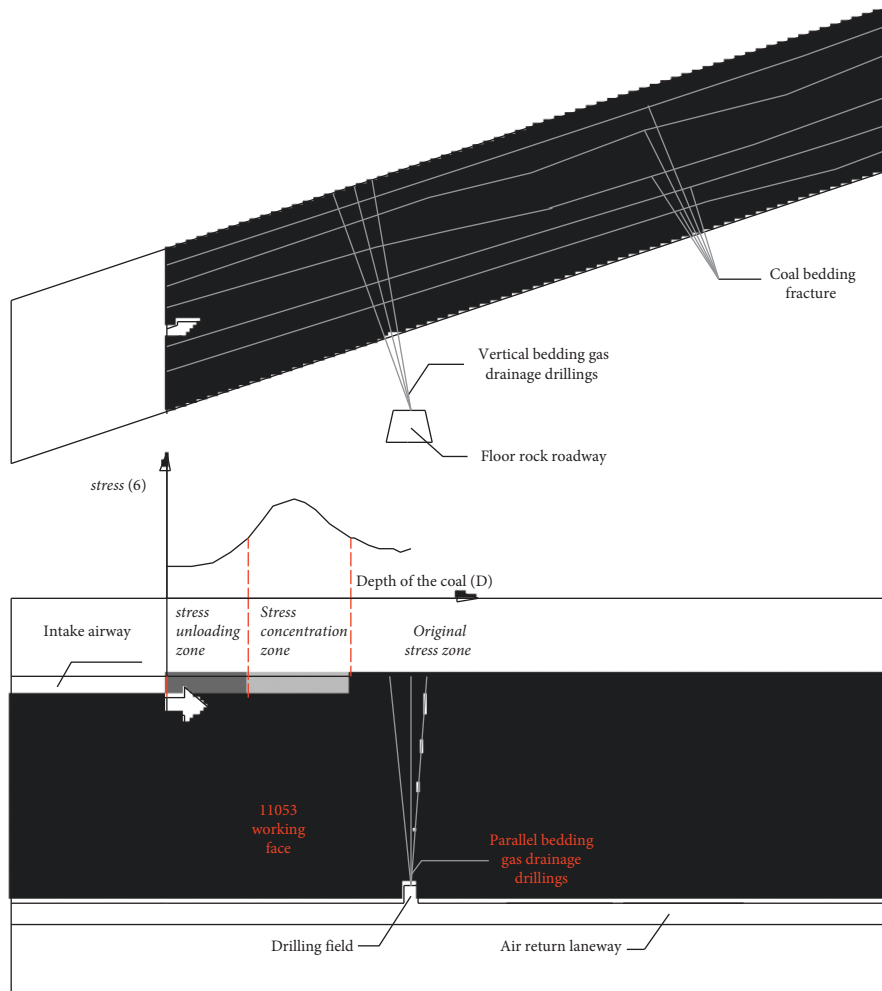


FIGURE 9: Gas drainage drillings layout along and through layers layout in 11,053 working face.

TABLE 7: Gas concentration of parallel bedding and vertical bedding drilling boreholes.

Ged (d)	Gc (%)		Ged (d)	Gc (%)		Ged (d)	Gc (%)		Ged (d)	Gc (%)	
	Pd	Vd		Pd	Vd		Pd	Vd		Pd	Vd
1	39.43	53.22	21	5.81	7.47	11	36.94	49.86	31	53.12	75.95
2	39.84	53.78	22	12.45	17.43	12	34.03	45.94	32	59.35	82.59
3	39.01	52.66	23	17.43	24.07	13	31.54	42.58	33	64.74	87.64
4	40.26	54.34	24	23.66	31.96	14	28.22	38.1	34	68.89	84.23
5	40.67	54.9	25	28.22	38.6	15	24.9	33.62	35	67.65	86.71
6	39.84	53.78	26	31.96	45.65	16	22.41	30.25	36	68.89	87.11
7	40.26	54.34	27	35.28	51.88	17	19.51	26.33	37	67.65	85.12
8	41.09	55.46	28	39.01	57.69	18	16.19	21.85	38	67.23	87.63
9	39.84	53.78	29	43.58	63.08	19	11.21	15.13	39	68.06	85.42
10	39.01	52.66	30	46.9	68.48	20	6.23	8.4	40	68.89	83.45

Notes. Ged – gas extraction days, Gc – gas concentration, Pd – parallel bedding drilling, and Vd – vertical bedding drilling.

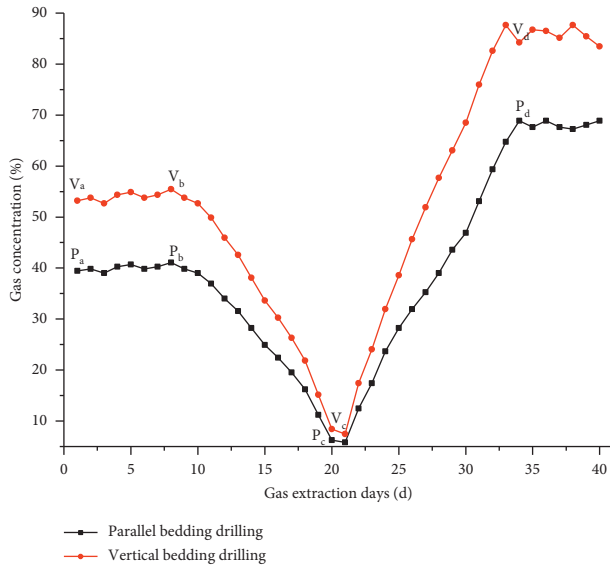


FIGURE 10: Curve about gas drainage concentration with time of parallel and vertical bedding drilling boreholes.

(sections P_c – P_d and V_c – V_d in Figure 10). This stage was equivalent to the stress unloading stage in the experimental process. In the whole unloading process, the permeability in the vertical bedding direction of the coal body was also always greater than that in the parallel bedding direction.

6. Conclusion

- (1) In the stress loading process, the permeability of the parallel bedding coal sample would approach 0. Therefore, gas drainage boreholes should not be arranged in a direction along the bedding in the severely compressed seam.
- (2) In the stress unloading process, it could be seen that the permeability of the parallel bedding coal samples are always lower than that of the vertical bedding coal samples during the whole unloading process. Therefore, in the stress-relieved coal seam, gas drainage boreholes should be arranged vertically to the bedding fissure to maximise the gas drainage effect.
- (3) Field engineering practice also proves that when gas drainage is arranged in the coal seam containing bedding cracks, the drilling direction should be perpendicular to the bedding direction as far as possible, so as to improve the gas drainage effect.

The results of laboratory study and engineering practice provide some guidance for the rational arrangement of gas drainage boreholes and improvement of gas drainage concentration in the coal mine. This ensures the sustainability of the gas drainage effect and is of great significance to reduce the occurrence of mine gas accidents.

Data Availability

The data used to support the findings of this study are included within the article.

Conflicts of Interest

The authors declare that they have no conflicts of interest.

Acknowledgments

The authors gratefully acknowledge the financial support from the National Natural Science Foundation of China (52174168), the Science and Technology Innovation Team Program of Henan Universities (22IRTSTHN009), the Science and Technology Project of Henan Province for Tackling Key Problems (222102320466), the Research and Cultivation Fund of Henan University of Engineering (PYXM202017), and the Research Project of Education and Teaching Reform of Henan University of Engineering (2021JYYB001).

References

- [1] J. Liu, H. Sun, L. Yi, and C. Jie, “Current situation and development trend of coalbed methane development and utilization technology in coal mine area,” *Journal of China Coal Society*, vol. 45, no. 1, p. 258, 2020.
- [2] X. Chen, R. Liu, and B. Xie, “Productivity model of fractured horizontal wells in shale oil reservoirs with bedding fractures considered,” *Xinjiang Oil & Gas*, vol. 18, no. 1, pp. 73–79, 2022.
- [3] F. Zhang, “Gas technology of uniform pressure sealing gas drainage in fissure development area,” *Safety In Coal Mines*, vol. 51, no. 3, pp. 79–83, 2020.
- [4] W. Zhang, C. Zheng, S. Xue et al., “Study on gas drainage characteristics based on permeability anisotropy of coal,” *Safety in Coal Mines*, vol. 51, no. 7, pp. 6–11, 2020.
- [5] G. Yue, H. Liu, J. Yue, and M. W. Li, “Influence radius of gas extraction borehole in an anisotropic coal seam: underground in-situ measurement and modeling,” *Energy Science & Engineering*, vol. 7, no. 3, pp. 694–709, 2019.
- [6] X. Huang, “Experimental study on influence of structural anisotropy of coal upon gas permeability,” *Mining Safety and Environmental Protection*, vol. 39, no. 2, pp. 1–3, 2012.
- [7] R. Pan, Y. Cheng, and J. Dong, “Research on permeability characteristics of layered natural coal under different loading and unloading,” *Journal of China Coal Society*, vol. 39, no. 3, pp. 473–477, 2014.
- [8] B. Deng, X. Kang, and L. I. Xing, “Effect of different bedding directions on coal deformation and permeability characteristic,” *Journal of the China Coal Society*, vol. 40, no. 4, pp. 888–894, 2015.
- [9] P. Cen, K. Tian, E. Wei, S. Liu, and C. Bi, “Axial effect of gas seepage in bedding fractured coal under multistage loading and unloading and its application,” *Safety In Coal Mines*, vol. 52, no. 12, pp. 9–14, 2021.
- [10] S. Wang, D. Elsworth, and J. Liu, “Permeability evolution in fractured coal: the roles of fracture geometry and water-content,” *International Journal of Coal Geology*, vol. 87, no. 1, pp. 13–25, 2011.
- [11] Y. Wu, J. Liu, D. Elsworth, and H. X. Siriwardane, “Evolution of coal permeability: c,” *International Journal of Coal Geology*, vol. 88, no. 2–3, pp. 152–162, 2011.
- [12] H. Li, S. Shimada, and M. Zhang, “Anisotropy of gas permeability associated with cleat pattern in a coal seam of the Kushi coalfield in Japan,” *Environmental Geology*, vol. 47, no. 1, pp. 45–50, 2004.

- [13] D. Yu, Z. Yang, Y. Guo, Y. G Yang, and B Wang, "Inversion method of initial geostress in coal mine field based on FLAC^{3D} transverse isotropic model," *Journal of China Coal Society*, vol. 45, no. 10, pp. 3427–3434, 2020.
- [14] K. Tian and G. Wang, "Gas seepage behaviors revealed by two kinds of typical soft and hard raw coals under high pressure water," *International Journal of Earth Sciences and Engineering*, vol. 9, no. 2, pp. 866–871, 2016.
- [15] J. Wei, D. Wang, and W. E. I. Le, "Comparison of permeability between two kinds of loaded coal containing gas samples," *Journal of China Coal Society*, vol. 38, no. Supp. 1, pp. 93–99, 2013.
- [16] X. Yuan, B. Liang, and W. Sun, "Research on permeability evolution model for coal seam being drained by pressure relief," *China Safety Science Journal*, vol. 26, no. 2, pp. 127–131, 2016.
- [17] A. L. A. M. A. K. M. Badrul, N. Masaki, Y. O. S. H. I. A. K. I. Fujii, F Daisuke, and K Jun-ichi, "Effects of confining pressure on the permeability of three rock types under compression," *International Journal of Rock Mechanics and Mining Sciences*, vol. 65, pp. 49–61, 2014.
- [18] J. Liu, *Seepage Characteristics of Loaded Coal under True Triaxial and Its Application in Gas Extraction*, China University of Mining and Technology, Beijing, China, 2017.
- [19] R. Pan, *The Permeability Evolution Characteristics of Loaded Coal and Its Application in the Drainage of Pressure-Relief Gas*, China University of Mining and Technology, 2014.
- [20] H. Yu, F. Chen, W. Chen, J. Yang, J. Cao, and K. Yuan, "Research on permeability of fractured rock," *Chinese Journal of Rock Mechanics and Engineering*, vol. 31, no. S1, pp. 2788–2795, 2012.
- [21] M. Thommes, K. Kaneko, and A. V. J. P. F. J. K. S. W Neimark, "Physisorption of gases, with special reference to the evaluation of surface area and pore size distribution (IUPAC Technical Report)," *Pure and Applied Chemistry*, vol. 87, no. 9-10, pp. 1051–1069, 2015.
- [22] Y. Liu, "Experimental analysis of coal permeability evolution under cyclic loading[J]," *Journal of China Coal Society*, vol. 44, no. 8, pp. 2579–2588, 2019.
- [23] D. Wang, J. Wei, and G. Yin, "Investigation ON change rule OF permeability OF coal containing gas under complex stress paths," *Chinese Journal of Rock Mechanics and Engineering*, vol. 31, no. 2, pp. 303–310, 2012.
- [24] M. Jing and X. Yuan, "Experimental research ON core stress sensitivity OF carbonate rock," *Natural Gas Industry*, vol. 20, no. S, pp. 114–117, 2002.
- [25] State Administration of Coal Mine Safety, *Rules for Prevention and Control of Coal and Gas Outbursts*, Coal Industry Press, 2019.
- [26] J. Gao and S. Hou, "Dynamic distribution of gas pressure and emission Around adiving roadway," *Journal of China Coal Society*, vol. 32, no. 11, pp. 1127–1131, 2007.
- [27] F. Cai and Z. Liu, "Simulation and experimental research on upward cross-seams hydraulic fracturing in deep and low-permeability coal seam," *Journal of China Coal Society*, vol. 41, no. 1, pp. 113–119, 2016.
- [28] X. Kong, E. Wang, Q. Liu, and Z. D. Z. Y. Li, "Dynamic permeability and porosity evolution of coal seam rich in CBM based on the flow-solid coupling theory," *Journal of Natural Gas Science and Engineering*, vol. 40, pp. 61–71, 2017.
- [29] J. Fu, X. Fu, and Y. Jiang, "Fundamental study on gas drainage and extraction from pressure-relieved zone of a single seam with low gas permeability," *Mining Safety & Environmental Protection*, vol. 39, no. 1, pp. 4–7, 2012.